Integrity Evaluation of Offshore Wind Turbine MP-TP Connection Technologies

A Thesis submitted for the Doctor of Philosophy in

Renewable Energy Marine Structures (REMS PhD)

by

Alessandro Annoni

Glasgow, April 2024

Department of Naval Architecture, Ocean & Marine Engineering

University of Strathclyde, United Kingdom

G1 1XQ

Abstract

To reach net-zero emissions in the UK by 2050, in accordance with Paris agreement (2016), the imperative role of renewable energy production has become evident globally. With the exponential growth in the installed capacity of offshore wind energy in the UK and around the world, the industry is continuously increasing the capacity of wind turbines, subsequently requiring larger structures to support them. Offshore wind turbines often consist of a foundation, a transition piece, and a tower. One critical component of the offshore wind turbine structures is the connection between the Monopile (MP) foundation, which is largely employed in the majority of offshore wind turbines currently installed around the world, and the Transition Piece (TP). This thesis investigates the suitability of both current and alternative MP-TP connection technologies to provide an in-depth knowledge of the advantages and disadvantages of each technology for potential use in future offshore wind farms.

In this research study Finite Element Analysis (FEA) and analytical calculations are employed to investigate three distinct MP-TP connection technologies: threaded connection, C1 wedge connection and Slip Joint technologies. Further investigations have been carried out by re-analysing the existing fatigue data on various size and threaded connections available in the literature. Furthermore, through conducting new fatigue tests, this thesis contributes a comprehensive evaluation of the accuracy of the fatigue design curves recommended in international standards for large-scale bolted connections. The findings from this study underscore the potential of the existing flanged bolted connection technology as well as two novel technologies — namely C1 connection and Slip Joint — to address current and future challenges associated with the increasing size of offshore wind turbine structures. Moreover, they highlight the need for various feasible alternative solutions for MP-TP connections to be considered and employed in future offshore wind farms. This thesis provides a comprehensive analysis of the advantages and disadvantages of the mentioned MP-TP technologies. It identifies areas for further research to address the existing gaps in knowledge and enhance understanding of these innovative technologies for deployment in future offshore wind farm projects.

Acknowledgements

Declaration

I hereby declare that this thesis is the result of my original research and has not been previously submitted for examination which has led to the award of a degree. Information derived from the published and unpublished work of others has been acknowledged in the text and references are provided in the list of sources.

Table of Contents

List of Figures

xi

List of Tables

xiii

Nomenclature

Chapter 2 Evaluation of Aerodynamic Loads on Offshore Monopile Structure

A	Circular area covered by blades rotation
$A_{V,i}$	Vertical sectional area for i-section of tower
A_i	Circumferential area section
b	Distance of load barycenter of wind pressure from the ground
c	Distance from neutral axis
C_D	Drag coefficient
D	External tower diameter
d	Internal tower diameter
$F'_{wind,pressure}$	Equivalent wind load pressure
$F_{wind,blade}$	Horizontal load from drag result of window on blades
$F_{wind,pressure,i}$	Air pressure load on tower
h	Specific height
H_L	Horizontal load component
I	Moment of Inertia about neutral axis
K	Von Karman constant
L	Scale factor / Monin-Obukhov length
L_n	Distance of nacelle from ground
M_L	Momentum component
M	Bending moment load
R	External tower radius
r	Internal tower radius
V_L	Vertical load component
v_f	Friction velocity
V_h	Wind speed at specific height h
V_{hub}	Wind speed at the hub heigh
V_i	Local wind speed
z_0	Surface roughness length
α	Friction coefficient or Hellman exponent
P_{air}	Air pressure
σ	Stress
σ_{max}	Maximum stress
$\xi\left(\dfrac{z}{L}\right)$	Solar radiation function on the site

Chapter 3 Error! Not a valid result for table.

$\Delta S*$	Corrected Stress range
$\Delta\sigma$	Defined stress range
$\Delta\sigma_c$	Reference stress value of the fatigue strength to $_{Nc}$
$\Delta\sigma_D$	Fatigue limit for constant amplitude stress at N_D
$\Delta\sigma_L$	Cut-off limit for stress range at N_L
A	Bolt cross-sectional area
c	Distance of the interested point from the axis
C_d	Parameter that correlates mean S-N curve with SD
d_3	Screw's root bolt diameter
F_{app}	Applied load
f_c	Friction coefficient between collar surfaces
F_{max}	Max applied load
F_{min}	Min applied load
f_t	Friction coefficient between threads surfaces
h	Thread heigh
I	Moment of inertia
J	Second polar moment
K_T	Torque coefficient
Log a	Intercept of mean S-N curve
Log ā	Intercept of S-N design curve
*Log a**	Corrected intercept of mean S-N curve
M	Bending load on threads
m	S-N curve slope
N	Predicted number of cycles to failure for $\Delta\sigma$
$N*$	Corrected number of cycles
n_c	Number of engaged threads
N_R	Design lifetime (cycles) related to constant stress range
R^2	Coefficient of determination
R_3	Screw's root bolt radius
r_c	Collar radius
r_T	Thread radius
S_A	Stress amplitude
S_A*	Corrected Stress amplitude
SD	Standard deviation
S_L	Stress limit
s_{LogN}	Standard deviation on *Log N*

S_M	Mean stress
S_r	Stress range
S_{UTS}	Ultimate tensile stress
S_{VM}	Von Mises stress
T	Torque load
t	Thickness
t_{ref}	Reference thickness
x	Distance from flat surface
x_c	Distance from barycentre
α	Half of thread angle
λ	Lead angle
τ	Tangential stress
Ω	Degree of bending

Chapter 4 C1 Wedge Connection

$\Delta d_{horizontal}$	Total horizontal displacement
$\Delta d_{vertical}$	Total vertical displacement
a	Semi-major axis of ellipse
b	Semi-minor axis of ellipse
C	Monopile circumference
DF	Displacement Factor
D_{hole}	Hole diameter
D_{MP}	Monopile diameter
E	Young modulus
F_{bolt}	Preload bolt
$F_{fric,i}$	Friction load between block i and wedges
k_t	Concentration factor
l	Ligament width between holes
L	Distance between radius R_1 and R centers
LF	Load Factor
n	Number of holes around the circumference
ϕ	Inclination angle of tangential connection
R	Smaller radius
r	Ellipse radius
R_1	Larger radius
t	Wall thickness
W	Monopile segment width
α	Upper block wedge slope

β		Lower block wedge slope
θ		Maximum stress concentration factor angular position
μ		Friction factor
v		Poisson's ratio

Chapter 5 Slip Joint Connection

$\Delta L_{overlap}$	Total flange length
D	Average slip joint diameter
D_1	External monopile upper diameter
D_2	Transition piece flange slope
D_{MP}	External Monopile diameter
D_{TP}	Internal transition piece upper diameter
F_g	Gravity load
F_r	Resultant force
h	Flange height
L_{slip}	Total length left to cover
M_B	Momentum load from turbine
T	Wall thickness
X	Flange length multiplicator factor
α	Monopile flange slope
β	Internal transition piece bottom diameter
θ	Angular position
μ	Friction factor
σ_t	Hoop stress

Chapter 1 Offshore Wind Turbine (OWT) structure

1.1. Introduction

Fighting climate change by reducing carbon emissions and decreasing fossil fuels dependence are two main strategies highlighted in the Paris Agreement[1], adopted in 2015, and signed by 194 countries. This document stands as a landmark international accord aimed at addressing the global challenge of climate change. The agreement outlines a collective adherence to limit global warming to well below 2°C above pre-industrial levels, with efforts directed towards achieving a 1.5°C target. General objective of this agreement is the net-zero emissions goal by the year 2050, this is an imperative and urgent objective that reflects the common recognition of the need to mitigate the adverse impacts of climate change. As nations strive to meet this target, a transformative shift towards sustainable practices and renewable energy sources becomes crucial, ushering in a new era in the fight against climate change. As countries grapple with the complexities of this transformative journey, the net-zero goal becomes a linchpin in fostering international cooperation, driving technological advancements, and shaping policies that align with a sustainable, low-carbon future. As mentioned, the use of renewable energy is imperative to achieve the Paris agreement goals: in recent years the amount of energy provided by renewable energy has increased [2], as illustrated in Figure 1-1. One of the main renewable sources of energy is wind energy, which gets produced through the use of "wind turbines", i.e. the main focus of this thesis project.
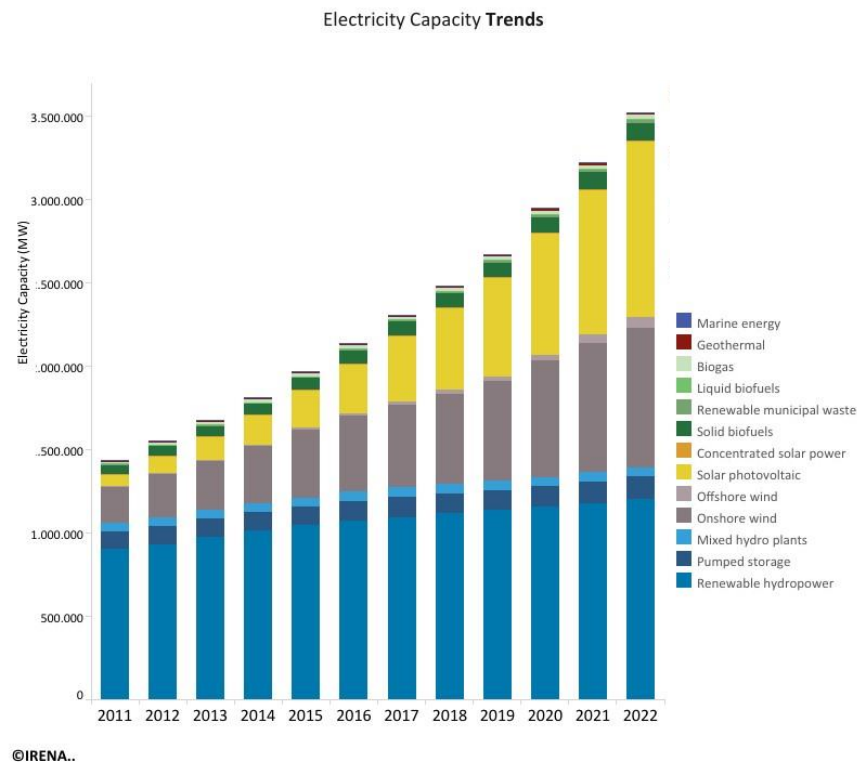
Figure 1-1: Electricity Capacity Trends[2]

In general, the term "Wind Turbine" refers to the entire structure, which can be categorized into two main sections: the support structure and the Rotor-Nacelle assembly (RNA). As depicted in Figure 1-2, the support structure, can be further divided into three key sections: Foundation, Substructure and Tower. The foundation specifically refers to the part of Monopile that extends under the mudline, the substructure encompasses the remaining portion of the monopile and the transition piece together and the Tower is defined as the cylindrical component linking the substructure to the RNA. Each of these sections plays a crucial role and warrants careful examination for distinct reasons. The foundation provides essential stability, the substructure acts as an intermediary support structure. Meanwhile, the tower serves to connect the substructure to the RNA, facilitating the overall functionality of the wind turbine.

The study of these individual sections is imperative due to their specific functions and significance in the overall performance, structural integrity, and maintenance considerations of wind turbines. Engineers and researchers investigate various aspects such as material strength, aerodynamics, and environmental factors to optimize the design and operation of these structures.
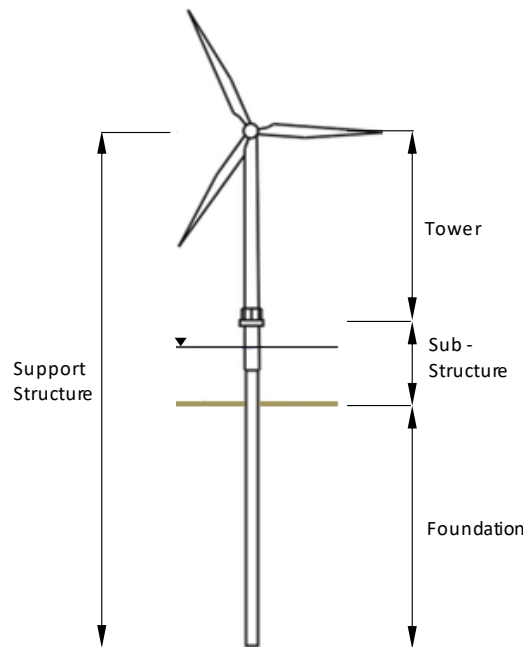
Figure 1-2: Support structure division for OWT

For the aim of this thesis, a deeper examination has been conducted on the foundations, which can be identified as the part of the structure in direct contact with the soil. The main objective of the foundations is transferring the loads from the structure to the soil. In order to do this, various factors need to be taken into consideration: key factors are deep water, composition of the seabed, metocean conditions and the turbine size. Secondary factors considered by the engineers are the local fabrication capabilities, the Transport and Installation (T&I), the Operation and Maintenance (O&M) and the decommissioning at the end of the life span[3]. The key factors that affect the design are described below.

Water depth is an evident and critical factor. Accessible shallow-water sites have already been exhausted in some parts of the world, and around 80% of global offshore wind resources are in water over 60m [3]. Secondly, the Seabed composition is an important factor, which requires

a clear understanding of the geotechnical condition at a WT farm site, as a weak soil can lead to excessive penetration, while a hard layer can limit the pile derivability.

Metocean Condition, derived from the combination of meteorology and oceanography words, encompasses the examination of atmospheric and oceanic factors in offshore endeavours. This study includes several factors, such as water current, offshore wind patterns, sea state, water proprieties and air temperatures. By gaining a deep understanding of local metocean conditions it is possible to optimize efficiency across all the stages of an offshore project, from initial planning studies to operational maintenance and future decommissioning.

The size of the turbine plays a key role in foundation design. As the turbine size increases, along with the rotor dimensions, the foundations must withstand higher levels of loading. Essentially, the larger the turbine and rotor, the more resilient the foundation needs to be to handle elevated loads. This emphasizes the critical significance of crafting foundations that can meet the growing demands posed by larger turbines and rotors in the field of renewable energy infrastructure.

Comparing offshore wind turbines to the onshore ones, the production of foundation for offshore WT is much more complex in terms of design and construction [4]. The majority of offshore wind farms are commonly located about 10 km off the coast in water depths of about 10m. Offshore wind turbines must be located above the crest level of the highest waves, and estimations indicate that the cost of an offshore wind unit is around two or three times that of an onshore wind unit. [4], [5] Considering the cost of foundations, offshore foundations account for an increase of 20–30% compared to onshore structures[6]. This contributes to the higher cost of offshore wind turbines compared to onshore ones. Therefore, an accurate selection of a suitable foundation type for offshore wind turbines is key to exploitation of offshore wind energy.

1.1.1. Foundation Design

Depending on the key factor previously presented, the OWT foundation can be designed in accordance with the concepts illustrated in Figure 1-3, the four main design for fixed bottom structure are the gravity-based (or GBS), the monopile (MP), the tripod and the jacket (lattice structure) foundation. In this section, the main characteristics of these design have been presented and resumed in Table 1-1.
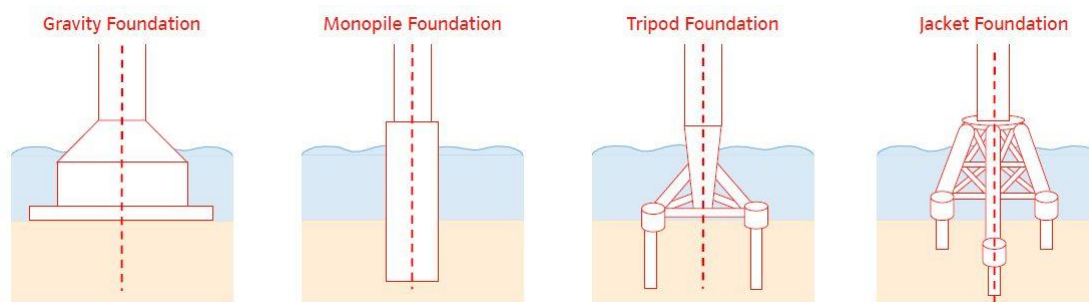
Figure 1-3 Main foundation concepts: Gravity-based foundation (GBS), monopile foundation (MP), Tripod foundation, Jacket foundation[7]

Gravity-based Foundation

The gravity-based foundation (or GBS), as its name suggests, utilizes gravitational force to stabilise its position[8], as illustrated in Figure 1-4a. The ballast commonly consists of rock,

iron ore, or concrete, that presents a large footprint to absorb moments from the wind and waves. Installation is conceptually simple: after positioning the foundation, it is filled with ballast, causing the body to sink, and settle on the seabed. The main disadvantages of this design involve seabed preparation, manufacturing, and transportation of the structure [9]. For the nature of foundation, stable ground conditions are essential preferably compacted clay, sandy soil, or rock. Another key factor is the manufacturing site: logistics including fabrication, transportation and installation must be well-organised. This technology is usually preferred for structures in shallow waters (<30 meters), although the deepest deployment is visible at the Fécamp (France) OWF with 50 meters depth. Other examples are Rødsand II (2008), Nysted (2003) in Denmark and Fécamp (2023) in France [10].

Monopile Foundation
The Monopile foundation design consists of a single steel tube pile made by plates rolled and welded together. This structure is presented in Figure 1-4b. Thanks to its relatively simple production, low cost, and manageable installation, along with its suitability for a wide range of exploitable water depths, the monopile the most widely used support structure concept. Depending on the seabed conditions, the installation method can involve hammering the pile into the seabed using a hydraulic hammer, for seabed with clay, sand, or chalk stratigraphy or drilling a hole to insert the foundation in rocky seabeds. When the structure follows the first procedure, the addition of a sub-structure called "Transition Piece" is required, while it is not necessary when installation is done by drilling.

The main issue about this type of foundation is related to the reduction of seabed around the monopile caused by water currents, known as scour[11]. This effect is mainly influenced by the metocean conditions of the site and the soil conditions. This effect causes an increased section of the pile exposed to sea loads, consequently altering the dynamic behaviour of the structure from the designed one. To mitigate this problem, one solution is protecting the soil around the monopile[12]. Different kinds of protection can be used, ranging from asphalt to concrete mattresses, but these installations can be very expensive. The most cost-effective method involves placing one (or multiple) layer of rocks around the structure so to reduce the scour effect.

According to WindEurope [10], example of Monopile foundation in Europe are Kaskasi (2018) in Germany, Vesterhav Syd (2016) in Denmark, Hornsea One and Two (2019 and 2022) and the Triton Knoll (2017) in UK and Sain-Nazaire (2012) in France.

Tripod Foundation
A Tripod foundation is designed to enhance the stability of the structure by using three legs diverging from a single node to the respective positions of the seabed, as illustrated in Figure 1-4c. The installation includes transporting the structure onto a barge to the designed location, then lifting the structure with a crane and the position adjustments using a smaller crane. Structurally, the main node, where the three legs meet the central column, is sensitive to fatigue.

Examples of Offshore Wind Farms (OWF) with Tripods foundations are Alpha Ventus (2010) and Global Tech I (2015) in Germany and Nogersund (1990) in Sweden [10].

Jacket Foundation
The Jacket foundation is based on a structure that can be classified by the number of structured legs: three or four. Generally speaking, the jacket structure is based on a frame structure pre-

assembled on land, with interconnected corner piles linked with bracing (Figure 1-4d). Compared to other foundations, Jacket foundations are relatively economical in terms of steel consumption. However, storage, logistics, and installation can be expensive, substantially increasing the overall cost. Typically, this type of foundation is used in intermediate water depths ranging from 50 to 60 m. Examples of OWF where this foundation is used are Moray East (2017) and Seagreen (2019) in UK, Dieppe / Le Tréport (2012) in France [10].
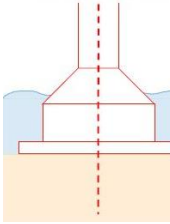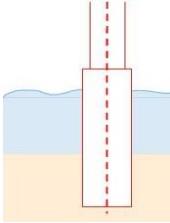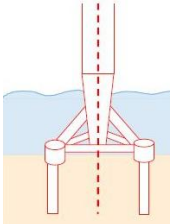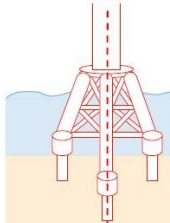
<table>
<tr><td>(a)</td><td>(b)</td></tr>
<tr><td>(c)</td><td>(d)</td></tr>
</table>

Figure 1-4 Size comparison between the four main foundation design: gravity based[13] (a), Monopile[14] (b), Tripod[15] (c) and jacket (d).

Table 1-1 Characteristics of the four main foundation designs in OW Farm

Type of Foundation		Characteristics	Water depths
Gravity Foundation (GBS)		Self-weight supported and foundations made by reinforced concrete with ballast. Required a preparation of the seabed. Required a logistic preparation for on place manufacturing and transportation	up to 30 meters (Fécamp (FR) at 50meters)
Monopile foundation (MP)		Simple design and structure made by steel foils rolled and welded together. Depending on seabed nature can require a drilling process. Constructed onshore and demands small seabed preparation.	up to 30 meters (Arcanis Ost 1 (DE) at 45 meters)
Tripod foundation		Expansion of the concept of the monopile foundation to adapt to deeper water depths. Provides better stability and improves the stiffness of the entire structure. Big and heavy structure, thus increases manufacturing and transportation costs	up to 50 meters
Jacket foundation		Higher cost of manufacturing and installation. High stiffness, making it high resistant to wave loads. Mostly used as a transitional substructure.	from 50 to 60 meters (some up to 80 meters)

1.2. MP-TP Connection

With the term MP-TP connection, we consider the section that allows load transmission between the Monopile and the Transition Piece, as pointed in Figure 1-5. This section is a critical point for the entire substructure, as it must withstand vertical and bending stresses exerted by the turbine, as well as the pressure load on the tower generated by the wind.
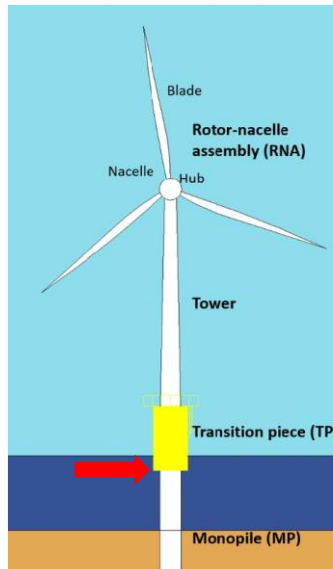
Figure 1-5 Offshore Wind Turbine structure, highlighting the MP-TP section[16]

In Figure 1-6, the timeline for the innovation of MP-TP connection is illustrated. The first connection design used as an MP-TP connection was the Grouted technology (Figure 1-7), which was massively used for the foundation of Oil and Gas platforms, especially in structures such as main, skit and cluster piles. The design is based on the use of tube-in-tube connection with the space between the two tubes filled with grout[17]. The principal methods of load transfer involve shear friction resulting from the normal stress induced by imperfections and roughness of the surface gaps and the compression of the grout.
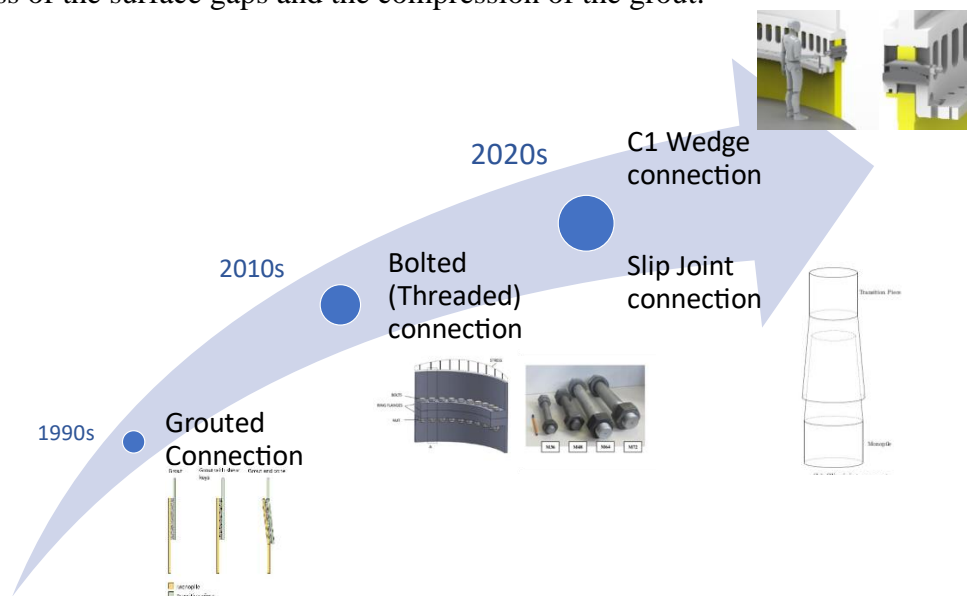
Figure 1-6 Innovation timeline for MP-TP connection in OWT industry

However, at the end of last decade, numerous grouted connection joints for different offshore wind substructures were found to be failing. The issue was found in the absence of shear keys on straight MP and TP surfaces. The bending load resulting the complexity of the offshore wind, comparing to the Oil&Gas Structure, and the wave loading were not taken into account during the designing process. Furthermore, the axial capacity of the connection was found to be significantly lower than the assumed during the scaled test, with manufacturing and installation tolerances increasing the bending stress[18]. Typical failure modes of the grouted connection were dis-bonding, cracking, wear, and compressive grout crushing failure. Trying to address the structural problems different design had been considered, with the focus on implementing series of shear keys on the surfaces in contact with the grout and utilizing a conical grouted connection.
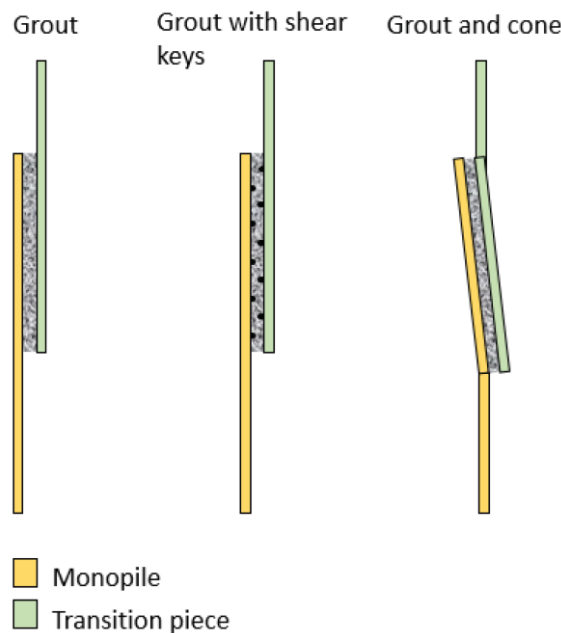
Figure 1-7 Grouted connection design: Grouted connection, Grouted connection with shear keys and Conical grouted connection[19]

Meanwhile, a variety of alternative solutions have been investigated as substitutes for grouted connections, many designers aimed at bolted connections as a better choice. The Bolted Flange connection is another technology widely used in the offshore Oil&Gas industry and was chosen as substitute of the grouted connection. In the offshore industry, this connection is based on the presence of two flanges welded on the two tubular sections and held together by a series of bolts along a circumferential path of holes, as illustrated in Figure 1-8a.

Nowadays, with the increasing demand of green energy, the offshore wind industry needs to increase the size of turbines, meaning an increase in the structure's diameter and wall thickness. This require that MP-TP connections follow the trend. Specifically for bolted connections, there are two possible solutions: increasing the number of bolts along the circumference or increasing sectional area by transitioning from M72 bolts to M100 (Figure 1-8b). While the first solution can be considered easier in terms of production, the assembly phase can be seen as critical as it requires longer assembly time. The second solution presents challenges in both production and assembly phases: a M100 bolt production would require new standardization and specific tolerances, during assembly, specific tools would be needed to apply the required

tensioning. In response to these challenges, companies like C1 Connection and Van Oord have designed innovative MP-TP connection layouts.
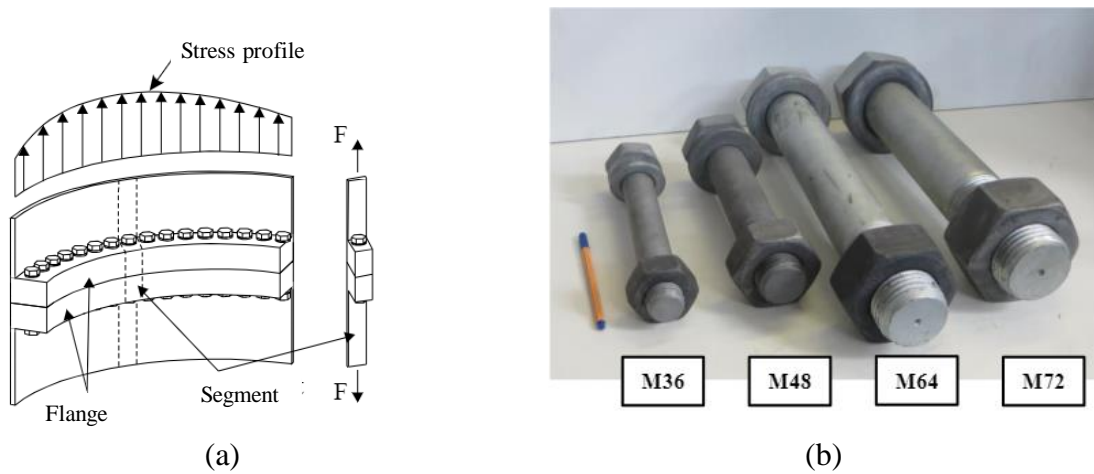
Figure 1-8 Bolted connection: L-flange bolt connection design (a)[20] and different bolts dimensions in comparison (b)[21]

C1 Connection, based in the Netherlands, has developed a device known as C1 Wedge Connection. This technology consists in redesigning the L-flanges by converting the vertical connection into a horizontal one. This is achieved through the design of a cylindrical lower flange for the MP section with a fork-shaped upper flange for the TP section. According to this concept, a series of elongated holes will be accommodated around the circumference of the geometry, allowing the positioning of the C1 wedge fastener. These are then pushed in using horizontal bolts, holding the two flanges together by creating a preload, as represented in Figure 1-9.
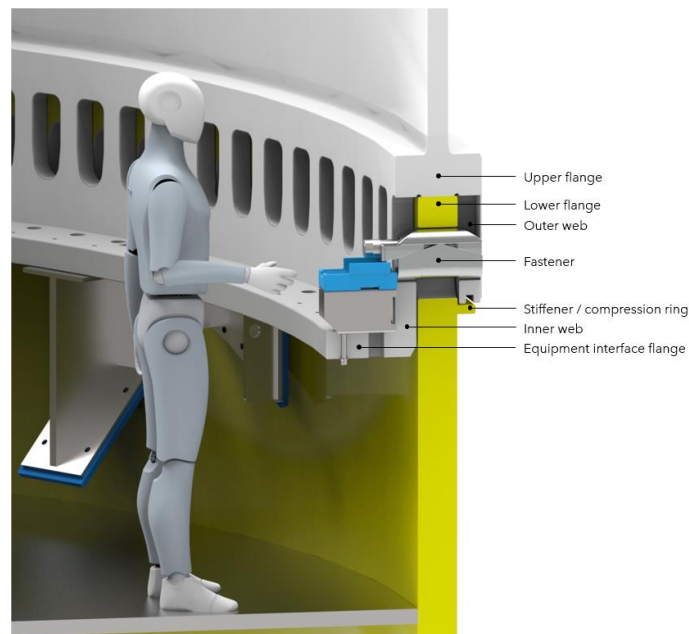
Figure 1-9 C1 wedge connection design[22]

In the meanwhile, Van Oord, based in the Netherlands, has presented a redesign of a technology used in the early stages of the OWT industry for the MP-TP connection: the Slip Joint. The concept of this connection can be easily visualized as *"two cups"* upside down, stacked on top

of each other, as presented in Figure 1-10. Tensile and compressive forces in the skin of the tubular tower are transferred through friction forces and, to a lesser extent, through contact forces between the two parts, without the external use of threads or welds.
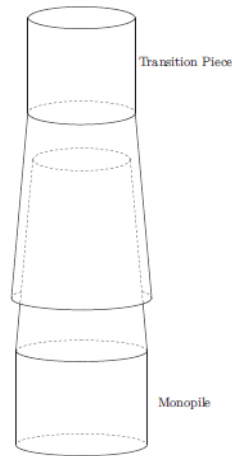
Figure 1-10 Slip Joint Connection layout[23]

1.3. Research Aim and Objectives

The overall aim of this thesis is to evaluate the integrity of offshore wind turbine MP-TP connection technologies, by identifying the Pros and Cons associated with each technology. To achieve these goals, each chapter includes a literature review of all three technologies. By developing FEA modelling and conducting large-scale fatigue testing, it has been possible to compare literature with real data. This approach allowed for the collection of comprehensive information and a comparison among the three technologies.

The main objectives of this study are divided into the examined technologies:

a) Threaded connection
  - To investigate the main standard curves used in the design for threaded connections.
  - To investigate the stress behaviour of large-scale samples.
  - To investigate through statistical analysis the data of fatigue tests presented in literature review, comparing the results with standards to understand the reliability of them.
  - To develop a mean stress correction method to analyse the fatigue life of preloaded studs.

b) C1 Wedge Connection
  - To analyse the connection behaviour and internal interactions.
  - To investigate through large-scale test the reliability of the connection.

c) Slip Joint Connection
  - To investigate the stress distribution along the flanges in function of geometrical parameters and interaction factors between the components.
  - To examine the stress distribution along the flanges under different external conditions, such as bending loads, and in presence of manufacturing imperfections.

1.4. Structure of the Thesis

In Chapter 1 , an introduction to the offshore wind turbine foundation has been presented, with a specific focus on the Monopile and Transition Piece connection and their evolution in the last decades.

A preliminary study of the wind load on the tower has been presented in Chapter 2. This study was conducted in order to understand and simplify the wind load on an offshore wind turbine structure, stress results have been used to perform FEA simulations in the subsequent simulations.

The threaded connection is described in 0. This chapter has been divided in two main sections, the first focused on studying the stress distribution along the engaged threads between the bolt and the nut, with variations in terms of friction coefficients. The second section aims to provide a deeper understanding of the standard S-N curves, with a statistical analysis developed using new fatigue results and already presented in literature. This section of study proposes a preliminary method, using Goodman mean stress correction, to predict different fatigue life under different mean stress values.

In Chapter 4, an independent study of the C1 wedge connection has been presented. The study has highlighted the analytical study of the geometry and fasteners of the connection. Based on these results, it has been possible to develop an independent FEA model of a real-size sample and subsequently a fatigue test has been developed.

Meanwhile, in Chapter 5, the Slip Joint connection has been discussed. The study has highlighted, through FEA model, how stress changes depending on different geometrical variables and material proprieties. A secondary study presented the behaviour of the connection under bending and in presence of manufacturing imperfections.

Chapter 6 provided a final comparison of the three main technologies. This chapter includes a discussion of pros and cons of each technology with the support of a weighted table. Additionally, conclusions are drawn and future work necessary for a deeper understanding of these technologies is outlined.

Appendices has been included at the end of this thesis. The fractography results for the seven M72 studs, presented in section 3.7, are illustrated with the region of crack initiation highlighted.

```
                    ┌─────────────────────────────────────┐
                    │ Chapter 1: Introduction to MP-TP     │
                    └─────────────────────────────────────┘
                                      │
                    ┌─────────────────────────────────────┐
                    │ Chapter 2: Analytical wind load on the │
                    └─────────────────────────────────────┘
                                      │
        ┌─────────────────────────────┼─────────────────────────────┐
```

Chapter 3: Threaded connection	Chapter 4: C1 wedge connection	Chapter 5: Slip joint connection
- Introduction	- Introduction	- Introduction
- Stress distribution along engaged threads and SCF	- Analytical and FEA analysis of stress distribution and how geometry affects it	- Analytical and geometrical analysis
- Study of standards (DNVGL-RP, Eurocode3 and BS7608)	- Large scale FEA analysis	- FEA analysis to understand how the maximum stress and distributed stress change in function of geometrical variables
- Large scale fatigue test -> fractography analysis	- Large scale fatigue analysis	-FEA analysis to understand how bending and imperfections affect the stress distribution
- Mean stress correction analysis		

```
        └─────────────────────────────┼─────────────────────────────┘
                                      │
                    ┌─────────────────────────────────────┐
                    │ Chapter 6: Discussion and Conclusion │
                    └─────────────────────────────────────┘
```

Chapter 2 Evaluation of Aerodynamic Loads on Offshore Monopile Structure

2.1. Global Offshore Wind Conditions

An OW turbine is usually subjected to two main dynamic load sources: sea waves, and wind. Since the MP-TP connection is usually above sea level, this type of source is not considered. For wind load, two main characterisations have been considered: the load applied from the blade drag and the pressure load on the entire tower. [24]

To calculate the loads magnitude, a study of the wind profile is necessary. Different mathematical approaches have been developed for this purpose.

One of these is the Monin-Obulkhov method, which represents the wind speed V at a height z through a log-linear profile described by Equation 2-1.

$$V_z = \frac{v_f}{K}\left[\ln\frac{z}{z_0} - \xi\left(\frac{z}{L}\right)\right]$$

2-1

Where v_f represents the friction velocity, K is the Von Karman constant (usually 0.4), z_0 is the surface roughness length and L is a scale factor known as Monin-Obukhov length. The function $\xi(z/L)$ is a solar radiation function on the site. This equation has provided valid results only for small period and for critical sites.

Another method is the Hellmann exponential load, which correlates the wind speed V of a specific heigh H to a referring speed V_0 at heigh H_0.

$$\frac{V_z}{V_0} = \left(\frac{H}{H_0}\right)^\alpha$$

2-2

With α as friction coefficient or Hellman exponent. This coefficient can vary in accordance with the type of surface on which the wind blows, as illustrated in Table 21[25], [26]. Factors such as - heigh, time of the day, time of the year, speed and temperature have been shown to influence it as it has been demonstrated in different parts of the world[25], [26], [27]

Table 2-1 Friction coefficient for various terrain characteristics

Terrain Characteristic	Friction Coefficient α
Smooth hard ground, calm water	0.10
Tall grass on level ground	0.15
High crops, hedges and shrubs	0.20
Wooded countryside, many trees	0.25
Small town with trees and shrubs	0.30
Large city with tall building	0.40

Last considered method is known as Logarithmic wind profile law, and it is calculated according to Equation 2-3.

$$\frac{V}{V_0} = \frac{\ln\dfrac{H}{z_0}}{\ln\dfrac{H_0}{z_0}}$$

<div align="right">2-3</div>

Where V is the wind speed at height H, V_0 the speed at height H_0 and z_0 is the roughness length which depends on the surface (Table 2-2)

<div align="center">Table 2-2 Roughness Classes and Length</div>

Roughness length z_0	Land cover types
0.0002	Sea, loose and snow
0.0002-0.0005	Concrete, flat desert, tidal desert
0.0001-0.0007	Flat snow field
0.001-0.0012	Rough ice field
0.0001-0.004	Fallow ground
0.008-0.03	Short grass and moss
0.02-0.06	Long grass and heather
0.04-0.09	Low mature agricultural crops
0.12-0.18	High mature crops ("grain")
0.35-0.45	Continuous bushland
0.8-1.6	Mature pine forest
0.4-0.7	Dense low buildings ("suburb")
0.7-1.5	Regularly built large town
1.7-2.3	Tropical forest

A comparison between the Hellman method and the logarithmic law was conducted to determine which one to use and the results have been presented in Figure 2-1, by considering a sea surface and a wind speed of 9.95 [m/s] at 100 [m] , using data from LAUTEC ESOX for coordinates N56 E7,50.

As shown in Figure 2-1, the curves are very close each other, the gap is 0.35 [m/s] at 10 [m]. Once defined a wind profile, it is possible to calculate the loads acting on the monopile. The first considered is the load applied horizontally, resulting from the wind drag on the blades.

$$F_{wind_{blades}} = \frac{1}{2}\rho_{air}AV_{hub}^2C_D$$

<div align="right">2-4</div>

Where ρ_{air} is the air density, A is the circular area covered from the blades, V_{hub} is the wind speed at the hub heigh, and C_D is the drag coefficient.
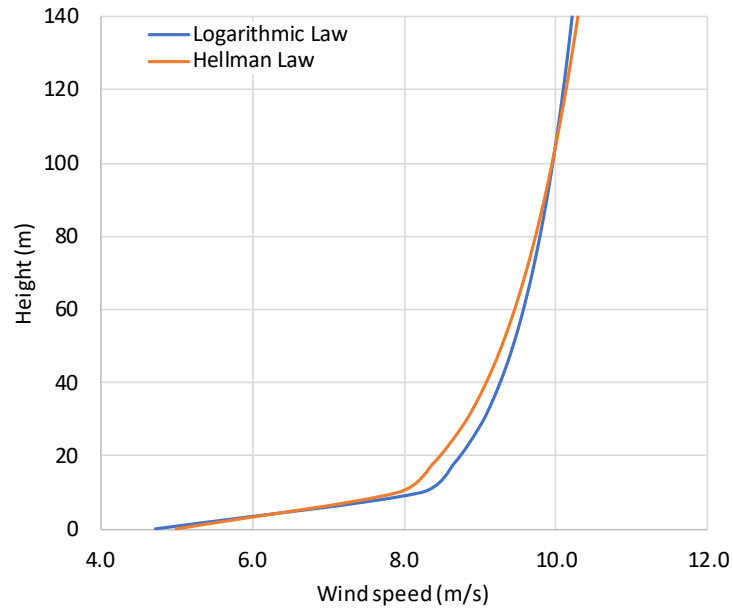
Figure 2-1: Hellman Law compared to Logarithmic speed profile Law

This load will be applied at the top of the tower (nacelle position) with an horizontal direction aligned with the wind direction.

The second load type is the air pressure on the tower. Because this load is function of the wind speed, the tower has been divided into different sections to be able to calculate local loads.

$$F_{wind_{pressure},i} = A_{V,i} C_D V_i^2$$ 2-5

Where $A_{V,i}$ is the cross-sectional area of the vertical section considered, C_D is the drag coefficient of the tower and V_i is the local wind speed.

A simplification of what has been illustrated for Equation 2-4 and 2-5 has been illustrated in Figure 2-2.
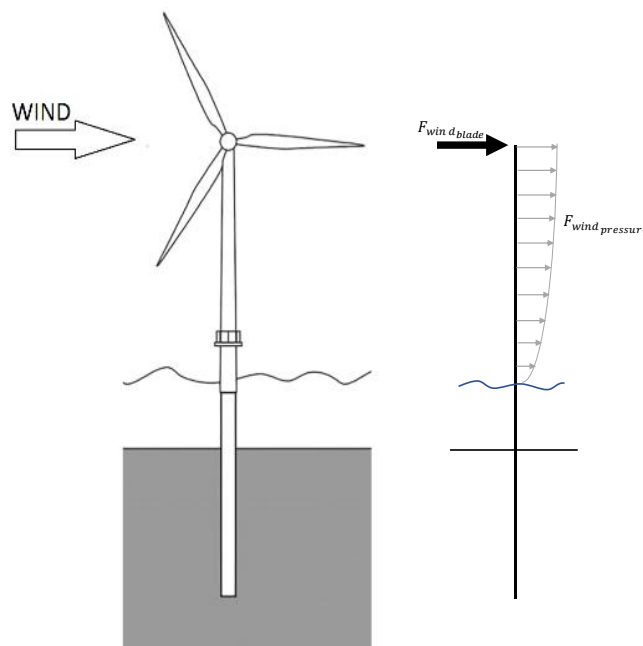
Figure 2-2 OWT wind loads schematization of a monopile offshore structure

14

To calculate the local stress all along the tower of the OWT, a reaction forces study has been developed (Figure 2-3).
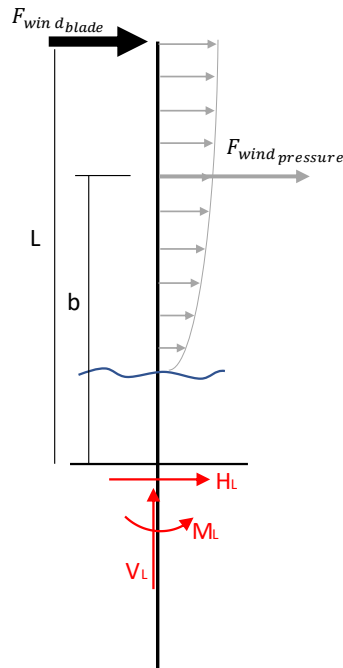
Figure 2-3 Reaction Force on a monopile offshore structure

$$\begin{cases} \sum V_L = 0 \\ \sum H_L = 0 \\ \sum M_L = 0 \end{cases} \qquad \text{2-6}$$

$$\begin{cases} V_L = 0 \\ H_L + F_{wind_{blade}} + F'_{wind_{pressure}} = 0 \\ M_L - F_{wind_{blade}} L_n - F'_{wind_{pressure}} b = 0 \end{cases} \qquad \text{2-7}$$

Where $F'_{wind_{pressure}}$ represents the equivalent load of the wind pressure located to a distance b (barycentre of the load) from the ground, L_n is the total distance from the nacelle to the ground.

From equation 2-7 the values of the three reaction forces have been calculated.

$$\begin{cases} V_L = 0 \\ H_L = -F_{wind_{blade}} - F'_{wind_{pressure}} \\ M_L = F_{wind_{blade}} L_n + F'_{wind_{pressure}} b \end{cases} \qquad \text{2-8}$$

To estimate the stress along a specific section, Equation 2-9 has been used, in accordance to Figure 2-4.

15

$$\begin{cases} V_L = 0 \\ H_L = F_{wind_{blade}} + \sum F_{wind_{pressure,i}} \\ M_L = F_{wind_{blade}} a + \sum F_{wind_{pressure,i}} x_i \end{cases} \qquad \text{2-9}$$
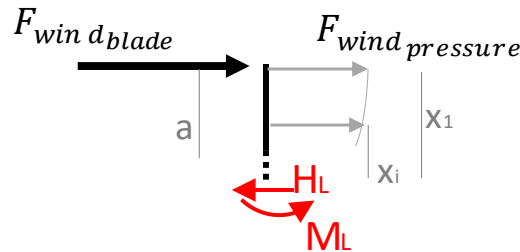
Figure 2-4: Schematic load consideration along segment of tower

Once calculated the bending load, it is possible to evaluate the vertical stress for each section through.

$$\sigma = \frac{Mc}{I} \qquad \text{2-10}$$

Where c is the distance from neutral axis, and I is the area moment of inertia about the neutral axis. For the area moment of inertia for a hollow circular section is

$$I = \frac{\pi}{64}(D^4 - d^4) \qquad \text{2-11}$$

Through Equation 2-10, the stress value can be calculated depending on the c value. As showed in Equation 2-12, the critical stresses have been calculated, where σ_{MAX} and σ_{MIN} represent the value on the external radius R of the tower and σ_{max} and σ_{min} the stress values on the internal radius r. Graphic results have been represented in Figure 2-5.

$$\sigma = \begin{cases} \sigma_{MAX} = \dfrac{MR}{I} \\ \sigma_{max} = \dfrac{Mr}{I} \\ \sigma_{MIN} = -\dfrac{MR}{I} \\ \sigma_{min} = -\dfrac{Mr}{I} \end{cases} \qquad \text{2-12}$$

16
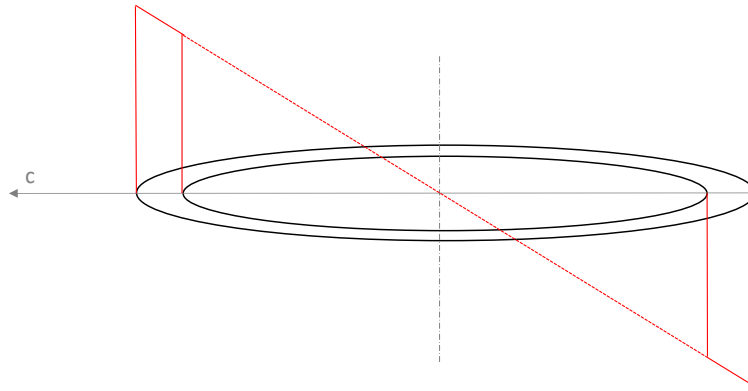
Figure 2-5: Bending stress results
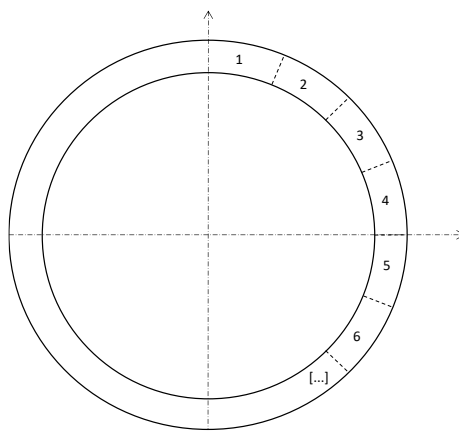
Figure 2-6: Section division

To calculate the maximum global load under which a segment is subjected, the circumference has been divided into equal sections, as illustrated in Figure 2-6. From this, the maximum vertical load can be calculated as shown in Equation 2-13.

$$F = \sigma_{MAX} A_i \qquad\qquad \text{2-13}$$

2.2. Real Data

The global average offshore wind speed is around 8.6 [m/s] as shown in Figure 2-8, with countries such as UK where the value is around 9.75 [m/s], as reported in Table 2-3, for some of the Wind Farms outside the United Kingdom shores.

Table 2-3 Average and Maximum wind speed in a period from 1990 to 2019

WT project	Status	Mean wind speed @ 100m	Max wind speed @ 100m
West of Duddon Sands	Fully commissioned	9.25	36.44
Robin Rigg West	Fully commissioned	8.08	32.24
Race Bank	Fully commissioned	9.15	29.44
N1	Development	10.00	36.50
Kincardine	Fully commissioned	6.46	19.15
E1	Development	10.14	35.56
E2	Development	10.15	35.11

Usually, wind turbines operate with a speed starting from 4[m/s], reach maximum power at 11 [m/s], and have a cut-out set at 25 [m/s] for security purposes, as illustrated in Figure 2-7.
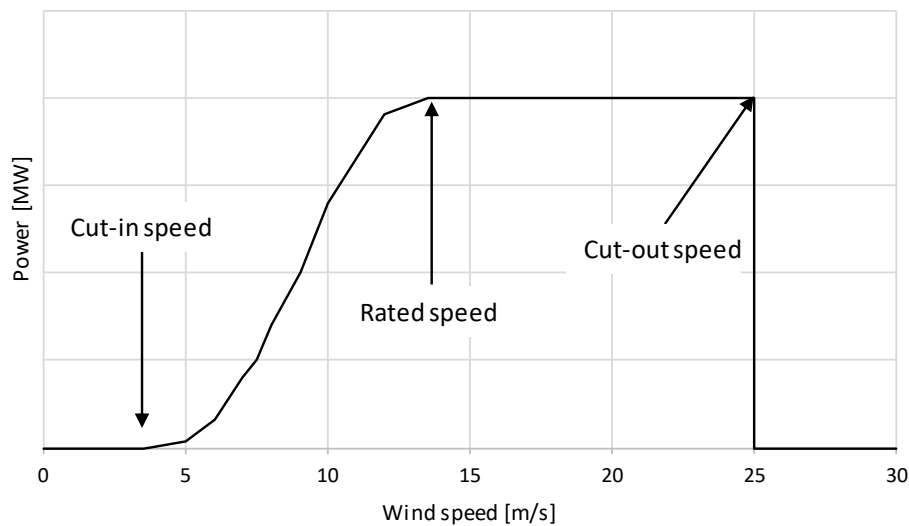
Figure 2-7 Typical wind turbine power-out curve
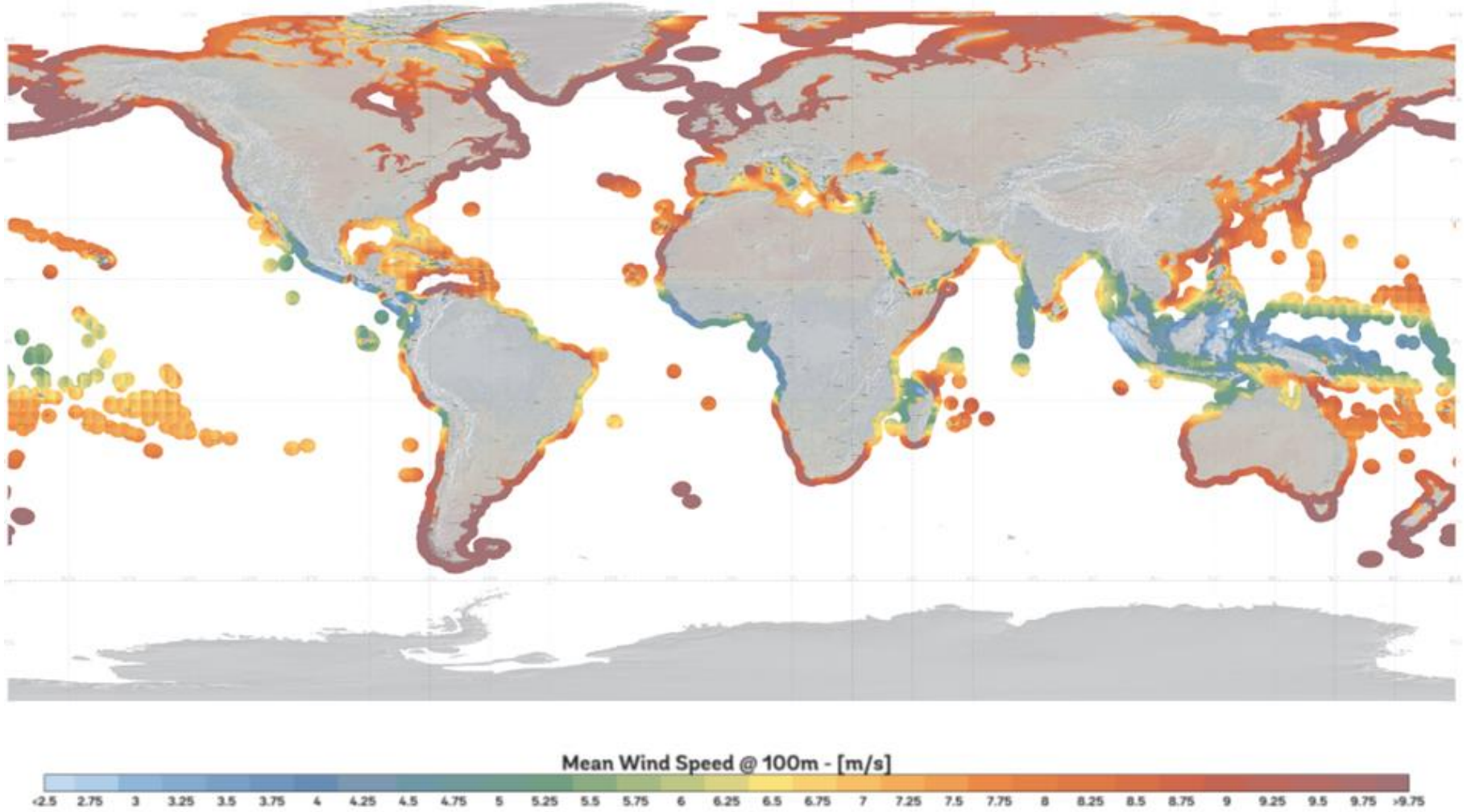
Figure 2-8: Global mean wind speed @100 [m] from GWA App, Technical University of Denmark (DTU)

2.3. Load Along Tower

According to the wind Logarithmic Law profile, five different curves have been plotted for different speeds at 100 [m] above the sea level: 6.5, 9.5, 16, 20 and 25 [m/s] as illustrated in Figure 2-9.
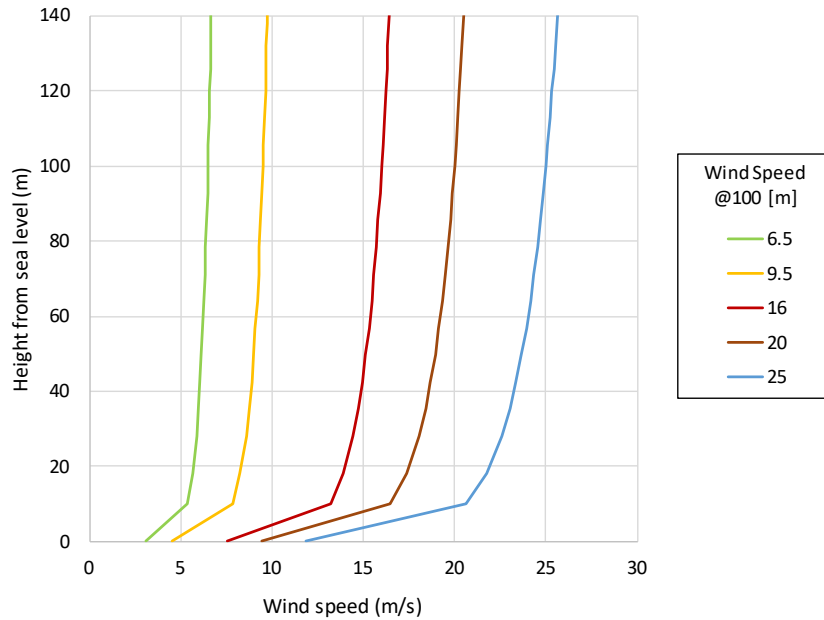
Figure 2-9 :Speed profile for different wind speed at 100 [m]

For the load study, the dimensions used are for a generic 10 [MW] turbine[28], [29] and have been reported in Table 2-4.

Table 2-4 Generic dimension for 10 [MW] turbine

Part	Value
Hub height above sea level	120 [m]
Rotor Radius	95 [m]
Tower diameter	7.7 [m]
MP wall thickness	80 [mm]

Since the cut-out speed is around 25 [m/s], this speed has been considered the critical point and further calculations have been developed with it. Through Equation 2-9, the momentum have been calculated and reported in Table 2-5, dividing the momentum from the Drag force and from the wind pressure, reporting as well the total momentum.

Table 2-5 Load condition for a 10[MW] OWT under 25 [m/s] wind speed

Height	Wind speed	Drag Load	Local wind pressure load	Total horizontal load	Drag Momentum	Cumulative Wind pressure momentum	Total Momentum	Maximum Stress	Maximum Local Stress
m	m/s	kN	kN	kN	kNm	kNm	kNm	MPa	MN
120	25.3	4463	35.6	4498.6	0	0	0	0	0.00
112.8	25.2		35.3	4533.9	3.21×10^4	2.56×10^2	3.24×10^4	9	0.16
105.6	25.1		34.9	4568.9	6.43×10^4	7.67×10^2	6.50×10^4	18	0.31
100	25.0		34.7	4603.5	8.93×10^4	1.36×10^3	9.06×10^4	25	0.44
92.8	24.9		34.3	4637.8	1.21×10^5	2.37×10^3	1.24×10^5	34	0.60
85.6	24.7		33.8	4671.6	1.54×10^5	3.63×10^3	1.57×10^5	44	0.76
78.4	24.5		33.4	4705.0	1.86×10^5	5.13×10^3	1.91×10^5	53	0.92
71.2	24.4		32.9	4737.9	2.18×10^5	6.87×10^3	2.25×10^5	62	1.08
64	24.1		32.3	4770.2	2.50×10^5	8.85×10^3	2.59×10^5	72	1.25
56.8	23.9		31.7	4801.9	2.82×10^5	1.11×10^4	2.93×10^5	81	1.41
49.6	23.7		31.0	4833.0	3.14×10^5	1.35×10^4	3.28×10^5	91	1.58
42.4	23.4		30.3	4863.2	3.46×10^5	1.34×10^4	3.60×10^5	100	1.73
35.2	23.0		29.4	4892.6	3.78×10^5	1.90×10^4	3.98×10^5	110	1.92
28	22.6		28.3	4920.8	4.11×10^5	2.21×10^4	4.33×10^5	120	2.09
18	21.7		26.2	4947.0	4.55×10^5	2.59×10^4	4.81×10^5	133	2.32
10	20.6		23.6	4970.6	4.91×10^5	2.98×10^4	5.21×10^5	144	2.51
0.1	11.8		7.8	4978.4	5.35×10^5	3.51×10^4	5.70×10^5	158	2.75

Chapter 3 Threaded Connection

3.1. Chapter Content

This chapter focuses on the study of the behaviour of the threaded connection that uses M72 gr10.9 bolts to secure the bottom flange in the transition piece with the top flange in the monopile foundation. Section 3.3, presents a simplified analytical calculation to determine the stress distribution along the engaged threads, calculating the axial and shear components of the loads involved. The results of this approach have been compared with the results presented in literature.

In Section 3.4, a Final Element Analysis (FEA) has been developed in Abaqus software to investigate the variation of the stress distribution along the engaged treads under different load level and utilising different friction coefficients. Subsequently, the impact of the plasticity effect on the Stress Concentration Factor (SCF) has been discussed.

A review of the main fatigue life standards has been presented in Section 3.5, where the differences between them have been highlighted. Subsequently, the standards codes have been compared with statistical S-N curves developed from fatigue results, presented in literature for the 4 main bolts dimensions of M36, M48, M64 and M72.

Large-scale fatigue test results performed on M72 studs are presented in Section 3.7. The data points obtained from experiments have been statistically analysed and compared with the standard S-N curves and the results presented previously. Also, fractography analysis has been carried out and the macroscopic results are reported in APPENDIX.

A mean stress correction approach has been presented in Section 3.8. Through the use of Goodman correction, a prediction model based on the pre-load level of the threaded connection has been suggested and discussed.

3.2. Introduction to the Technology

A threaded joint is essentially a connection method where two or more components are securely fastened together using threaded fasteners like bolts. When designing a threaded connection, several critical factors come into play, such as shapes, functions, dimensions, materials, the service environment, and the working loads. It is important to note that these factors can differ significantly from one industry to another, with each industry typically having its unique and customary joint configurations. Common standards and guidelines used for the design of bolted joints in industry are the BS EN 14399-1:2005, DASt-Guideline 021 (2006) and the DIN 6914.

3.2.1. Connection Design

The typical layout for a connection using a bolt, a nut, and the use of washers, each serving its own purpose, is schematically shown in Figure 3-1.
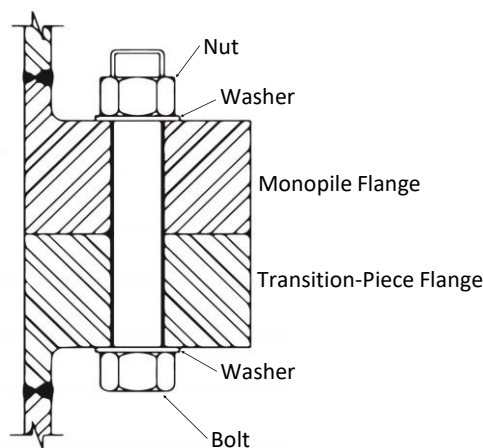
Figure 3-1: Configuration of Threaded connection in an Offshore Wind Turbine

Bolt

The bolt is defined as a type of threaded fastener with an external male thread, whose goal is to keep the joint together in combination with the nut[30]. The bolt terminology used in this chapter is demonstrated in Figure 3-2.
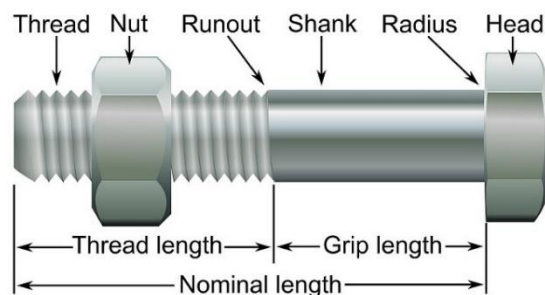
Figure 3-2: Bolt terminology[31]

In the offshore industry the number of bolts along the section depends on different factors, such as the radius and thickness of the flange of the joint, the size of the bolt and the expected load. An investigation[32] has illustrated how these parameters affect the tension of the bolt with the main observations summarised as follows:

- Bolt tension decreases with the increasing number of bolts.

- Flange thickness affects bolt tension.
- The maximum bolt tension decreases as flange width increases.

Fatigue failures of bolts typically occur in the three main areas of stress concentration, specifically: 65% occur in the root of the first loaded thread, 20% in the thread run-out region, and 15% occur in the head-to-shank radius[33], [34]. Figure 3-3 presents the main critical locations.
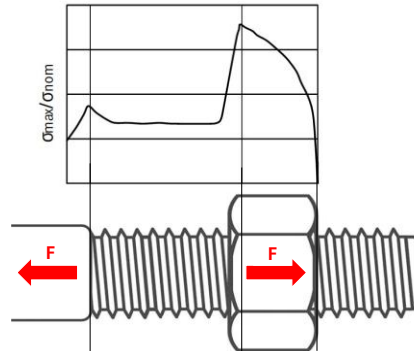
Figure 3-3: Schematic illustration of stress distribution in a threaded connection under pre-load, F (re-produced based on the information presented in [34])

Nut

The purpose for the nut is to generate bolt tension by rotating and advancing on the bolt threads. To perform the optimal mating, the nut needs to have a thread form that is not identical to the bolt and sufficient material plasticity to allow the threads to deform upon tightening and adjust to distribute the load over the threads rather than just the first few [35].

Nuts are designed to ensure that the bolt will fail under tension before the nut strips. Usually, the failure happens when the nut thread shear strength cannot carry the load, this is caused by an insufficient thread height, or if the nut is significantly weaker than the bolt. To prevent this, the nut is designed with enough threads and is made with material with different Young's modulus.

Washer

Washers play a pivotal role in the creation and maintenance of integrity within bolted connections. Their primary function in the joint is twofold: first, to prevent damage by efficiently distributing the force applied to them over a larger area, and second, to prevent the head of the bolt from embedding to deeply into the material [17]. The high-stress environment in which washers operate, especially in terms of load distribution, typically makes them a one-time-use component. This is due to plastic deformation that can occur under such high stress, which can compromise their effectiveness in subsequent uses.

3.2.2. Bolt Material

Bolt material is selected based on different factors, such as load capacity and environment resistance. BS EN 14399-4:2015 defines the material proprieties for high-strength structural bolting assemblies for preloading. The bolt material, in accordance with the European standard EN ISO 898-1 and DIN 6914, is identified as Hochfest Vorgespannt (HV). According to German standard, the connection is made using thinner nets and shorter threads lengths in order to obtain the required ductility for the engaged threads. According to Standards the class used to indicate these bolts is Class 10.9, indicating an Ultimate tensile strength of 1000 MPa and

900 MPa as Yield stress. Stress-Strain behaviour of 10.9HV does not show any yield plateau, this defines a more sensitive behaviour to plastic failure due to overtightening during preloading and therefore it requires more site control.

3.2.3. Tensioning

The goal of tensioning, or preloading, the bolt is the application of enough clamping load to ensure the stability of the joint. It is possible to consider the bolt and the entire joint as spring elements, where tightening the bolt compresses the assembly. In industry, four methods of tightening for bolting connection are available, which are presented in the European standard BS EN 1090-2: Torque, Combined, HRC and Direct tension indicator method. A brief description of each of these methods is presented below[36].

Torque Method

This method provides tightening the bolt assembly using a torque wrench operated by hand or power. The entire process requires applying torque continuously and smoothly. It is a two-step process: first, all bolts need to be tightened to 70-75% of required load, then a second round of torquing is typically done at 110% of required load to compensate any torque relaxation after wrench remotion.

Combined Method

Combination of Torque Method and the traditional 'part-turn' method. Preloading occurs in two steps. The first step, similar to the torque method, is applying a torque load to all bolts up to 75% of the required value. The second step involves applying a predetermined rotation to each bolt to a specified angle, depending on the bolt length. The required torque is calculated from data obtained from the EN 14399-2.

High Resistance Calibrated (HRC) Method

This method requires a specific shear wrench equipped with two co-axial sockets (one for the nut and one for the bolt), which torque one against the other. The HRC is based on two steps: 1. first tightening occurs when the wrench outer socket (nut) stops turning. This step may be repeated multiple times and need to be completed for all the bolts before proceeding to step two.

2. Second step is achieved when the spline end of the wrench shears off at the break-neck.

Direct Tension Indicator (DTI) Method

This method is applied on direct tension indicators by monitoring the force, in accordance with EN 14399-9 guidelines, which suggest the minimum achievable preload (see Figure 3-4). This method does not define any torque load value. The first step consists of tightening the bolt, until the protrusions on the TDI starts to deform, indicating that approximately 50% of the preload has been applied. This step must be completed for all bolts before proceeding. Second step consist in applying the final load, the specified bolt force is achieved when the gap is closed. The force applied will not be less than the specified preload.
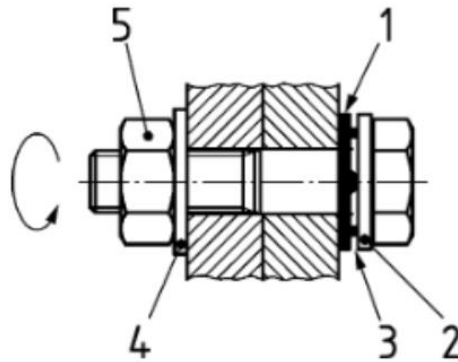
Figure 3-4: DTI bolt assemble in accordance to BS EN 14399-9:2018. 1) Direct Tension Indicator (DTI, 2) bolt, 3) gap, 4) washer, 5) nut

3.2.4. Specific Issues

In the literature, different issues associated with threaded connections have been studied and briefly explained in this section. These problems mainly revolve around relaxation, tensioning order of the bolts and corrosion.

Bolt Load Loosening

The bolt is subjected to different factors that can affect its tightening over time. Two phenomena presented in the literature are referred to relaxation and the tightening order of the bolt. Relaxation is a phenomenon that can be categorized in short-term and long-term, with the former occurring immediately after the preload application (a few hours to few days) without considering the external load, while the latter considers the relaxation that occurs over a longer period, typically a few months (Figure 3-5). Self-loosening has been studied and presented in the literature considering different factors, such as vibration and load nature (axial, shear and rotational) [17], [37], [38], [39], [40], [41], [42], [43], [44], [45], [46].

Short-time relaxation often occurs when some contact surfaces of the joint exceed the yield point and plasticity develop. This phenomenon occurs mostly as result of irregularities in the contact surfaces of the assembly. During the pre-loading phase, the contact area in the thread connection is smaller compared to the entire joint, this means that the local stress is high. If irregularities are present, reducing the contact area, can increase stress beyond the yield point[17]. Long-time loosening occurs primarily due to the cyclic loading in the operational life cycle of the joint assembly, but it can also result from low temperature creep[47], which is a time-dependent phenomenon.

The tightening sequence of bolts along the flange has been studied to see its correlation with load loosening[48]. As it has been observed, whenever one bolt near another is tightened, it results in a loss of load in the adjacent bolts.
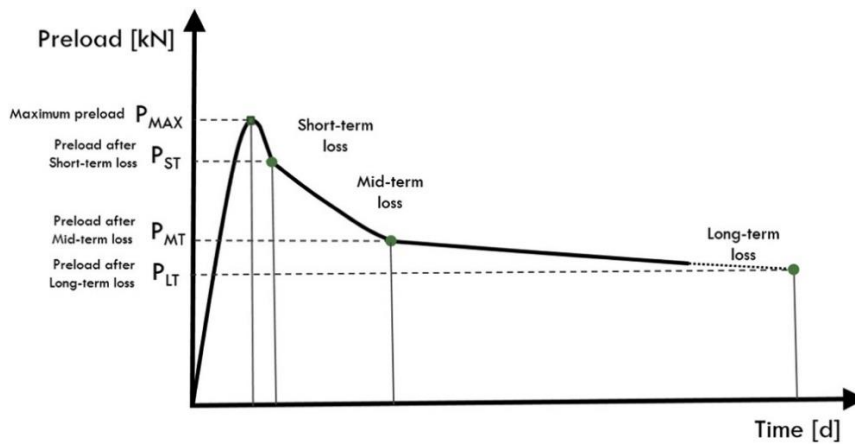
Figure 3-5: Preload relaxation in time[49]

Corrosion

One of the most critical life-strength challenge for threaded connections, especially in the offshore environment, is corrosion[30]. Corrosion can affect the stability of the clamping force[50] and the life of the single components. Different techniques have been implemented in the offshore industry to reduce the corrosion in the structure, for bolts the main technique is coating. As demonstrated in the literature[51], coating can increase the service life of the bolt, however a small imperfection of the surface can reduce it.

3.3. Analytical Stress Distribution Calculation

Creating a perfect model to analyse threaded connections is challenging due to the involvement of various parameters that must   be considered. In the past, different models have been developed to calculate the stress distribution along the engaged threads. A first simplified model can be developed by deriving the sum of axial deformations of the bolt and nut to the deformation of the thread, which was treated as a cantilever beam subjected to bending action. The normal resultant force between threads can be assumed to act on the midpoint of the cantilever beam.

In 1948, Sopwith[52] implemented the model considering the Young's modulus on the radial compression of the thread and the radial compression of the thread. Later on, Kenny and Patterson [53] and Goodier [54] obtained similar results through photoelastic technique and extensometers measurements, respectively. In 1980, Yamamoto[55] implemented Sopwith' model, considering in the model the thread contacts stiffness, introducing the inclination effect of the thread root, the shear deformation of the root. Recently the Yamamoto model has been compared with FEA models [56] and implementation have been made by adding the thread friction[57].

In this chapter, an analytical model has been developed utilising a simplified approach. In this approach, the bolt has been considered as a beam, with the threads as cantilevers. However, compared to Sopwith's model, the sectional shape of the thread has been considered. Additionally, along with the axial and bending stress on the threads, the shear and the torque stress have been implemented in the model. The considered stresses can be divided in two different groups based on the applied load: specifically axial and bending component are generated by the axial load (preload), while torque and shear components by the torquing load applied through the preload.

Results of the four different stresses have been considered separately for superposition. The main values of the parameters that identify the basic profile (Figure 3-6) are standardised in BS ISO 68/2:2023[58]. For this study the following parameters have been taken into consideration: D_{min}, which is as internal diameter of the bolt, P, which is the bolt pitch, H, which is the height of fundamental triangle, α, which is the thread angle, and n_t, which is the number of engaged threads.
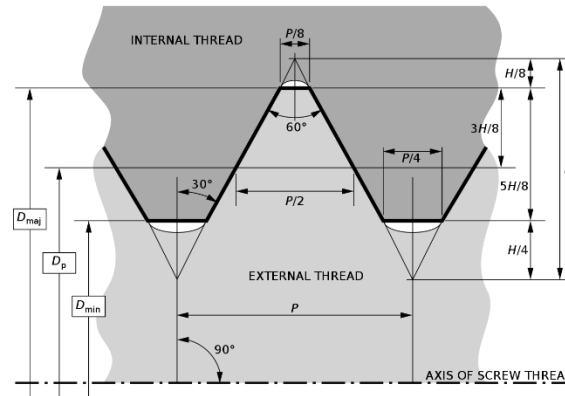
Figure 3-6: Basic profile of all ISO metric screw threads for threaded connection (ISO 68-1), referring as external thread for bolt and internal for nut

3.3.1. Axial Load

To calculate the axial stress on the bolt, it has been simplified as a cylindrical beam of diameter d_3. The applied load (F_{app}) is the tension created during the pre-loading phase of the bolt and the nut (Figure 3-7). For simplification and to focus the calculation only on the interaction between the nut and the bolt, the interaction between the washer and the nut have not been implemented in the calculation.
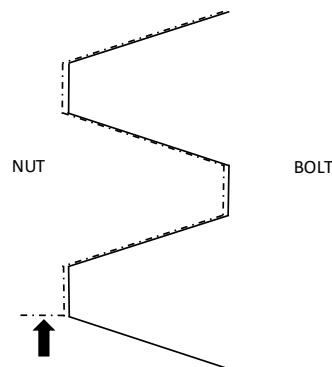
Figure 3-7: Axial stress layout

This axial stress has been calculated in Eq.3-1.

$$\sigma = -\frac{F_{app}}{A} = -\frac{F_{app}}{\frac{\pi}{4} d_3^2} = -\frac{4 F_{app}}{\pi d_3^2}$$

3-1

3.3.2. Bending Stress

The Bending Stress is caused by the interaction between the bolt and nut threads (Figure 3-8).
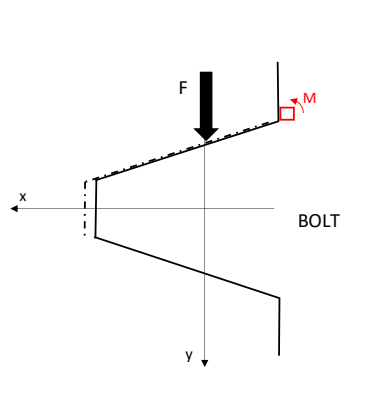
Figure 3-8 Bending stress layout in a threaded connection

The general formula to calculate the stress is presented as Eq.3-2.

$$\sigma = \frac{M\,x}{I}$$

3-2

where M is the momentum created from the load F, x is the distance of the considered point from the load applied point, and I is the Momentum of Inertia. In this equation, the Momentum M can be calculated as:

$$M = F\,x_c$$

3-3

where x_c is the distance from the barycentre of the trapezium in the x-direction, and its value is equal to x_c, which can be calculated as:

$$x_c = \frac{h}{3}\,\frac{2a+b}{a+b}$$

3-4

To calculate the Momentum of Inertia I, it is necessary to simplify the entire engaged surface of the bolt in contact as a wall of trapezium section (Figure 3-9) of a length equal to

$$l = n_c\,\pi\,hD_3$$

3-5

From this, it is possible to calculate the Momentum of Inertia of the contact area as a rectangular one

$$I = \frac{1}{12}\,base\;heigth^3 = \frac{1}{12}(n_t\,\pi\,D_3)\frac{h}{\cos\alpha}$$

3-6

29
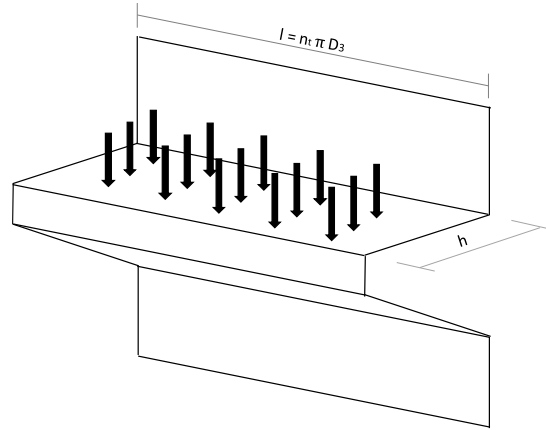
Figure 3-9: Thread surface simplification

The resulting equation to calculate the bending stress can be described as:

$$\sigma = \frac{(F\,x_c)\,x_c}{\frac{1}{12}\,(n_t\,\pi\,D_3)\,\frac{h}{\cos\alpha}} = \frac{12}{\pi}\frac{\cos\alpha}{}\,\frac{F\,x_c^2}{n_t\,D_3\,h} \qquad 3\text{-}7$$

3.3.3. Pure Shear Stress

The torque applied to a screw is overcoming the friction between the nut and the screw threads. This friction opposes the relative motion between them. This action generates a pure shear stress at the juncture where the threads meet the screw's root. The general shear stress formula is presented in Equation 3-8 where V represents the tangential shear force and A is the area where the tangential force is applied.

$$\tau = \frac{V}{A} \qquad 3\text{-}8$$

To calculate this tangential shear force, you can equate it to the torque divided by the radius of the screw's root R_3, as presented in Equation 3-9.

$$V = \frac{2T}{D_3} \qquad 3\text{-}9$$

The area over which this tangential shear force acts is analogous to the region highlighted in Figure 3-10, which shares the same dimensions as the rectangle we used to describe bending forces.

$$A = (n_t\,D_3\,\pi)\,b \qquad 3\text{-}10$$

Consequently, the resulting tangential shear stress formula is proposed in Equation 3-11.

$$\tau = \frac{\frac{2T}{D_3}}{(n_t\,D_3\,\pi)\,b} = \frac{2}{\pi}\frac{T}{n_t\,D_3^2\,b} \qquad 3\text{-}11$$
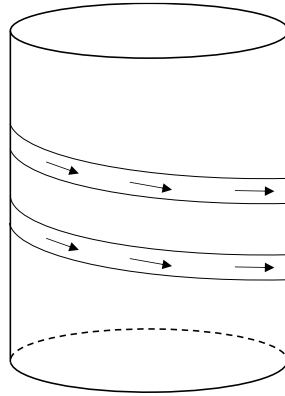
Figure 3-10: Pure shear stress layout

3.3.4. Torque Load

As presented in the introduction, most of the tightening methods in the offshore wind industry achieve the preload force by applying a torque T to the nut or the bolt head. In the bolt, this stress needs to be considered only in the engaged region between the bolt and the nut, as illustrated in Figure 3-11.
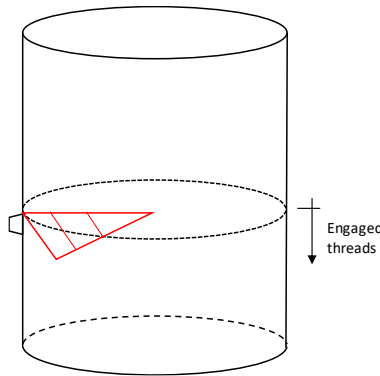
Figure 3-11: Torque stress layout

The torque stress τ is calculated as presented in Eq.3-12.

$$\tau = \frac{T\,c}{J} \qquad \text{3-12}$$

where c is the distance from the axis to the point of interest and J is the second polar moment of area of the cross section.

The distance considered from the axis is the minimum radius R_3. To calculate the second polar momentum, the circular equation has been considered under the hypothesis of cylindric bean (Eq.3-13):

$$J = \frac{\pi}{32}D_3^4 \qquad \text{3-13}$$

The torque load T is the product of three factors: the axial preload F_{app}, the diameter D_3, and a torque coefficient K_T. Eq.3-14 illustrates the formula to calculate the torque coefficient, as a function of r_t which is the mean thread radius, r_c which is mean collar radius, f_t and f_c which

31

are the friction coefficients between the thread surfaces and the collar surfaces, λ which is the lead angle and α which is half of thread angle (30 deg for ISO thread).

$$K_T = \frac{r_t}{D_3} \frac{\tan\lambda + f_t \sec\alpha}{1 - f_t \tan\lambda \sec\alpha} + \frac{f_c r_c}{D_3} \qquad \text{3-14}$$

In Eq.3-15 the simplified formula has been reported. As it is possible to see, the shear stress from torsion is variable only under the bolt dimensions D_3 and the friction coefficient between the surfaces presented in T.

$$\tau = \frac{T \frac{D_3}{2}}{\frac{\pi}{32} D_3^4} = \frac{16\,T}{\pi\,D_3^3} \qquad \text{3-15}$$

3.3.5. Results from Analytical Calculations

In Table 3-1 the different stress and shear components have been resumed. As seen in this table, each component is affected by the thread geometry (α, base (b) and height (h) of thread) and the bolt diameter D_3, however only bending and the pure shear components are variable in function of the number of engaged threads n_t.

Table 3-1 Resume of stresses formulas

	Stress direction	Formula
Axial	σ	$\dfrac{4\,F}{\pi\,D_3^2}$
Bending	σ	$\dfrac{12\cos\alpha}{\pi}\dfrac{F\,x_c^2}{n_t\,D_3\,h}$
Pure shear	τ	$\dfrac{T}{n_t\,D_3^2\,b}$
Torque	τ	$\dfrac{16\,T}{\pi\,D_3^3}$

In summary, it is possible to calculate the Von Mises Stress on the elemental cube. Using Eq.3-1, 3-7, 3-11 and 3-15 it is possible to use the general Von Mises equation

$$S_{VM} = \sqrt{\frac{\left(\sigma_x - \sigma_y\right)^2 + \left(\sigma_y - \sigma_z\right)^2 + (\sigma_x - \sigma_z)^2 + 6\left(\tau_{xy}^2 + \tau_{xz}^2 + \tau_{yz}^2\right)}{2}} \qquad \text{3-16}$$

From Eq.3-16, it is possible to calculate the stress distribution along all the engaged threads of the bolt. In Figure 3-12, the stress distribution along 10 engaged threads n_t have been calculated for M72 bolt, under an axial stress of 120 MPa (F_{app}=500 kN) considering a friction coefficient of 0.5.
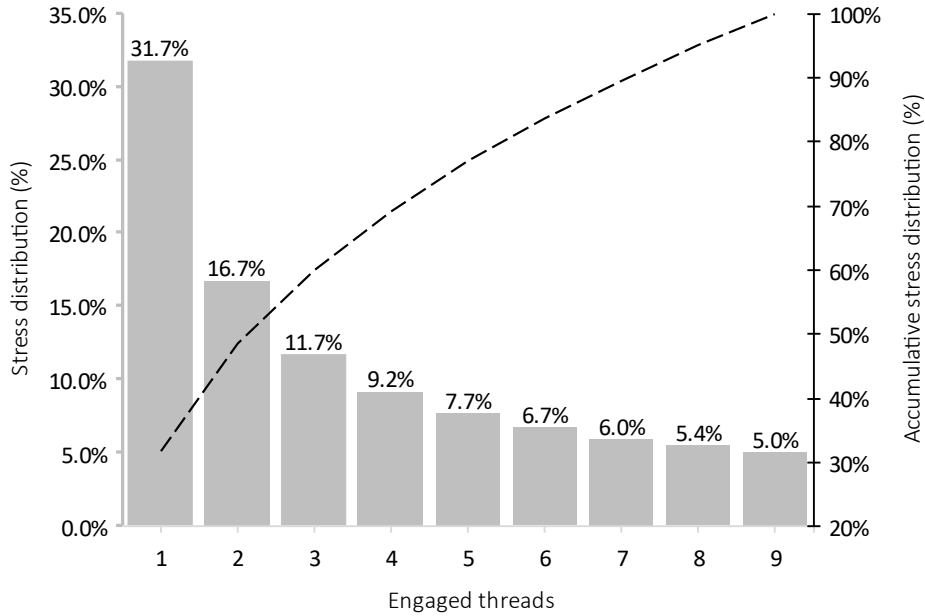
Figure 3-12: Percentage of stress distribution calculated from analytical approach along the first 9 engaged threads

A comparison between literature[53], [59]and the analytical evaluation has been summarised in Table 3-2 using the same conditions showed as for Figure 3-12. The results between the literature and the mathematical calculation are very close to each other, showing the possibility to predict the stress distribution for each thread. However, because it has not implemented with the Young's module as in the Sopwith's or the Yamamoto's model, it cannot be applied on system with the presence of plastic deformation.

In literature, the stress is mainly considered for the first 6 threads, mainly because the most considered area is around the first three threads.

Table 3-2 Comparison between Literature, Mathematical evaluation for Nt = 9 and relative error for 185 MPa and 0.5TT

N_t	Literature %	Analytical %	Error %
1	34.0	31.71	-2.29
2	23.0	16.69	-6.31
3	16.0	11.68	-4.32
4	11.0	9.18	-1.82
5	9.0	7.6	-1.40
6	7.0	6.6	-0.40
7	0.0	5.96	+5.96
8	0.0	5.42	+5.42
9	0.0	5.01	+5.01

As shown in Table 3-2, the percentage distribution along the engaged threads presented in the literature has a value of 0% for the threads after the number 7; reason for this is a consideration of only seven engaged threads in literature. However, considering the presented model with n_t equal to 7 it is possible to see a result with a smaller scatter compared to the difference between the literature and n_t = 9 (Figure 3-13 and Table 3-3).
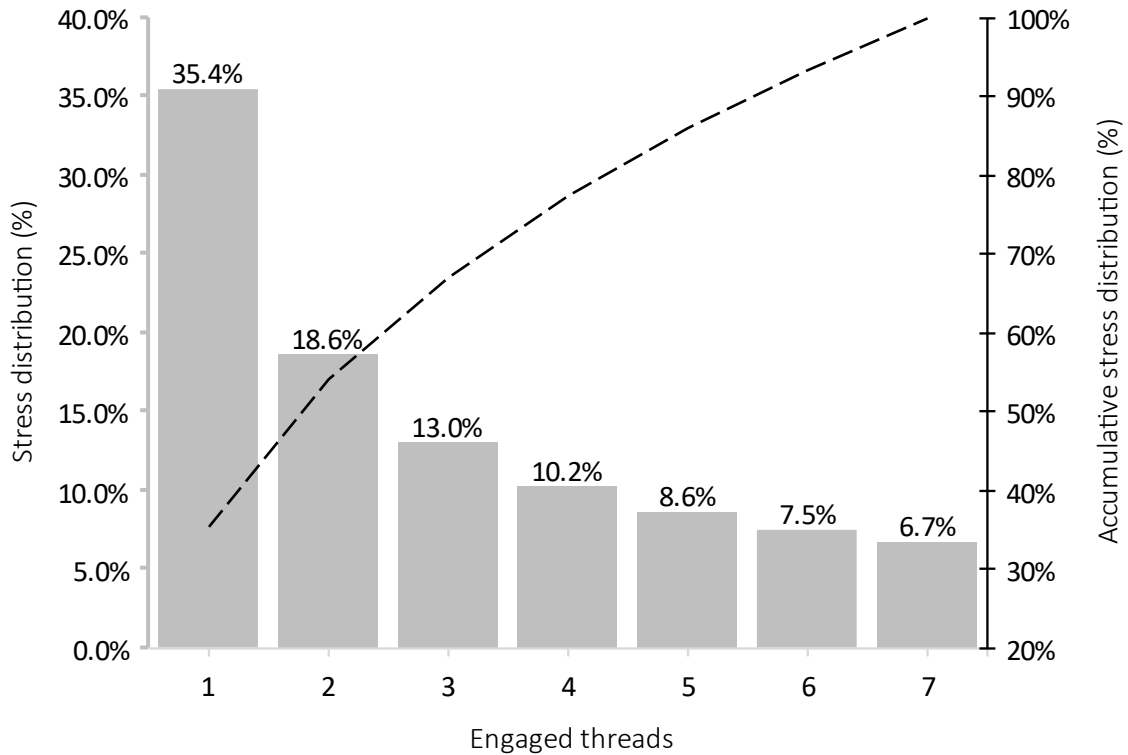
Figure 3-13 Percentage of stress distribution calculated from analytical approach along the first 7 engaged threads

Table 3-3 Comparison between Literature, Mathematical evaluation for Nt = 7 and relative error for 185 MPa and 0.5TT

N_t	Literature %	Analytical %	Error %
1	34.0	35.4	-5.01
2	23.0	18.6	+2.46
3	16.0	13.0	+2.10
4	11.0	10.2	+2.07
5	9.0	8.6	+2.04
6	7.0	7.5	+2.40
7	0.0	6.7	+2.33

3.4. Final Element Analysis

A sequence of finite element analyses has been developed to investigate the effect of preload applied during the assembly phase of bolts and nuts on the stress distribution along the engaged threads. The primary focus of these analyses is estimating the variations in stress levels at the interfaces between the bolt and nut, with specific attention paid to altering the friction coefficient between these surfaces and adjusting the preload applied to the bolt. Nowadays, the main bolt dimension used in the offshore wind industry is the M72, fabricated from grade 10.8 steel, with the main dimensions summarised in Table 3-4.

34

Table 3-4 Main thread size for M72

Dimension	
Diameter [mm]	72
Pitch [mm]	6
H [mm]	0.866

As demonstrated in the literature[19], [60] the stress distributions along engaged threads for a 2D axial-symmetric, and a three-dimensional model are quite similar. For this reason, a 2D axial-symmetric geometry has been considered for the simulations. Different simulations have been conducted to see the effect of the static friction coefficient based on different levels of preload, indicated as percentage (%) of the Yield Stress of the bolt material.

The bolt and nut materials are grade 10.9 and 8.8 stainless steel, respectively, with the main material properties reported in Table 3-5 and the stress strain curve illustrated by Figure 3-14.

Table 3-5 Properties for grade 10.9 and 8.8 steel

	Material	Young Module (MPa)	Yield Stress (MPa)	UTS (MPa)	Strain (UTS) (-)
Nut	8.8	210	640	810	0.022
Bolt	10.9	210	940	1056	0.088
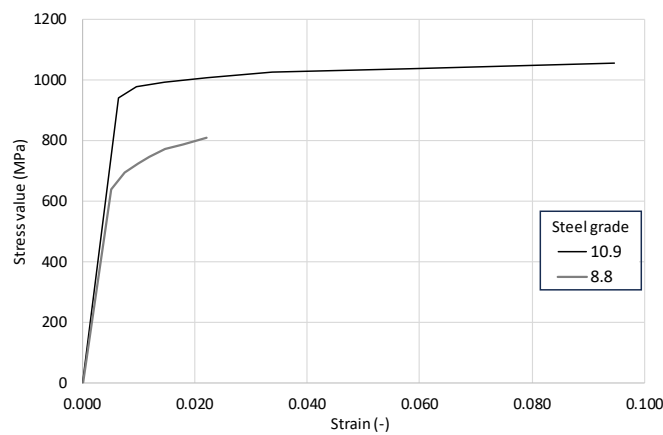
Figure 3-14 Stress-Strain curve for 10.9 and 8.8 stainless steel

The Boundary Condition (BC) have been chosen to simulate a real case loaded bolt (Figure 3-15a). For this reason, as illustrated in Figure 3-15b, a fixed BC has been applied on the internal surface where the nut surface is in contact with the washer and the axial-symmetric BBC has been highlighted in red. The load has been applied on the body section (pink arrows), as illustrated in Figure 3-15b. The interaction used between the nut and the bolt is the Tangential Behaviour contact propriety with different friction coefficients.

(a)   (b)
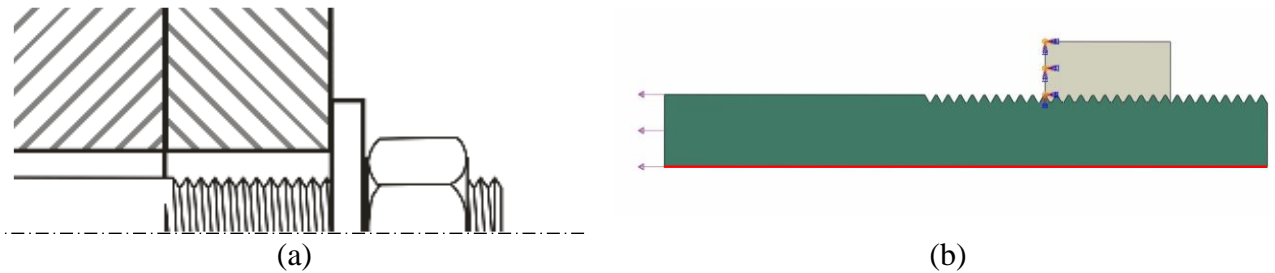
Figure 3-15: Bolted connection concept (a) and Bolted connection 2D axial symmetric simplification for FEA(b)

In Table 3-6, have been reported the friction coefficient that have been used and relative lubrification material considered.

Table 3-6 Static Friction coefficient considered for FEA analysis

Contact material	Static Friction Coefficient
Frictionless	0
	0.05
Lard	0.11
Lubricated and greasy	0.15
	0.23
Cleaned and Dry	0.5-0.8

The mesh used for the nut and bolt assembly is a 3-node linear axisymmetric triangle (CAX3), chosen to best accommodate the irregular body shape and work under the axisymmetric body. As illustrated in Figure 3-16, five different meshes have been developed: Table 3-7 reports the number of elements, the minimum size and the resulting Stress for the two components. As seen in the results for meshes #2, #3, #4 and #5 the stress result is similar with R^2 factor close to 1. Given that fewer elements can be related to a lower computational time, mesh #2 has been selected as the final FEA model. In Figure 3-17, the comparison between 0.5 and 1.0 [mm] elemental size has been reported.
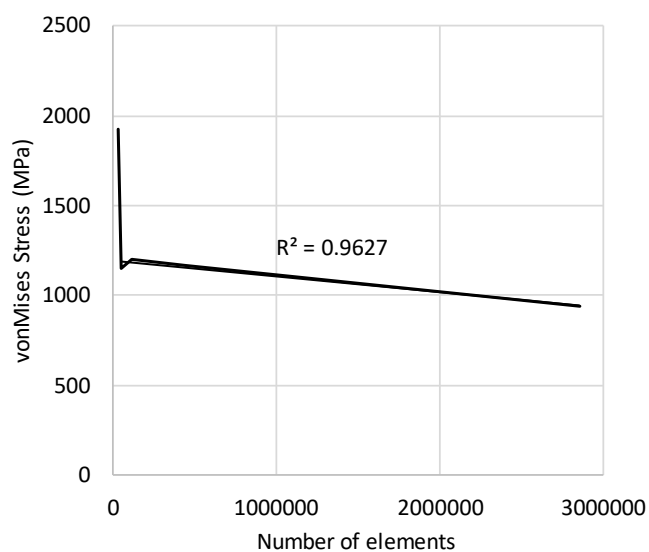
Figure 3-16: Mesh sensitivity analysis

Table 3-7 Mesh sensitivity analysis results

Mesh number	Local MP element number	Element size critical region [mm]	Maximum Mises Stress [MPa]
#1	31912	1	1927
#2	47191	0.75	1155
#3	109276	0.5	1200
#4	437375	0.25	1168
#5	2857415	0.1	938

(a)   (b)
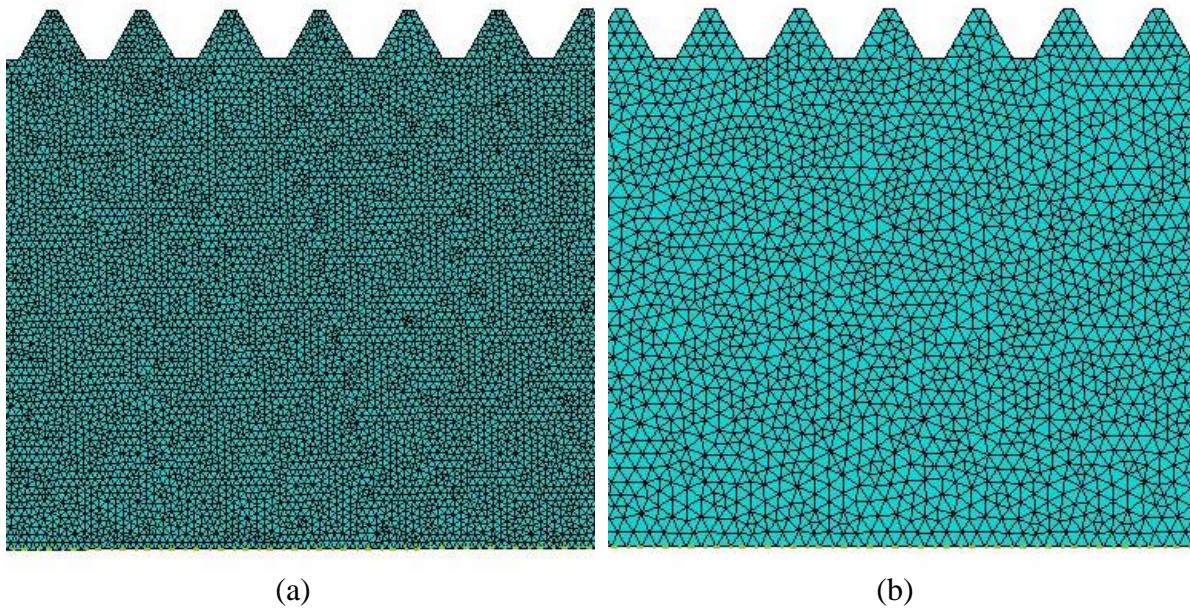
Figure 3-17: Mesh size comparison between elemental size of 0.5mm (a) and 1mm (b)

3.4.1. FEA Results

Results of the simulations have been reported in Figure 3-19 and Figure 3-20 showing the maximum Mises Stress per each engaged thread. These results take into account the stress distribution, the influence of friction coefficient on stress and the effect of the plasticity with the stress concentration factor, as reported in Figure 3-21 for bolt and in Figure 3-22 for the nut. To understand the results, Figure 3-18 provides a visualization, it shows the axial (S22) stress distribution along the engaged threads under the applied load equal to the 60% of Yield stress and with 0.23 friction coefficient. As shown, in the region where the nut interacts with the washer there is a compression zone (light green), while at the bottom of the bolt thread the axial stress is positive (tensile stress).
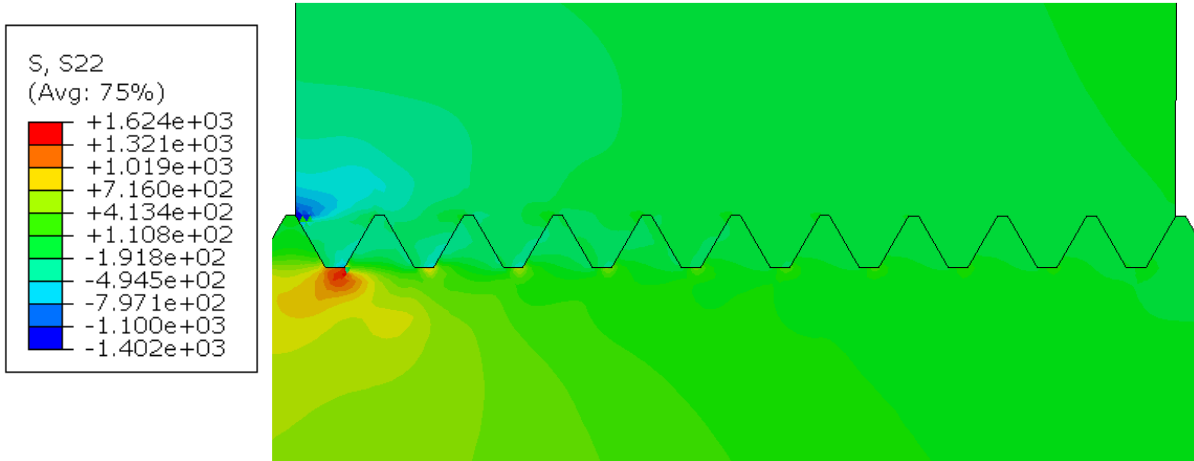
Figure 3-18: FEA results for axial-symmetric simulation of M72 bolt under 60% yield stress and friction coefficient of 0.23

From Figure 3-19 and Figure 3-20, two important considerations emerge. The first consideration pertains to stress distribution along the threads of both the bolt and nut under equal friction coefficient. As illustrated in Figure 3-19 and Figure 3-20, it is possible to see that as stress increases the initial engaged thread absorbs most of the stress. However, at low preloads (10 and 20% of the Yield Stress) the majority of stress is located in the first thread. As the load increases, threads start to enter in elastic-plastic region, making the stress distribution trend more challenging to predict. Similar results are presented in literature[61], showing how the stress distribution changes in accordance with the load applied. Increasing the load up to 40-50% of the Yield stress, stress distribution on the first threads increases gradually until reaching a maximum value, followed by a hyperbolic distribution among the remanent threads.

Another significant consideration is in the increase of the friction coefficient factor between the contact surfaces of the nut and the bolt. As this coefficient increases, a proportional rise in stress magnitude. The consideration is valid for both the bolt and nut, higher friction coefficient corresponds to increased stress. However, this difference is lower for the first thread, which is subjected to higher stress, and for the ones that are in elastic-plastic region, compared to the ones in pure elastic region. Conversely, for threads farther from the initial one, it is possible to observe the opposite phenomenon: as friction increases, stress decreases.

To better comprehend the results obtained from simulations, a consideration about the Stress Concentration Factor (SCF) is necessary. To calculate the local SCF the ratio between the maximum triaxial stress and the average applied load has been considered, as illustrated in Equation 3-17. Triaxial stress has been considered instead of the pure axial stress for the complexity of geometry of the bolt.

$$SCF = \frac{S_{max}}{S_{mean}}$$ 3-17

By taking as an example the stress distribution along the bolts and nut threads with a friction coefficient factor of 0.23, the SCF variation along the engaged threads have been considered for different preloads, results are presented in Figure 3-21 and Figure 3-22.

Plasticity effect makes a significant contribution to the stress distribution along the engaged threads. As previously discussed, the SCF follows the expected trend of distribution, where the

first thread is more subjected to stress compared to the other ones. However, this trend persists until the first thread starts to deform in an elastic-plastic manner, resulting in reductions in the obtained values.

Similar results can be seen when considering the SCF for the nut (Figure 3-22). For lower applied stress (10% and 20% of the Yield stress) the stress distribution remains the same. As soon as the first thread enters in elastic-plastic region, the stress distribution changes, decreasing until reach similar SCF value along all the engaged threads for higher applied stress values (around 1.0 for applied stress > 90% YS)
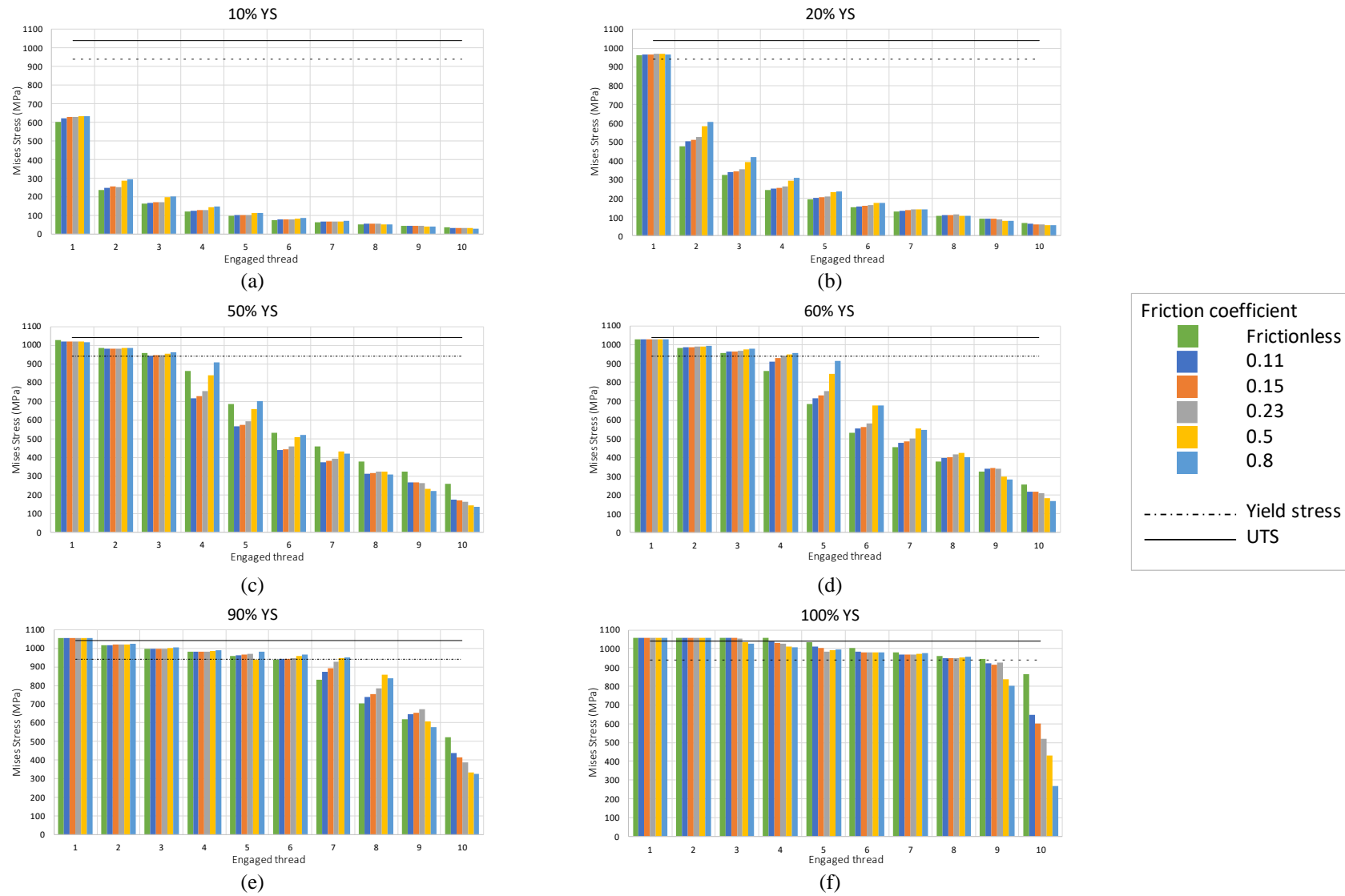
Figure 3-19 Stress distribution along the first 10 engaged threads of the bolt in function of different friction coefficient and under different load magnitude: 10% (a), 20% (b), 50% (c), 60% (d), 90% (e) and 100% (f) of the Yield stress of the grade 10.9 steel
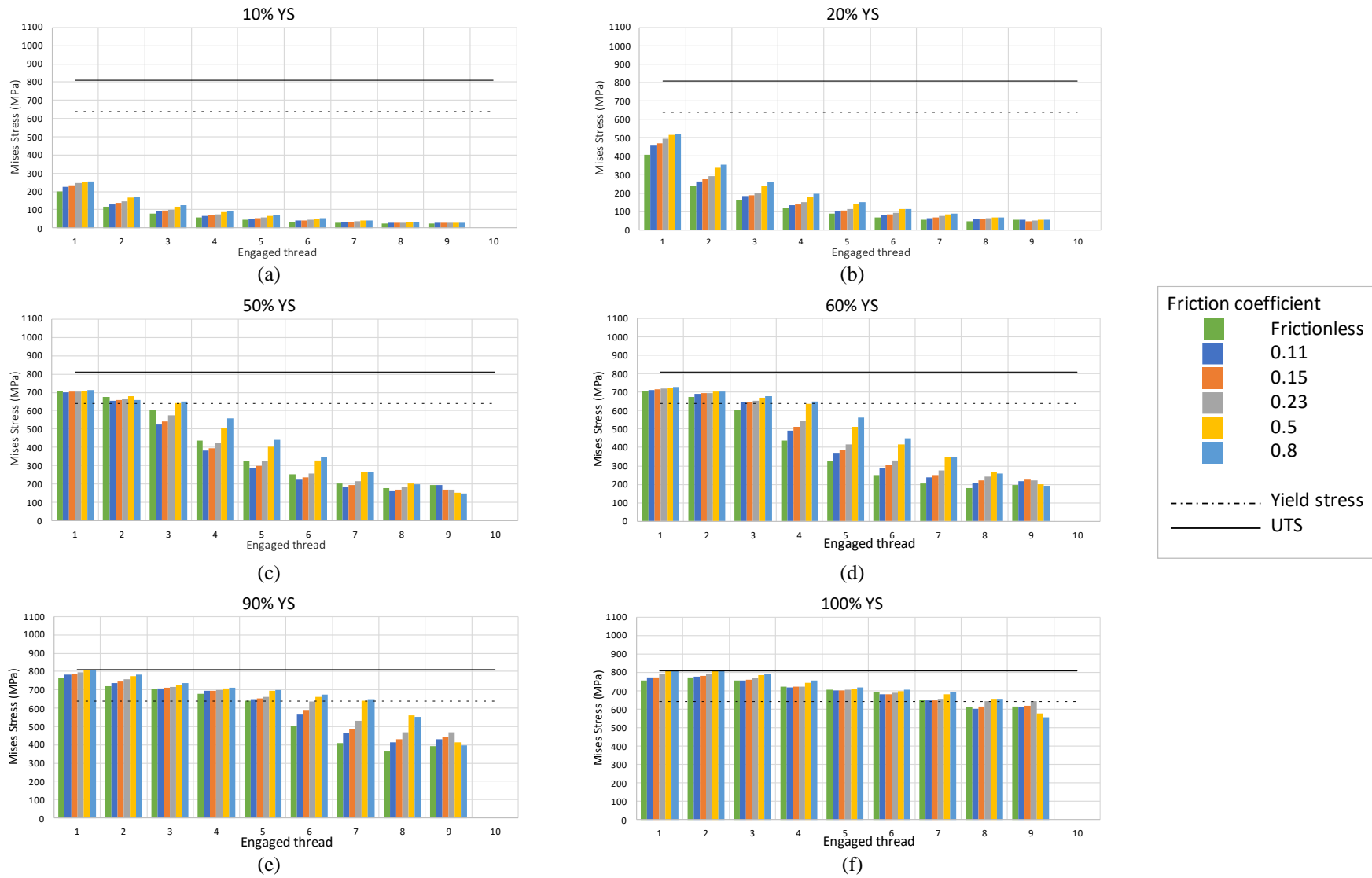
Figure 3-20 Stress distribution along the first 9 engaged threads of the nut in function of different friction coefficient and under different load magnitude: 10% (a), 20% (b), 50% (c), 60% (d), 90% (e) and 100% (f) of the Yield stress of of the grade 8.8 steel
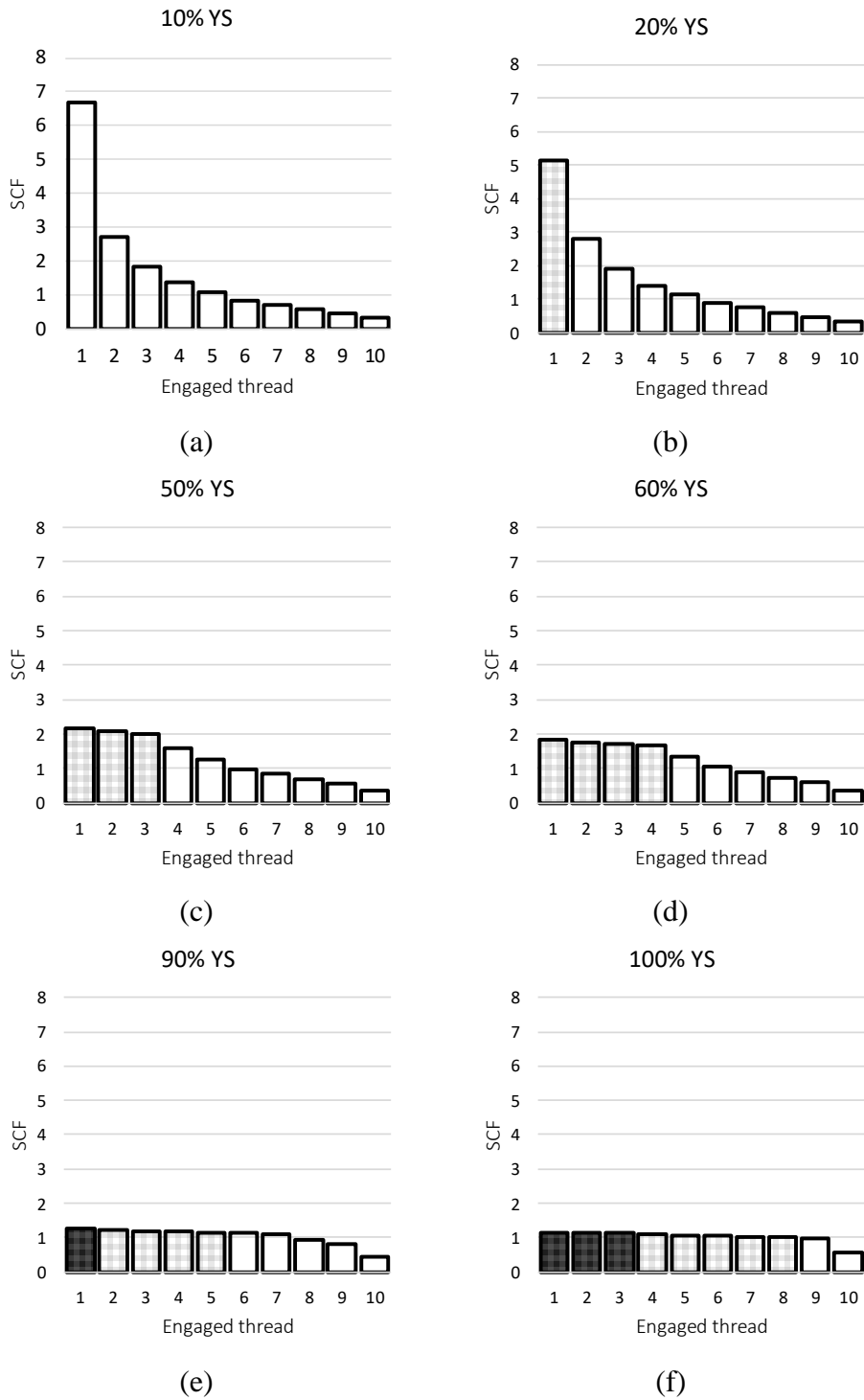
Figure 3-21: Stress concentration factor distribution along the engaged threads for the bolt, highlighting the pure-elastic (empty), elastic-plastic (diagonal stripes) and plastic (dotted) threads
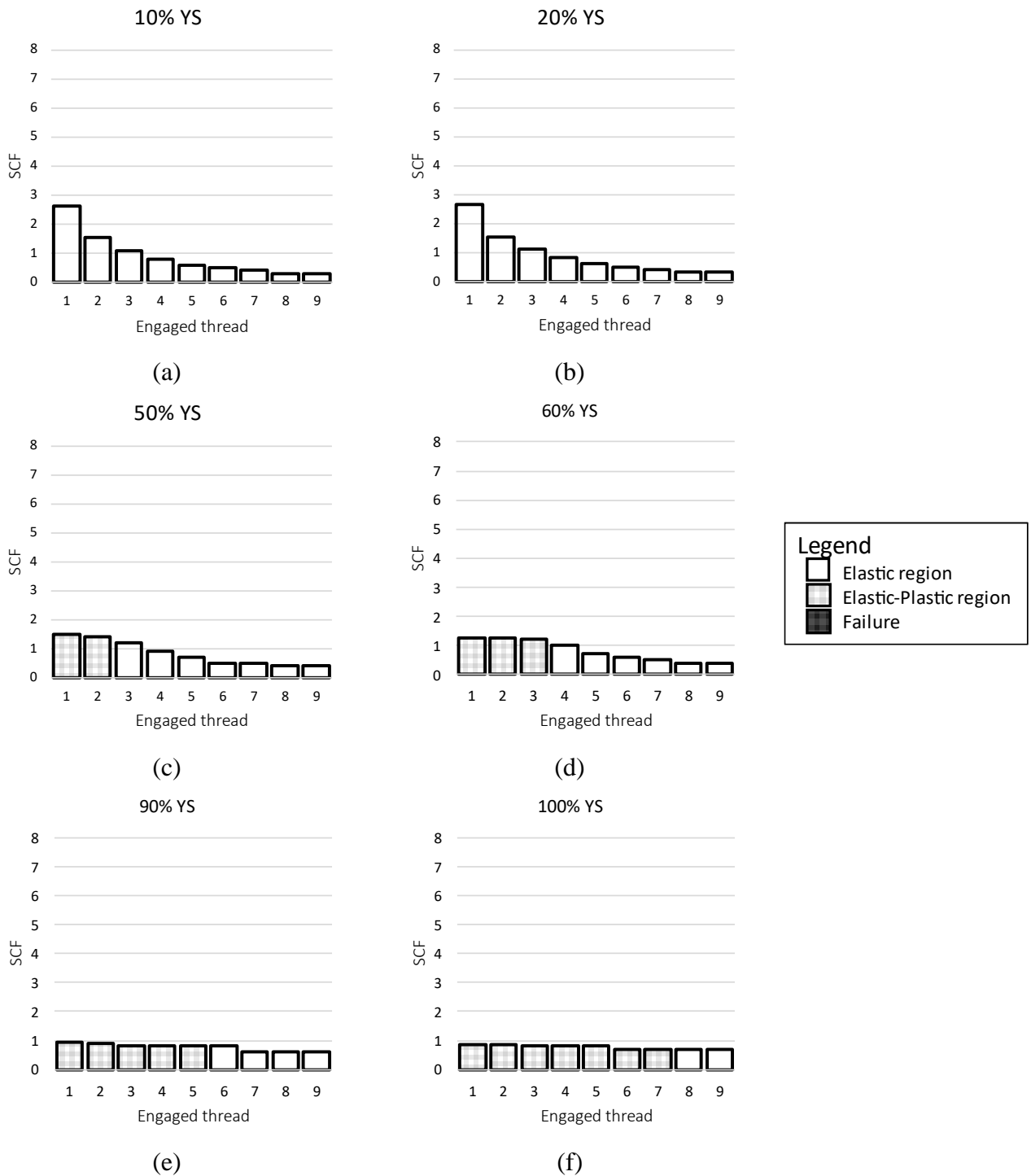
Figure 3-22: Stress concentration factor distribution along the engaged threads for the nut, highlighting the pure-elastic (empty), elastic-plastic (diagonal stripes) and plastic (dotted) threads

3.5. A Review of International Fatigue Standards

As part of the fatigue life prediction for mechanic components, the fatigue design curve (also known as S-N curve) is utilized. In industry, three main standards are usually used for the design of threaded connections against fatigue failure, each of which is presented below.

3.5.1. Eurocode 3 EN 1993-1-9

This standard provides methods for the assessment of fatigue resistance of components subjected to fatigue loading. This standard is applicable to most of grades of structural steels, stainless steels, and unprotected weathering steel. The curves do not cover the sea-water corrosion effect and damages coming from high temperatures (>150°C). This standard does not cover the post fabrication treatments aimed at improving the fatigue strength of the component.

The S-N curve considers four main parameters:

- $\Delta\sigma_C$ reference stress value of the fatigue strength to $N_c = 2\times10^6$ cycles
- $\Delta\sigma_D$ fatigue limit for constant amplitude stress ranges at the number of cycles to N_D
- $\Delta\sigma_L$ cut-off limit for the stress ranges at the number of cycles N_L
- N_R design lifetime expressed as number of cycles related to a constant stress range

For constant amplitude nominal stress ranges, the fatigue strength can be obtained as

$$\Delta\sigma_R^m N_R = \Delta\sigma_C^m\, 2\times 10^6$$

$$3\text{-}18$$

For $N \leq 5\times10^6$ with $m = 3$

$$\Delta\sigma_R^m N_R = \Delta\sigma_D^m\, 5\times 10^6$$

$$3\text{-}19$$

For $5\times10^6 < N \leq 10^8$ with $m = 5$

And the cut-off can be calculated as

$$\Delta\sigma_L = \left(\frac{5}{100}\right)^{\frac{1}{5}} \Delta\sigma_D = 0.549 \times \Delta\sigma_D$$

$$3\text{-}20$$
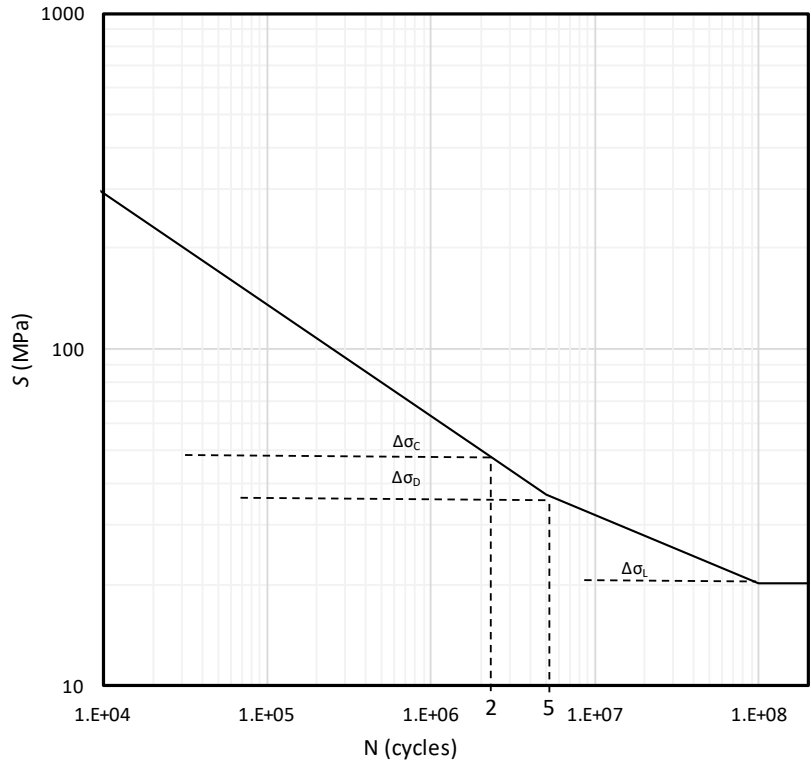
Figure 3-23 S-N curve for bolts under direct stress ranges (FAT50) according to Eurocode 3 EN1993-1-9

3.5.2. DNVGL-RP-C203

This standard provides a series of S-N curves for different types of plates, bolted connection, and welded joints, each one divided into different classes depending on the geometry of the detail, stress fluctuation direction and the manufacturing and inspection method.

The basic curve follows the logarithmic equation described below.

$$\log N = \log \bar{a} - m \log \Delta\sigma \qquad \text{3-21}$$

where $\Delta\sigma$ is the stress range, N is the predicted number of cycles to failure for $\Delta\sigma$, m slope of S-N curve, and $\log \bar{a}$ is the intercept of the design S-N curve with the log N-axis which can be calculated as:

$$\log \bar{a} = \log a - 2s_{logN} \qquad \text{3-22}$$

where *log a* is the intercept of mean S-N curve with the log N-axis and s_{logN} is the standard deviation of *log N*.

For bolts under axial load, the standard classified them as class F1 or G. The difference lies in the manufacturing process to which the bolt or the threaded rod is subjected: F1 includes all samples that have been subjected to cold-rolled threads without subsequent heat treatment, such as hot galvanization, while category G denotes samples made with cut threads and rolled threads, followed by heat treatment, such as hot galvanisation.

45
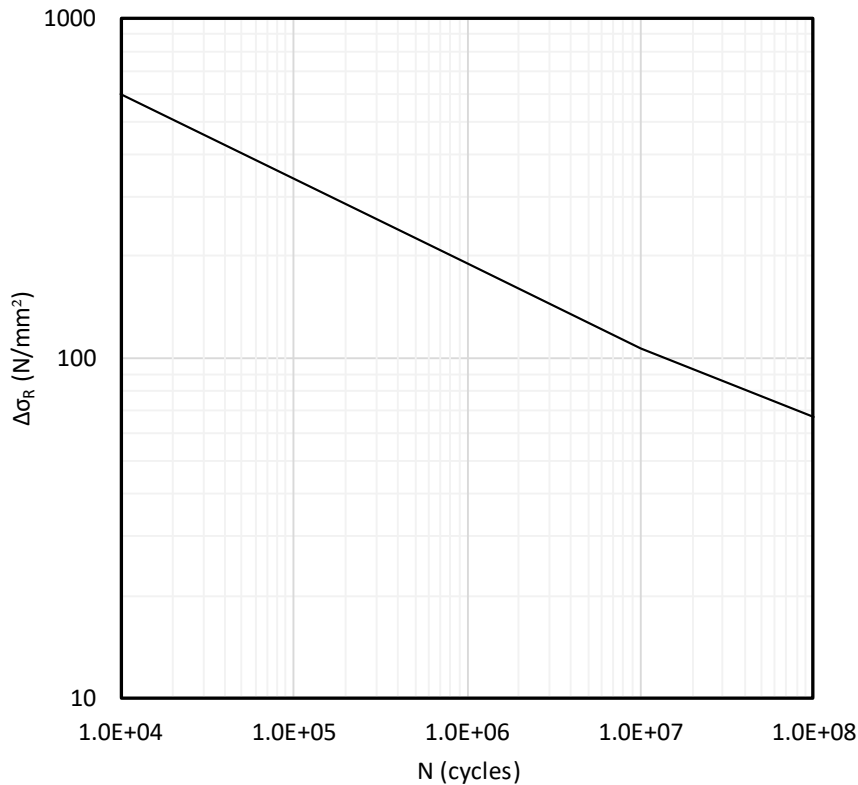
Figure 3-24 S-N curve for bolts under direct stress ranges according to DNVGL-RP-C20393-1-9

3.5.3. BS 7608 - 2014

This standard provides methods to determine the fatigue life of steel component subjected to stress fluctuations. The standard covers ferritic and low alloy steel material, austenitic and duplex stainless steels, and components such threaded fastener and welds in stell casting machined components.

Each design class curve follows the relation between Stress range *Sr*, and Number of cycles to failure *N*, under constant amplitude loading condition illustrated with Eq.3-23 and 3-24.

$$\log N = \log C_d - m \cdot \log \Delta\sigma \qquad\qquad 3\text{-}23$$

$$S_r^m N = C_d \qquad\qquad 3\text{-}24$$

where *m* is the inverse slope of $\log S_r$ - $\log N$ curve and C_d is the parameter defining the relationship with mean curve with a standard deviation.

In the BS code the class to identify the threaded fasteners is Class X under the following consideration:

a) Applicable for bolts with cut or ground threads, as well as for rolled threads.
b) If rolling is performed after the heat treatment, the fatigue strength needs to be increased by a 25%,
c) If the bolt is electroplated or heat threated the fatigue strength needs to be reduced by a 20%.

46

In Figure 3-25 the S-N curve for class X has been plotted with the correction discussed previously.
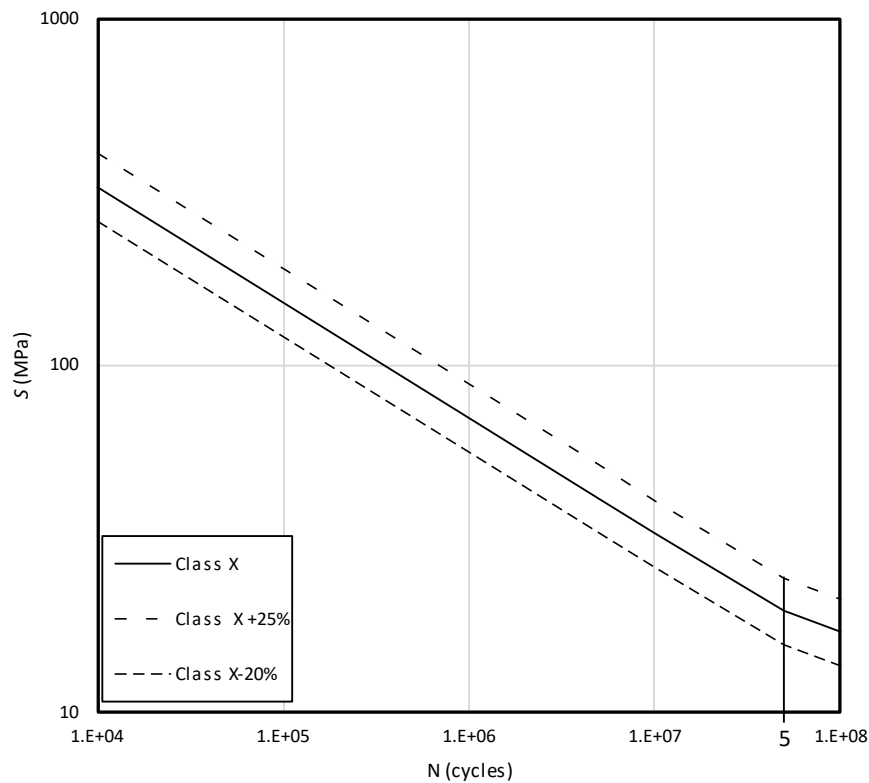
Figure 3-25: S-N curve for bolts under direct stress range for Class X, Class X+25% and Class X-20% according to BS 7608- 2014

3.5.4. Comparison among the S-N Curves

In the three standards presented, significant differences in fatigue lives can be obtained depending on which standard is followed. One of such is the consideration the seawater corrosion (with and without cathodic protection) presented in the DNVGL-RP C203 and BS 7608 but absent in Eurocode3. Another consideration is that only the BS 7608 takes into consideration the fatigue strength improvement based on the heat treatment.

The three S-N curve standards provide a formula when the component dimension is larger than the considered for the curves previously presented. This analytical adjustment is known as thickness correction, and the equation to calculate it have been reported in Table 3-8 specifying the correlated standards.

Table 3-8 Thickness correction calculation in accordance with standards

Standard	Thickness correction	Thickness reference	
EC3 EN1993-1-9	$\left(t_{ref}/t\right)^{0.25}$	30 mm	
DNVGL-RP-C203	$\left(t_{ref}/t\right)^{0.25}$	25 mm	
BS 7608-2014	$\left(t_{ref}/t\right)^{0.25}(1 + 0.18\Omega)$	25 mm	Ω is the degree of bending (0 for bolts)

47

In the equations it is possible to see how the reference thickness t_{ref} takes two different values, depending on the standard considered: 25 mm for the DNVGL-RP and BS 7608 and 30 mm for the Eurocode3. As illustrated from Johnston [51], the disparity between these two references can affect the life prediction of the bolt and create some discrepancies in the choice of the code.

Furthermore, when comparing the three different codes with the same thickness (or diameter in the bolt case), it is possible to notice how the three curves are pretty close. In Figure 3-26, the three curves have been plotted for a diameter of 30 mm. It is evident that the Eurocode3 is a code a bit less conservative compared to the DNVGL-RP and the BS 7608, while the latter two are closer to each other.
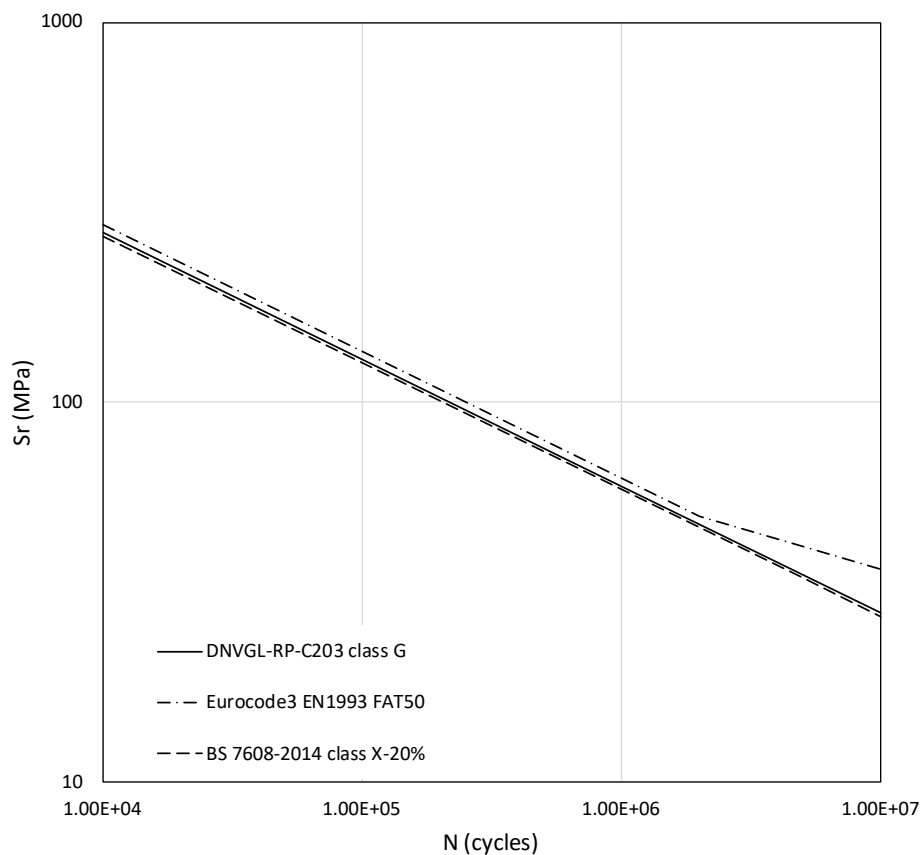
Figure 3-26: Comparison between S-N curves for a t=30 mm, in accordance with the three main standard codes

3.6. Analysis of the Literature Fatigue Data

In literature numerous fatigue failure tests have been conducted on different types of bolted connections, resulting in a large dataset for different size of bolts loaded under axial fatigue load. However, this data-cloud gets smaller further the increase of the sample size.

In this section, data points presented in literature regarding axial load fatigue tests on bolts have been collected. Tests involving special types of threaded connections (e.g. self-locking) and those conducted considering corrosive environments have been excluded. A logarithmic statistical analysis has been employed to compare the main S-N curves with the different bolt

size data points collected for M36[21], [36], [62], [63], [64], M48[65], [66], M64[36], [51] and M72[51]. All data analysis presented exclude run-out points.

Figure 3-27 represents the study results[21], [36], [62], [63], [64] developed for M36 bolts, taking into consideration different surface treatments: black (or uncoated) bolts, normal temperature (NT) and High temperature (HT) hot-dip galvanised bolts. Comparing the three different lines representing the results of the log-log statistical analysis at the 97.7% of failure probability, two main results can be considered by taking into account the slope of the curve and which standard code better describe the results. The curve slopes of the three typologies of bolts studied reveals a slight difference. There is a reduction in fatigue strength for the galvanized specimen around the 20-25% compared to the black bolts caused by crack initiation from the zinc coating, as recent research has [21], [63]. The codes that better fits the uncoated bolts is the class F1 of DNV code, while the Eurocode3 FAT 50 fits the galvanized samples more accurately, while the most conservative code is the BS 7608 for coated (class X-20%) and uncoated (class X).

In Figure 3-29, the results for M64 bolts have been plotted for both uncoated and galvanised samples[21], [36], [51]. Figure 3-28, and Figure 3-30 illustrate the statistical study for M48[65], [66] and M72[51] data points found in literature, respectively. In Table 3-9 the main results of the statistical analysis have been reported. In this table the slope value m, the intercept $Log\ \bar{a}$, and the standard deviation (SD), and the coefficient of determination R^2 have been reported. Comparing all the curves with the relative SN curve classes, it is evident that the studies converge on the result that the best standards fitting the statistical analysis for galvanised models is the Eurocode3 FAT50, while the DNVGL-RP-C203 and the BS 7608-2014 are the most conservative. Meanwhile for uncoated bolts study presented in Figure 3-29 both classes F1 and class X can be representative. This differences can be linked to the choice of 30mm as reference thickness for the thickness correction as well as the poor statistical population of tests.

Table 3-9 Data analysis coefficient for the main bolt size (97.7% failure probability)

	M36			M48	M64		M72
	Uncoated	NTG	HTG		Uncoated	Galvanised	
m	3.75	3.23	3.36	2.16	3.37	2.89	2.66
$Log\ \bar{a}$	13.315	11.881	12.121	9.733	12.153	11.130	10.429
SD	0.155	0.111	0.140	0.165	0.158	0.066	0.146
R^2	0.923	0.945	0.921	0.796	0.925	0.987	0.931

The second consideration regarding the curve slope, as presented in Section 3.5, is that all the codes provide a slope value of 3 for N lower than 1×10^7 cycles. However, as reported in Table 3-8, the slope per each bolt size differs from the suggested value. Another parameter considered is the intercept of the curves ($Log\ \bar{a}$). The galvanisation has presented a reduction in fatigue strength compared to the uncoated ones leading designers to prefer the latter. However, as discussed in [51], galvanised bolts demonstrate better resistance to corrosion in seawater with cathodic protection, although any damage or incomplete heat treatment could lead to the strength reduction.
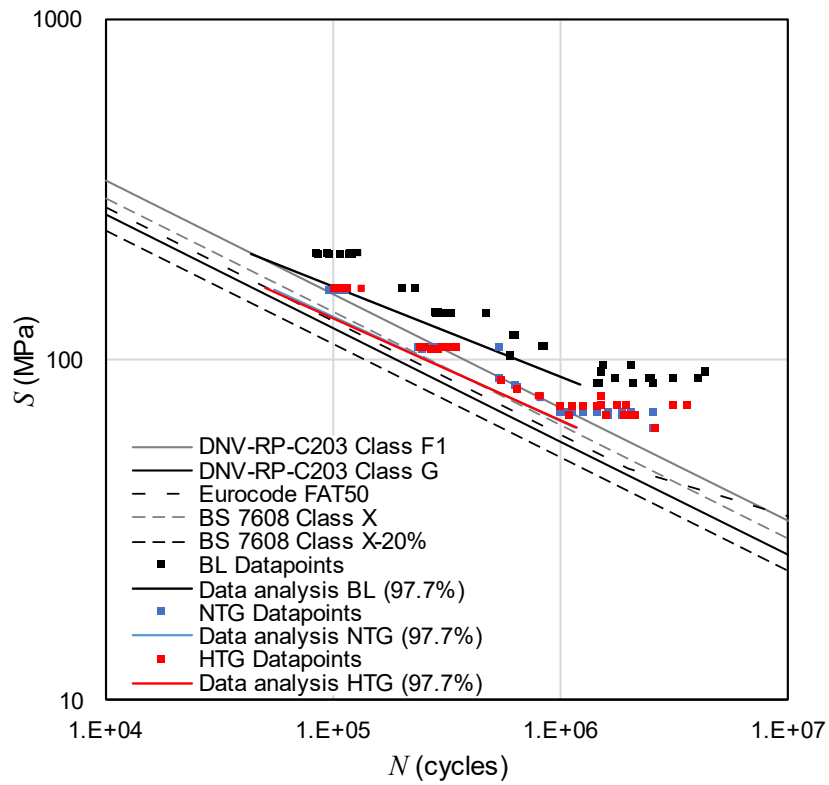
Figure 3-27 Data cloud for M36 bolts, for the different heating treatment
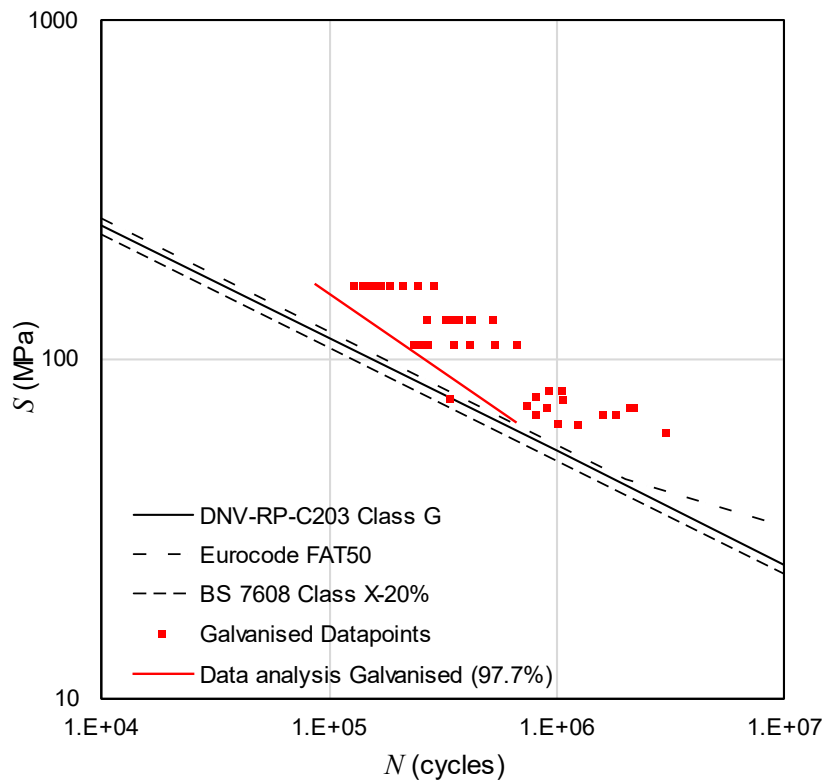
Figure 3-28 Data cloud for M48 bolts

50
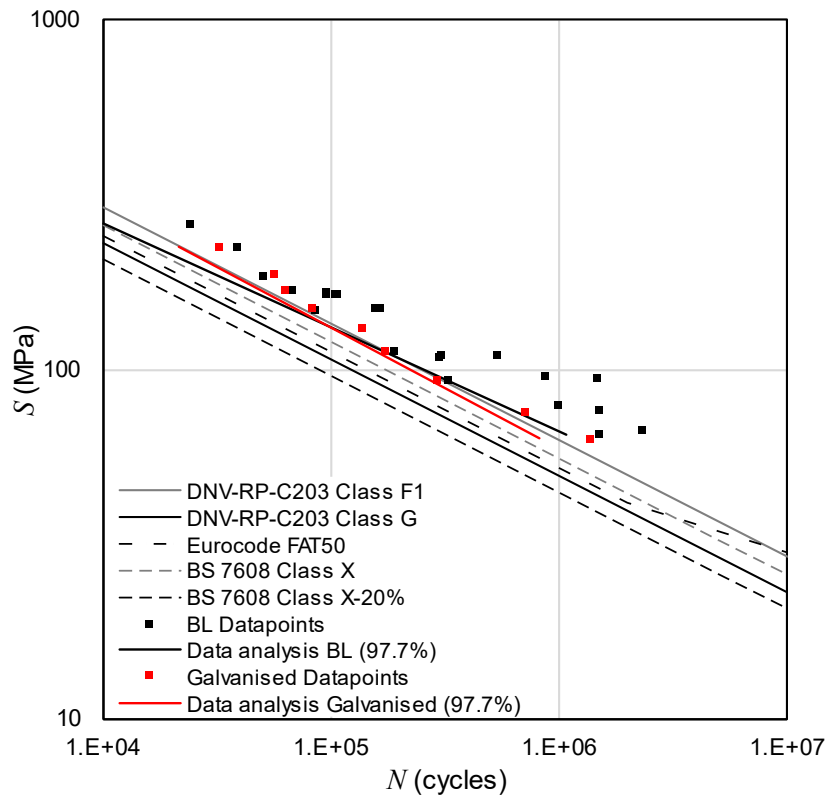
Figure 3-29 Data cloud for M64 bolts, for the different heating treatment: uncoated (black) and galvanised (red)
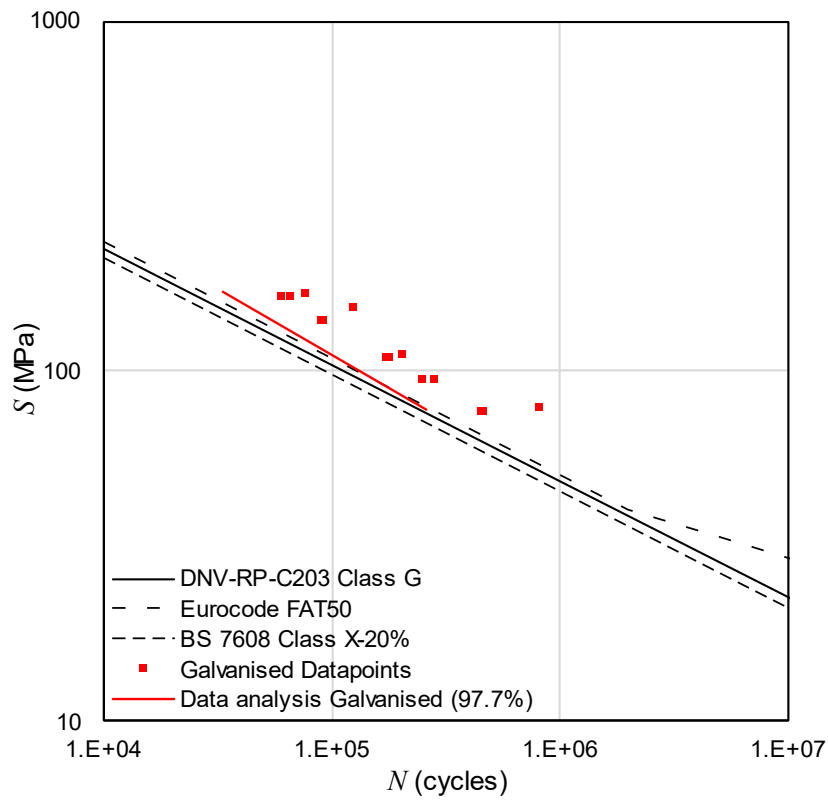
Figure 3-30 Data cloud for M72 bolts

A second statistical data analysis has been developed by merging the results for uncoated and galvanised samples for M36 bolts. In Table 3-10 the main results have been presented, reporting the results already discussed above for the uncoated and galvanised (NTG and HTG) samples, the statistical analysis results for a combined data analysis and the values suggested from DNV and BS codes. Figure 3-31 illustrated the graphical results. From the analysis, it is evident that the slope of the different types of bolts is between 3.23 and 3.75. However, the slope of the combined results gets approaches the standard value ($m=3$) with a value of 2.948. Similar considerations can be taken for the curve intercept $log\ \bar{a}$, which moves from a range of 12.120-13.315 to a 11.214, bringing it closer to the suggested value in the Eurocode3 FAT50 and DNV class G presented in the relative standards.

Table 3-10 M36 statistical analysis for Uncoated, Normal Temperature (NTG) and High Temperature (HTG) galvanised M36 bolt compared to results for combined data

	BL	NTG	HTG	Combined data	DNV Class G	DNV Class F1	BS Class X	BS Class X-20%
m	3.75	3.23	3.36	2.95	3.00	3.00	3.00	3.00
$Log\ \bar{a}$	13.315	11.881	12.121	11.214	11.398	11.699	11.968	9.574
SD	0.155	0.111	0.140	0.251				
R^2	0.923	0.945	0.921	0.760	-	-	-	-
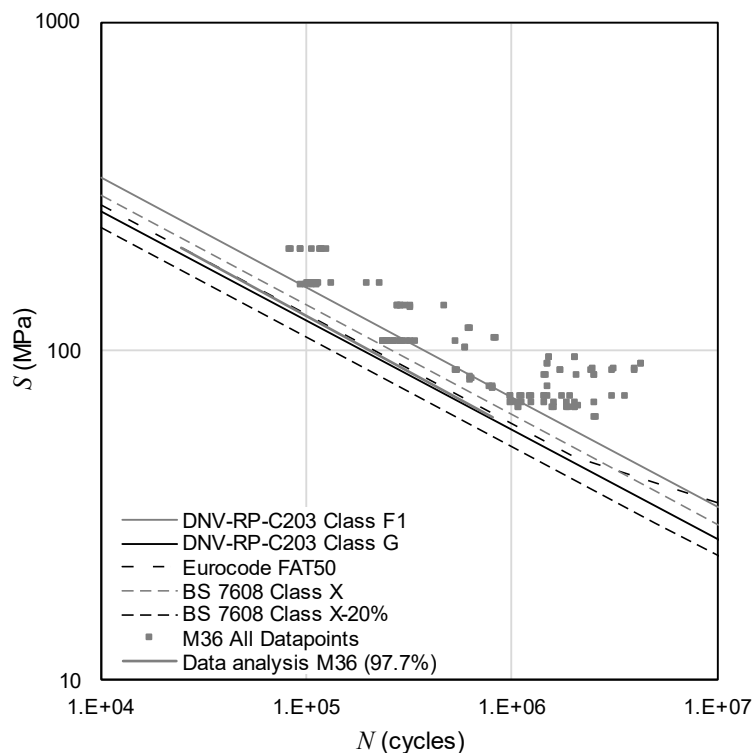
Figure 3-31: Comparison of combined fatigue data points for M36, with the thickness corrected fatigue design curves from various standards

Same analysis developed for M36 has been done for M64 bolts (Table 3-11 and Figure 3-32). Results of the combined data show a slope of 3.228, which stays in the range described by the uncoated and galvanised curves (2.895-3.374), while the intersection to the curve ($Log\ \bar{a}$) gets closer to the value of 11.968 from the BS code. Comparing these results with the statistical analysis done for the M36, it is possible to see how the M64 results are not as similar to the standards, one possible reason for this disparity is the decrease in data population as the bolt size increases.

Table 3-11 Statistical analysis for Uncoated and Galvanised (NTG+HTG) M64 bolt compared to combined data results and standards parameters

	Uncoated	Galvanised	Combined data	DNV	BS
m	3.37	2.89	3.23	3.00	3.00
$Log\ \bar{a}$	12.153	11.130	11.769	11.699	11.968
SD	0.158	0.066	0.170		
R^2	0.925	0.987	0.910	-	-
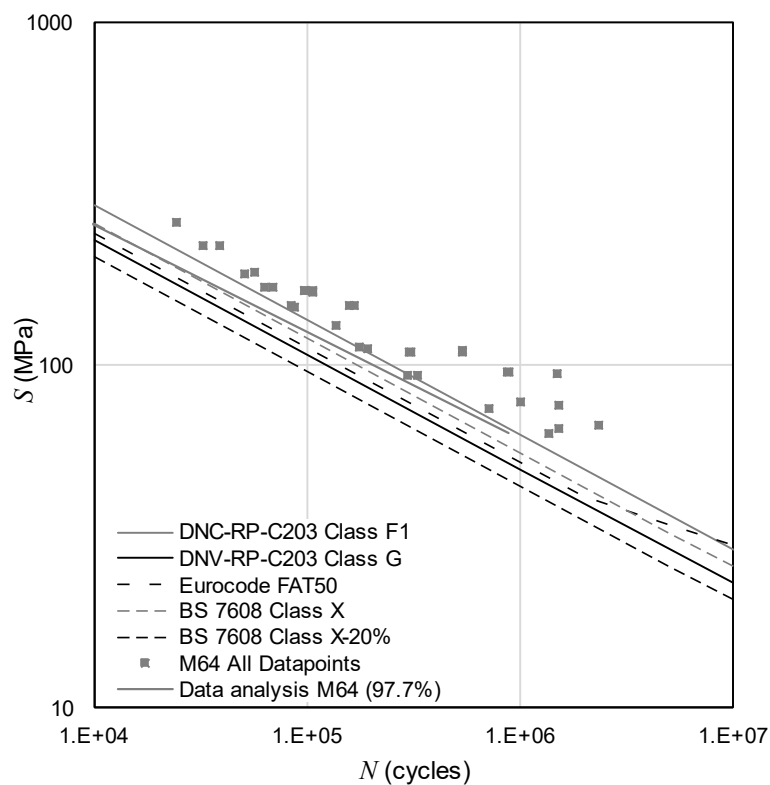
Figure 3-32: Comparison of combined fatigue data points for M64, with the thickness corrected fatigue design curves from various standards

Taking into consideration the results obtained by merging the data points from different surface treatment for M36 and M64, a final log-log statistical analysis has been developed to compare the entire data cloud test without considering the heat treatment and the sample size. The results were subsequently compared with the two main standards that proved to be the most accurate, and the findings are reported in Table 3-12.

As seen in this table, the result of the analysis conducted on the literature data shows numbers that are not very close to the ones presented in the standards. However, if the value for the

intercept of the mean S-N curve (*Log a*) is considered, these values become very close (11.678). An important note is that these results could lead to misleading calculation of life strength of bolts of different sizes and heat treatment, as illustrated in the previous analysis.

Table 3-12 Confrontation between standard and statistical analysis coefficient

	Data-cloud analysis	DNV	BS
m	2.963	3.000	3.000
Log ā	11.182	11.699	11.968
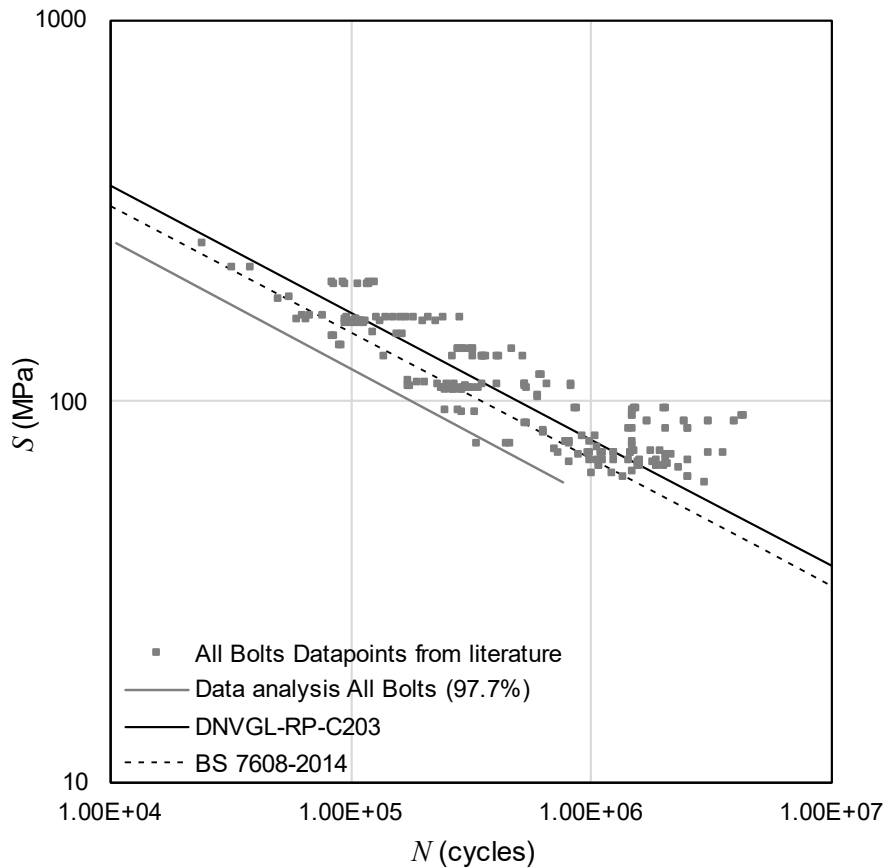
Figure 3-33: Data-cloud from literature of all pure axial fatigue test in dry environment

3.7. New Fatigue Tests on M72 Bolts

M72 bolts made of grade 10.9 steel are widely used in MP-TP connections of fixed-bottom OWTs in the UK and Europe, however as highlighted from Figure 3-30 there is a limited number of fatigue data points available in the open literature on this thread size. Possible reason for this is linked to the fact that the performance of fatigue tests on large-scale threaded connections is relatively expensive because of the material costs, the operational costs of the fatigue test machines with high load capacities, and relatively low frequencies in large-scale testing which make the tests very time consuming. In order to further investigate the fatigue behaviour of M72 threaded connections under tensile loading conditions and to improve the design and integrity assessment of bolted flange MP-TP connections, seven new fatigue tests, denoted M01—M07, were carried out in this study on hot-dip galvanised M72 studs and the results from these tests are presented in this section, with the relative discussion of fractography and statistical analysis. Subsequently, the results are compared with the codes discussed in Section 3.5, to verify if the main standard S-N curves and the relative size factor for bolts and threaded connection under axial load are accurate or, eventually, if any corrections can be suggested.

Fatigue tests were performed at TWI Ltd facilities using a servo-hydraulic test machine with a load capacity of 2500kN (Figure 3-34). Fatigue tests were performed under constant amplitude loading condition with uniaxial loading direction, and two nominal mean stress S_m values were applied to build new knowledge on fatigue performance of MP-TP threaded connection. Five tests were performed under the mean stress of $S_m = 202$ MPa (M01-M05) with another two tests under $S_m = 624$ MPa (M06 and M07). For each of the mean stress values considered in this study, various values of stress range were implemented in different tests to build a new knowledge on the fatigue performance of MP-TP threaded connections. All tests were run at 1Hz frequency and continued until the failure was occurred in the threaded connections. The values of maximum stress S_{max}, minimum stress S_{min}, stress range S_r (or S, which is the difference between S_{max} and S_{min}) and mean stress S_m are reported in Table 3-13 for each of the new tests performed in this study.

Table 3-13: Fatigue test data for M72 gr.10.9 bolts under constant uniaxial stress conditions

	S_{max} (MPa)	S_{min} (MPa)	S_r (MPa)	S_M (MPa)
M01	281.9	123.7	158.2	202
M02	270.2	134.4	135.8	202
M03	256.7	147.1	109.6	202
M04	272.4	132.4	140.0	202
M05	249.5	154.7	94.8	202
M06	679.0	568.5	110.5	624
M07	693.7	553.4	140.3	624
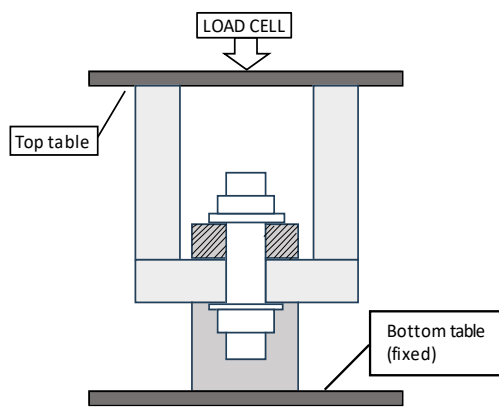
(a)	(b)	(c)

Figure 3-34: Schematic set up of the M72 bolt fatigue test (a) and picture of the fatigue test set up of servo-hydraulic machine in TWI Ltd facilities (b) and (c)

3.7.1. Test Results

The results of the test have been documented in Table 3-14, with a S-N graph depicted (Figure 3-35).

Table 3-14 Uniaxial constant load fatigue stress for M72 gr10.9 bolts

	S_r (MPa)	N (Cycles)
M01	158.2	2.35×10^5
M02	135.8	1.73×10^5
M03	109.6	5.60×10^5
M04	140	4.58×10^5
M05	94.8	5.59×10^5
M06	110.5	3.82×10^5
M07	140.3	1.89×10^5
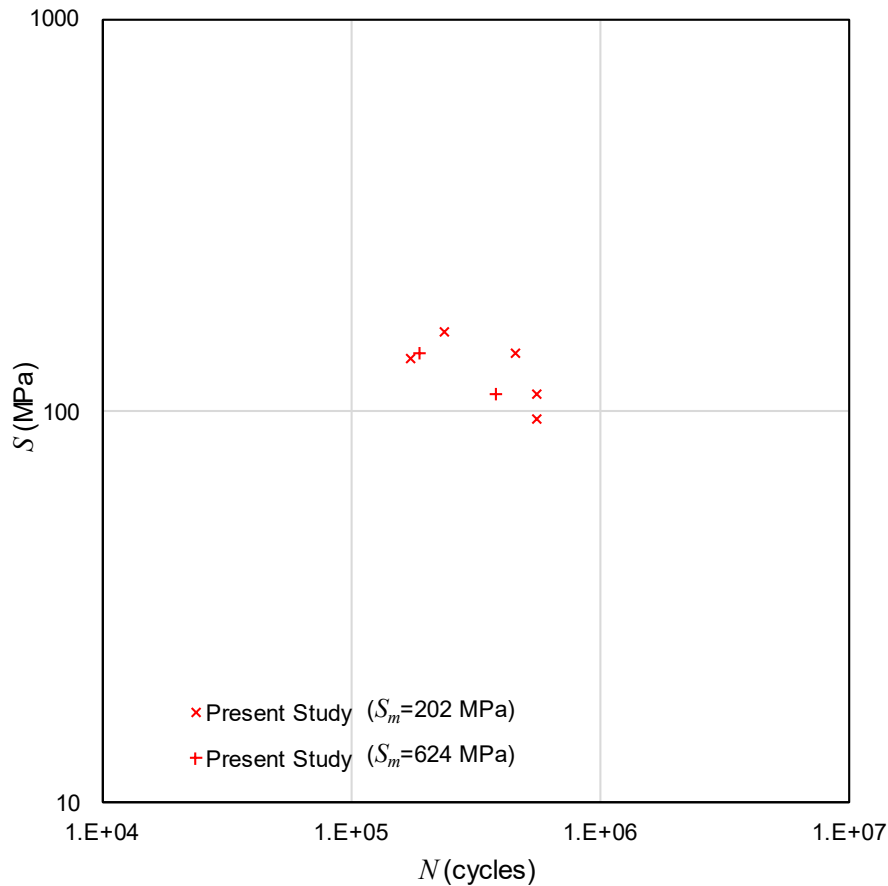
Figure 3-35: Fatigue Test results for 5 samples under 202MPa (square) and 2 samples under 624 MPa mean stress (triangles)

A preliminary statistical analysis was conducted on the results obtained from the seven tested samples (see Figure 3-36), and the findings were compared with those obtained from literature data on M72 bolts, summarised in Table 3-15. Subsequently, the new test data were combined with the literature data on M72 bolts, and a new regression analysis was performed. The results obtained from the line of best fit from all three of these regression analyses are presented in Figure 3-37. As seen in this table, the result of the analysis conducted on the literature data shows numbers that are not very close to the ones presented in the standards, one possible reason for this disparity is the decrease in data population as the bolt size increases, as similarly discussed for M64 samples.

Table 3-15 A summary of data analysis results from the new data set and combination of the literature data and new data on M72 threaded connections

	Annoni's data	Combined literature and new data
m	2.00	2.32
$log\ \bar{a}$	9.384	9.727
SD	0.167	0.214
R^2	0.516	0.607
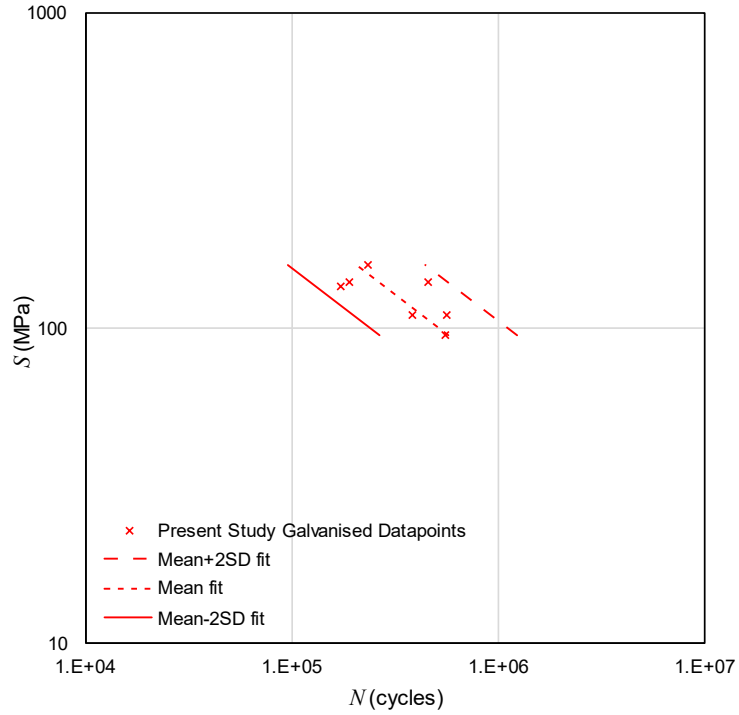
Figure 3-36: Results for M72 galvanised bolt Annoni's samples (red cross) comparing statistical analysis at 97.7% of failure probability (red line) with main standards
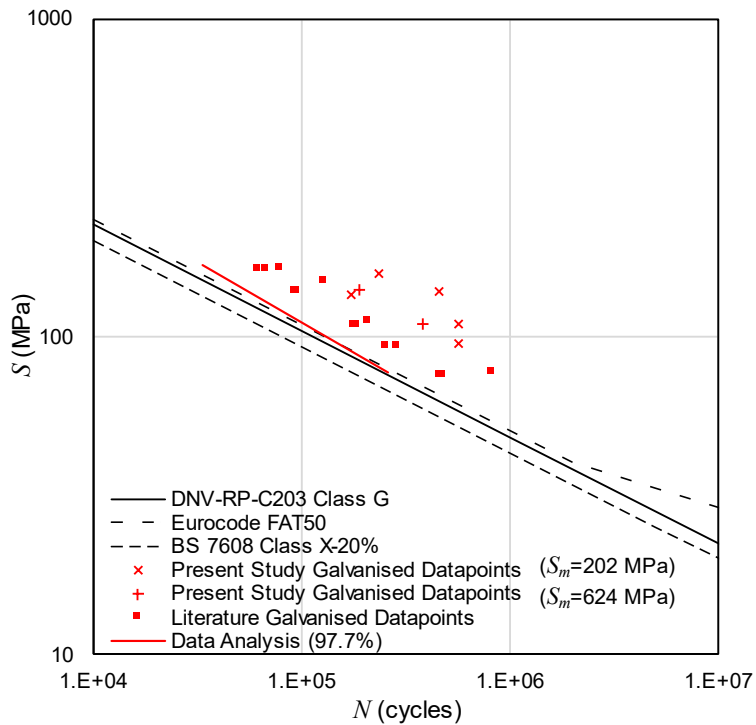
Figure 3-37: Results for M72 galvanised bolt merging Annoni's (red cross) and literature's (red square) results, comparing statistical analysis at 97.7% of failure probability (red line) with DNV standard

3.7.2. Fractography Analysis

The overall failure patterns of all bolts were visually examined to identify fracture initiation, defining morphology similarities such as number of initiation crack points and, eventually, the presence of secondary points or the section of the final stress area. Figure 3-38 presents the recreated fractography map of all seven bolts tested under fatigue loading conditions in this study. The crack initiations have been reported with black arrows, while the red arrows indicate the direction of the crack propagation. Moreover, the fast fracture region is shown in green.

All the sample failure occurred at the first engaged thread with a monoplane propagation direction except for M03, that showed fracture at different which will be presented separately at the end of the discussion. All the examined samples have a final area that presents shear lips [67], allowing the definition of the final fracture stage. The area has been calculated through image software and reported in Table 3-16 as percentage of area $A_\%$. Because the final areas are relatively small, it has been possible to verify the failure as a tension-tension mild-stress concentration at low nominal [68].

As illustrated in Figure 3-38, most of the samples present multiple crack initiation sites of similar size, with exception of M05 and M06 that presented a main initiation point. Secondary initiation points have been detected from the position of secondary beach lines for M01, M02, M05 and M07. In accordance with the secondary crack initiation position, a more marked crack growth region was observed for M04, M06 and M07.

In the case of the M02 sample, a series of larger cracks were detected on one side of the fracture surface, suggesting that crack initiation started from there. However, no beach mark was found to confirm this direction. Similarly, in the case of M05, a major crack and two smaller one was observed near the first crack. From the position of the smaller cracks, two secondary regions have been identified. It has been possible to comprehend that the main crack was the largest and the two secondary areas have merged with it.

As illustrated in Figure A, sample M03 exhibited a failure that differed from the other samples. In this sample, different crack initiation points of different dimensions were detected all around the circumference of the first engaged thread. Moreover, the propagation of the crack occurred on different planes that converged on the final failure region.

Table 3-16 Failure Area $A_\%$ for tested sample (excluding M03)

Sample	Fast fracture Area ($A_\%$)
M01	33.8
M02	32.9
M03	N/A
M04	17.8
M05	51.1
M06	30.9
M07	22.1
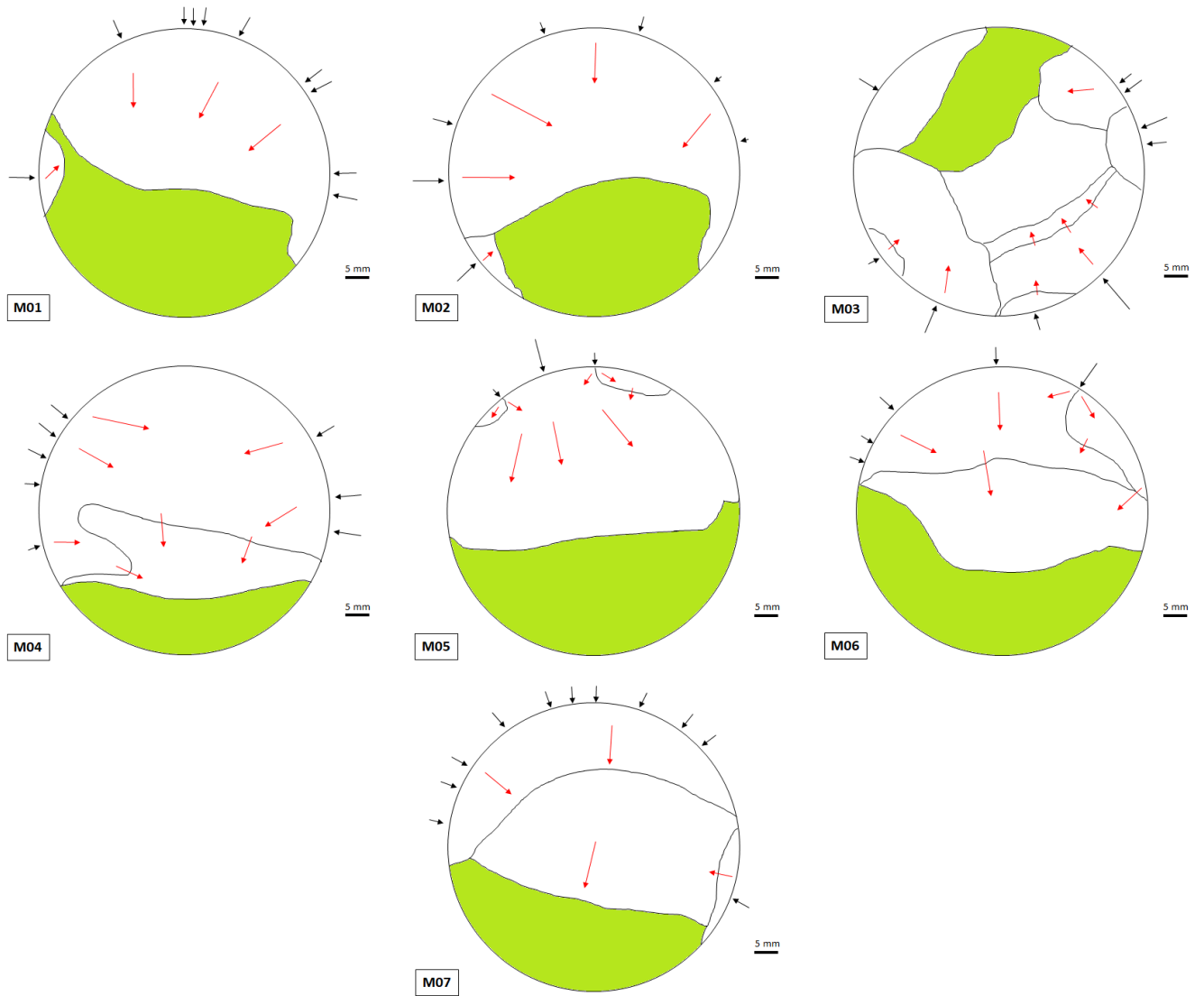
Figure 3-38 Fractography results for the seven M72 samples tested. The black arrows illustrate the crack initiation and the red arrows the fatigue crack propagation. The fast fracture region has been highlighted in light green.

3.8. Analysis of the Mean Stress Effect on Fatigue Behaviour of M72 Threaded Connections

The influence of mean stress on the fatigue behaviour of engineering materials has been evaluated using the Goodman approach. As described by Equation 3-25, Goodman correlates the stress amplitude (S_A), the stress limit (S_L), the mean stress (S_M) and the ultimate tensile stress (S_{UTS}) of a component.

$$S_A = S_L \left(1 - \frac{S_M}{S_{UTS}} \right)$$
<div align="right">3-25</div>

In order to evaluate the mean stress effects on the fatigue life of the M72 threaded connections, the results obtained from the fatigue test presented in Section 3.7 have been considered for two different values of mean stress. The ultimate tensile strength (S_{UTS}) for grade 10.9 steel threaded

connections can be assumed as 1040 MPa. However, the exact value of the fatigue endurance limit SL for the examined grade of steel and stud size is unknown. Therefore, two different Goodman equation have been considered to analyse the relative stress amplitude (S_{A1} and S_{A2}), as shown in Equation 3-26. From this, it is possible to calculate a normalised Goodman equation, determining the relative effect of different mean stress levels, as illustrated in Equation 3-27.

$$S_{A_1} = S_L \left(1 - \frac{S_{m_1}}{S_{UTS}}\right) \text{ and } S_{A_2} = S_L \left(1 - \frac{S_{m_2}}{S_{UTS}}\right) \qquad \text{3-26}$$

$$\frac{S_{A_2}}{S_{A_1}} = \frac{\left(1 - \frac{S_{m_2}}{S_{UTS}}\right)}{\left(1 - \frac{S_{m_1}}{S_{UTS}}\right)} \qquad \text{3-27}$$

where S_{m1} is the first mean stress value employed in the present study's experiments (S_{m1} = 202 MPa), S_{m2} is the second mean stress value, S_{A1} is the stress amplitude corresponding to S_{m1} and S_{A2} is the stress amplitude corresponding to S_{m2}. As seen in Equation 3-27, the Goodman analysis allows calculating the equivalent stress amplitude that would produce the same fatigue life as S_{m1} at a different mean stress of S_{m2}.

Considering S_A as half of the stress range S, the mean fit to the fatigue data at S_{m1} = 202 MPa has been used to predict the relative fatigue curves for S_{m2} of 470, 564, 620 and 658 MPa, which correspond to 50%, 60%, 66% and 70% of the yield stress of the material, receptively, in accordance to Equation 3-27. The results from this analysis are shown in Table 3-17 and Figure 3-39. As seen in Table 3-17, different levels of mean stress values were considered in this study to initially investigate the gradual change in the prediction of the fatigue life with an increase in the mean stress value, and subsequently evaluate the accuracy of the predicted fatigue lives at S_{m2} = 624 MPa, mean stress used for the testing of M06 and M07 samples presented in previous section.

It can be seen in Table 3-17 and Figure 3-39 that an increase in the mean stress value leads to a reduction in the intercept of the mean curve *log a* while the inverse slope *m* remains unchanged. This indicates that at the increase of the mean stress is associated a reduction in terms of fatigue life of the threaded connections. Finally, as illustrated in Figure 3-39, Goodman approach allows to predict the fatigue life for samples tested under mean stress of 624 MPa; it is overly conservative compared to the two data points available at this mean stress.

Table 3-17 Resume of main parameters for SN curve under mean stress of 202 MPa and relative mean stress levels

S_m	m	logC (mean value)	SD
202MPa	-1.85	9.447	0.1914
470 MPa (50% YS)	-1.85	9.131	0.1914
564 MPa (60% YS)	-1.85	8.986	0.1914
620 MPa (66% YS)	-1.85	8.884	0.1914
658 MPa (70% YS)	-1.85	8.809	0.1914
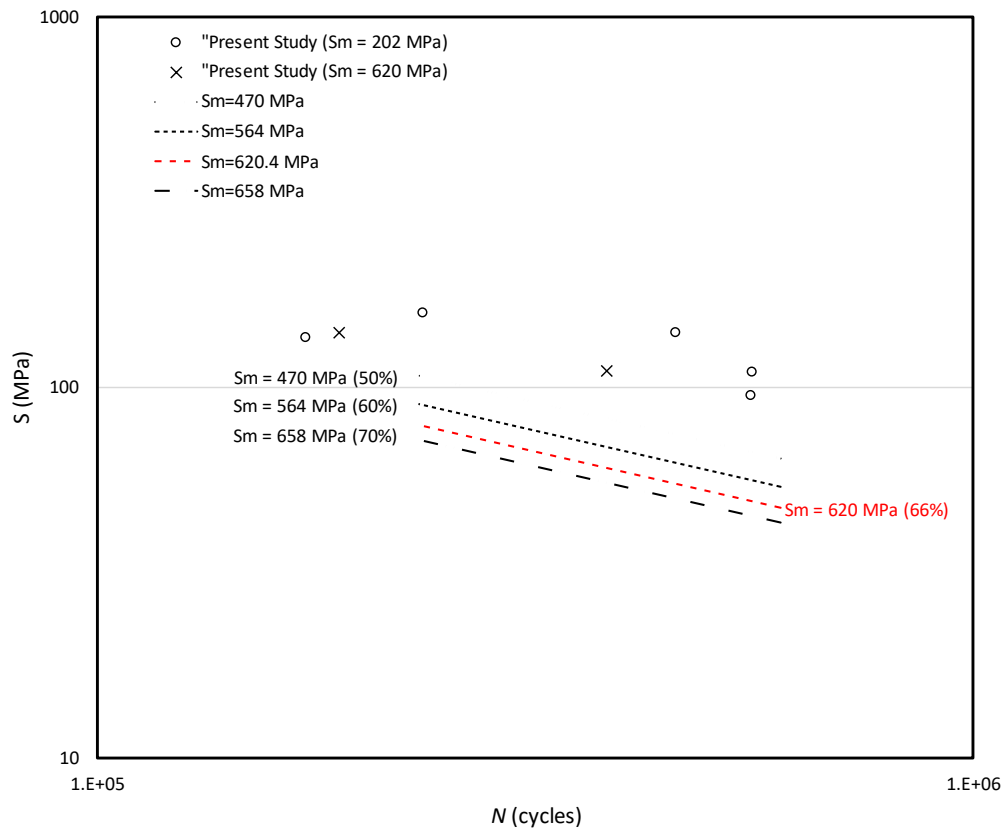
Figure 3-39: Comparison between statistical analysis result of sample tested under S_m=202 MPa and different mean stress levels, in accordance with Goodman correlation

According to the procedure presented by C. Johnston[69], the Goodman prediction can be modified and improved by introducing the notch effect of the thread as SCF value at the first engaged thread. Doing this, a modified stress amplitude S_A^* is defined and calculated in accordance with Equation 3-28.

$$S_A^* = S_A \times SCF$$

3-28

In accordance to Equation 3-28, an FEA simulation, similar to the ones presented in section 3.4.1, has been developed under a mean stress of 620 MPa (66% of Yield stress). The distribution of the stress concentration factor (SCF) has been presented in Figure 3-40. Result of this simulation provided a SCF value equal to 1.52, similar value (1.6) has been used by C. Johnston for a sample under a nominal stress of 70% of Yield stress.

62
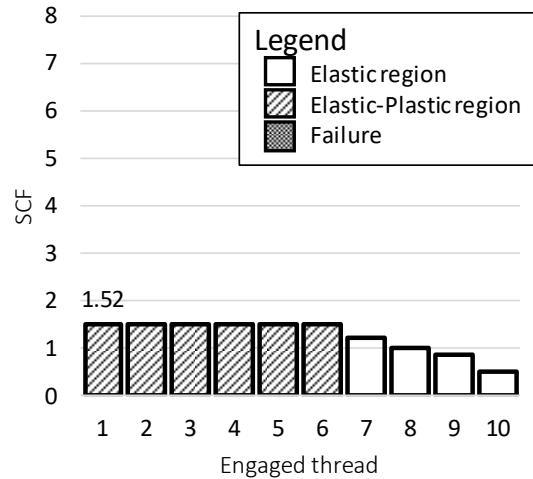
Figure 3-40 Stress concentration factor distribution along the engaged threads for the bolt under 624 MPa

According to stress distribution results at various applied load levels obtained from finite element simulations demonstrated in Figure 3-21(a) and Figure 3-40, the SCF values obtained at the first engaged thread under 202 MPa and 624 MPa mean stress levels are found to be approximately 5 and 1.5, respectively. By incorporating the SCF value corresponding to the estimated mean stress of S_{m_2} using Equation 3-28 in conjunction with the Goodman analysis in Equation 3-27, a modified Goodman prediction can be obtained the results of which are presented in Figure 3-41 and Table 3-18.

These results show that for the two experimental data points on M72 studs tested at the mean stress of 624 MPa, the Goodman method introduces a significant percentage of error ranging between 37% and 45% with a high degree of under prediction. However, using the modified Goodman method the predicted points fall very close to the experimental data points, significantly reducing the percentage of error to much lower values ranging between 5% and 18%. This analysis confirms that the employment of the SCF value of 1.5 at the first engaged thread obtained at the mean stress value of equivalent to 66% of the yield stress of the stud material results in satisfactory predictions of the fatigue trends at this mean stress level using the modified Goodman approach.

In conclusion, the application of the Goodman method for estimating the fatigue life under different mean stresses results in under prediction of fatigue lives at the higher mean stress of 624 MPa while the employment of the stress concentration factor at the first engaged thread in the modified Goodman analysis significantly reduces the percentage of error and the estimated values from this approach fall very close to the experimental data points.

Table 3-18 Comparison between predicted datapoint in accordance to mean stress level, datapoint collected by fatigue test under S_m of 624 MPa and corrected datapoints

N	S (experimental)	S (Goodman)	Error	S (Modified Goodman)	Error
3.82×10^5	111	61	45%	91	18%
1.89×10^5	141	89	37%	133	5%
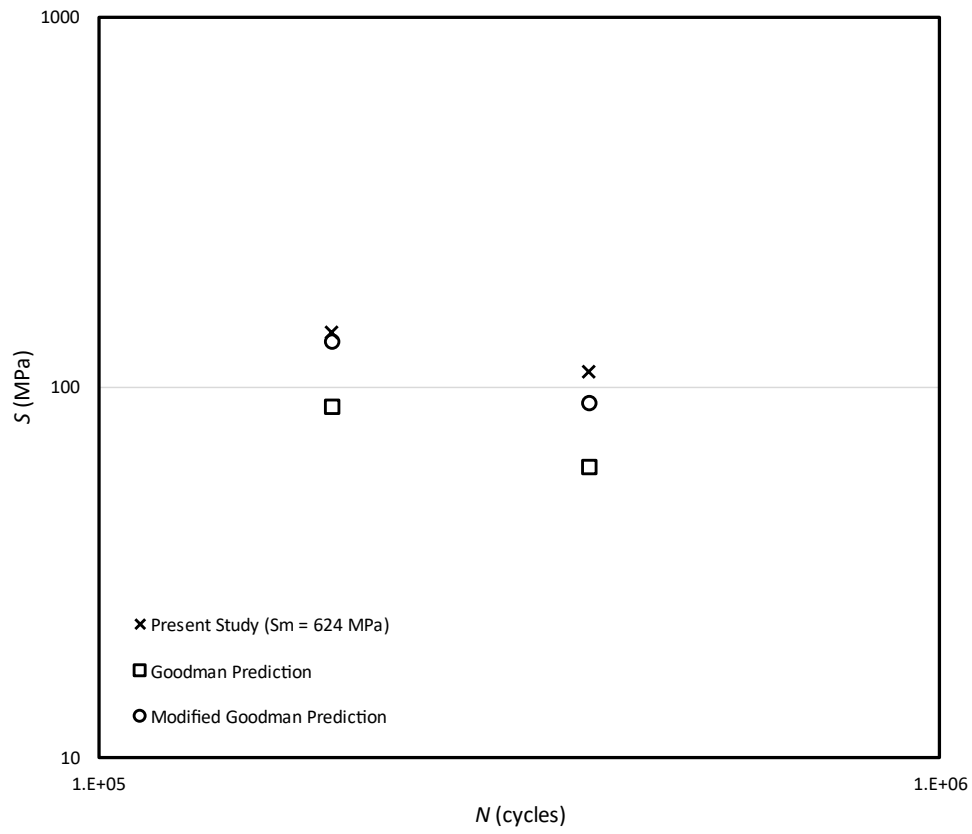
Figure 3-41: Comparison of the Goodman and modified Goodman prediction with the experimental data on M72 studs at mean stress of 264 MPa

3.9. Summary

As this chapter showed, the results can be divided in two main studies: firstly, an analytical study on the stress distribution and how the friction coefficient affect the results (study developed through FEA modelling) and, secondly, the study of S-N curves comparing test results from literature and from fatigue life results tested for the purpose of this thesis.

In accordance to the analytical study and the friction coefficient influence on the stress distribution the following results can be collected:

- From the analytical model, developing the stress distribution along the engaged threads has shown a distribution that agree with the expected trend presented in literature. However, these results become inaccurate as soon as plasticity is taken into consideration.
- Friction coefficient has been found to have insignificant impact on the stress distribution along the engaged threads, however it affects the local stress. As demonstrated from the 2D-FEA model the impact of the friction coefficient decreases at the increase of pre-load applied.

The study of the three main S-N curves from standards and the comparison with the results converged to the following conclusion:

- The main international standards (BS, DNV, EN) were considered to compare the test results presented in literature with the standard design curves. As revealed by a statistical analysis the S-N curves are based on parameters that need verification, such as the thickness correction, the intercept and the slope of the curves.
- New large-scale fatigue tests were performed on M72 bolts, and the results were analysed using regression fits as well as fractography analysis.
- The statistical analysis of the data results presented in literature alongside the data presented in this thesis has highlighted differences between the predicted curves and the actual results. However, has been illustrated how this difference diminishes as soon as the data points are considered all together without dimension or surface treatment division.

A mean stress correction method has been presented. The formula and parameter utilised led to satisfactory results, showing how it is possible to predict the fatigue life for different mean stress starting from datapoints at lower level. While a Goodman correlation can be considered a more conservative prediction a modified Goodman prediction, through consideration of relative SCF, shows a more realistic result. Meanwhile these results highlight the need to correct for mean stress when combining test data from bolts tested at different mean stress levels.

Chapter 4 C1 Wedge Connection

4.1. Chapter Content

This chapter focuses on studying the behaviour of the C1 Wedge Connection designed in C1 Connection under vertical load, presenting a design process to achieve the optimal layout in terms of hole geometry and fastener design.

Section 5.3, presents analytical studies supported by Final Element Analysis (FEA) to analyse the main component of the C1 connection layout: the hole and the fastener. In section 4.3.1, the study has focused the structural behaviour in presence of one hole and a series of holes around the circumference and how the hole-shape can affect the load effect, a further study to optimize the stress distribution along the hole has been presented. In Section 4.6, a preliminary analytical study has been developed analysing the how the wedge slope (α and β) affects the performance of the device in terms of load and movement of the single components.

In Section 4.7, a large-scale segment case has been studied, developing an FEA model, and subsequently testing a large-scale sample under fatigue test. In Section 4.7.1, the FEA analysis has been presented and discussed. This analysis aims to understand how the segment of the structure reacts under a tensioning load. Finally, in Section 4.8, a large-scale fatigue test is presented, analysing and comparing the results on a S-N curve.

The aim of the present study is to conduct an analytical evaluation and finite element analysis (FEA) to understand the technological benefits of the C1 wedge connection concept. In order to achieve this goal, the following objectives have been defined and thoroughly investigated: i) to design the hole geometry, ii) to predict the stress-distribution around the hole geometry, and iii) to evaluate the strength under different loading conditions in a real-case scenario.

4.2. Introduction to Technology

Offshore wind is an efficient and reliable source of renewable energy that is exponentially expanding worldwide, particularly in Europe. Offshore Wind Turbines (OWTs) consist of three general components: foundation, tower and the transition piece (TP) in between. The dominant type of foundation which is successfully employed in many offshore wind farms to support OWTs is monopile (MP) [70], [71]. One of the significant engineering challenges associated with the design and operation of OWTs is the connection technology between the monopile and the transition piece (MP-TP). Over the past three decades the MP-TP concepts, widely utilised in offshore wind farms, are grouted and flange bolted connections. The grouted connection has been historically used for many years in the offshore Oil & Gas industry and was the first technology employed for offshore wind turbine MP-TP connections. With this technology, the transition piece is set on the monopile and plugged on it, by aligning the two axes and the gap between the two cylinders is subsequently filled in with grout. Despite the advantages offered by the well-known grouted connection technology, a number of fatigue failures were observed in commissioned OWTs in the 2010s . This prompted the offshore wind industry to consider alternative technologies for MP-TP connections in subsequent offshore wind projects.

As a result of these challenges, the industry has heavily shifted towards flange bolted connections (also known as threaded connections). With this technology, L-flanges are welded to the bottom of the transition piece and the top of the monopile, and they are secured together with large-scale bolts and nuts which are equally spaced around the circumference of the MP-TP geometry. This technology offers several benefits such as a direct load path and easy access for inspection and monitoring. However, threaded connections are affected by environmental and operational loading conditions and pre-load relaxation and fatigue cracks may occur in the bolt and nut connection, which would affect the structural integrity of the OWTs [17], [34], [72]

According to European reports [73], the offshore wind installed capacity in Europe is continuously increasing and the turbine dimensions are growing accordingly. This means that larger wind turbines will require larger and stronger foundations. Therefore, it becomes necessary to re-evaluate the use of threaded technology and consider alternative technologies for MP-TP connections in future OWTs.

One of the new and promising MP-TP concepts that has been proposed in recent years to overcome the current issues faced by industry is the C1 wedge connection. This technology involves redesigning the L-flanges by converting the vertical connection into a horizontal one through the design of a cylindrical lower flange for the MP section with a fork-shaped upper flange for the TP section, as illustrated in Figure 4-1.
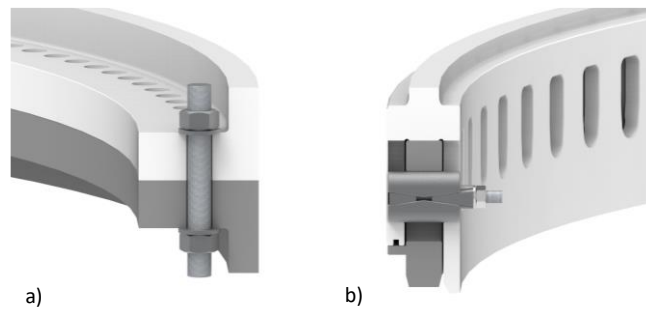
Figure 4-1: Comparison layout between (a) threaded connection and (b) C1 Wedge Connection

According to C1 Connection [74], this concept is designed as a series of elongated holes that will be accommodated around the circumference of the geometry allowing the positioning of the C1 wedge fastener. The device includes five main components, as illustrated in Figure 4-2: an upper block, a lower block, an inner and outer wedge, and a threaded system, which can be either a stud-nut or a bolt system. The lower block rests on the lower part of the upper flange (TP) while the upper block, after the complete installation, is in contact with the upper part of the lower flange (MP).To allow the proper function of the device the outer wedge has been designed with a threaded hole, where the threaded system is in contact, while the inner wedge an oversized hole to allow the bolt/stud can freely rotate. Through the torque of the bolt, the wedges are pulled together. The slopes of the wedges (identified in this chapter as α and β) convert the horizontal load on from the bolt into a vertical preload.
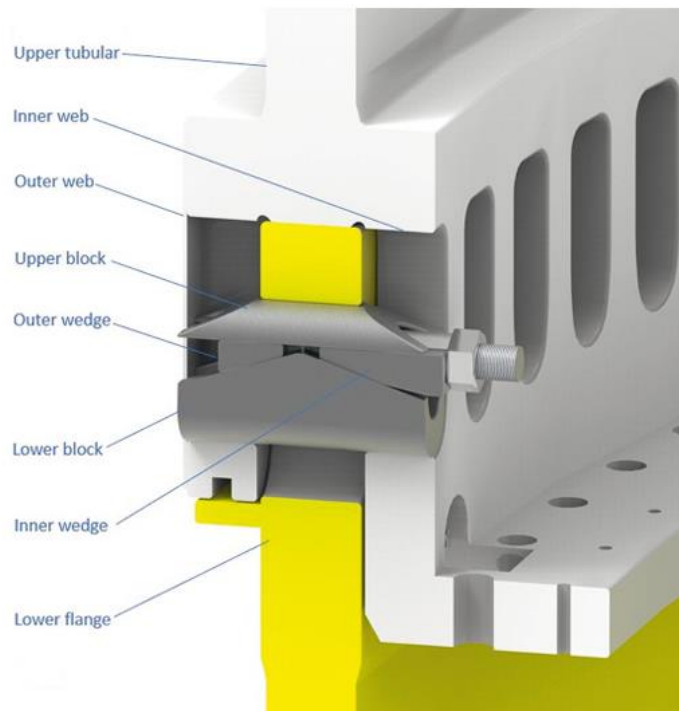
Figure 4-2: C1 fastened composition[74]

68

4.3. Preliminary Study of C1 Connection Layout

4.3.1. Study of Structures with Embedded Holes

In this section, analytical studies have been conducted to understand the structural behaviour and engineering analysis of OWT monopile foundations in the presence of circumferential holes. For this purpose, perfect circles have been initially considered for the geometry of the hole and the modified hope geometries which result in better structural performance have been considered at the later stage of the study.

A simplified layout of the monopile geometry with circumferential hole is demonstrated in Figure 4-3. For simplicity, the geometry of the holes has been assumed to be perfect circle. Based on this assumption, the external circumference of the monopile C can be calculated according to the following equation:

$$C = \pi D_{MP} = nl + nD_{hole} = nW \qquad \text{4-1}$$

where n is the number of holes along the circumference, D_{hole} is the hole diameter, D_{MP} is the external tower diameter, l is the ligament width between the holes and W is the monopile's width segment described as the summation of l and D_{hole}.

Moreover, the following equations would describe the correlation between different parameters such that:

$$l = \frac{\pi D_{MP} - nD_{hole}}{n} \qquad \text{4-2}$$

$$\frac{l}{D_{hole}} = \frac{\pi D_{MP} - nD_{hole}}{nD_{hole}} = \frac{W - D_{hole}}{D_{hole}} = \frac{W}{D_{hole}} - 1 \qquad \text{4-3}$$

where W is the monopile equal section described as $\frac{\pi D_{MP}}{n}$.
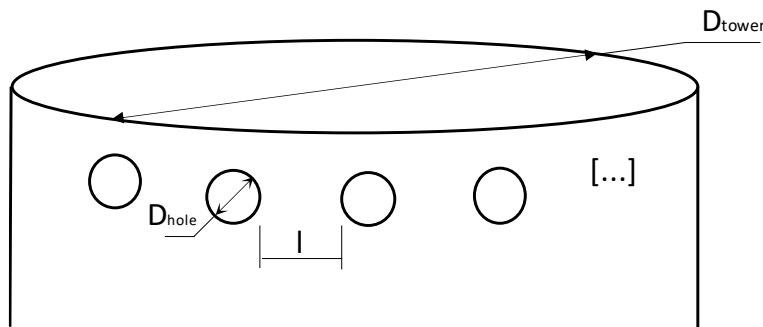
Figure 4-3: Simplified MP geometry for wedge connection concept with circumferential holes

In order to facilitate analysis, the simplification presented in Figure 4-3 has been implemented by considering the second part of Equation 4-1, dividing the entire MP-TP connection into a series of ligaments and holes in succession. Consequently, it becomes feasible to define the entire circumference as a series of segments of equal width W, as illustrated in Figure 4-4. For the further analysis provided in this chapter, each segment has been assumed to have a hole located at the centre of the segment length W.
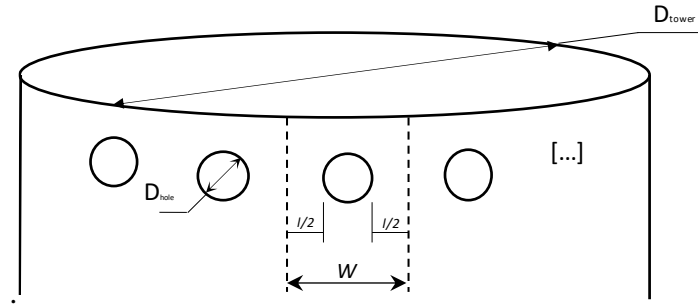
Figure 4-4: Segmentation of MP geometry for wedge connection concept

4.3.2. Engineering Stress Analysis of Cylinders with Several Holes around the Circumference

Presence of holes, notches or in general imperfections can lead to structural failures due to increased   local stresses close to the edge of the holes/notches. Therefore, it is essential to perform comprehensive stress analysis on the structures with such features. It is worth noting that according to the basic engineering principles, under fatigue loading conditions where stresses applied to the structure are below the material's yield stress, the local stresses in structures with holes and notches depend on the geometry of the hole and are insensitive to material properties. However once stress exceeds the yield point, the local stresses will be influenced by the mechanical properties of the material (i.e. tensile curve).

There are two main methods to calculate the stress concentration factor (SCF), hence the local stresses in the presence of holes and notches, for a given geometry: (a) analytical solutions, available for relatively simple geometries, or (b) Final Element Analysis (FEA), using software packages like Abaqus for more complex geometries. Both approaches have been considered in this analysis. The results from both methods have been presented below and compared.

Single Hole Geometry

Analytical solutions are available to calculate the SCF for a single hole and for a series of holes [75]. For an elliptical hole-shape the stress concentration factor K_t can be calculated using Equation 4-4.

$$K_t = 1 + \frac{2a}{b} = 1 + 2\sqrt{\frac{a}{r}} \qquad for\ 0 < \frac{a}{b} < 10 \qquad \text{4-4}$$

where *a* and *b* are the semi-major axis and semi-minor axis of the ellipse (see Figure 4-5). For a single circular hole in infinite plane under in-plane uniaxial load, the SCF can be calculated as 3 using Equation 4-4 by assuming *a=b*. Meanwhile considering a more complex hole geometries, like the C1 wedge connection hole geometry designed for industrial applications (which will be presented in the next paragraphs), requires additional geometrical considerations, taking results from an elliptical hole (Figure 4-5) and a rectangular hole with rounded corners (Figure 4-6).

70
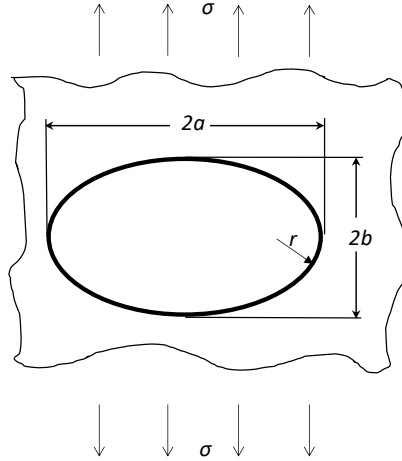
Figure 4-5: Geometry definition for a general elliptical hole shape in infinite plate

For the rectangular hole with rounded corners (see Figure 4-6), the SCF can be defined using the following equation, according to Sobey (1963) and ESDU (1970)[76]:

$$K_t = C_1 + C_2 \frac{a}{b} + C_3 \left(\frac{a}{b}\right)^2 + C_4 \left(\frac{a}{b}\right)^3 \qquad \text{4-5}$$

For $0.05 \leq \frac{r}{2a} \leq 0.5 \; and \; 0.2 \leq \frac{a}{b} \leq 1.0$, where r is the fillet radius presented at the square edges and the C_1, C_2, C_3 and C_4 parameters can be describe using the following equations:

$$C_1 = 14.815 - 22.308 \sqrt{\left(\frac{r}{2a}\right)} + 16.298 \left(\frac{r}{2a}\right) \qquad \text{4-6}$$

$$C_2 = -11.201 - 13.789 \sqrt{(r/2a)} + 19.200 \left(\frac{r}{2a}\right) \qquad \text{4-7}$$

$$C_3 = 0.2020 + 54.620 \sqrt{\left(\frac{r}{2a}\right)} - 54.748 \left(\frac{r}{2a}\right) \qquad \text{4-8}$$

$$C_4 = 3.232 - 32.530 \sqrt{(r/2a)} + 30.964 \left(\frac{r}{2a}\right) \qquad \text{4-9}$$
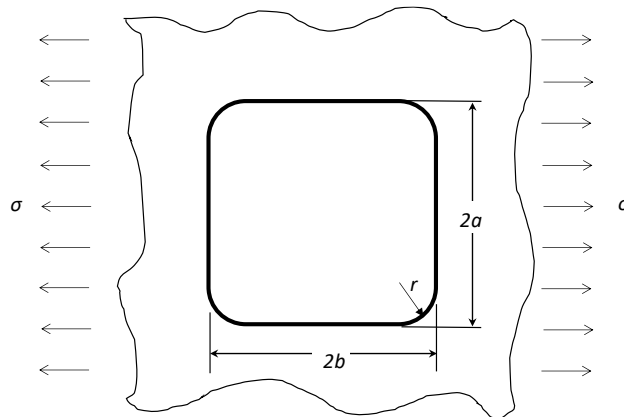
Figure 4-6: Geometry for rectangular hole with rounded corners in infinite-width plate

To compare the results for an elliptical hole and the rectangular hole, the Stress Concentration Factor (K_t) has been calculated in function of the *a/b* ratio and under the following considerations: a) The elliptical hole has been considered with a *a/b* ratio between 0.1 and 10 and b) the square hole has been considered accordingly to the two *r/2a* limits (0.05 and 0.5) in accordance with the conditions of Equation 4-5.

Results have been plotted in Figure 4-7, where it can be observed that K_t is affected by the a/b variation. Secondly, as result it is possible to see the particular cases for the different studied equations:

- For Equation 4-4, represented by the blue curve, for *a/b*=1 is represented by a circular hole.
- For Equation 4-5 in case where *r=a*, represented by the yellow curve, the squared hole becomes a circular hole for *a=b*.
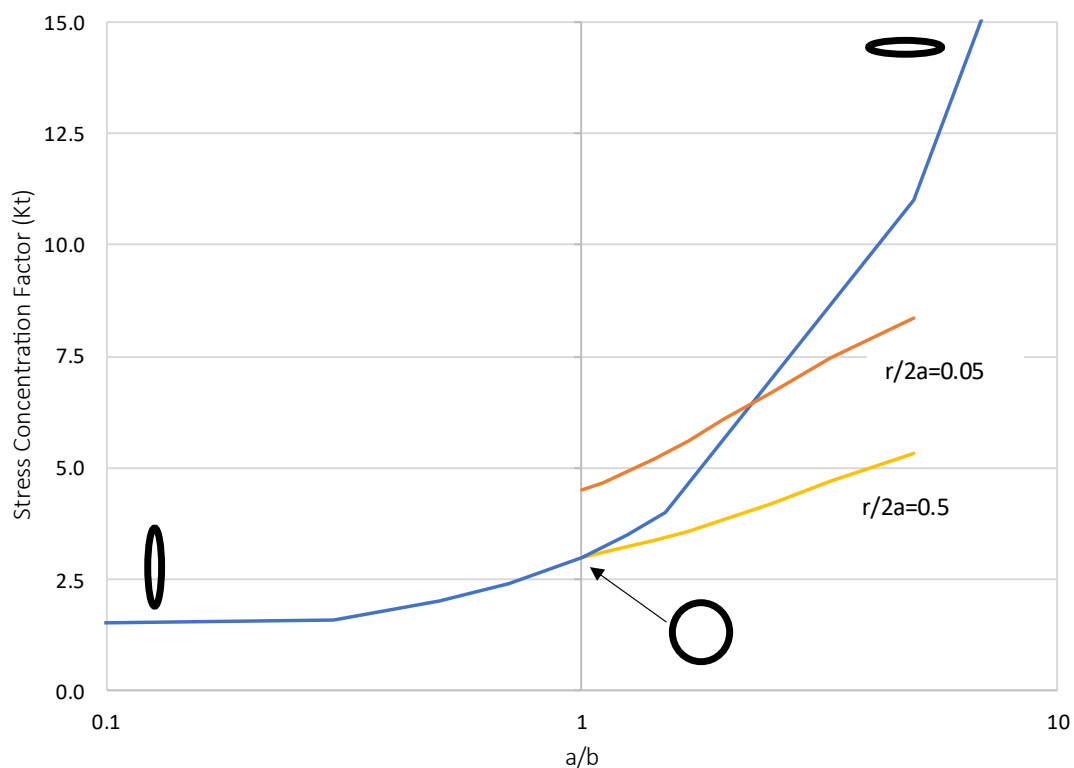
Figure 4-7: Comparison of Stress concentration factor for single hole in function of a/b ratio for elliptic (blue), and square holes (yellow for r/2a=0.5 and orange for r/2a=0.05)

For cases where the length of the hole 2b is larger than the hole diameter (*2a=D*), Equation 4-5 is not valid anymore. For this reason, FEA modelling was employed to predict the SCF on (a) a circular hole, and (b) a rectangular hole with rounded corners, which is referred to as stadium shape hole geometry. The simulations were built up by considering a plate of 240 mm width, 300 mm height, and 20 mm thickness. The hole geometries considered in the analysis were embedded at the centre of the plate. The simulations were run using linear elastic conditions and to consider the stress distribution in steel structures with holes, the material proprieties taken into consideration are for theS460 steel, as presented in Table 4-1 according to BS EN 1993-1-1:2022. Boundary conditions were presented in Figure 4-8. An Encastre (i.e. fixing displacement and rotation in all directions) was applied on the bottom of the plate and a uniform

load of 2.3 [MN] was applied on the upper surface, considering the maximum load at 18 [m a.s.l.] in accordance to Table 2-5.

Table 4-1 Elastic material proprieties for S460 steel, according to BS EN 1993-1-1:20222

Input data	
E [GPa]	210
Poisson's ratio pin (ε_{wall})	0.3
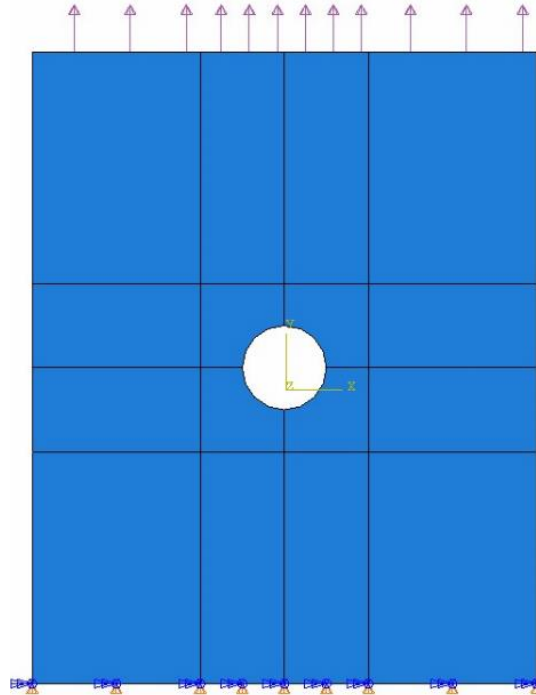
Figure 4-8: BC applied on one single hole FEA simulation

The obtained results from these simulations are reported in Figure 4-9 comparing the stress distribution with a single circular hole under the same conditions. The main observations from the comparison of FEA results between the circular hole and stadium shape geometry are:

- the SCF for the stadium shape hole is 2.4, compared to the circular hole geometry of 3.
- for the stadium shape, four critical zones of high local stress were identified, whereas for the circular geometry, the number of high stress zones is limited to two.
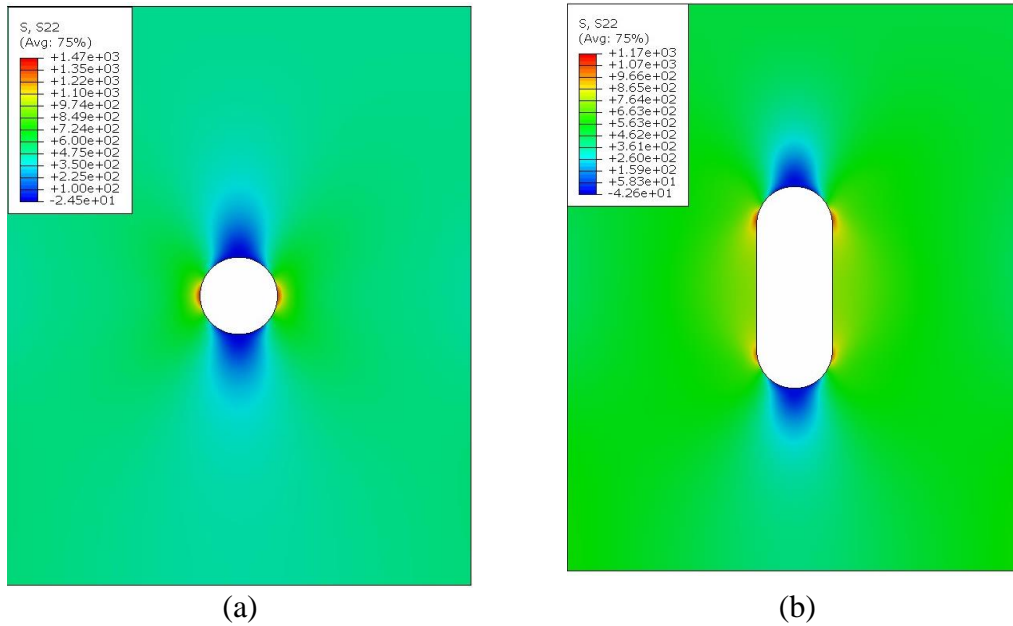
Figure 4-9: Vertical stress (S22) distribution results for single circular hole (a) and single stadium-shape hole (b)

With the aim of reducing the stress concentration factor around the hole shape, the stadium shape has been redesigned as a double radius stadium shape (see Figure 4-10). The geometry is composed by a smaller radius R and a larger radius R_1 which have the centres distanced by a length L. The tangential line that connects the two radius has an inclination of an angle Φ. Through FEA simulations, a study for a single hole has been developed, using the same wall geometry and material proprieties used for the circular and stadium hole. The geometric parameters used for the creation of the double radius hole have been resumed in Table 4-2.
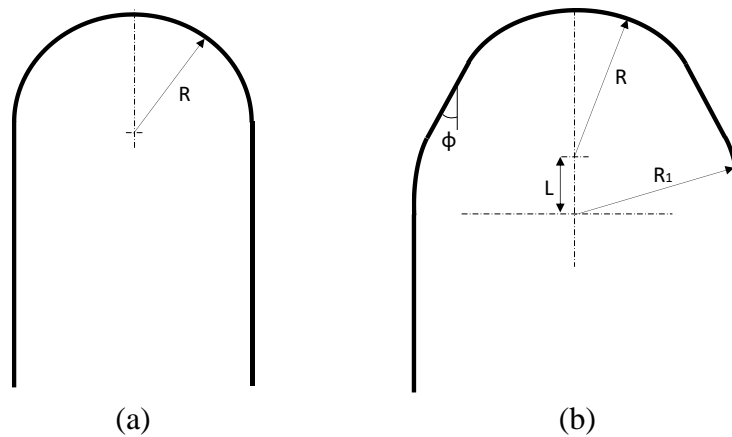
Figure 4-10: Differences between stadium shape (a) and double radius shape (b) geometry

Table 4-2 Geometrical parameter for double radius hole geometry used for single hole FEA analysis

Hole dimension	[mm]
R	17.5
R_1	20.0
L	7.0

The result of the FEA simulation is presented in Figure 4-11. Comparing the results presented for the circular hole and the stadium shape with those obtained with the double radius hole, it is possible to notice a decrease of the SCF, starting with a value of 3 for the circular hole, decreasing to 2.44 for the stadium hole up to a value of 2.36 for the double radius. The stress distribution along the horizontal axis for the section passing through the main radius centre has been plotted in Figure 4-12 for the three-hole shapes. As it is possible to see the stress distribution along the x-axis is lower for the stadium and double radius shapes compared to the circular hole. However, this result needs to be considered with the position of the maximum stress, which appears to be located in a higher position along the wedge of the hole for the double radius compared to the stadium. In Table 4-7 the main stress results of the three-hole shapes have been summarised.
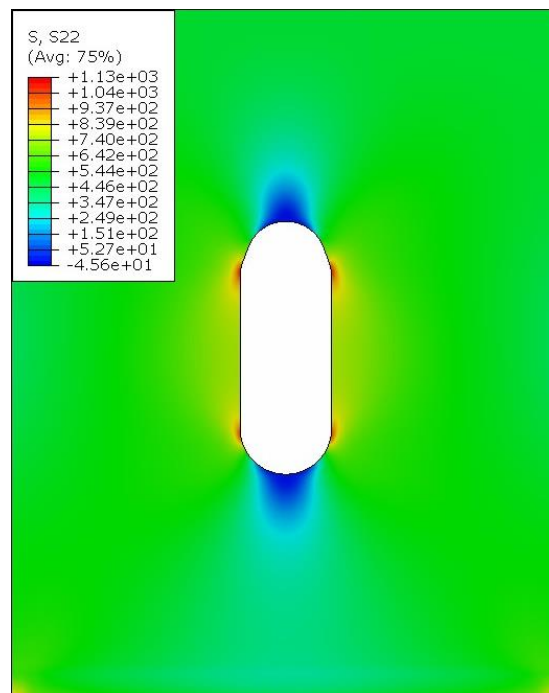
Figure 4-11:Vertical stress (S22) distribution results for double radius hole shape

Table 4-3 Comparison of maximum stress and SCF for circular, stadium and double radius hole shape and relative difference compared with circular hole shape

	Circular shape	Stadium shape		Double radius shape	
			Δ		Δ
$S_{22,max}$ (MPa)	1470	1170	-20.41%	1130	-23.13%
SCF	3.00	2.44	-18.67%	2.36	-21.33%

Figure 4-12: Vertical stress (S22) distribution along the x-axis for circular hole (solid line), stadium (dash line) and double radius hole shape (dash-dot line)

Series of Holes

To calculate the stress concentration factor for a single row of circular holes in an infinite plate, the following equations has been presented by W. Pilkey [75]:

$$K_t = 3.000 - 0.9916 \left(\frac{d}{L}\right) - 2.5899 \left(\frac{d}{L}\right)^2 + 2.2613 \left(\frac{d}{L}\right)^3 \quad for\ 0 \leq \frac{d}{L} \leq 1 \qquad 4\text{-}10$$

where d is the hole diameter and L is the distance between the centres of the holes.

Similarly, for a series of elliptical-shape holes (Figure 4-13) in an infinite-width plate the stress concentration factor can be calculated, in accordance with Schulz (1941) and Nisitami (1968)[76], as:

$$K_t = \left[1.002 - 1.016 \left(\frac{2a}{L}\right) + 0.253 \left(\frac{2a}{L}\right)^2\right]\left(1 + \frac{2a}{b}\right) \qquad 4\text{-}11$$

$$for\ 0 \leq \frac{2a}{L} \leq 0.7\ and\ 1 \leq \frac{a}{b} \leq 10$$
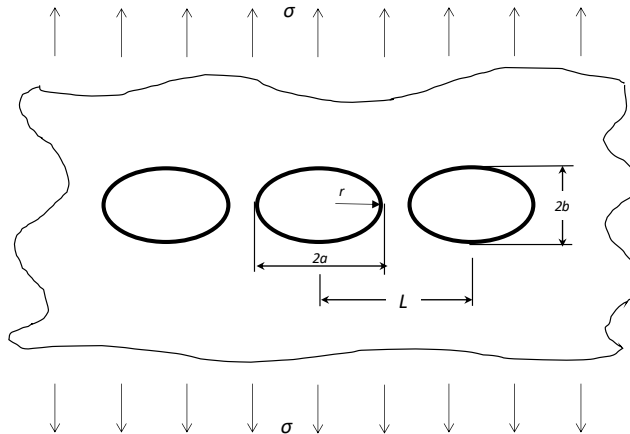
Figure 4-13: Generali design for infinite series of elliptical-shape holes

76

To compare the stress concentration factor variation for circular and elliptic hole shape series, equation 4-10 and 4-11 have been plotted in Figure 4-14 For a circular hole series the only parameter of interest are the diameter D and the distance L for the elliptic hole the elliptic axis affect the K_t result. Therefore, the elliptical results have been considered for three a/b conditions (1, 2.5 and 5). Figure 4-14 illustrates how, independently from the hole shape, an increase of D (or decrease of L) results in a decrease in the stress concentration factor. Furthermore, K_t for elliptical holes increases wiht the increase of the major-axis length $2a$ in correlation of $2b$. Similar to Figure 4-7, for a/b equal to 1, the elliptical curve merge with the circular hole curve for the geometrical correlation presented in Equation 4-12.

$$\frac{a}{r} = \left(\frac{a}{b}\right)^2$$ (4-12)
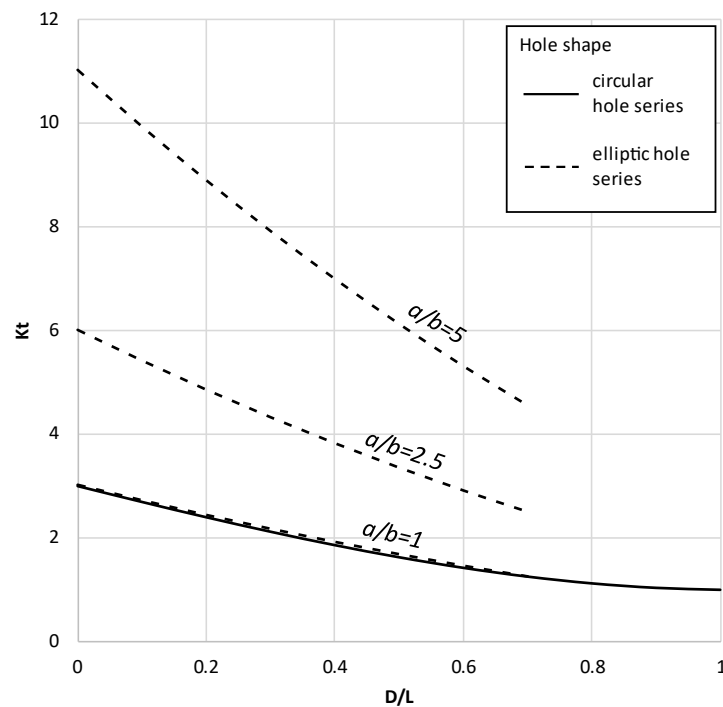
Figure 4-14: Comparison of stress concentration factor in accordance with the variation of distance between holes of an infinite row for circular- (solid line) and elliptic-hole shape (dashed line)

In Equation 4-11, one of the conditions for the correlation to exist is that a is always bigger than b ($a/b \geq 1$). However, as presented in Page 71 the longer axis of the elliptical hole should be aligned to the tower axis ($a/b<1$) instead to be perpendicular as previously presented. As presented in the study with one hole, a double radius hole shape presents some advantages in terms of stress distribution compared to the stadium hole shape. Consequently, further simulations have been designed, employing the double radius configuration as the primary focus.

FEA modelling has been employed to predict the SCF for a series of double radius-shape holes, the study considered 2 different values for diameter ($2R_1=D$) as well as five different l/D ratio have been included, in the specific ratio of 0.8, 0.85, 0.9 and 1.00. Subsequently, a similar study has been conducted to compare the stadium shape result with the circular shape hole. Similarly, to the previous study, three diameters have been considered (D=22, 40 and 115

[mm]) and a variation of *l/D* ratio of 0.8, 0.85 ,0.90, 0.95 and 1.00 has been considered. The material propriety used for these bunch of simulation are the same used in the case of the single hole: the elastic Young's modulus of $E = 210,000$ MPa and Poisson's ratio of $v = 0.3$.

Results of the FEA analysis have been reported in Figure 4-15 and Figure 4-16 as variation of K_t, in function of the *l/D* ratio for the different diameter for the double radius shape and for the circular hole shape respectively. Meanwhile, Figure 4-17 and Figure 4-18 illustrate the stress distribution from the FEA simulations with *D*=22mm, results are presented in terms of concentration factor and have been compared along the unitary ligament length *l* between the holes for the two hole shapes, respectively. As results from the comparison between Figure 4-15 and Figure 4-16 ,the stress concentration factor for a series of holes tends to be higher for lower values of *l/D,* independently from the hole shape considered. This result finds correlation to studies presented in literature [77]. Furthermore, comparing the stress distribution between Figure 4-17 and Figure 4-18, it is possible to identify that the stress distribution is quite different in terms of magnitude between the two holes shape. For the circular hole-shape it is possible to see how the value of K_t is higher, for same *l/D* value, compared to the double radius shape, even though the difference between the maximum value and the lowest value of K_t (ΔK_t) are different. Comparing the results for *l/D*=0.8 and 1.0, for both hole shape series, ΔK_t increases at the increase of l/D ratio (as reported in Table 4-4). If the mean value of K_t (Equation 4-11) is calculated for the different *l/D*, it is possible to see how the value increases as the ligament length between the holes decreases (see Table 4-5) [78], [79].

Table 4-4: Comparison between Stress concentration factor Kt along the ligament for different l/D values for series of double radius- and circular-hole shape

l/D	Double radius shape series			Circular shape series		
	$K_{t,max}$	$K_{t,min}$	ΔK_t	$K_{t,max}$	$K_{t,min}$	ΔK
0.8	2.70	2.09	0.61	3.27	1.92	1.35
1.0	2.48	1.83	0.65	3.09	1.66	2.24

Table 4-5: Comparison between average Stress concentration factor Kt along the ligament for different l/D values for series of double radius- and circular-hole shape

l/D	Double radius shape series	Circular shape series
	$K_{t,mean}$	$K_{t,mean}$
0.8	2.39	2.59
1.0	2.11	2.37

$$K_{t,mean} = \frac{K_{t,max} + K_{t,min}}{2} \qquad \text{4-13}$$
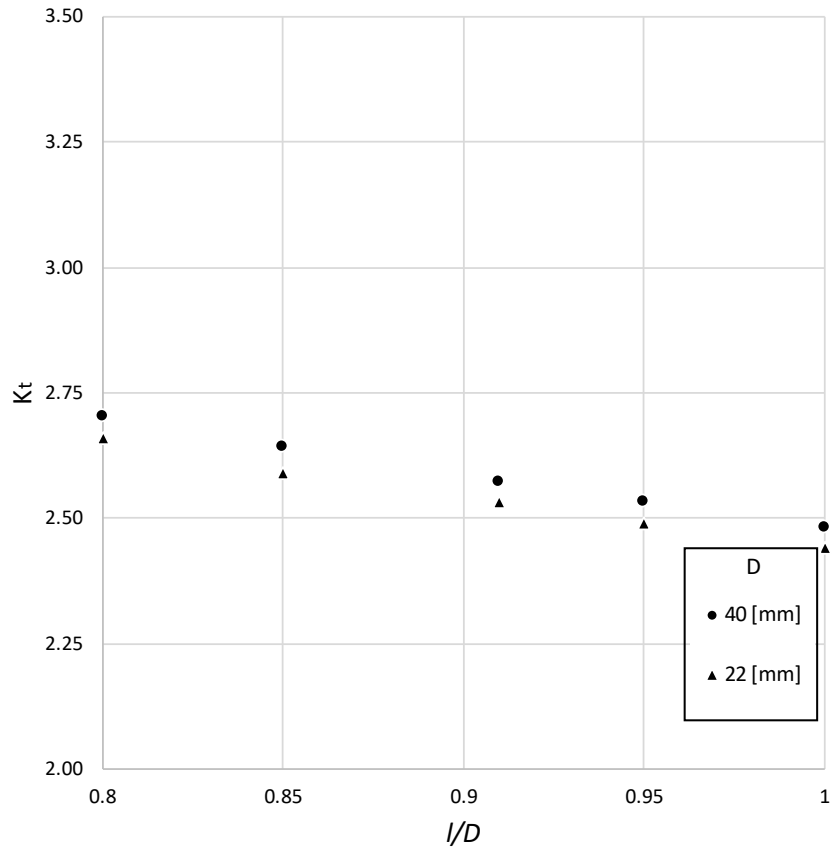
Figure 4-15: SCF variation in function of l/D for single raw of infinite double radius shape holes
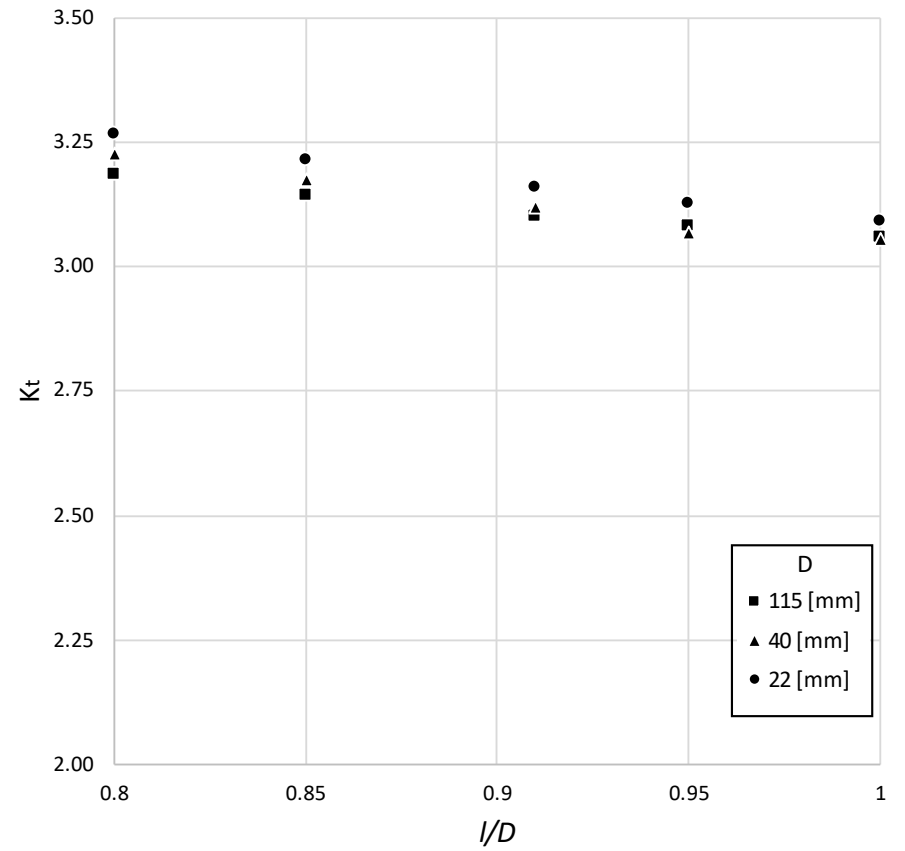
Figure 4-16: SCF variation in function of l/D for single raw of infinite circular holes

79
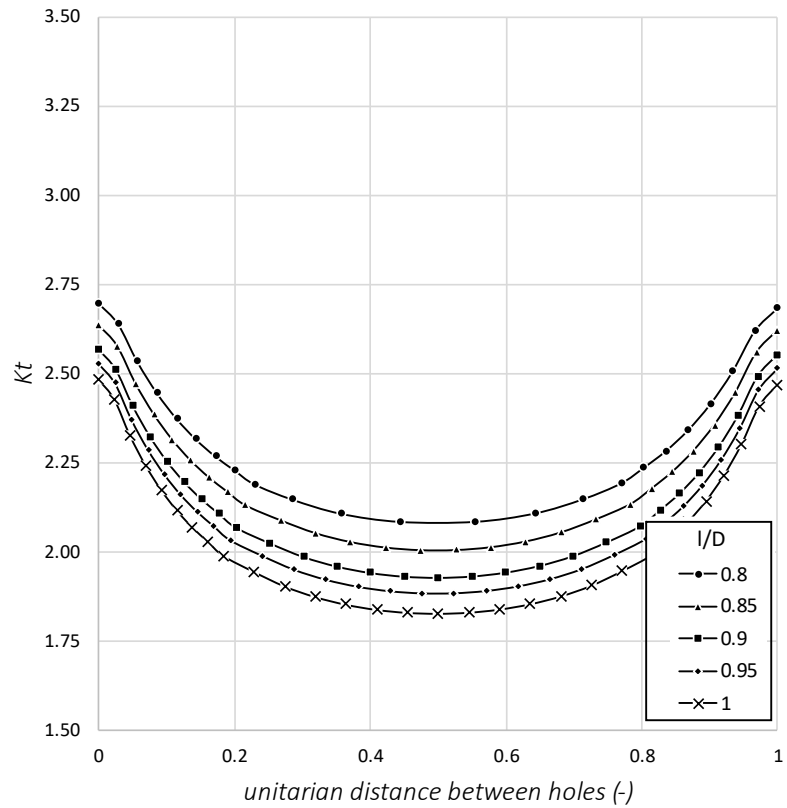
Figure 4-17: Stress concentration factor distribution in accordance with different l/D ratio for single row of infinite double radius holes
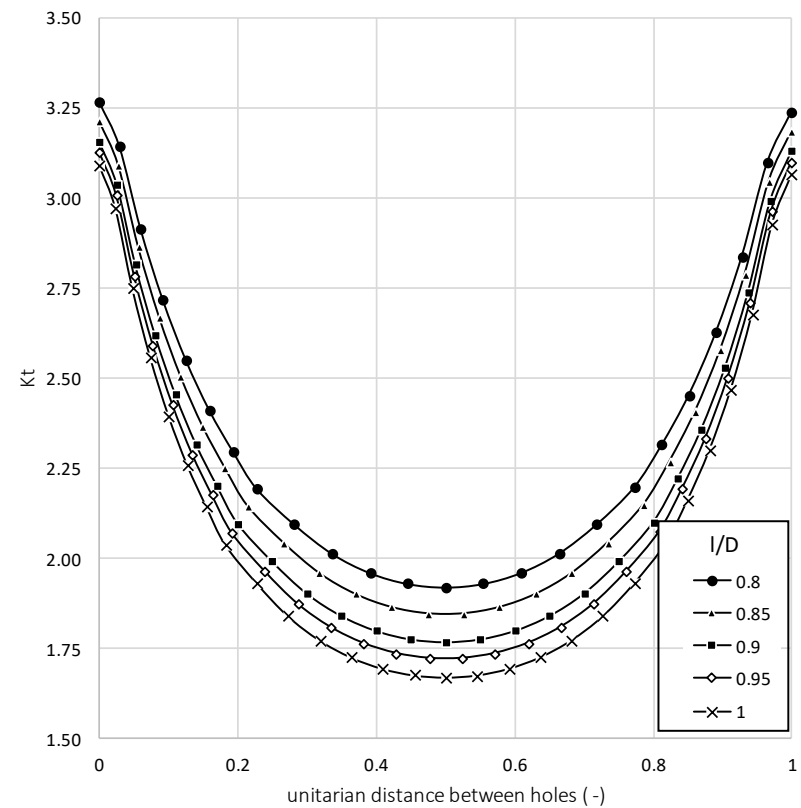
Figure 4-18: Stress concentration factor distribution in accordance with different l/D ratio for single row of infinite circular holes

Analysis of Pin Effects

In this section, results from Finite element analysis (FEA) simulations are presented. To allow the connection between the Monopile and the Transition Piece, the C1 connection device, compounded by the blocks and the wedges, gets place in the hole and subsequently through the horizontal load push the blocks against the internal surfaces of the MP and TP holes. This system can be simplified, focusing on the interaction between one hole and the relative block, as a wall with a pin-loaded lug. Three FEA models were developed to analyse the different stress distribution along the minimum cross section for a hole, which is under the action of a pin/block.

The same geometries and material proprieties, as those presented in section 4.3.2, were employed in the FEA simulations, as reported in Table 4-6. For the pin geometry, a half cylinder of radius 17 mm with the thickness of 20 mm was created and added to the model. The boundary condition implemented in the simulations were fixed on the bottom of the wall and the load has been applied on the bottom of the pin (pink arrows) pushing it upwards against the wall with a Total Force distribution of magnitude 2.3 [MN], as illustrated in Figure 4-19. The load magnitude has been selected as result from the calculations presented in Table 2-5.

Table 4-6: pin-lug material proprieties

Input data	
E_{hole} [GPa]	210
E_{pin} [GPa]	210
Poisson's ratio wall (ε_{wall})	0.3
Poisson's ratio pin (ε_{pin})	0.3
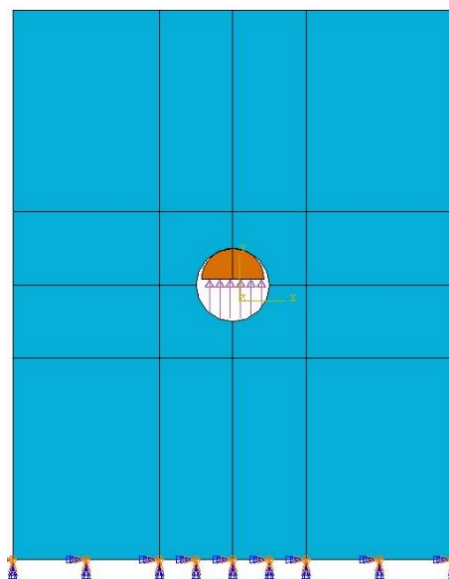
Figure 4-19: BC applied on one single hole under pin effect FEA simulation

81

The results from FEA simulations with the pin geometry are shown in Figure 4-20, showing how the stress is distributed in the wall, with a compression zone (blue region) near the contact between the hole surface and the pin and a stretching area (red region) near the smallest section. Considering the maximum stress value along the hole edge, comparing the stresses with the maximum stress along the circular hole shape, a reduction of 3.6% is reached through the use of a stadium shape and a reduction of 15.25% using the double radius hole shape. Furthermore, when comparing the axial stress distribution along the smallest section (see Figure 4-21) it is possible to observe a similar reduction of the stress concentration factor K_t. In Figure 4-21, the axial stress along the minimum cross-sectional area has been plotted for the three simulations, showing the reduction of stress on the edge of the hole. However, moving away from the edge of the hole, the curves tend to overlap one each other. The maximum stress concentration factor for the circular hole reaches a value of 5.70, while for the stadium hole is 4.93 and 4.64 for the double radius geometry, meaning that compared to the circular hole shape a reduction of stress along the horizontal section of 13.54 and 18.55% can be reached through the use of stadium hole and double radius hole-shape respectfully. All results have been summarised in 7.

(a)   (b)   (c)
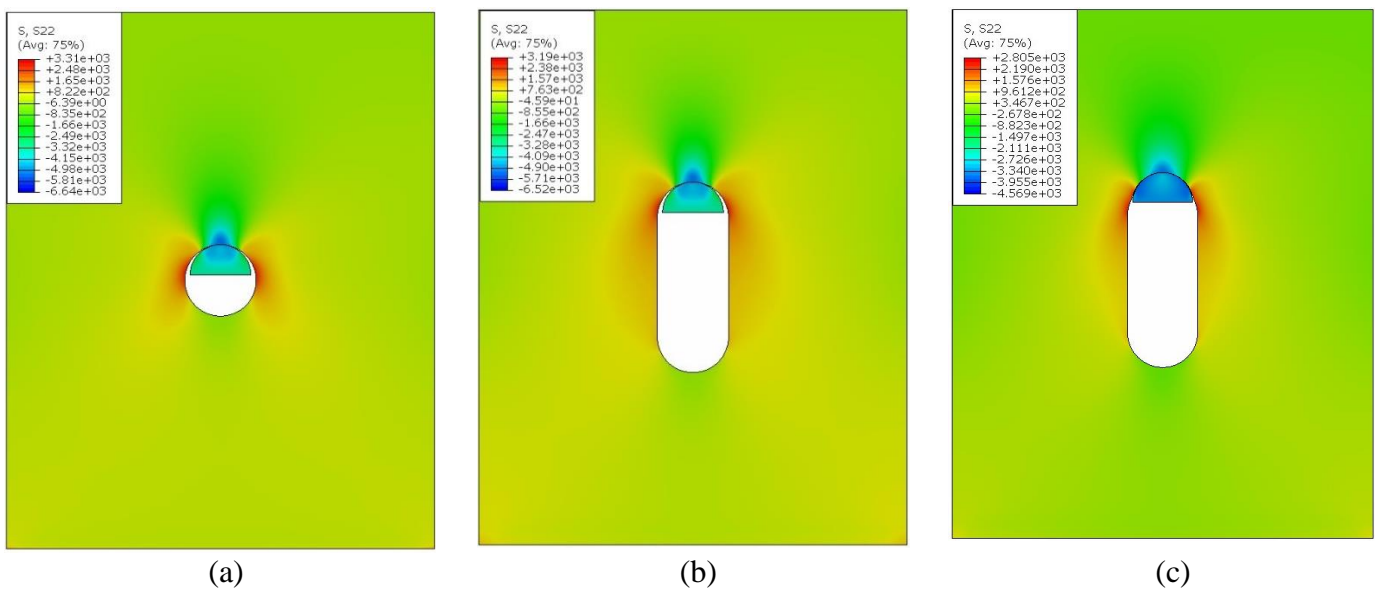
Figure 4-20: FEA results for single circular hole (a), stadium hole (b) and double radius hole (c) under the effect of a pin

Table 4-7 Comparison of maximum stress and SCF for circular, stadium and double radius hole shape and relative difference compared with circular hole shape

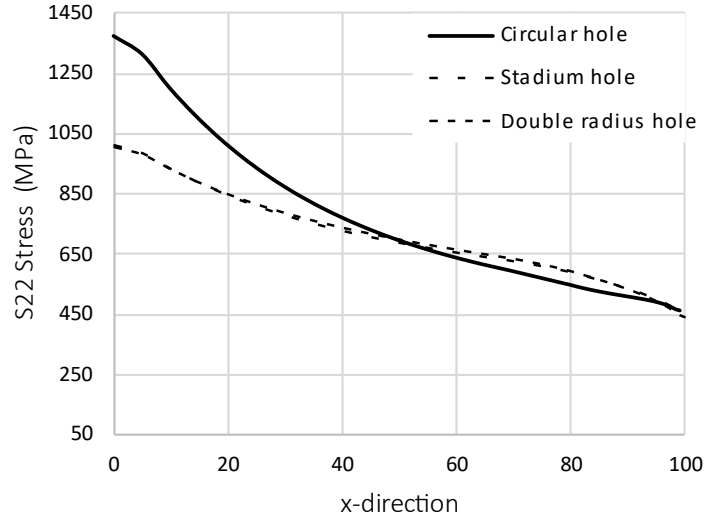|	Circular shape	Stadium shape	Δ	Double radius shape	Δ
S_{max} (MPa)	3310	3190	-3.60%	2805	-15.60%
SCF	5.70	4.93	-13.54%	4.64	-18.55%
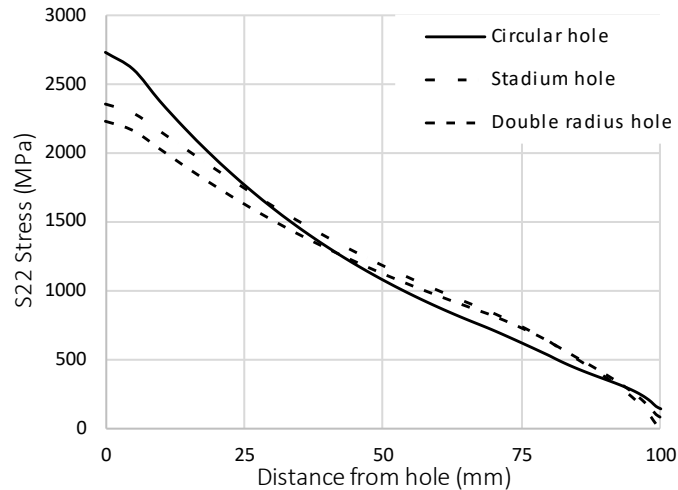
Figure 4-21: Vertical stress (S22) distribution along the x-axis for circular hole (solid line), stadium (dash line) and double radius hole shape (dash-dot line) under pin effect

For a general hole under effect of pin the location of the maximum stress change, indeed the point that is most subjected to stress tend to move along the circumference in direction of the contact point between the pin and the hole. The angle that gets create between the point with maximum stress and the horizontal gets the name of angle θ [76]. This parameter has been used to develop a hole double radius optimization and results have been presented in section 4.5.

To understand the stress behaviour in the case of a series of holes, each one under effect of a pin, a simulation has been developed only for the circular hole shape. Same simulation presented for a single circular hole under pin effect has been modified by applying on the two vertical surfaces a X-symmetry (i.e. by fixing horizontal displacement and rotation along y- and z-axis), this boundary condition has been used to simplify the simulation while obtaining same result as running a series of holes. Results have been presented, in Figure 4-22 a comparison between the results presented for the simulations without symmetry and with symmetry are illustrated. Main result of the simulation is that the maximum axial (S22) stress is reduced of 220MPa. In Figure 4-23 a comparison of the stress distribution along the x-axis for the simulation without symmetry and with symmetry is presented, the stress distribution along the ligament tends to be lower for the simulation run with the symmetric BC compared to the one without. Similar results have been reported in the cases presented in Paragraph 0, meaning that the effect of a series of holes will be affected by the ligament length *l* and the hole diameter *D*.

83
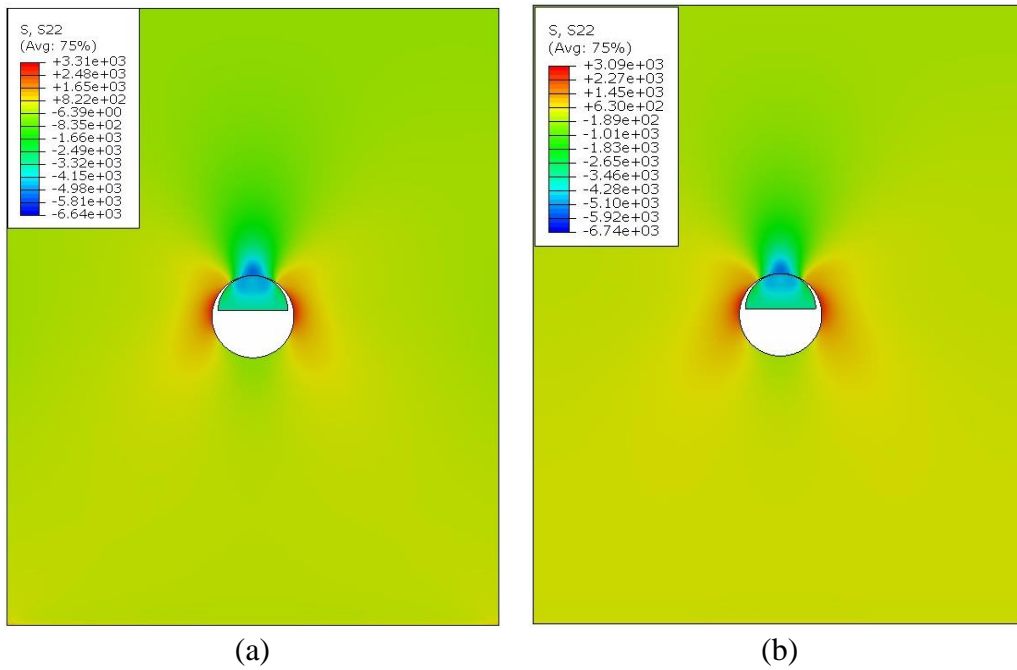
Figure 4-22: FEA results for single circular hole without symmetry(a) and with symmetry(b) on the vertical surfaces
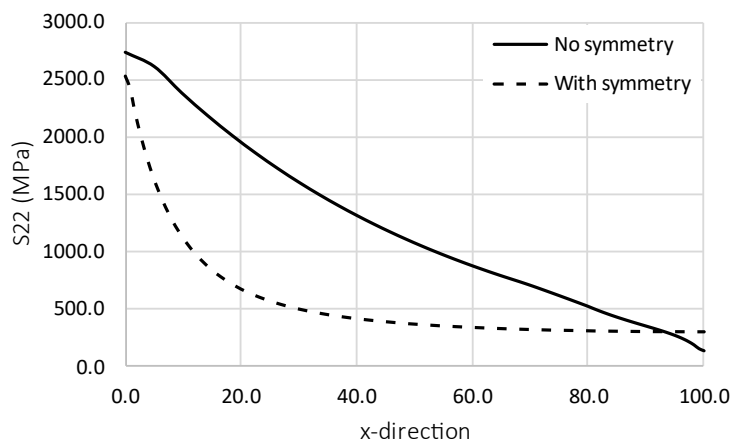
Figure 4-23: Stress distribution along x-direction for simulation without (solid line) and with X-symmetric BC (dash line)

4.4. Hertz Model

Another method to quantify the stress of a hole under a pin interaction is the analytical Hertz model. This model has been commonly used to calculate the contact stress in engineering calculations [80], and it is based on three assumptions: 1- the surfaces are smooth and frictionless, 2- the contact area is small compared to the size of the bodies, and 3- the bodies are under little deformation and in the state of full elasticity.

According to the Hertz model, the total contact length, *2b*, between pin and lug can be calculated using:

$$2b = 2\sqrt{\frac{2F}{\pi t} \cdot \frac{(1 - \varepsilon_1{}^2)/E_1 + (1 - \varepsilon_2{}^2)/E_2}{1/D_1 + 1/D_2}}$$ 4-14

where F is the total applied load, t is the cylinder length, D_i is the diameter for the pin (D1) and the hole (D2), and ε_i and E_i are the Poisson's Ratio and Young's modulus for the pin and lug material.

To calculate the contact angle $2\alpha_i$ the following equation can be used:

$$2\alpha_i = 2a\sin\left(\frac{2b}{D_i}\right)$$ 4-15

The maximum pressure can be calculated as:

$$p_{max} = \frac{2F}{\pi b t}$$ 4-16

Finally, the stresses along the x, y and z directions can be described using the following equations:

$$\sigma_x = -2\varepsilon p_{max}\left(\sqrt{1 + \frac{z^2}{b^2}} - \left|\frac{z}{b}\right|\right)$$ 4-17

$$\sigma_y = -p_{max}\left(\frac{1 + \frac{2z^2}{b^2}}{\sqrt{1 + \frac{z^2}{b^2}}} - 2\left|\frac{z}{b}\right|\right)$$ 4-18

$$\sigma_z = -\frac{p_{max}}{\sqrt{1 + z^2/b^2}}$$ 4-19

As mentioned previously, the Hertz model requires a frictionless contact surface; however, as illustrated in [81] it is possible to create an updated model to take into consideration the friction coefficient. In a real-life scenario, the friction coefficient is a non-zero value, for instance in the case of steel-on-steel contact without lubrification or finishing processing, the friction coefficient can be taken as μ=0.15. The frictionless assumption provides simplified solutions for engineering problems.

Hertz model was used to develop an optimised hole shape by taking into consideration the contact angle. For this purpose Equation 4-15 has been plotted in Figure 4-24 considering the input data in Table 4-8.

Table 4-8: Hertz model data

Input data	
D_{hole} [mm]	100
t [mm]	80
E_{hole} [GPa]	210
E_{pin} [GPa]	210
Poisson's ratio wall (ε_{wall})	0.3
Poisson's ratio pin (ε_{pin})	0.3
Applied load [N]	2.3×10^6

As seen in Figure 4-24, a prediction of the angle of contact (2α) as a function of the ratio between the pin diameter and the hole diameter has been calculated. The curves are generated based on frictionless surface contact, so it is known that the predicted values are only estimated and may not be 100% accurate for a real case scenario with non-zero friction coefficient value.
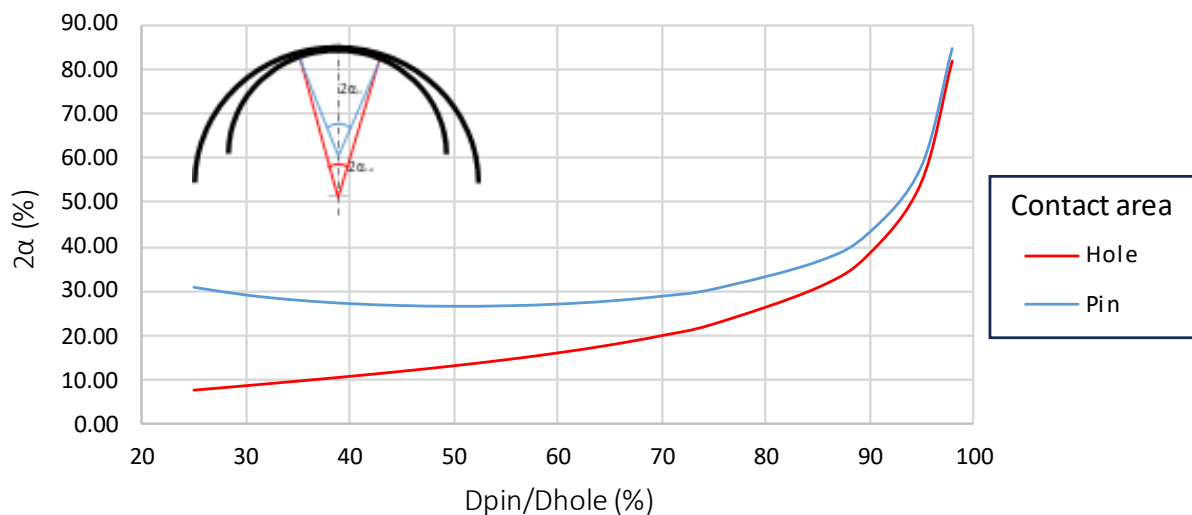
Figure 4-24: Hertz model angle contact

In the next step, the stress distribution along the y and z directions are considered to decide which D$_{pin}$/D_{hole} ratio to use. Equation 4-18 and 4-19 have been plotted in Figure 4-25 and the generated curves show how higher stresses are obtained for smaller diameter ratios, while for ratio close to 1, the stress is smaller due to the higher contact surface area, under the same load condition. Based on this preliminary consideration, a D_{pin}/D_{hole} ratio of 0.99 is selected and will be considered for the next phase of the analysis. This decision has been taken in order to reduce the stress along the two axial directions.
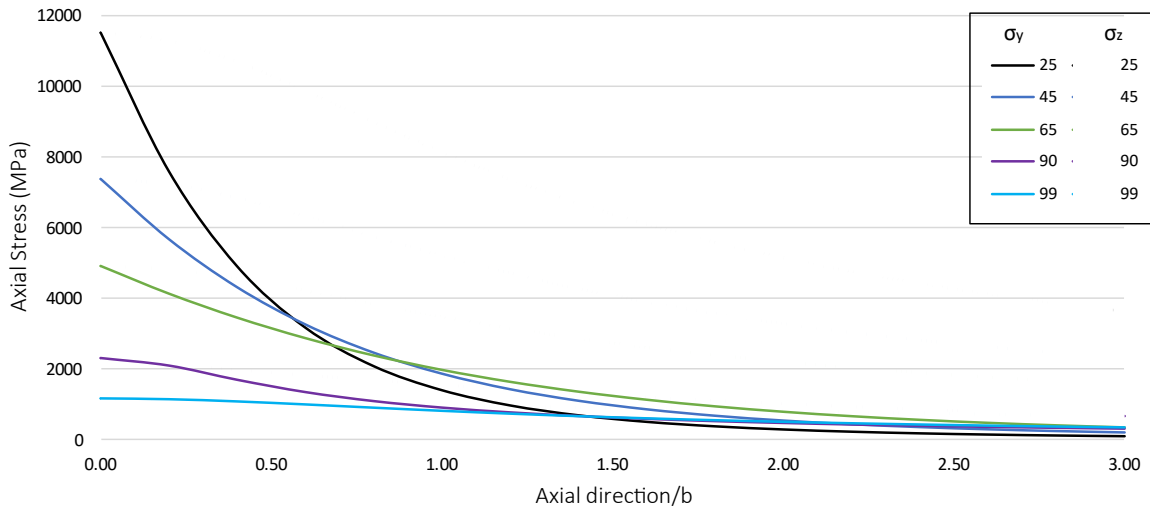
Figure 4-25: Stress profile along Y (solid) and Z (round dot) axis for different Dpin/Dhole ratio: 0.25 (black), 0.45 (blue), 0.65 (light green), 0.9 (purple) and 0.99 (azure)

4.5. Double Radius Hole Shape Design

As presented in paragraph 4.3, the hole geometry has been subsequently transformed in a double radius stadium shape. In this section an optimization of the shape has been developed running two groups of FEA simulations and illustrated in the next sections. In this section the first group has been studied focusing on the change of stress concentration factor (SCF), in accordance with the slope of the tangential edge of the two radius Φ. In Section 4.7.1 the study focused on how the SCF is affected by the plastic proprieties of the material.

The aim of optimizing the hole shape is to be able to move the maximum stress as far away as possible from the contact area. For this analysis a series of FEA models have been studied and the main dimensions have been reported in Table 4-9 and Table 4-10. The dimensions have been scaled considering a l/D ratio of 1.9 considering D as the diameter of larger radius ($2R_1$).

Table 4-9: FE Analysis variable dimensions

Simulation	1	2	3	4	5
W [mm]	159.5	174	166.75	159.5	174
R_1 [mm]	55	57.5	60	55	57.5
L [mm]	10	10	10	20	20

87

Table 4-10 FE Analysis constant dimensions

Dimension	Value
R [mm]	50.5
H [mm]	250
c [mm]	50
t [mm]	40
E_{hole} [GPa]	210
E_{pin} [GPa]	220
v_{wall}	0.3
v_{pin}	0.3

The results obtained from the purely linear elastic analysis have been reported in Figure 4-26. The two main factors reported are the SCF and the angular position, θ, of the maximum stress point from the centre of the D_1 circle. In this analysis the SCF has been used as qualitative value, considering that the pure elastic behaviour in the FEA simulation will not be taken as the final result, but for the design optimization of the hole, the smallest possible value will be found.

θ can be interpreted as the position of the maximum stress value relative to the contact area. A θ value close to 90° means that the maximum stress point aligns exactly with the maximum Hertz contact pressure point, while a θ value close to 0° means that the maximum stress is located at the beginning of the R_1 radius. For design purposes, a low θ angle will be considered. Based on the explanations provided above and the obtained results illustrated in Figure 4-26, the possible design models are the simulation with a value of Φ between 14.5° and 22° (simulation number 3 and 4 in Table 4-9). For simplicity, a value $\Phi = 14.5°$ has been chosen for further simulations. This decision has been taken for the smaller value of θ and K_t compared to the simulation with tangential slope of 22°. Hence, this model is considered for further analysis by employing plastic properties in the simulation.
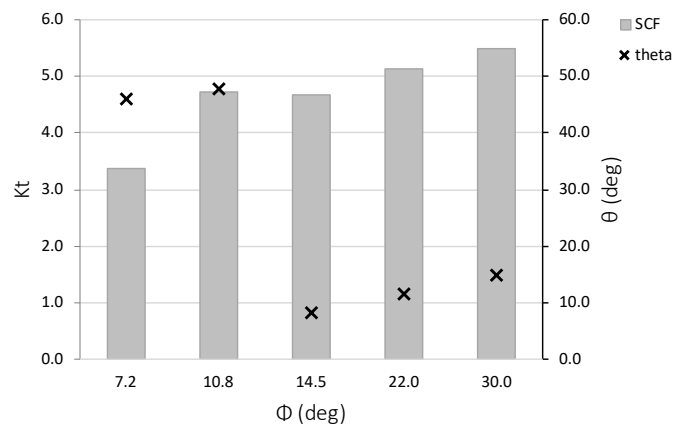
Figure 4-26: Stress profile: SCF (column) and angular position (square) for pure-elastic FEA analysis

88

4.6. Analytical Analysis of Fastener

The C1 wedge connection fastener consists of two blocks (upper and lower), two wedges (inner and outer) and a lateral bolt. The design of the fastener allows for a high preload to be applied through relatively easy and low load tightening of the lateral bolt. By torquing the lateral bolt, the two wedges will be pushed toward each other, and this mechanism would pull the upper and lower blocks away from each other. This movement will introduce a preload in the connection, which would subsequently create a contact between the MP and TP. To understand the C1 wedge connection technology design, two main studies have been developed: the optimization of the hole shape and the fastener's performance. Two factors are analysed in the present study to understand the wedge connection performance: 1- load performance LF (Load Factor), and 2- displacement performance DF (Displacement performance). Both factors show the correlation between the vertical and horizontal components of load and displacement.

To calculate the preload force on the bolt F_{bolt}, Figure 4-27 has been considered to describe the forces as follows:

$$\sum F_{Hor} = 0 \qquad \text{4-20}$$

$$F_{bolt} = F_{hor_1} + F_{hor_2} + F_{friction_{1_{hor}}} + F_{friction_{2_{hor}}} \qquad \text{4-21}$$

$$F_{hor_i} = \frac{F_P}{2} \tan(\theta) \qquad \text{4-22}$$

$$F_{friction_i} = \frac{F_P}{2} \cos(\theta)\, \mu_i \qquad \text{4-23}$$

$$F_{frict_{i_{hor}}} = F_{frict_i} \cos(\theta) \qquad \text{4-24}$$

where the subscript i is referring to the upper block as 1 and the lower one as 2, and θ corresponds to α and β for the wedge slope of the upper and lower blocks, respectively.
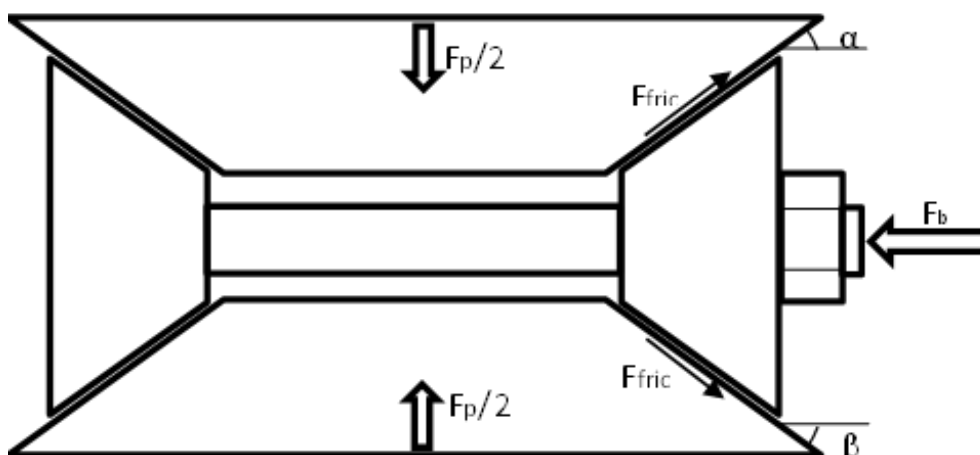
Figure 4-27: Free Body Diagram for C1 wedge connection

Considering a value of α for the upper wedge slope and β for the lower wedge slope, Equation 4-20 can be rewritten as:

$$F_{bolt} = \frac{F_P}{2}[\tan(\alpha) + \tan(\beta)] + \frac{F_P}{2}\mu[\cos^2(\alpha) + \cos^2(\beta)]$$

4-25

From Equation 4-25, it can be observed how the system is affected by the wedge angle inclination of the upper and lower block and from the friction coefficient between the blocks and the wedge.

In Equation 4-26 the Load Factor, LF, has been described as:

$$LF = \frac{F_P}{F_{bolt}} = \frac{2}{[\tan(\alpha) + \tan(\beta)]} + \frac{2}{\mu[\cos^2(\alpha) + \cos^2(\beta)]}$$

4-26

To define the total vertical displacement ($\Delta d_{vertical}$), the schematic displacement has been studied through the use of Figure 4-28. As illustrated in Equation 4-27, the total vertical displacement can be calculated as:

$$\Delta d_{vertical} = \Delta d_{horizontal}[\tan(\alpha) + \tan(\beta)]$$

4-27

In Equation 4-28 the Displacement Factor has been calculated

$$DF = \frac{\Delta d_{vertical}}{\Delta d_{horizontal}} = \tan(\alpha) + \tan(\beta)$$

4-28
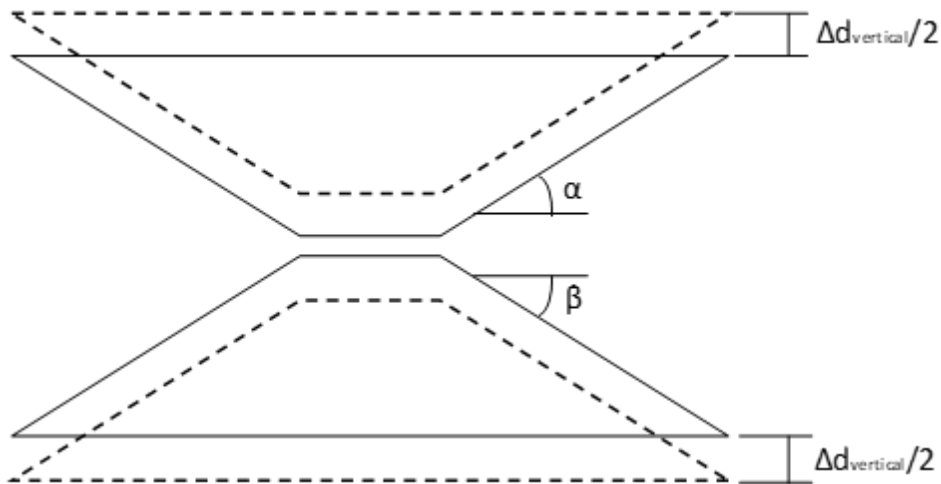
Figure 4-28: Total vertical displacement

Load Factor *LF* (Equations 4-26) and Displacement Factor *DF* (Equation 4-28) are plotted in Figure 4-30 and Figure 4-31, respectively as function of α and β angles and considering a friction coefficient of 0.05. As seen in these figures, the Load Factor is inversely proportional to the increase of the wedges slope, which means that for higher values of *α* and *β* a lower value of *LF* is achieved. Conversely, it is possible to achieve a value tending to infinity for a layout with slopes tending to 0. Instead, as represented in Figure 4-31, the Displacement Factor has a direct proportion to the wedges slope, meaning that for lower slope values a lower *DF* is reached compared to higher slope values. For these opposite behaviour between *LF* and *DF* in correlation of the slope, a compromise between the two factors needs to be made. However, it is essential to consider the practical implications of the correlations between these two factors:

- With a low *LF* value, a higher preload needs to be applied to reach a defined value to allow the connection to properly work. Meanwhile, a higher *DF* means that a bigger vertical displacement of the blocks can be easily reached with a small horizontal displacement.
- With a high *LF* value, a higher vertical load can be easily reached with a relatively smaller horizontal preload, meanwhile a smaller *DF* means that a smaller vertical displacement (compared to the horizontal) is necessary.

Under these considerations, the first case, at parity of vertical load, would require more specific machinery to apply the high preload required, compared to the second case. When considering displacement, a smaller vertical displacement has more advantages compared to a larger one. This is because a higher vertical displacement would require longer holes need to be machined along the MP-TP connection section, thereby increasing the manufacturing cost of the entire connection. In conclusion, a higher LF with a smaller DF is preferred, this preference finds correlation in literature where the wedge slope is preferred to be lower than 20°[74].

As described previously, the study previously presented have been run with a friction coefficient between the block and the hole of 0.05. in Figure 4-29 have been presented two different cases (*α=β* and *2α=β*) to study the variation of LF at different friction coefficient (0.07, 0.10, 0.15). As illustrated, at same amount of *β*, at the decrease of friction coefficient an increase of LF is detectable, under this consideration it is clear that the reduction of friction between the blocks and the wedges is necessary to improve the efficiency of the fastener, This reduction of friction coefficient can be done by reducing the surfaces roughness, the use of different materials and/or the use of lubricants between the surfaces.
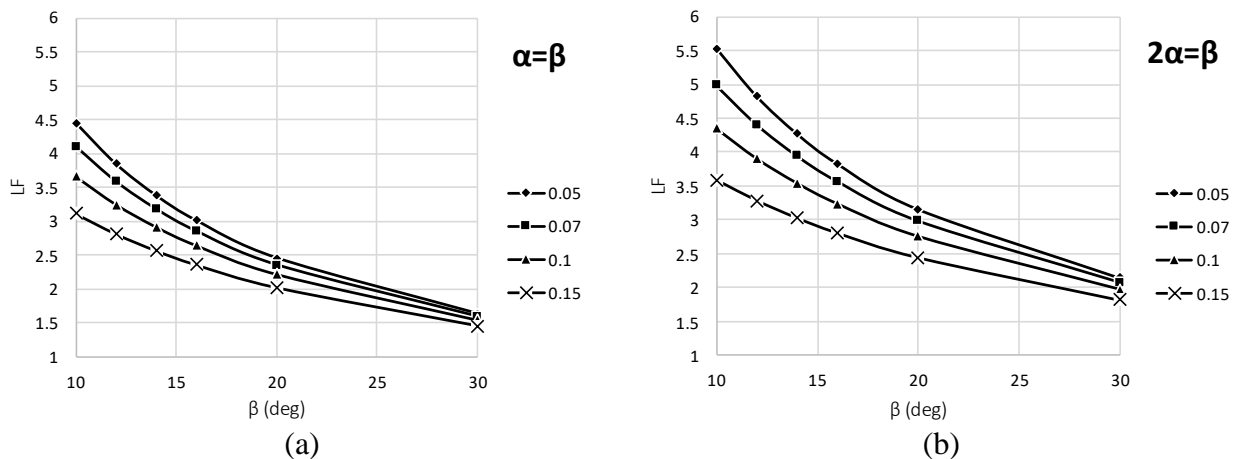
Figure 4-29: LF variation with different friction coefficient factor for different slope wedge inclination: (a) α=β and b) 2α=β. Friction coefficient factors: 0.05 (diamond), 0.07 (square), 0.1 (triangle) and 0.15 (cross)
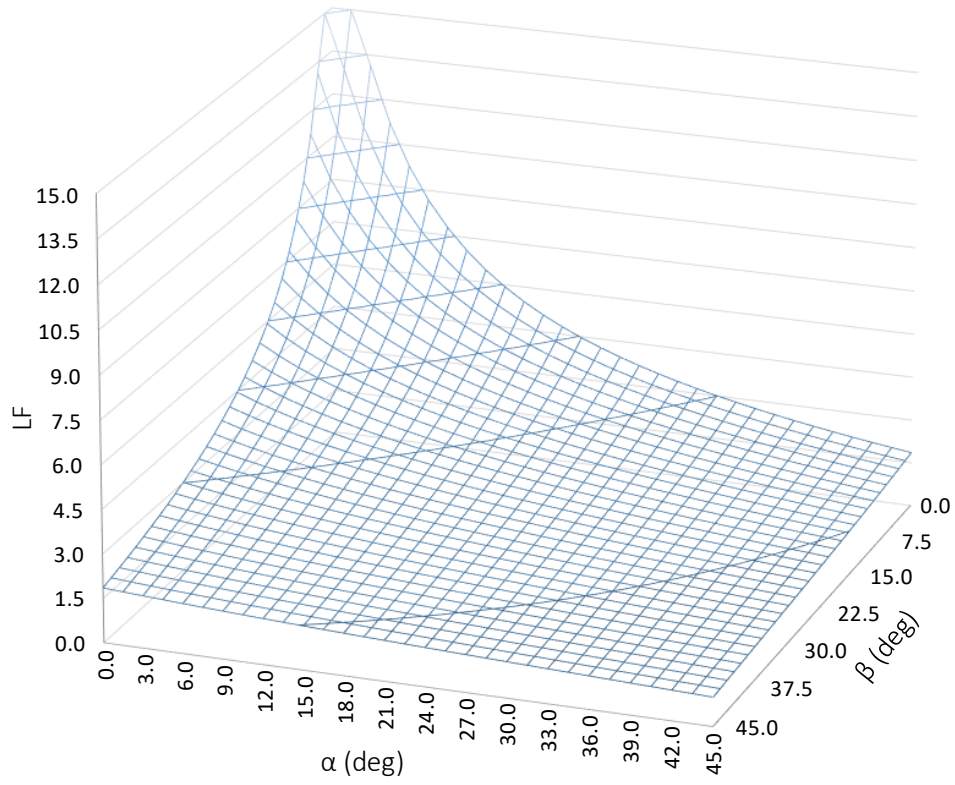
Figure 4-30: Load Factor (LF) variation against alfa and beta
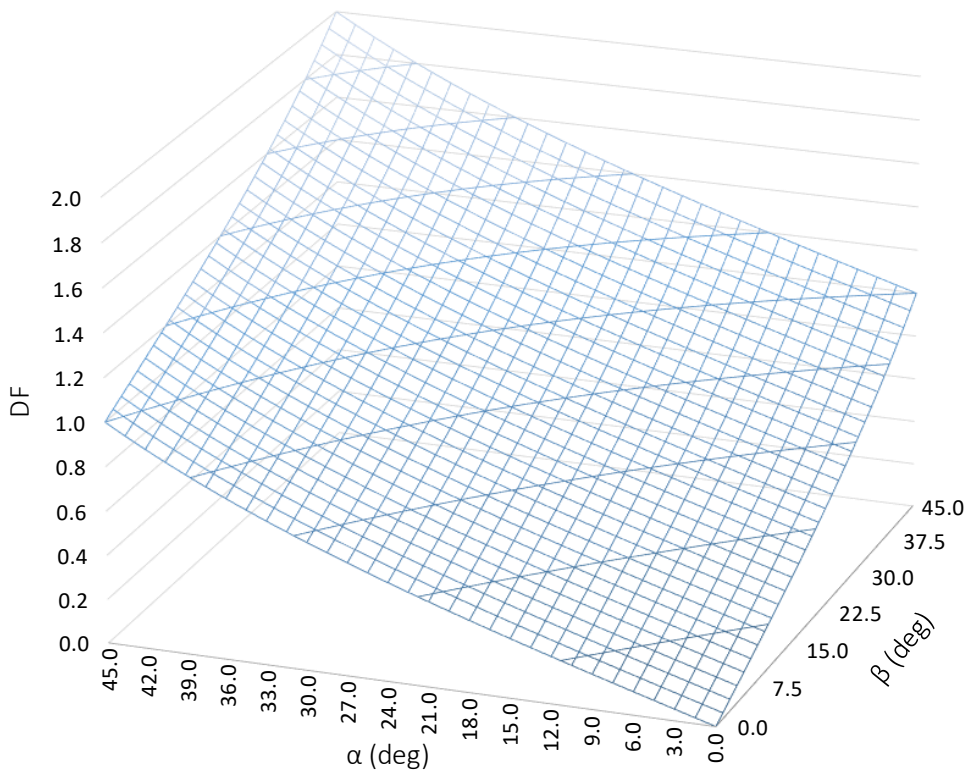
Figure 4-31: Displacement Factor (DF) variation against alfa and beta

4.7. Analysis of Large-Scale Wedge Connection Segment

In order to analyse the structural response of the wedge connection, a large-scale testing and FEA analysis were conducted on a wedge connection segment. The detailed FEA analysis and fatigue tests results are presented and discussed in this section.

4.7.1. FEA Analysis

Under the global loading condition, illustrated in Chapter 2, for a critical case where the wind speed is 25 [m/s], height is 120 [m] and the tower diameter is 7.7 [m], a total momentum of 133 [MPa] can be considered at a height of 18 m above sea level. This value has been considered as the position of the MP-TP connection section. Considering n as number of circumferential segments, Equation 4-3 provides the possibility to calculate W that would be used to find the cross-sectional segment area, to calculate the maximum load coming from the bending load. Considering the larger diameter hole equal to 115 [mm] and a l/D of 2.02 [7][16] W takes a value of 220 [mm]. Considering a wall thickness of 80 [mm], the cross-sectional area takes a value of 17410 [mm^2]. Under the maximum local stress from momentum solicitation, the local load can be calculated, and its value is 2.3 [MN]. This value has been considered as the critical load of the structure and utilised for the FEA model, and subsequently as the maximum load applied during large-scale fatigue test.

Geometry and Material Proprieties

The simulation developed in this section considers the results presented in Section 4.5 and 4.6, specifically regarding the hole shape and the fastener considerations about α and β value. Furthermore, the simulation considers an elastic-plastic model to describe the material behaviour. The main dimensions of the connection have been reported in Table 4-11 the friction coefficients considered are reported in Table 4-12. In Table 4-11, R is the main hole radius of the contact area between the block and the hole, R_1 is the secondary radius, R_{block} is the block radius (R_{pin} showed previously), ϕ is the slope of the tangential edge (presented in page 87), $α$ and $β$ are the slope angle of the upper and lower block , t_{MP} and t_{TP} are the wall thickness of Monopile and Transition piece respectfully. Materials considered for this simulation are S460NL (Stress-Strain curve in Figure 4-32) for the Monopile and Transition Piece components, for the rest of components (wedges and blocks) the 34CrNiMo6 alloy steel has been [84], the respective material proprieties have been reported in Table 4-13.

Table 4-11: FEA model dimensions and material proprieties

	Dimension
R [mm]	50.5
R_1 [mm]	57.5
R_{block} [mm]	50
$ϕ$ [deg]	20
$α, β$ [deg]	8
t_{MP} [mm]	80
t_{TP} [mm]	40

Table 4-12: Friction coefficients employed in the FEA model

Contact surface	μ
Block-Wedge	0.06
MP-TP	0.1
Wedge-Wall	0.1

Table 4-13 Elastic proprieties for S460N and 34CrNiMo6

Input data	S460NL	34CrNiMo6
Elastic Young's modulus [GPa]	212	205
Poisson's ratio [-]	0.3	0.3
Density [Ton/mm^3]	7.8 10^{-9}	7.73 10^{-9}
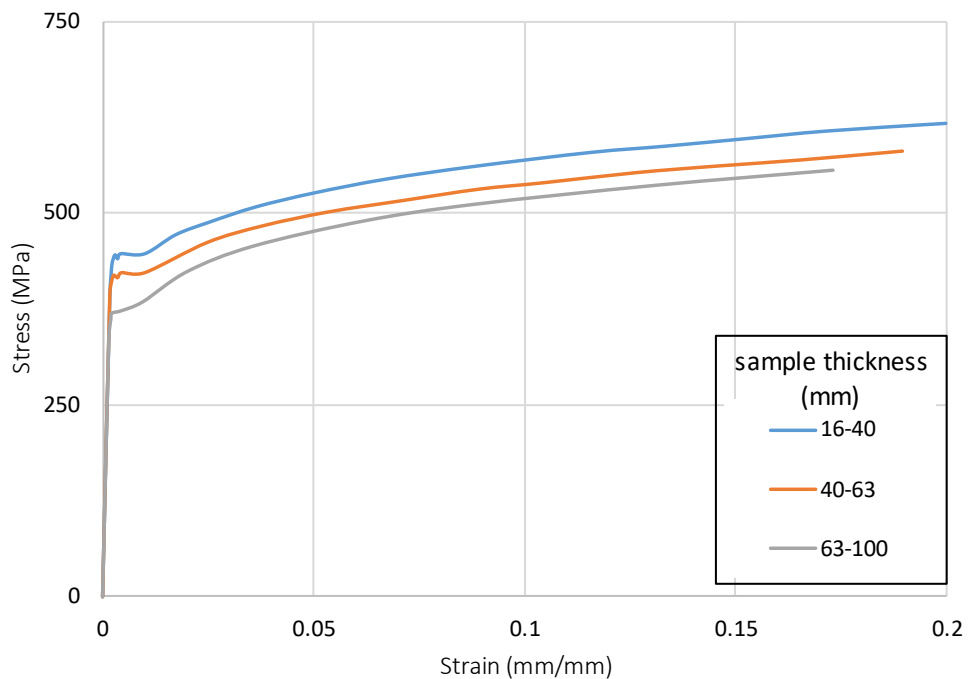
Figure 4-32: S460N Stress-Strain curves in function of sample thickness[84]

The load application in the simulation was applied in two steps: a preload phase and the 2.3MN load application. The first phase is necessary to avoid any movement of the connection which could cause a premature failure of the entire structure. For this reason, a 2.4 MN preload (F_P) was applied. The second phase was the application of 2.3 MN load on the top of the fork shape section (TP). The load application timeline defined in various simulation steps can be seen in Figure 4-33.
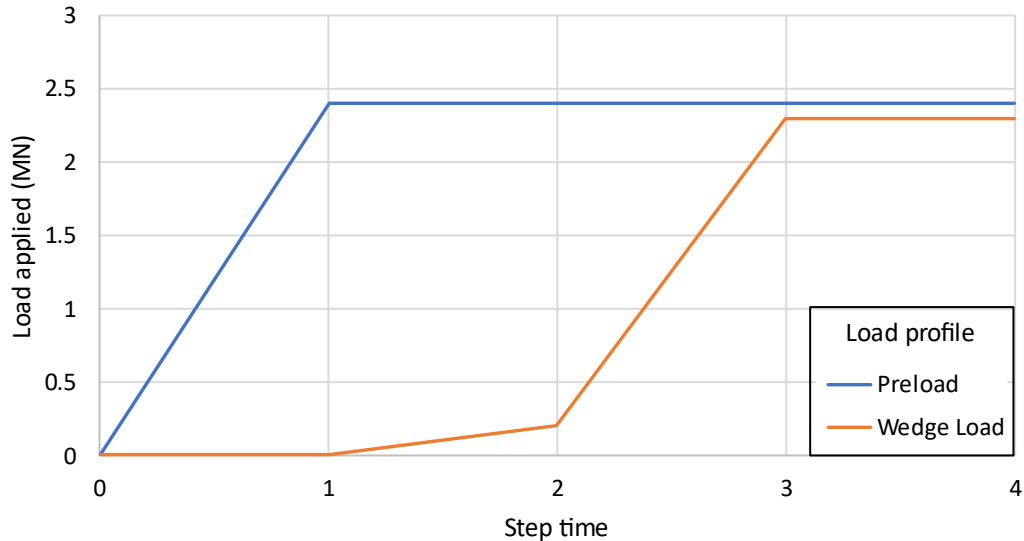
Figure 4-33: FEA Load application in different steps: Vertical preload (blue) and Vertical load (orange)

Boundary Conditions

Figure 4-33 illustrate the load application following the steps of preload through the fastener and the application of the preload with the interaction between the Monopile (orange), the transition piece (green) and the fastener (grey). These load applications have been performed as follow:

- The preload has been applied through the simulation of the bolt action that would get closer the two wedges, as illustrated from orange arrows in Figure 4-34(a). To simplify the simulation, the bolt has been removed and a series of simulations have been conducted where different displacements have been tested until the desired vertical load on the structure has been reached.
- The vertical load has been applied through the application of 2.3 [MN] on the lower surface of the MP segment, as illustrated by pink arrows in Figure 4-34(b).

while fixed BC has been applied on the two top surfaces, as illustrated in Figure 4-35.

(a)   (b)
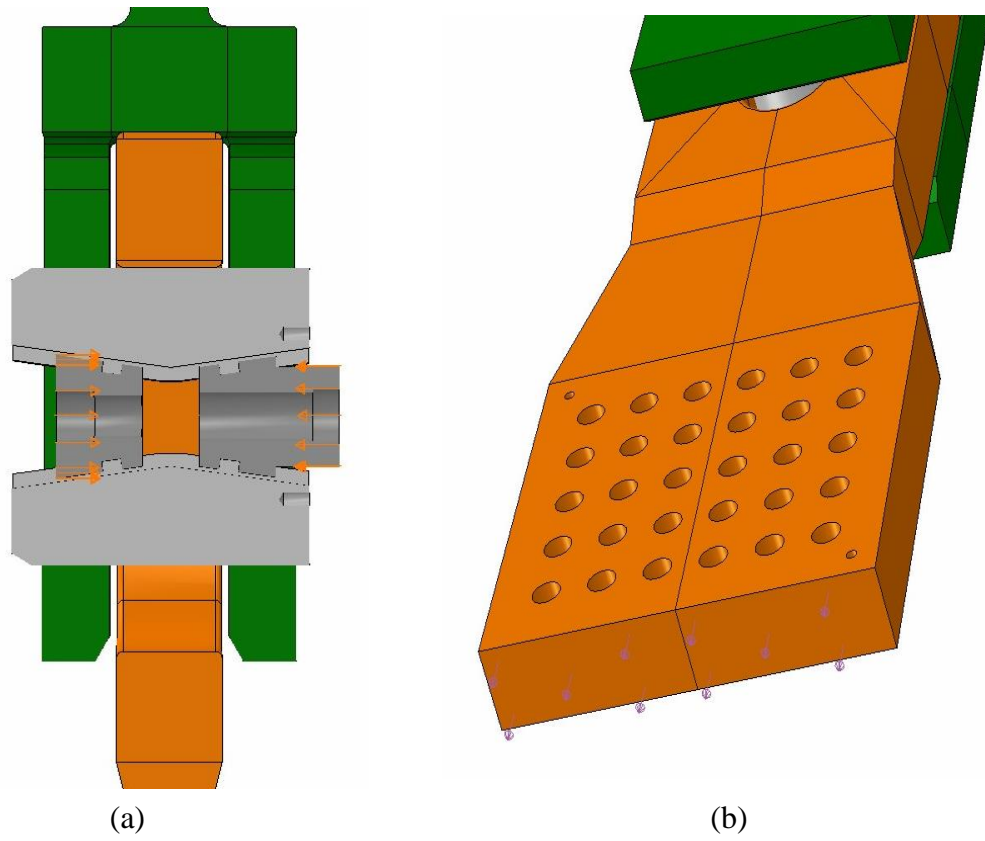
Figure 4-34: BC applied to FEA simulation for a Large-scale wedge connection: preload application (a) and vertical load (b)
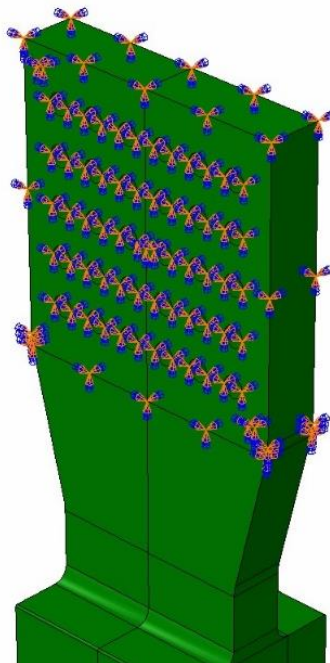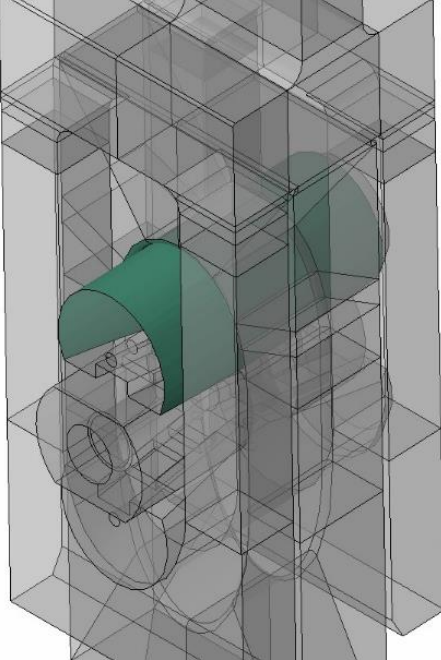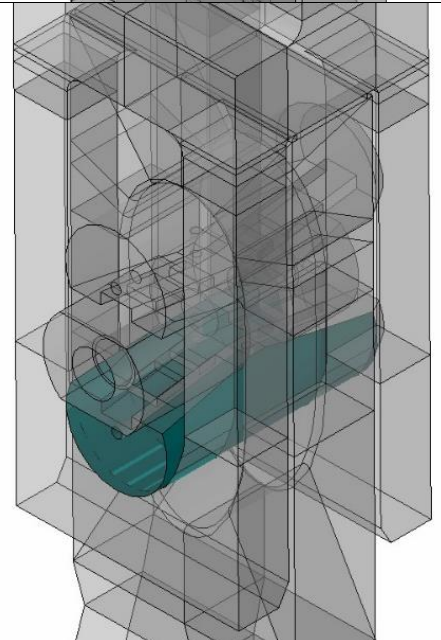
Figure 4-35: Encaster BC applied on TP segment

In order to develop the analysis, the following interaction and respective friction coefficient between the components have been considered, under suggestion of C1 Connection.

Surfaces in contact	Friction coefficient μ	Image
Upper fastener block with MP upper hole surface	0.10	
Lower fastener block with TP lower hole surfaces	0.10	

Contact surfaces between wedges and blocks	0.06	
MP top surface and bottom fork TP surfaces	0.10	
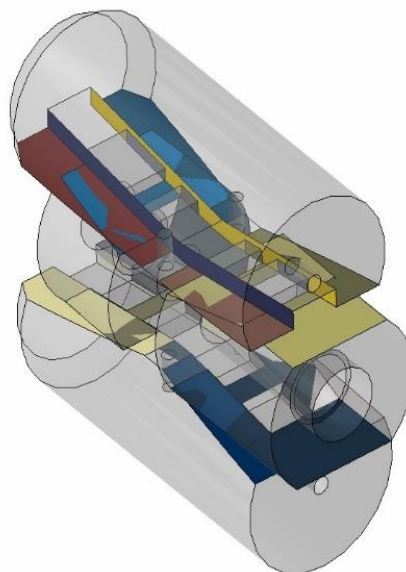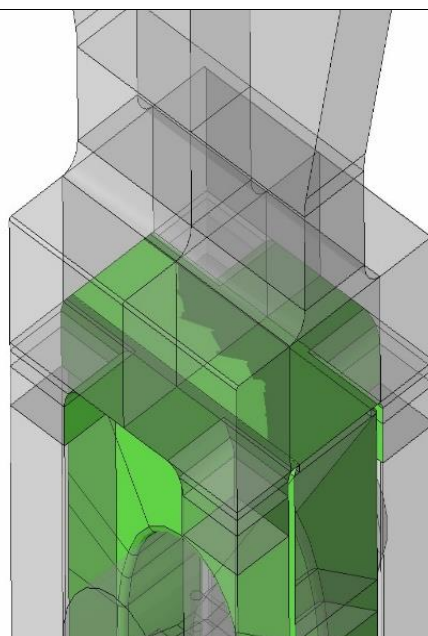
Mesh Sensitivity Analysis

The aim of the mesh sensitivity analysis is to create a mesh density for the FEA model that can give the most accurate results in the most relatively efficient process. The mesh density has been studied to have the higher density in the most critical region and a lower for less critical region. For a preliminary study the system has been simplified with the only MP section in contact with the upper block. For the Monopile and Transition piece samples have been used a 8-node brick element (C3D8R) and for the fastener a (C3D10). These two element-types have been chosen for the following reasons:

- C3D8 R is an 8-node linear brick with reduced integration that has been chosen. Although it can introduce distortions in the simulation, for the small mesh size this problem can be reduced. The reduced integration has been used for a time-consuming purpose.
- C3D10 is a 10-node quadratic tetrahedron. For the mesh complexity of the block and wedge geometry this mesh-type has been chosen.

As previously illustrated, the C1 wedge hole geometry has two main hotspots in terms of maximum stress, for this reason the mesh has been developed with a higher density in these two areas, identified from the red square in Figure 4-36.
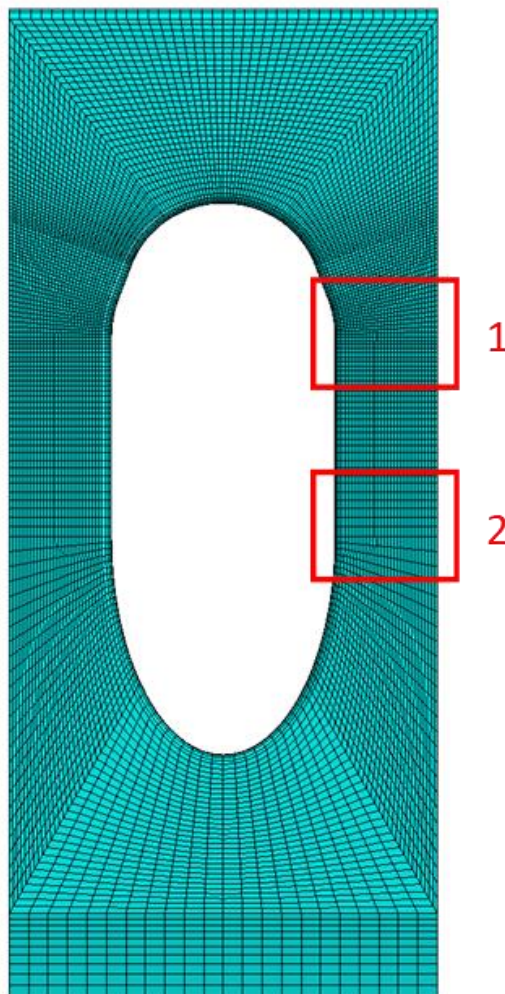
Figure 4-36: Critical region for MP sample: region 1 near the contact region between the fastener and the hole and region 2 in presence of the shape change

As illustrated in Figure 4-37, five different mesh have been developed. Table 4-14 reports the element number, the minimum size and the stress resulted for the critical region. As seen in the results for the mesh #2, #3, #4 and #5 the stress result is similar with just 12 MPa of difference. Because a minor number of elements can be related to less computational time, the mesh #2 has been chosen as final FEA model. All the main dimensions for all the other components have been reported in Table 4-15.
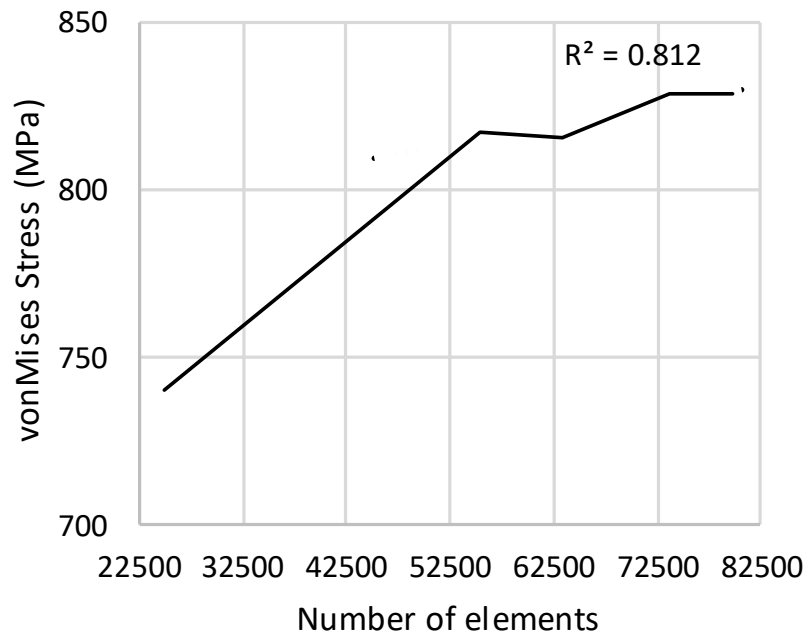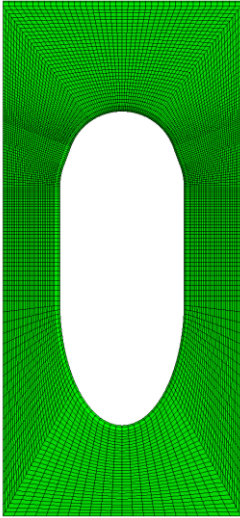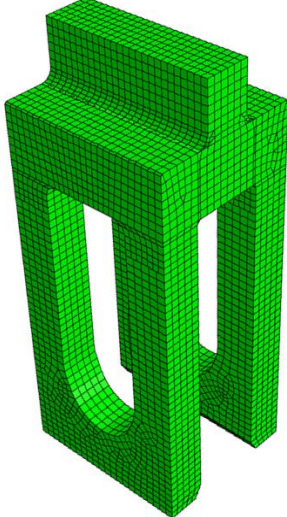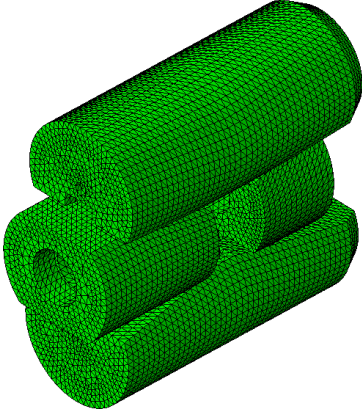
Figure 4-37: Mesh sensitivity analysis

Table 4-14 Mesh sensitivity analysis results

Mesh number	Local MP element number	Element size critical region [mm]	Maximum Mises Stress [MPa]
#1	24797	$10 \times 10 \times 10$	740
#2	55294	$3 \times 2 \times 5$	817.2
#3	63292	$3 \times 3 \times 5$	816
#4	73612	$1.37 \times 3 \times 5$	828.4
#5	79804	$1.37 \times 2 \times 5$	828.4

Table 4-15 Final Mesh size

Component	Element type	Element size	Image
Lower Part (MP)	C3D8R	3 x 2 x 5 [mm]	
Upper Part (TP)	C3D8R	10 [mm]	
Fastener	C3D10	5 [mm]	

FEA Results

Three main results from FEA simulations have been considered: stress distribution in both load steps, the axial stresses and contact angle comparisons with the results obtained from the Hertz model. The stress distribution has been studied for the two flanges separately, each in preload and load step. As illustrated in Figure 4-38, the high stress region (red region) has a von-Mises stress value close to the yield stress, by considering different thicknesses (80 mm for MP and 40 mm for each web leg of the TP) in the FEA model.

(a)   (b)

(c)   (d)
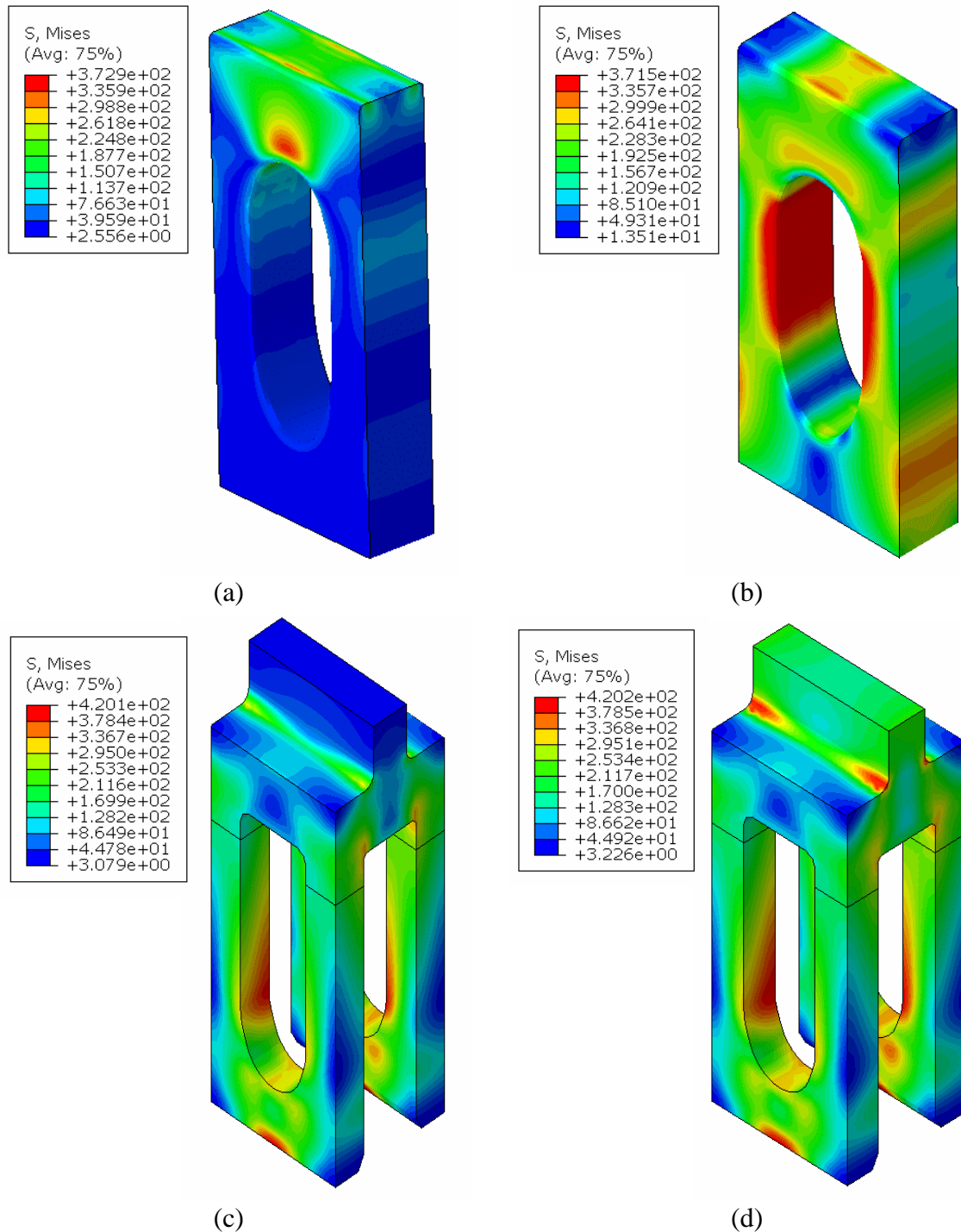
Figure 4-38: FEA results in preload step for MP (a) and TP (c) and external load step for MP (b) and TP (d)

The FEA results have been compared with the Hertz model presented in Section 4.4, focusing on the axial stress distribution along the y and z axis and the contact angle. As seen in Figure 4-39, the results from FE analysis are lower than the mathematical model estimation. This can be linked to the assumptions under which the Hertz model has been developed (frictionless and elastic behaviour) and the interaction between the fastener components that can absorb part of the stress. Secondary, the contact angle between the block of the fastener and the pin can be considered. Utilising the values used for the FEA simulation for the smaller hole radius R of 50.5 [mm] and the block radius R_{block} of 50[mm], presented in Table 4-11, it is possible to calculate the ratio between the radius of 0.99.According to Figure 4-24, this ratio should correspond to a contact area 2α equal to 81.75°.However, exporting the contact surface from the FEA results, the contact angle is 125°, indicating an increase of 53% compared to the Hertz model prediction.
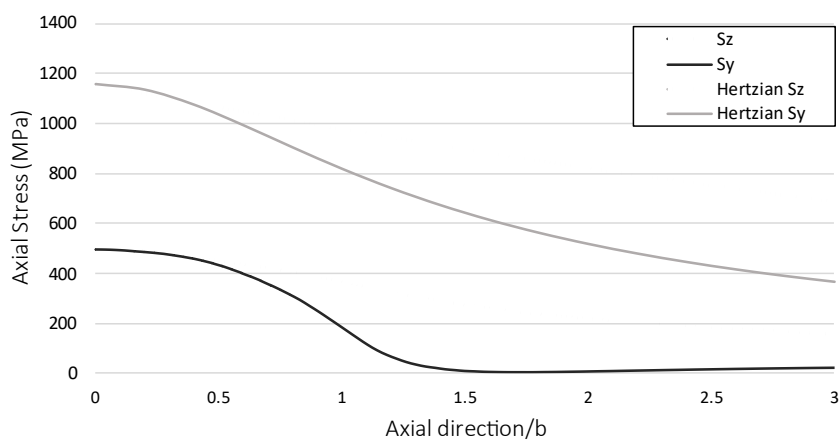
Figure 4-39:Axial Stress FEA results (black) compared to Hertz model (grey)

The stress distribution of the S33 component on the contact area between the upper block of the fastener and the MP hole has been plotted in Figure 4-40. As it is possible to see, the distribution is not constant along all the surface but has picks near the external edge of the MP. This behaviour has been already reported for a pin-loaded lug with clearance [81] and can be reason for a shape optimization for eventual further layout.
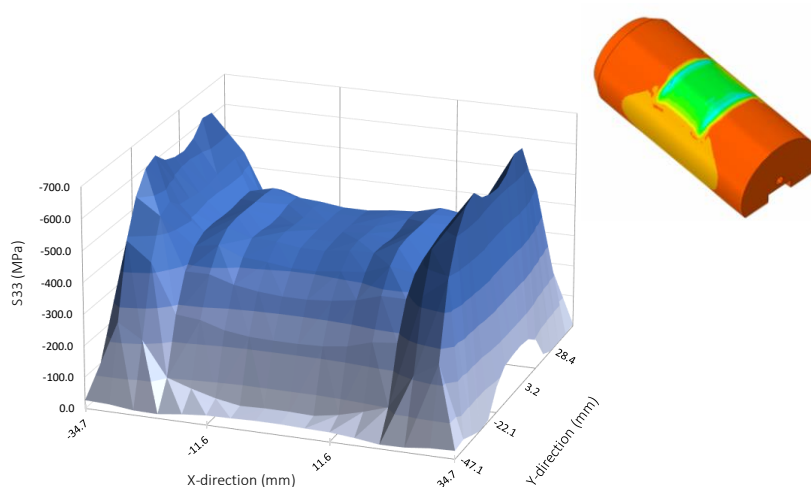
Figure 4-40: 3D S33 distribution on upper block contact area

According to Equation 4-26, with a symmetric slope between the upper and lower wedge of 8°, the LF is equal to 5.28. As presented at page 93, a vertical load of 2.4 MN has been applied to secure the fastener in the connection, according to this value it is possible to calculate the horizontal load applied to the bolt through the LF coefficient, giving a final value of 430 [kN], which agrees with analytical studies [84].

According to the FEA analysis, the hotspot section of the MP segment has been studied in terms of maximum axial stress and of stress distribution. The highest stress has been localized, in accordance to Figure 4-36, in the critical region 1, showing a maximum axial stress of 403.15 [MPa] which, comparing to the S460NL (Figure 4-32) Yield stress (416 [MPa]) for a wall thickness of 52 [mm], is lower. Meanwhile, the distribution along the x- and y-axis (in reference to Figure 4-41) have been plotted. Along the y-direction (see Figure 4-42(a)) there is high stress region near the hole edge which tents to reduce as one moves farther from the hole. In Figure 4-42(b), the axial stress distribution along the x-axis shows that the stress is mostly constant, with a reduction of around 20 [MPa] near the inner and outer surfaces of the sample.

This simulation has been developed without symmetry in the Y-direction, as it would have been in a real case scenario, to be able to further predict the stress concentration in a real fatigue test (presented in page 105). However, as it has been presented in the hole study of Section 4.3.1, the stress distribution changes in function of the ratio between the ligament *l* and the hole diameter *D*. The general trend, comparing a single hole with a series, would be, at the increase of l/D, a general decrease of stress and maximum stress near the holes [78].
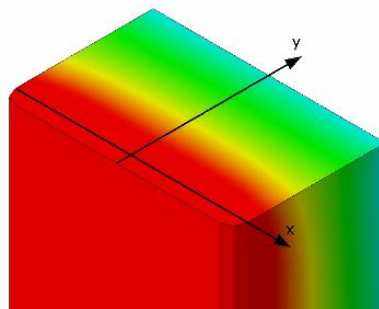
Figure 4-41: Hotspot section for Monopile component

| (a) | (b) |
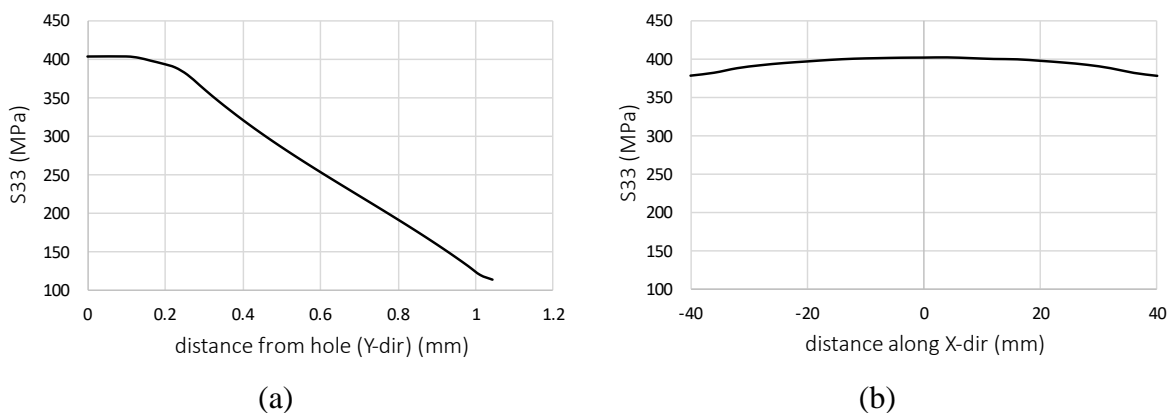
Figure 4-42: S33 along the Y-direction (a) and X-direction (b)

One last consideration that can be made through the use of FEA software such Abaqus is the calculation of the mass for the single components through the implementation of the single

volume and material density which, according to the geometry discussed in this chapter, the fastener presented (considering the bolt, the blocks and the wedges) has a mass of around 15 [kg]. Considering the entire MP-TP connection the number of fasteners required increases drastically with an increase in the diameter. For example, for C1 wedge connection a *l/D* ratio of 2.02[74], [84] on a 7m tower diameter result in around 110 fasteners for a total mass of 1650 kg. These considerations have been taken only on the preliminary FEA analysis and without any optimisation of the C1 wedge connection, which can reduce the volume of the fastener, which could potentially reduce the mass.

4.8. Fatigue Tests

Once developed the FEA model and gained confidence in the consistency of the results, a large-scale sample has been manufactured in order to analyse the behaviour of the technology.

4.8.1. Description

The test was conducted on a single segment of the wedge connection circumference. Other full-scale tests have been preliminary performed but on smaller samples [74], [85]. It is worth noting that the full-scale testing of the full circumference for the wedge connection technology requires exceptionally high load carrying capacity machines in laboratory testing, hence a single segment was considered in the design of experiments. The geometry used is the same discussed in the FEA model previously discussed. To allow the load application a grip region has been created through adding of two pair of plates at the top and at the bottom of the sample, each couple fixed using 30 M20 grade 10.8 preloaded bolts, see Figure 4-43.

The material used for the experiment is the same illustrated for the FEA models. For the gripping sections a pair of plates S460M connected to the sample by 30 preloaded M20 grade 10.8 bolts have been used per each sample, as illustrated in Figure 4-43. The bolt used in the fastener is a M36 bolt.

(a)   (b)
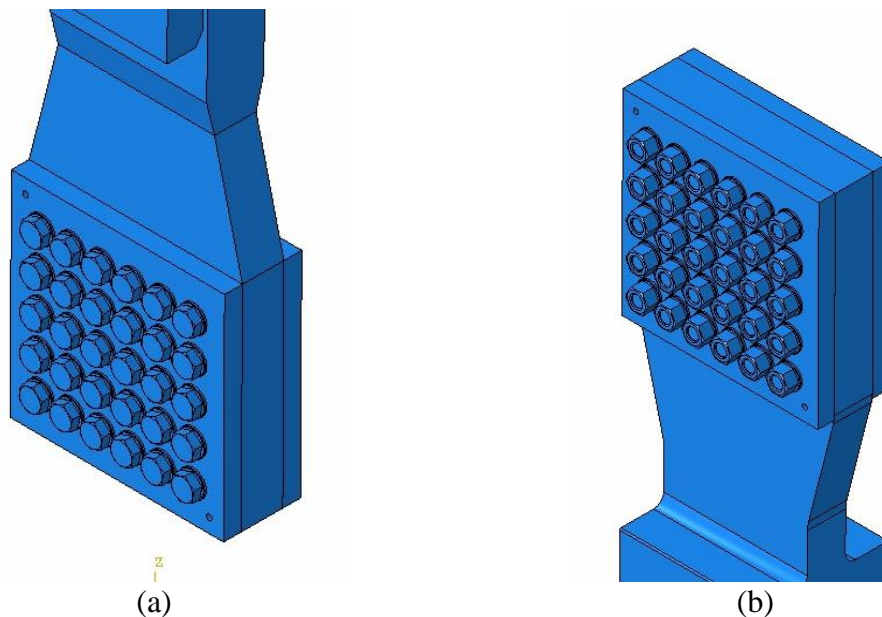
Figure 4-43: Gripping region set up for bottom sample MP (a) and upper sample TP (b)

The test has been divided into three main steps: assembly of the flanges and the fastener, application of the preload and the application of a cyclic load of 200-2300 [kN].

105

The assembly phase is composed by:

- alignment of the upper and lower flange,
- insert and assembly of the fastener and the application of the lubrification on the internal contact surfaces,
- Torquing of the M36 bolt, pulling the wedges together until the upper block is in contact with the lower flange.

The preload phase has been made with the upper and lower flanges at rest (without any external load applied). A hydraulic tensioner has been used to torque the M36 bolt applying the 430 [kN] horizontal preload. The torquing has been done twice to avoid any loss of tensioning before the start of the test. After this phase a vertical load of sinusoidal magnitude has been applied with the characteristics reported in Table 4-16.

Table 4-16 Load application in load phase

Load	Magnitude
Minimum	200 [kN]
Maximum	2.3 [MN]
Amplitude	2.0 [MN]
Frequency	1 Hz

For accurate monitoring of the test specimen, strain gauges were attached the critical regions of the geometry, presented in Figure 4-36, and local stain values were continuously monitored throughout the test. Data from 12 uniaxial Strain Gauges were collected using a data acquisition system, and positions of the sensors are illustrated in Figure 4-45.
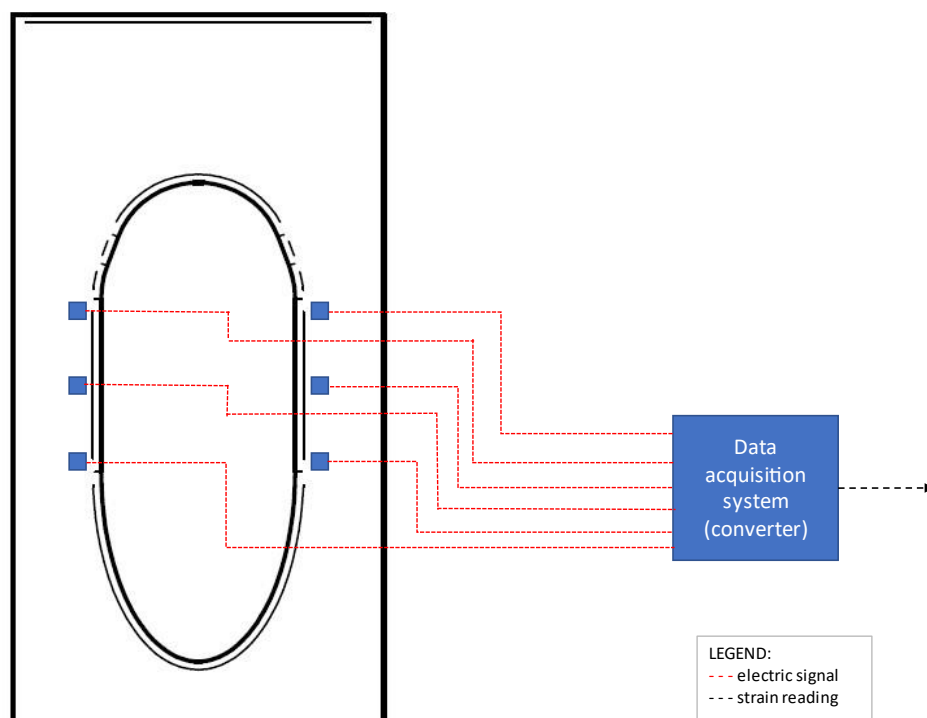
Figure 4-44 Data collection system from Strain Gauges

106

The aim of these sensors is to capture eventual strain variation in the bottom sample to detect fractures initiation. Three main sections have been selected: the top hotspot (section A), the middle section (section B) and the low hotspot (section C), as illustrated in Figure 4-45. Itis worth noting that in Figure 4-45, only half of the strain gauges are shown, same number of strain gauges were attached to the opposite face of the sample.
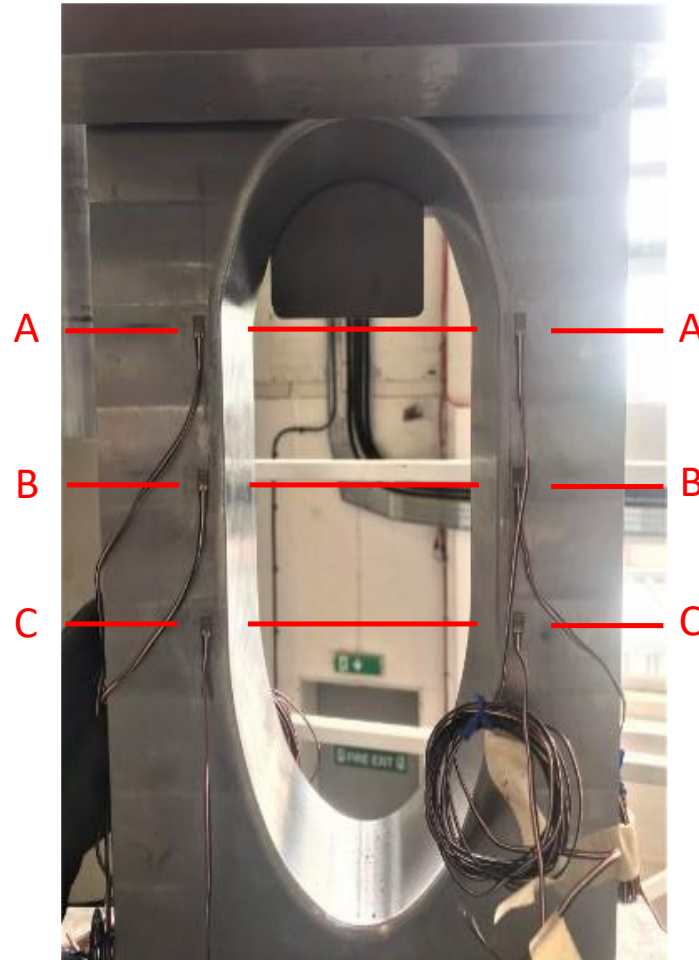
Figure 4-45: Uniaxial Strain Gauges sensor position on MP-sample

4.8.2. Results

Results of the large-scale fatigue test have been reported in terms of strain reading and fracture detection. In Figure 4-46,the Strain Gauges readings during the test have been reported. The readings have been taken starting from the preload phase, which recorded a strain up to 2000 [μstrain]. Subsequently, the reading continued during the entire test. As illustrated, some readings tend to show high values of strain. This result can have different meanings, ranging from the detection of a crack initiation to a malfunction of the sensor itself. However, for the complexity of the sample it will not be possible to understand it until the end of the experiment. Two peak regions can be individuated during the readings: the first peak around 9.5million cycles for the sensor B4 (mid region) and a second around 1.25million cycles for the sensors at the top region A2 and A4, as well as in the mid region for B1 and B2.
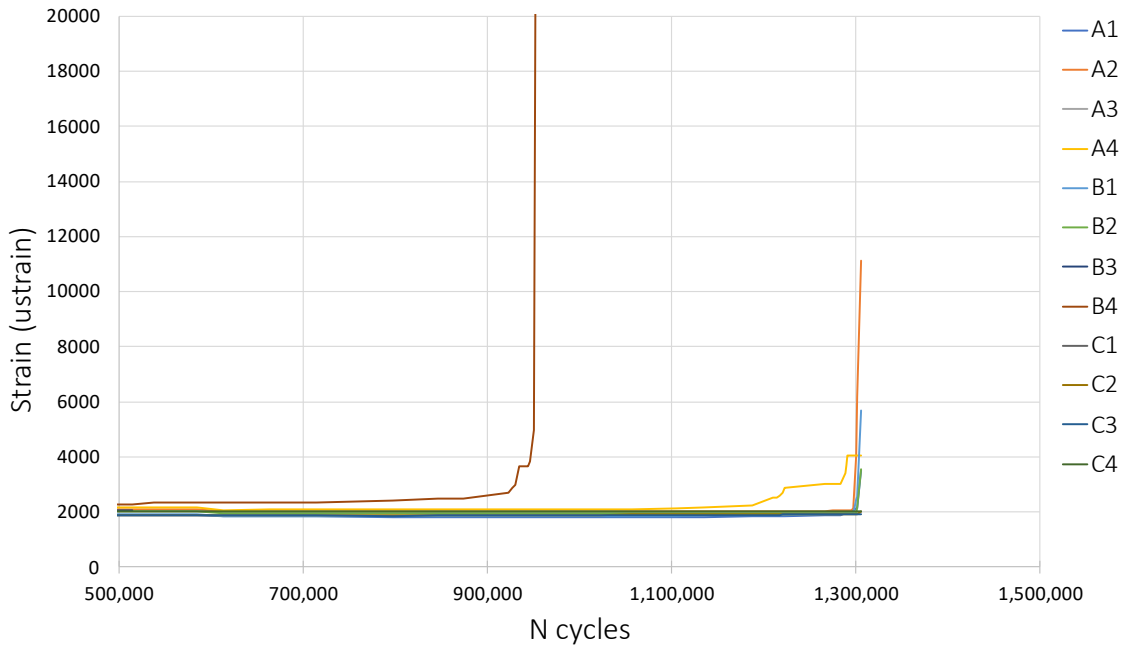
Figure 4-46: Uniaxial Strain Gauges sensor results during the fatigue test

Strain Gauges results reported an average value around 2000 [µstrain], this value can be utilised to calculate the average stress value and compare it with the FEA modelling, in according to Equation 4-29[86].

$$S = E \cdot \varepsilon$$

4-29

Where E is the Young's module and ε is the strain detected from the Strain gauges. Utilising the equation presented the average maximum stress is of 420 [MPa], which agree with the FEA modelling results presented in Figure 4-38(b).

After 1.3million cycles and with no displacement greater than 3 [mm] observed on the testing machine, the test was considered as runout. Because any visible fracture was visible on the sample and, as previously discussed, some strain gauge reported variation on the strain during the test, a Dye Penetrant Inspection (DPI) has been developed to verify any crack initiation on the surface. DPI, also known as Liquid Penetrant Inspection (LPI), is a non-destructive testing technique. The principle of this technique is the drawn of a liquid by capillarity into a defect and, after the use of a developer substance the surface imperfection (e.g. cracks) can be visible on human-eyes [87].

The test has been developed through the following steps once removed the fastener and subsequently the sample from the machine:

- The surface has been cleaned of any traces of lubricant or general dirt.
- A layer of penetrant liquid has been applied on the surface.
- After a period of 20 minutes, the excess of penetrant has been removed and the layer of development has been applied.
- Visual inspection has been developed.

Figure 4-47: Dye Penetrant Inspection (DPI or LPI) of the sample after 1.3million cycles under 2.1 MN amplitude load for main surface (a) and two lateral surfaces (b) and (c) illustrate the

108

results from the inspection. If any fracture were present, through the DPI, they would be highlighted in red. However, as visible from Figure 4-47: Dye Penetrant Inspection (DPI or LPI) of the sample after 1.3million cycles under 2.1 MN amplitude load for main surface (a) and two lateral surfaces (b) and (c), no red region was detected apart from the points where the strain gauges were attached meaning that the strain reading from the Strain Gauges were mostly erroneous or indicative of a malfunctioning of the sensor itself (as for sensor B4).
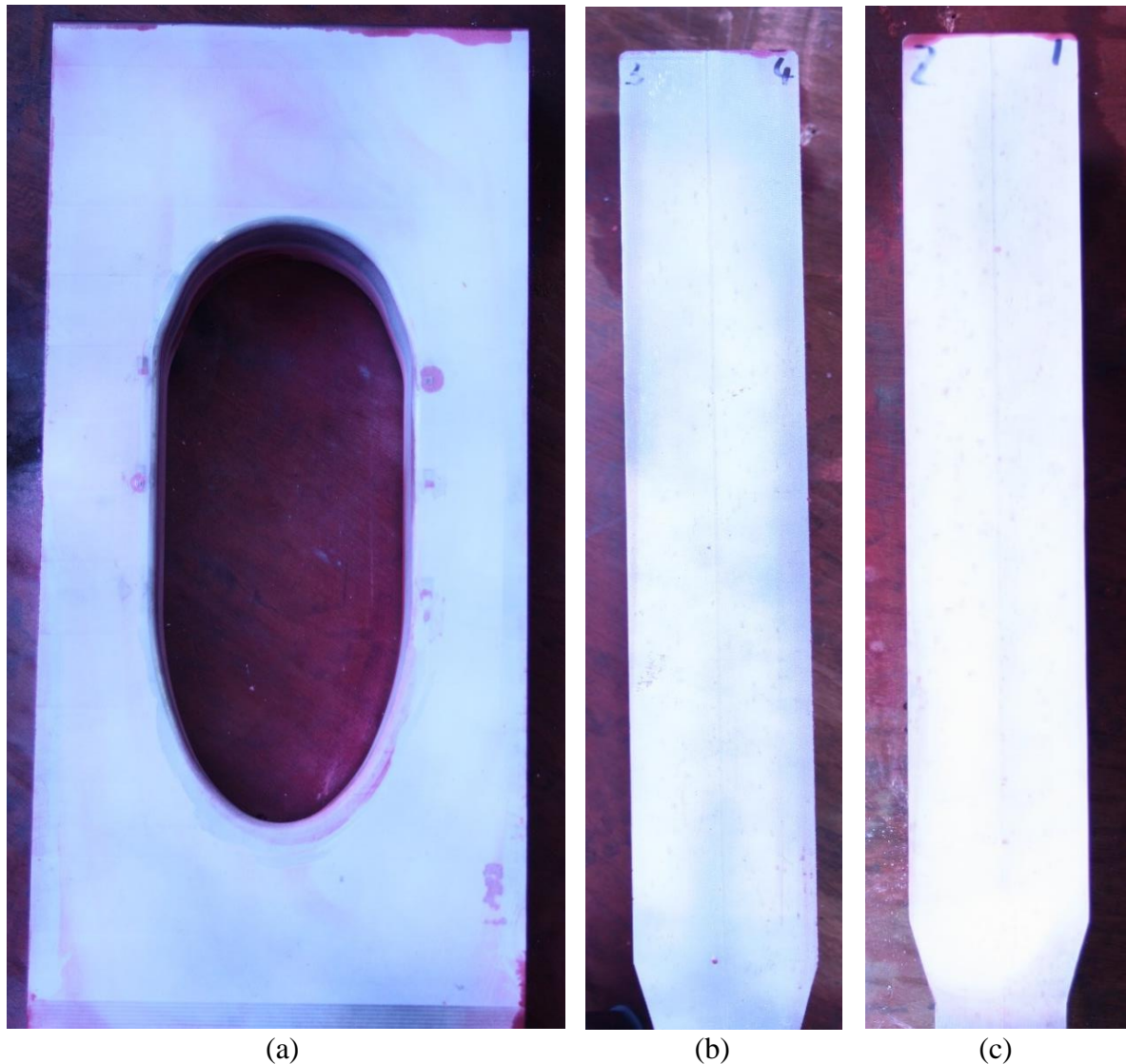
| (a) | (b) | (c) |

Figure 4-47: Dye Penetrant Inspection (DPI or LPI) of the sample after 1.3million cycles under 2.1 MN amplitude load for main surface (a) and two lateral surfaces (b) and (c)

4.9. Comparison of Results with Standards

According to Section 4.7.1, the lower flange (MP segment) is the most susceptible to high stress value, which could potentially lead to fatigue failure. Therefore, the first step to design the fatigue test is to determine the closest detail class to the wedge connection geometry.

According to Section 3.5 for bolts, the most accurate standard curve is the DNVGL-RP-C203. The critical section of the MP-segment can be simplified as an extruded plate with sharp edges. For this reason, according to the standard, the B1 curve is the most accurate to predict the

fatigue behaviour of this segment. The basic curve follows the logarithmic equation described below.

$$\log N = \log \bar{a} - m \cdot \log \left(\Delta\sigma \left(\frac{t}{t_{ref}} \right)^k \right)$$
4-30

where $\Delta\sigma$ is the stress range, N is the predicted number of cycles to failure for $\Delta\sigma$, m slope of S-N curve, t thickness of the sample and t_{ref} the reference thickness (25mm), k is the thickness component, and $\log \bar{a}$ is the intercept of the design S-N curve with the log N-axis which can be calculated as:

$$\log \bar{a} = \log a - 2s_{logN}$$
4-31

Detail class for B1 curve, in accordance with DNVGL-RP-C203, are resumed in Table 4-17. As it is possible to see the thickness component k is 0, meaning that the B1 curve is not affected by the thickness correction. The B1 curve has been plotted in Figure 4-48.

Table 4-17 S-N curve details for B1 category in air, in accordance with DNVGL-RP-C203

Category	$N \leq 10^7$ cycles		$N > 10^7$ cycles		Fatigue limit at 10^7 cycles	Thickness component k
	m	$\log \overline{a_1}$	m	$Log \overline{a_2}$		
B1	4.0	15.117	5.0	17.146	106.97	0
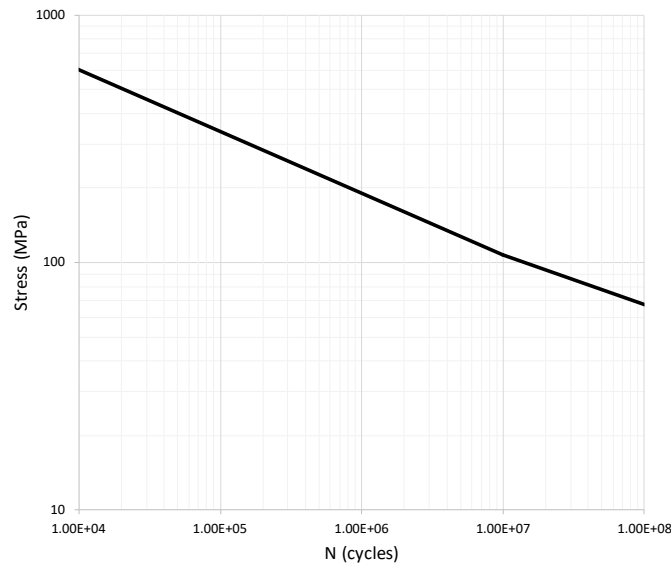
Figure 4-48: B1 curve in air (DNVGL-RP-C203)

Through Equation 4-30, it is possible to predict the number of cycles to failure utilising the stress obtained in the FEA results (Page 102). The maximus stress value reached in the critical section is around 400 [MPa], from this value it is possible to predict the number of cycles to failure for a value of 51thousand cycles. However, as presented in Section 4.8, no crack has been found over a number of cycles of 1.25million. This result demonstrates good fatigue resistance from the C1 wedge wall layout. However, as mentioned at the beginning of this section, only one large-scale specimen has been tested. meaning that the value provided lacks statistical significance in design terms.

4.10. Summary

As this chapter presented, in accordance with results derived from analytical study and from FEA analysis and large-scale fatigue test, the following results can be highlighted.

From the analytical analysis (section 4.3 - .6), the following results can be considered:

- As is well-known, the presence of imperfections along a wall can highly affect its integrity. However, considering a series of holes along a wall can reduce this risk if a correlation between the ligament *l* between the two holes and the diameter of the holes *D* are taken under consideration.
- Different hole shapes have been considered and the effect of hole shape has been studied. Results show how a hole shape with double radius can be an optimal solution (compared to a stadium shape), in terms of stress distribution and the location of maximum stress.
- Fastener design has been studied, while load and displacement efficiency (LF and DF respectively) have been analysed and discussed. A friction correlation between LF has been discussed as well.

Studies of the technology through the use of Finite Element Analysis (section 4.7) and Large-Scale fatigue test (Section 4.8) have been developed and a resume of results are:

- From FEA analysis it is possible to see how the maximum stress value is present in one of the critical sections for the MP segment. However, this value is slightly lower compared to the yield stress value of the material. Stress distribution along different sections or surfaces have been presented and discussed.
- Set up for a large-scale fatigue test has been presented and results have been compared with S-N curve from DNVGL-RP-C203 (category B1). According to this code, the number of cycles to failure of the critical region should be around 51thousand cycles. However, the test on the sample have been considered as run-out after 1.25 million cycles and through the use of a DPI test no crack initiation has been detected.

In conclusion, the MP-TP connection design presented in this chapter has proven to be a valid and promising solution for the threaded connection.

Chapter 5 Slip Joint Connection

5.1. Chapter Content

This chapter is focused on studying the behaviour of the Slip Joint connection designed in Van Oord under vertical load, studying the variation of Stress in relation to different variables.

Section 5.3, presents analytical studies concerning geometrical and load effect evaluation. The first part has been used as starting point to create the FEA models by calculating and determining the different variables involved in the design of the Slip Joint technology. The second part will illustrate stress calculations for the connection.

In Section 5.4, a Final Element Analysis (FEA) has been developed in Abaqus to investigate the variation of the Maximum stress and stress distribution along the MP- and TP-flanges in function of different variables. Aim of this section is to explore how the different variables affect the outcome.

In Section 5.5, two cases have been studied to analyse the variation of stress. In Section 5.5.1, the case of imperfect conicity from the flanges has been studied. This analysis aims to understand how the structure reacts to incomplete interaction between surfaces. And finally, in Section 5.5.2, a study of bending has been developed for the connection of Slip-Joint, analysing the stress variation along the entire circumference on the Transition Piece and the Monopile.

5.2. Introduction to Technology

The Slip Joint connection can be easily visualised simply as two cups upside down on top of each other, as illustrated in Figure 5-1. In the slip-joint the tensile and compressive forces in the skin of the tubular tower are transferred through friction forces and for a small part through contact forces between the two parts. The frictional forces between the two conical surfaces in contact result from the weight of the structure and the load variations coming from the operational wind turbine.
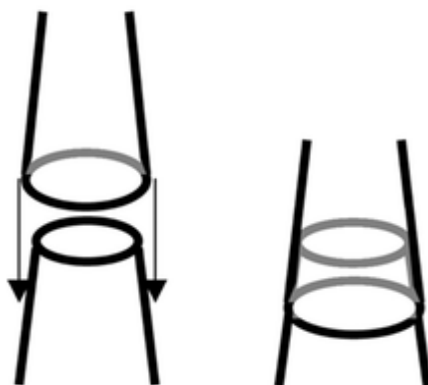
Figure 5-1: "Two cups" slip joint connection layout[88]

The first offshore wind turbine designed with Slip Joint connection was in the Netherlands by WindMaster. However, after the bankruptcy of the company and the subsequent acquisition of the company from the Lagerwey B.V. in 1998 the technology has not been widely implemented in industry [89]. Recently the Slip Joint connection has been redesigned by Van Oord in the Netherland and in 2020 the first full-size submerged installation was carried out at the Borssele Site V offshore wind farm[90].

As reported in DOWEC report of 2003[89], the Slip Joint installation, designed by WindMaster, was designed to be installed in three steps: the lower tower is connected to the foundation (Monopile) by bolted connection, then the bottom part of the upper tower slips on the lower part (Slip Joint connection), and finally the nacelle with the blades is installed. In terms of time, it was reported that for the same amount of time to install one bolted MP-TP connection, WindMaster was able to install four Slip Joint towers.

Van Oord presented a new Slip Joint connection design, simplifying the structure using two conical flanges, with slope of around 1 to 2 [deg], respectively welded to the upper part of the monopile and on the bottom of the Transition Piece. With this design it is possible to install the TP, and eventually the entire tower, directly on the Monopile, as illustrated in Figure 5-2 for Borssele Site V[91]. According to reports, the overall time for installation of the transition piece from the deck to the installation field was around 30 minutes.

Figure 5-2 Borsselle V Transition Piece installation[91]

In Figure 5-3 the settlement of the TP in during the first year of installation, considering before and after the installation of the wind turbine generator (WTG), has been presented [90]. The blue line represents the measured settlement from the sensors, whereas the dashed line is indicative for the absence of energy to the sensors. It can be observed that after the WTG installation, the measured settlement decreases to reach an almost horizontal asymptote around 25% of the maximum settlement. According to Van Oord, the total settlement in 25 years, which is the WTG lifetime, is expected to arrive up to 45%, as illustrated from the red dashed line.
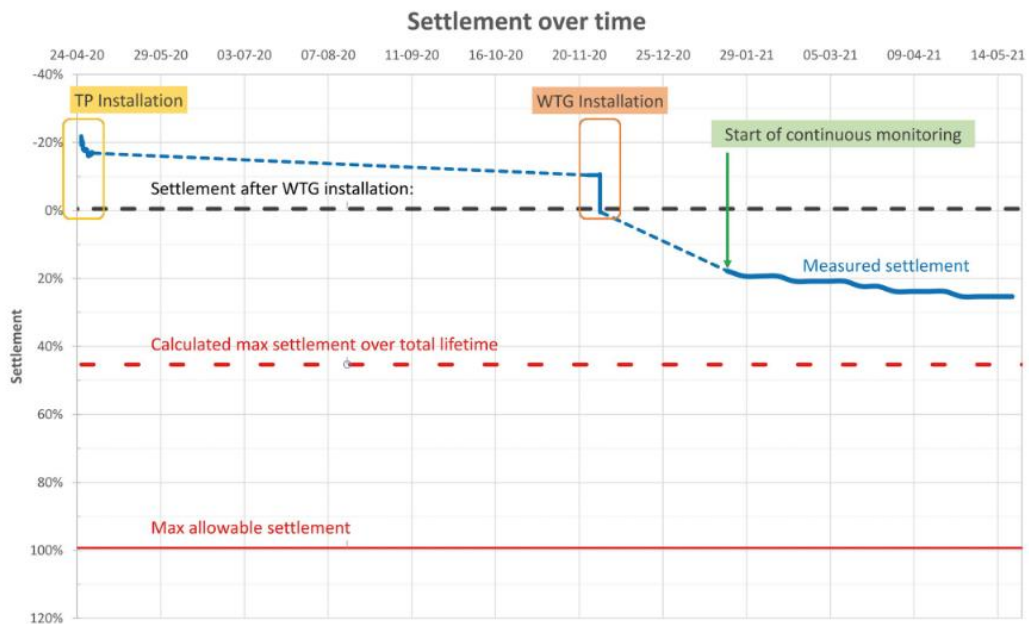
Figure 5-3 Settlement over time from first Slip Joint connection in Borssele V[90]

114

5.2.1. Design and Assembly Challenges

While the design of this technology may be considered simple compared to other technologies, the process of design and assembly needs to face different challenges for the successful application of the Slip Joint Connection[23], [89], [90]: vertical alignment of the monopile, corrosion and geometry imperfections.

In the "traditional" installation, the transition piece (TP) usually provides the opportunity to correct the vertical alignment of the tower. It is essential to consider that even for a minor misalignment from the vertical direction could result in a significant offset of several meters.

The slip-joint has no extra corrosion protection other than the layer of paint covering the entire outside and inside of the tower. According to the maintenance chief in the DOWEC report, regular inspections have shown that no significant corrosion has occurred in 7 years. For the offshore installations, two main options to reduce corrosion can be found in positioning the slip-joint connection above or under the sea level. While the first solution makes the inspection easier, it exposes the connection to the highest corrosive atmosphere (splash zone). Meanwhile, considering a sub-sea level layout can provide, as suggested in literature by the use of a cathodic protection, a better corrosion resistance at the cost of a more difficult inspection caused by the necessity to reach the area.

As explained and discussed by Van Oord, a small manufacturing tolerance can have a significant impact on the design of the connection. For this reason, it is important to understand the range of tolerance at the beginning and then evaluate the possible worst cases, while the main imperfection can be identified in the inclination of the two conical sections. Defining as angle α for the inclination of the Monopile flange and β for the Transition Piece, three main conditions can be reached, as illustrated in Figure 5-4. The first condition ($\alpha>\beta$) is the optimal one, it allows the TP-flange to slip on the MP-flange slowly, deforming itself and increasing the connection. Indeed, the second and third case could provide some problems in terms of stress distribution, going to reduce the connection propriety. This is due to the lower slip on the MP-flange (despite having a higher stress distribution) for the case $\alpha=\beta$ and for both small contact and slip area for the case where $\alpha<\beta$.

α>β	α=β	α<β
(a)	(b)	(c)
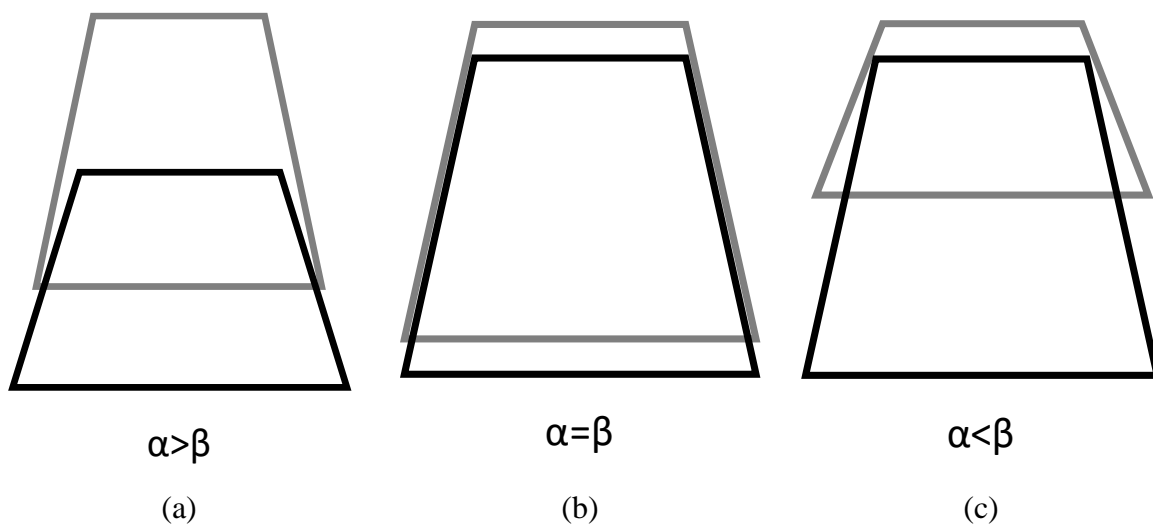
Figure 5-4: Slip joint initial contact in function of slope conditions: initial contact at bottom ($\alpha>\beta$) (a), inverted coffee cup ($\alpha=\beta$) (b) and initial contact at the top ($\alpha<\beta$) (c)

Another design problem connected to the slope angle of the flanges can be faced during the installation of the Monopile, where the foundation tower gets hammered into the soil. If the cone angle is too steep, the flange could absorb all the forces from the hammering action, thus denying the penetrating force required. For this reason, small angles are preferred over larger values.

5.2.2. Interaction with New Technologies

The simplicity of the Slip Joint connection has prompted exploration into new technologies aimed at reducing foundation costs and increasing the lifespan of the entire structure. One of the new considerations that some companies are taking is moving towards TP-less designs, which involves a displacement of the Transition Piece with a smaller component that serves as the platform for technicians without any structural implementation. Sif-group is the company that is developing the design of Skybox, a TP-less design that utilises the slip joint connection to install the main platform over the top flange of the Monopile, as illustrated in Figure 5-5[92]. Another similar design comes from COWI, which installs different ladders directly on the Monopile and the platform on top of that, aiming to remove the Transition Piece from the structure[93]. Over the new design technology that aims to avoid the use of the Transition Piece, possible improvement to the design of a Slip Joint connection have been presented by Delft Offshore Turbine (DOT)[94]. Their patent proposes adding a coating between the external MP-flange surface and the internal TP-surface, to increase friction coefficient and/or reduce corrosion.
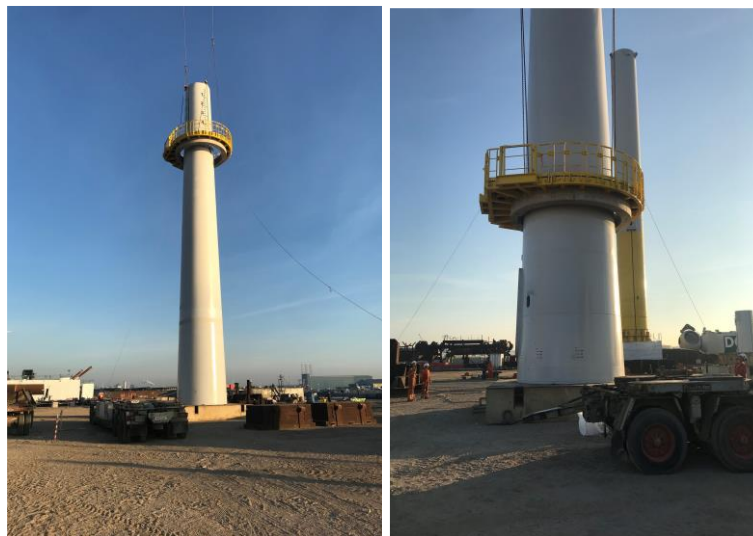
Figure 5-5: Skybox Lite of Sif Offshore Foundations[92]

5.2.3. Literature Gap

In the open literature, different authors presented investigations results on the dynamic analysis of the system[88], [95], [96], [97] and studies about speed drop have been presented[23]. However, few publications have been presented for slip joint connection in terms of stress distribution in function of the Slip Joint connection design[98], especially in offshore field.

In this section different consideration about some of the main input parameters of the geometry have been presented, which include overlap length, angle difference between TP and MP, contact area reduction and friction coefficient.

5.3. Analytical Studies

5.3.1. Geometrical Evaluation

The geometrical evaluation presented in this section has been used to create the FEA models presented in the next ones. Slip Joint connection, as previously presented, can be simplified as two reversed cups, one on top of the other, as presented in Figure 5-6.
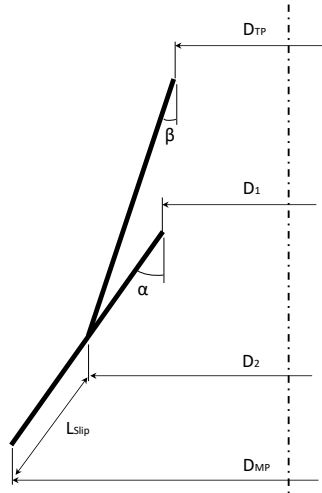
Figure 5-6: Slip Joint geometrical layout simplification.

The main dimensions have been defined below. The general flange length has been considered as $L_{overlap}$, where the value is usually variable of the diameter of the Monopile multiplied by a factor X (usually 1.5). The flange length must be the same for both components and L_{slip} which represents the total length that the upper flange must move to completely cover on the MP-flange. The following geometries dimensions have been defined for the Monopile:

- D_{MP} external MP bottom diameter
- D_1 external MP upper diameter
- α slope of the monopile flange

And for the Transition Piece:

- D_{TP} internal TP bottom diameter
- D_2 internal TP upper diameter
- β slope of Transition Piece flange

Defining the Monopile Diameter and the slope of both flanges, it is possible to calculate the external upper diameter of the Monopile. Defining x as the horizontal length of the flange, it can be calculated as the radial difference of the lower and the upper flange diameter, as illustrated in Eq. 5-1, as well as the catheter of the triangle with angle α, as illustrated in Eq.5-2).

$$x = \frac{D_{MP} - D1}{2} \qquad \text{5-1}$$

$$\sin(\alpha) = \frac{x}{L_{overlap}} \qquad \text{5-2}$$

According to this, it is possible to calculate the upper diameter of the Monopile flange D_1, as represented in Eq. 5-3.

$$D_1 = D_{MP} - 2L_{overlap} \sin \alpha \qquad \text{5-3}$$

Similar to D_1, the lower internal diameter for the Transition Piece flange (D_2) can be calculated starting from the MP-diameter, as presented in Eq. 5-4, 5-5 and 5-6.

$$x = \frac{D_{MP} - D_2}{2} \qquad \text{5-4}$$

$$\sin \alpha = \frac{x}{L_{slip}} \qquad \text{5-5}$$

$$D_2 = D_{MP} - 2L_{slip} \sin \alpha \qquad \text{5-6}$$

From the value of D_2, the upper diameter value of the Transition piece can be calculated, defining x as the horizontal radial length for the TP-flange, as described by Eq. 5-7, 5-8 and 5-9.

$$x = \frac{D_2 - D_{TP}}{2} \qquad \text{5-7}$$

$$\sin \beta = \frac{x}{L_{overlap}} \qquad \text{5-8}$$

$$D_{TP} = D2 - 2L_{overlap} \sin \beta \qquad \text{5-9}$$

From this point, the considerations taken are only for the condition where $\alpha > \beta$, for the simulations where $\alpha < \beta$ it is not possible to calculate the slip value and the contact point will be applied instead.

To calculate the slip length S_{slip}, the model presented in Figure 5-7 is used. Starting from the consideration that the length of the two flanges is the same ($L_{overlap}$), the value of slip has been considered as a portion of the entire length.
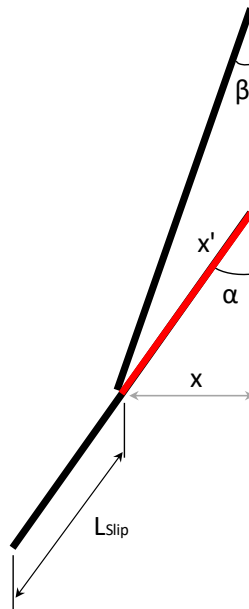
Figure 5-7: geometrical consideration to calculate Sslip

To calculate this length, it is necessary to calculate at first the portion of flange where the slip is not occurring (x') as illustrated in Eq. 5-10.

$$x' = L_{overlap} - L_{slip} \qquad \text{5-10}$$

From this consideration it is possible to calculate L_{slip}, considering x the horizontal projection of x' length, the steps illustrated in Eq.5-11,5-12,5-13 and 5-14 can be taken.

$$x = L_{overlap} \sin \beta \qquad \text{5-11}$$

$$x' = \frac{x}{\sin \alpha} \qquad \text{5-12}$$

$$x' = L_{overlap} \frac{\sin \beta}{\sin \alpha} \qquad \text{5-13}$$

$$L_{slip} = L_{overlap} \left(1 - \frac{\sin \beta}{\sin \alpha} \right) \qquad \text{5-14}$$

To design the different models developed in the next chapters, the wall thickness has been considered as well. For a generic flange with an inclination of generic angle γ (α for MP or β for TP) and thickness t, it is possible to calculate the radial difference x between the internal (d_{int}) and external (d_{ext}) diameters.

$$x = \frac{d_{ext} - d_{int}}{2} \qquad \text{5-15}$$

$$\cos \gamma = \frac{x}{t} \qquad \text{5-16}$$

From the definition of Eq. 5-15 and 5-16 it is easily possible to calculate Eq. 5-17.

$$d_{ext} = d_{int} + 2t \cos \gamma \qquad \text{5-17}$$

A summary of the main equations has been reported in Table 5-1, where the main variables of the geometry have been highlighted: D_{MP}, α and β with one more which is the X-value we consider for the $L_{overlap}$. These variables will be considered in the FEA analysis to see how the stress is affected by them.

Table 5-1 Resume of parameter used to define the slip joint geometry

Parameter	Formula	Variables	Eq.
D_1	$D_{MP} - 2L_{overlap} \sin \alpha$	α	5-3
D_2	$D_{MP} - 2L_{slip} \sin \alpha$	α	5-6
D_{TP}	$D_2 - 2L_{overlap} \sin \beta$	β	5-9
$L_{overlap}$	XD_{MP}	D_{MP}	
L_{slip}	$L_{overlap} \left(1 - \frac{\sin \beta}{\sin \alpha} \right)$	α, β	5-14

5.3.2. Load Evaluation

The DOWEC report[89] illustrated the calculation process applied in the WindMaster design. The geometrical values that have been considered are the MP- and TP-cone angle ($\alpha=\beta$), the average diameter of the slip joint d, wall thickness t and the height of contact length of the flanges h. The design loads that have been considered in the report are the gravity load F_g and the momentum M_b from the turbine.

The resultant force (F_r) that is applied on the flanges is calculated as illustrated in Eq.5-18.

$$F_r = \frac{F_g}{tan\alpha} \qquad \text{5-18}$$

If the load is considered all around the section (Eq.5-19), it is possible to calculate the tangential stress σ_t as a Hoop Stress, as calculated in Eq. 5-20.

$$P = \frac{F_r}{\pi\,d\,h} = \frac{F_g}{\pi\,d\,h\,tan\alpha} \qquad \text{5-19}$$

$$\sigma_t = P\frac{d}{2t} = \frac{F_g}{2\,h\,t\,\pi\,tan\alpha} \qquad \text{5-20}$$

As it is possible to see from Eq.5-20, the friction component has not been considered because the calculation presented can be used to maximise the load transmission, while adding the component of friction the stress should decrease, as reported in Eq.5-21 where μ represents the friction coefficient.

$$\sigma_t = \frac{F_g}{2\,h\,t\,\pi\,(tan\alpha + \mu)} \qquad \text{5-21}$$

Eq. 5-21 has been plotted in Figure 5-8, to compare the effect of the gravity load and the friction coefficient on the structure. The values used are for a length contact of 9 [m], a thickness t of 60 [mm] and a slope of 1.05 [deg], the gravity load and the stress have been considered as percentage increase. The results show how the tangential stress is affected from the friction coefficient compared to the increase of the mass applied. This result, even if purely analytical, shows an important characterization of the Slip-Joint technology that will be taken into consideration in this chapter.

For the bending stress, the original calculation method, presented in DOWEC report, assumes a linearly increasing distribution of the contact surfaces of the Slip Joint Connection. The final calculation is resumed in Eq.5-22.

$$\sigma_t = \frac{3\,M_B}{h^2 t} \qquad \text{5-22}$$

In conclusion, the total design stress is presented in Eq.5-23.

$$\sigma_t = \frac{F_g}{2\,h\,t\,\pi\,(tan\alpha + \mu)} + \frac{3\,M_B}{h^2 t} \qquad \text{5-23}$$
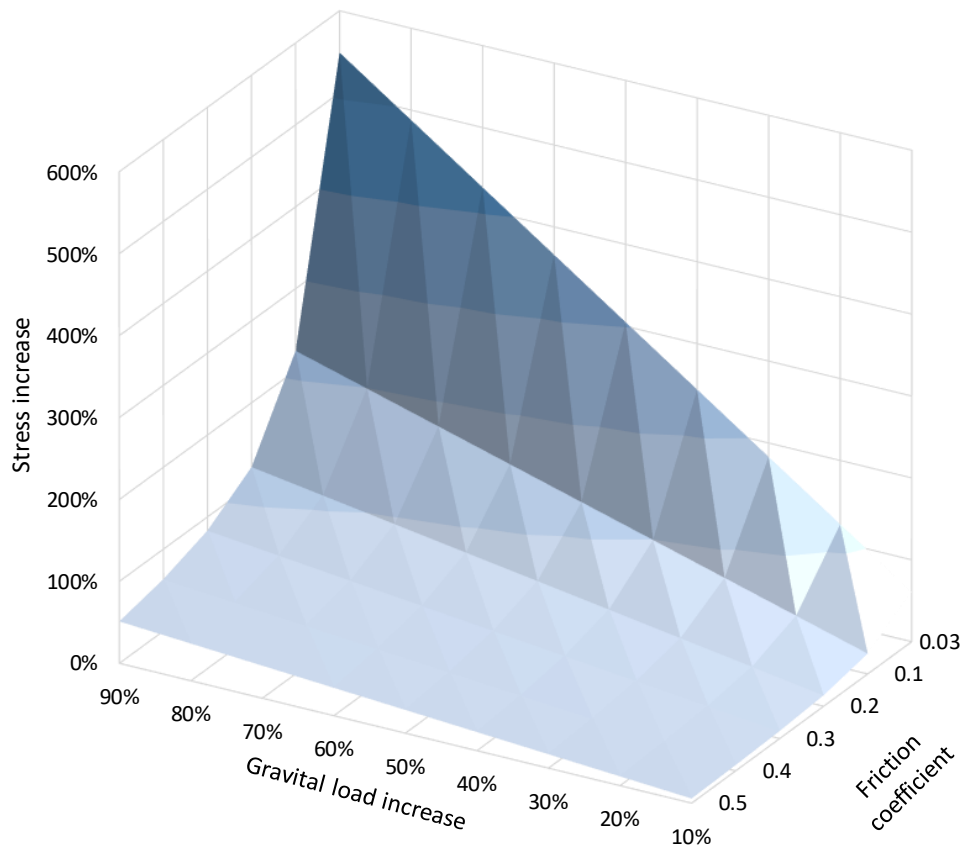
Figure 5-8: Stress incrementation in function of gravity load and friction coefficient

5.4. FEA Model

Several series of simulations have been conducted to analyse the variation of stress according to different combinations of variables. The combination presented in the next sections are:

- α angle and the overlap length variation, fixing the monopile diameter,
- Monopile diameter and the overlap length variation, fixing the angles α and β,
- α angle and the monopile diameter variation, fixing the factor X for the overlap length,
- β angle and the monopile diameter variation, fixing the factor X for the overlap length.

A mass sensitivity analysis was preliminary developed to analyse the stress increase and to decide the mass value to apply in all the simulations. Subsequently, a mass of 500±0.5 [Ton] was chosen as a uniform load. The value was applied by modifying the height of the tower of the Transition Piece.

To analyse the maximum stress distribution variation in function of the only geometrical components the friction coefficient used has been considered negligible (0.03). A stress variation in function of the friction coefficient has been subsequently presented considering two different surfaces layout: rusted-rusted steel (0.57-0.75) and coated-coated (0.14-0.42)[99].

For a clearer interpretation of the data the following identification code has been utilised to define the different combinations:

<div align="center">**SJ** – variable1 – variable2</div>

where **SJ** indicates the technology and the variable 1 and variable 2 are identified as:

- **XXX**-alfa (or beta), where the component XXX represents the angle variable multiplied by 100,
- x**AA**-overlap, where AA is the overlap multiplier multiplied by 10,
- D**Y**, where Y is the MP diameter in meter.

Results of the simulation are focused on the stress subjected form the flanges in contact, specifically studying the maximum Mises Stress and the Mises Stress along the flange.

5.4.1. Geometry and Material Proprieties

Materials considered for this simulation is S355 (Stress-Strain curve in Figure 5-9[100]) for the Monopile and Transition Piece components, the elastic proprieties of the material are resumed in Table 4-13.

<div align="center">Table 5-2 Elastic proprieties for S355</div>

Input data	S355
Elastic Young's modulus [GPa]	204
Poisson's ratio	0.3
Density (Ton/mm^3)	7.8 10^{-9}
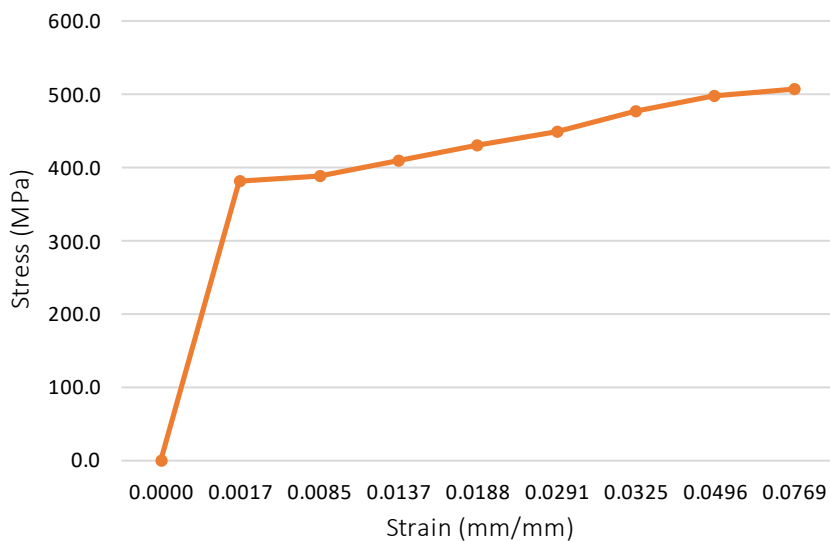
Figure 5-9: S460N Stress-Strain curves in function of sample thickness

A mesh sensitivity analysis has been developed to define the optimal mesh size (in terms of stress-results and computing time) on a general simulation with 6 [m] MP-diameter, α/β of 1.05°/1.00° and X=1.5. As illustrated in Figure 4-37, five different mesh have been developed with an element mesh type C3D8R that has been used for the MP and TP components

Table 4-14 reports the element number, the minimum size and the stress resulted along the MP-flange. As seen for the mesh #3 and #4 and #5, the stress result is similar with just 8 MPa of difference. Since a minor number of elements can be related to less computational time the mesh #3 has been chosen as final FEA model, all the main dimensions for all the other components have been reported in Table 5-3.
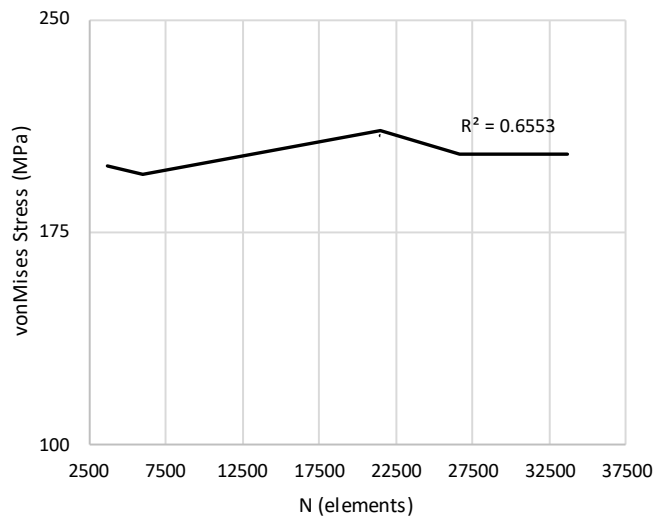
Figure 5-10: Mesh sensitivity analysis

Table 5-3: Mesh sensitivity analysis results

Mesh number	Local MP element number	Element size flange region [mm]	Maximum vonMises Stress [MPa]
#1	3690	400x200	198.7
#2	5994	250x200	195.6
#3	21505	200x100	211
#4	26600	150x150	202.7
#5	33669	200x200	202.8

5.4.2. FEA Simulations

Stress Variation in Function of Alfa and $\Delta L_{overlap}$ as Variable

In this section the interaction between the variation of the monopile flange slope with its length is analysed. The simulations developed in this section use the code SJ-XXX-alfa-xAA, in accordance with the general code previously defined. The simulations were developed using a 6[m] Monopile Diameter and the flange length was calculated with different values of X constant (1.0, 1.2, 1.5, 1.7 and 2.0), considering that 1.5 is usually the factor used in industry. A uniform mass of 500 [Tons] has been used and defined changing the TP-column height.

In Figure 5-11 the variation of the Maximum Mises Stress on Monopile and Transition Piece is plotted. As it is possible to see for alfa values higher than 1.20 [deg] the stress reaches a

plateau which is equivalent to the Yield Stress value (380 [MPa]), however the value never reaches the UTS of the material (500 [MPa]). Nonetheless, to thoroughly examine the variation of stress on the flange, relying solely on the maximum stress is insufficient. For this reason, in Figure 5-12 and Figure 5-13 same results have been plotted fixing one of the variables.

(a)   (b)
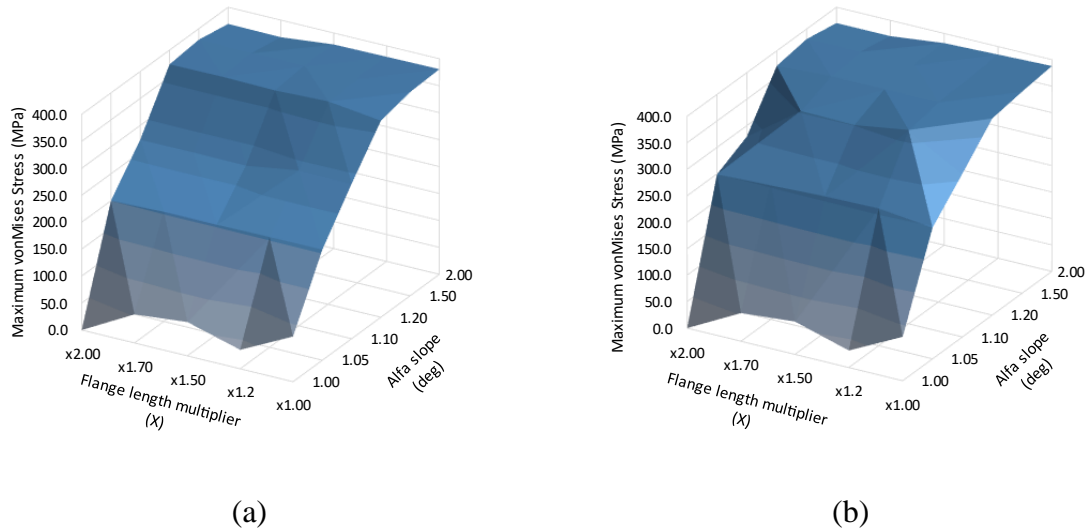
Figure 5-11: Maximum Mises Stress variation in function of Flange length multiplier (X) and Alfa angle for Monopile flange (a) and Transition Piece flange (b)

In Figure 5-12 the simulation results consider only the variation of the multiplier coefficient X. These results represent the simulation in the case where the slope angle of the Monopile is 1.05 [deg]. As it is possible to see the increase of the flange length do not change the maximum stress location. However, for longer flanges, the stress distribution is located for smaller region. These results can be affected by the contact region, where a higher value of X corresponds to a large quantity of contact area, as resumed in Table 5-4. These results show how the choice of X does not highly affect the structure, even though for the good function of the connection it is better to have a slip length available ($X \geq 1.5$). This consideration holds true from a designer's standpoint. However, increasing X produces an increase of cost of material used for a longer flange.

(a)   (b)
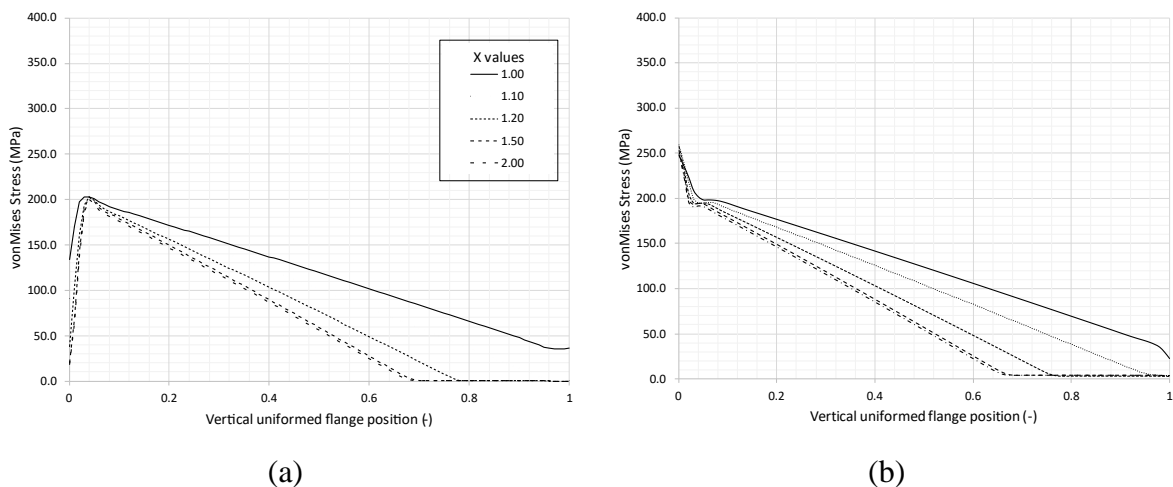
Figure 5-12: Comparison between Stress distributions for a 6[m] monopile diameter, considering fixed the slope of MP-flange and considering flange length factor (X), for the Monopile (a) and Transition-Piece flange (b)

Table 5-4 Flange length comparison for different X-values for a 6 [m] monopile diameter

X	% covered	contact length / total length
1.00	100	6.00 / 6.00
1.20	92	6.60 / 7.20
1.50	75	6.75 / 9.00
1.70	70	7.14 / 10.20
2.00	65	7.80 / 12.00

In Figure 5-13, the results of the Stress distribution along the flange have been plotted. The results have been considered by fixing the value of the slope length (X=1). As it is possible to see, where considering only the maximum stress the results for values of α higher than 1.2 [deg] reach the Yield stress, if the entire flange is considered the pick location change such as the total contact area of the flange. Meanwhile, for values of α lower than 1.2 [deg] it is possible to see a lower value of maximum stress but a higher distribution along the flange of the connection. This trend is attributed to the fact that the increase of the MP-flange slope, maintaining constant the TP-flange slope, changes the angle of incidence of the upper flange on the bottom one. This effect concentrates the load in a small region, leading to the observed outcomes.

(a)   (b)
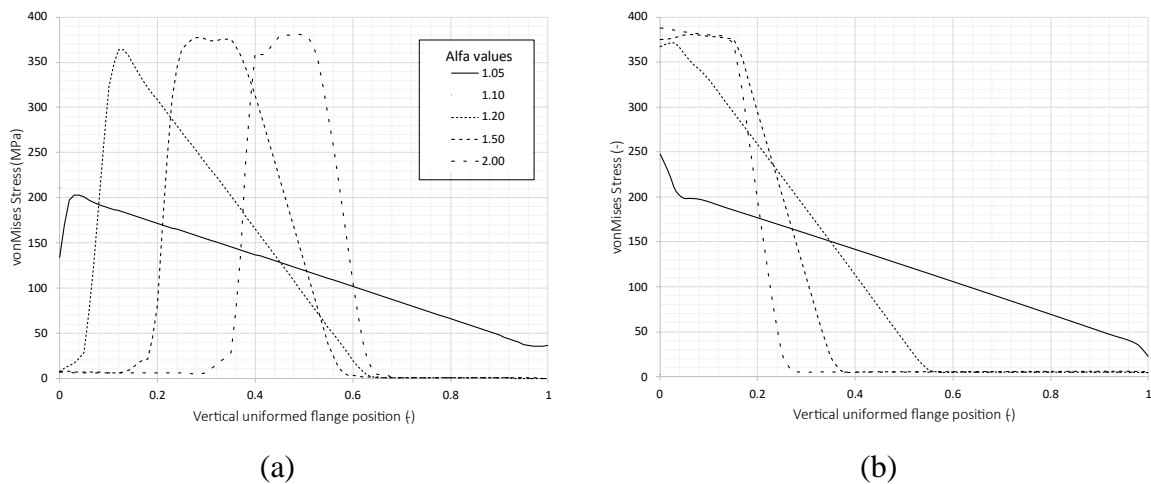
Figure 5-13: Comparison between Stress distribution, considering fixed the flange length factor (X) and considering the alfa value variable, for the Monopile (a) and Transition-Piece flange (b)

Stress Variation in Function of D_{MP} and $\Delta L_{overlap}$ as Variable

In this section the interaction between the variation of the monopile flange slope with the MP-diameter has been developed. The simulations presented use the code SJ-xAA-overlap-DY, in accordance with the general code previously defined. The simulations were developed using a slope combination α/β of 1.05/1.00 [deg], the Monopile Diameter has been considered in a range from 6 to 10 [m] and the flange length has been calculated with different X constant (1.0, 1.2, 1.5, 1.7 and 2.0). A uniform mass of 500 [Tons] has been used and defined changing the TP-column section.

In Figure 5-14 the variation of the Maximum Mises Stress on Monopile and Transition Piece flanges have been plotted. As it is possible to see, the Maximum stress value is not so affected from the flange length and from the monopile diameter, with a small variation around 200±50

125

[MPa], for this reason in Figure 5-15 and Figure 5-16 the stress variation has been plotted fixing one of the two variables.

(a)   (b)

Figure 5-14: Maximum Mises Stress variation in function of Flange length multiplier (X) and MP-diameter for Monopile flange (a) and Transition Piece flange (b)

In Figure 5-15, the Mises Stress distribution along the MP- and TP-flange have been plotted in function of the variation of the Monopile diameter (D_{MP}). As shown in the figure, the stress distribution is not heavily affected by the variation of the diameter considered, and the main variation is in terms of amplitude, where for higher dimensions a lower stress is reported.

(a)   (b)
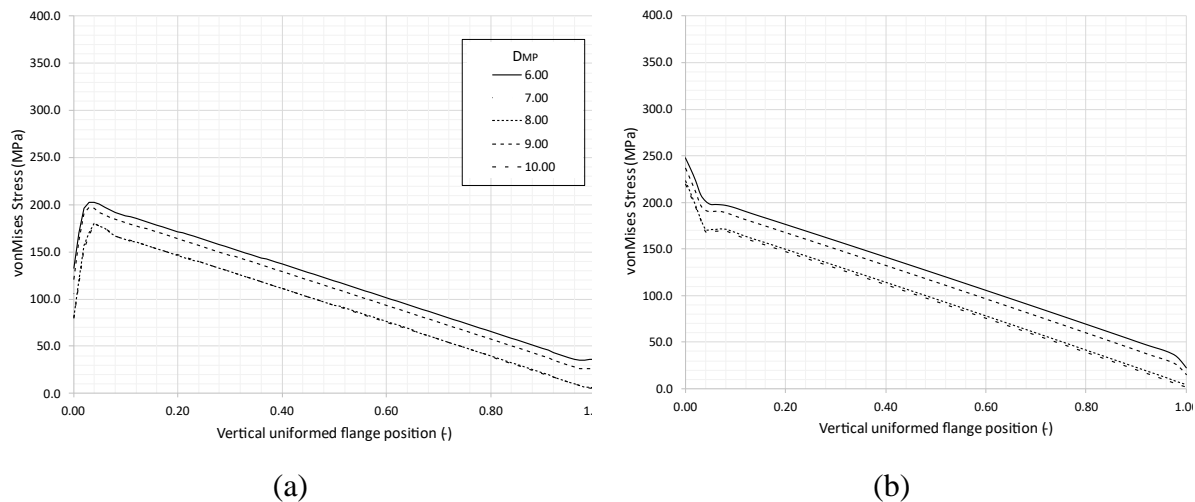
Figure 5-15: Mises stress distribution along flanges for different MP-diameter and with X constant (X=1.00) for Monopile (a) and Transition Piece contact surfaces (b)

In Figure 5-16 the Mises Stress distribution along the MP- and TP-flange have been plotted in function of the variation of the value of X. It is possible to see that, even if the Maximum stress is not affected from the flange length, the stress distribution changes significantly in accordance with the value of X. This result indicates that is necessary to consider a safety value of X, confirming the use of 1.5 as considered in industry, where the distribution is not along the entire structure and at the same time less material (compared to X=2) is used. In Table 5-5 the different value of flange length covered has been resumed.

| | (a) | (b) |

Figure 5-16: Mises stress distribution along flanges for different X-value and Monopile Diameter constant (6 m) for Monopile (a) and Transition Piece contact surfaces (b)

Table 5-5 Flange length comparison for different length factor for D_{MP} = 6 [m]

X	% covered	contact length / total length
1.00	100	6.00 / 6.00
1.20	92	6.48 / 7.20
1.50	74	6.66 / 9.00
1.70	66	6.73 / 10.20
2.00	56	6.72/ 12.00

Stress Variation in Function of Flange Slope and D_{MP} as Variable

In this section the interaction between the variation of the flange slope for the Monopile (Section 0) and Transition Piece (Section 0) and the Diameter size have been developed. The simulations have been defined in function of the parameters used with the code SJ-XXX-alfa (or beta)-DY, in accordance with the general code previously defined.

Stress Variation in Function of Alfa and D_{MP} as Variable (α > β)

The simulations were developed using a X value of 1.5 and fixing the Transition Piece flange slope (β) to 1.00 [deg], the MP diameter values have been considered in a range from 6 to 10 [m] and the MP flange slope value between 1.0 and 2.0 [deg]. A uniform mass of 500 [Tons] has been used and defined changing the TP-column section.

In Figure 5-17, the maximum Mises Stress has been reported for the developed simulations. As seen in this figure, the results show that for higher alfa values there is an increase in the Maximum stress, which is for a "cutting-effect" of the TP-flange on the MP-flange. Further considerations can be given observing how the Maximum stress increases at the increase of difference between the inclination of the flange: for smaller differences (α = 1.00-1.20 [deg]) the stress increases rapidly up to reach the Yield stress, for higher differences of inclination. This effect can be caused by a "cutting effect" by the TP-flange on the MP-flange.
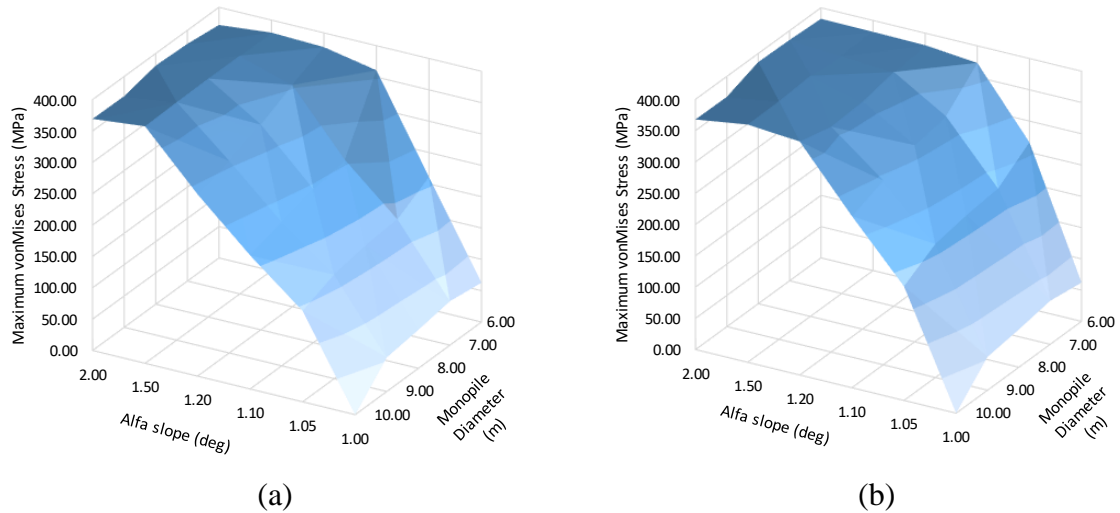
Figure 5-17: Maximum vonMises Stress variation in function of Alfa angle and Monopile Diameter for Monopile flange (a) and Transition Piece (b) flange

From the Maximum stress analysis, a secondary study focused on the Stress distribution along the flanges was conducted. Firstly, in Figure 5-18, the Stress distribution along the flanges considering the variation of the MP-flange inclination has been plotted. As it is possible to see, the distribution changes drastically in accordance with the slope considered. Starting from the equality between the α and β angle (1.00 deg), where the distribution is along the entire flange and almost constant. At the increase of the difference, the Stress distribution tends to get more concentrated in a smaller region, where for the MP-flange the stress gets focused in the centre of the flange, for the TP-flange the Stress gets focused at the lower part.
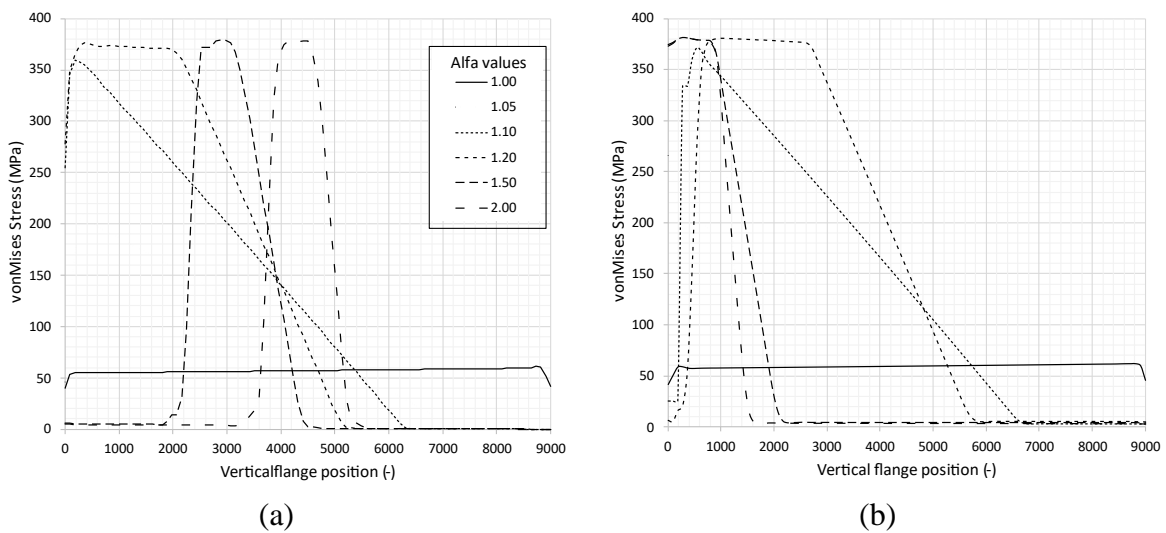
Figure 5-18: vonMises stress distribution along flanges for different α-slope and Monopile Diameter constant (6m) for Monopile (a) and Transition Piece contact surfaces (b)

Secondly, the Stress distribution along the flanges for different Monopile diameter has been plotted in Figure 5-19. As evident from the figure, the primary observation from the graph is that as MP diameter increases, the Maximum stress decreases while the relative contact area increases. The Stress variation results can be considered affected from the increase of diameter and the increase of a relative contact area. In the first scenario, an increase in the contact area,

128

given an equal applied mass, leads toa reduction of stress; while in the second case, the increase in real contact are results in a decrease in average stress.   (Table 5-6).

(a)   (b)
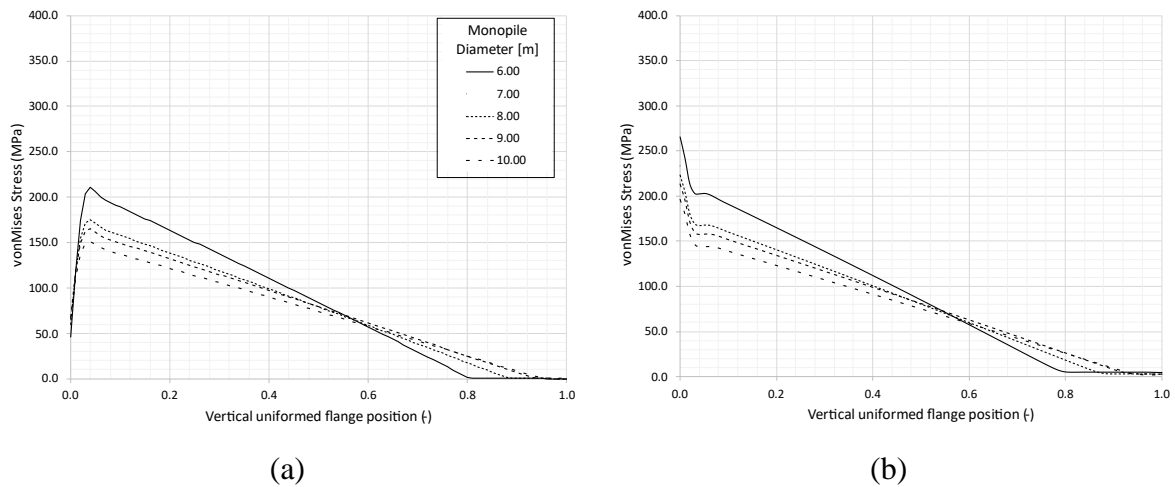
Figure 5-19: vonMises stress distribution along flanges for different Monopile diameter and α-slope constant (1.05deg) for Monopile (a) and Transition Piece contact surfaces (b)

Table 5-6 Flange length comparison for different Monopile diameter for α=1.05 [deg]

D_{MP}	% covered	contact length / total length
6.00	77	6.93 / 9.00
7.00	78	8.19 / 10.50
8.00	84	10.08 / 12.00
9.00	88	11.88 / 13.50
10.00	89	13.35 / 15.00

Stress Variation in Function of Beta and D_{MP} as Variable (β > α)

The simulations have been developed using a *X* value of 1.5 and fixing the Monopile flange slope (α) to 1.00 [deg], the MP diameter values have been considered in a range from 6 to 10 [m] and the TP flange slope value of 1.00, 1.05 and 1.10 [deg]. A uniform mass of 500 [Tons] has been used and defined changing the TP-column section.

In Figure 5-20, the maximum vonMises Stress has been reported for the developed simulations. As seen in this figure, the results show that, similarly to results presented in Section 0 for *α* variations, for higher values of *β* there is an increase in the Maximum stress caused by a reduction of initial contact area from the MP-flange on the TP-flange. Further consideration can be given, similarly to the α variation, observing how the Maximum stress increases at the increase of the difference between the inclination of the flange; for smaller differences (β = 1.00-1.05 [deg]) the stress increases rapidly up to reach the Yield stress, for higher differences of inclination.
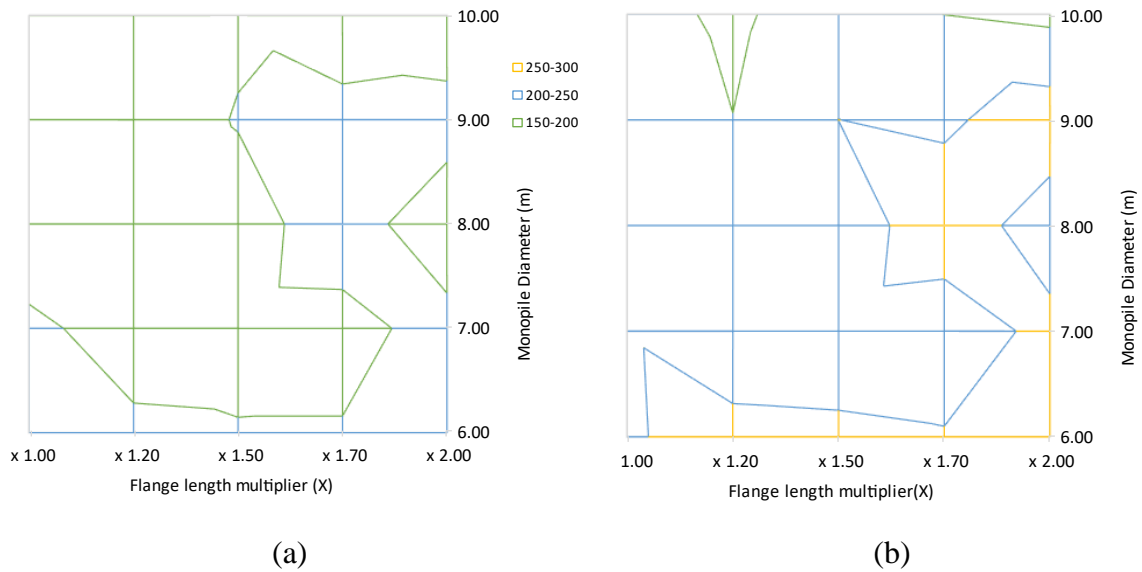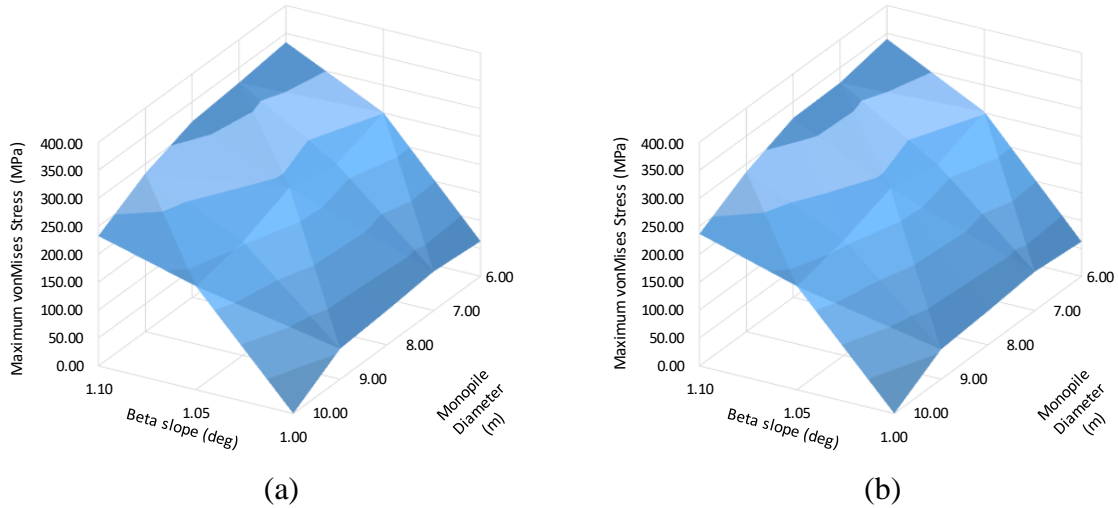
Figure 5-20: Maximum Mises Stress variation in function of Beta angle and Monopile Diameter for Monopile flange (a) and Transition Piece flange (b)

In Figure 5-21 the Stress distribution along the MP- and TP-flanges have been plotted comparing different β-slope, the values of α (1.00 deg) and of the Monopile diameter (6m) have been fixed. As it is possible to see an increase of the slope from the TP-flange is directly connected to an increase of stress along the flange and leads to to a decrease of contact area. However, an increase of difference between alfa and beta (with $\beta>\alpha$) leads to a stress concentrated around the Transition Piece upper diameter, causing a deformation of the tower itself, as illustrated in Figure 5-22.
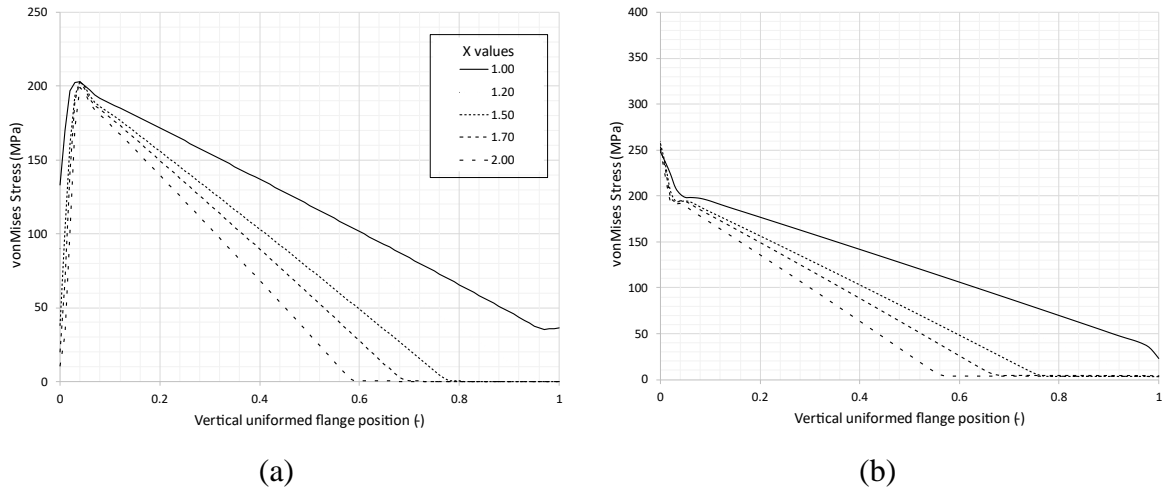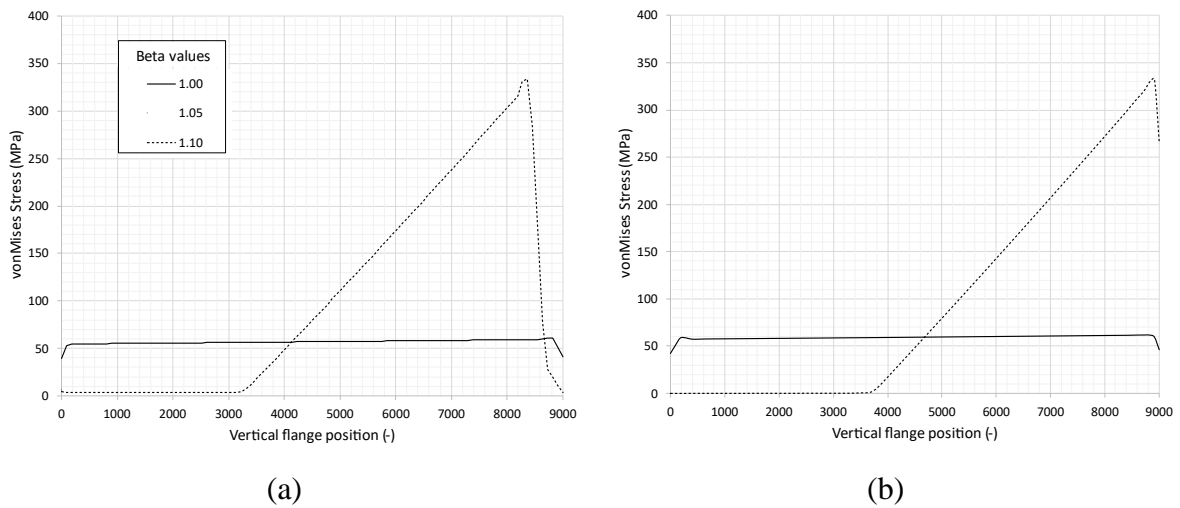

Figure 5-21: Mises stress distribution along flanges for different β-slope and Monopile Diameter constant (6 m) for Monopile and (a) Transition Piece contact surfaces (b)

130
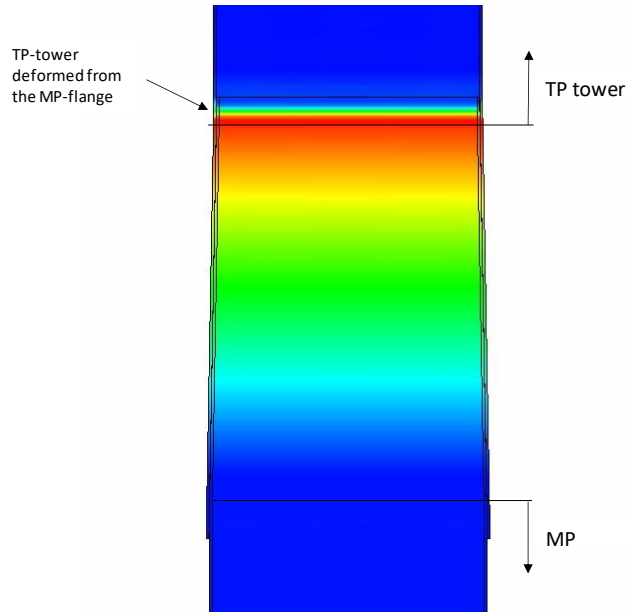
Figure 5-22: Stress distribution for SJ connection with β>α, highlighting the flange position and the beginning of the cylindrical parts for MP and TP

In Figure 5-23, the Stress distribution along the flanges for different Monopile diameter has been plotted. As it is evident, comparing the variation in function of the diameter, the increase of MP size creates a decrease of the Maximum stress and the relative contact area. Similarly, to the results presented in section 0 for $\alpha>\beta$, the percentage of contact for the flange length has been reported in Table 5-7. It is possible to observe that for $\beta>\alpha$ the contact surfaces are almost halved, even if the stress has similar magnitude. This evaluation shows that even if the composition of the slope angles can be evaluated for $\beta>\alpha$, the safest condition should be $\alpha>\beta$.

(a)   (b)
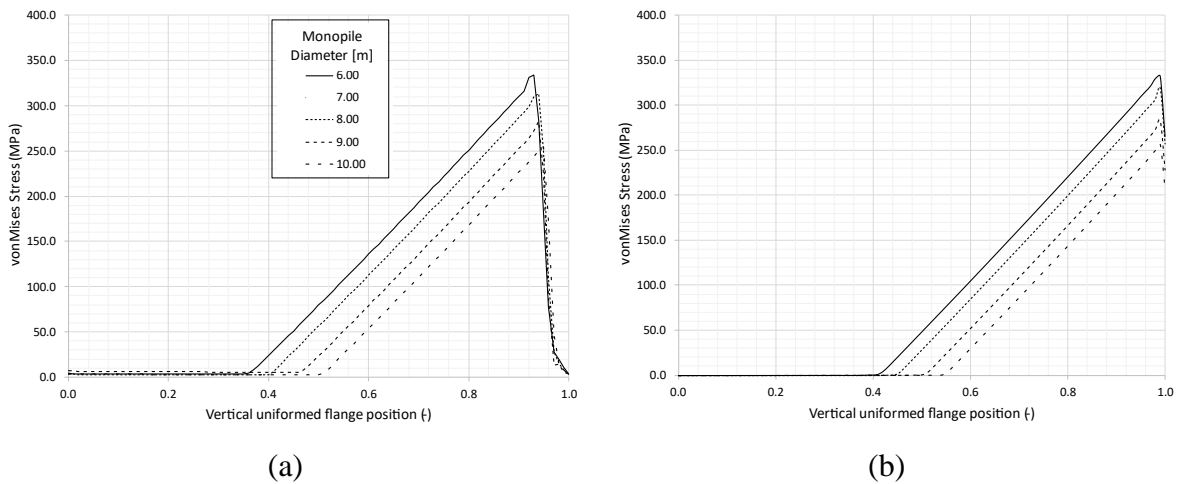
Figure 5-23: Mises stress distribution along flanges for different Monopile Diameter and α/β-slope constant (1.00/1.10 deg) for Monopile (a) and Transition Piece contact surfaces (b)

131

Table 5-7 Flange length comparison for different Monopile diameter for β =1.10 [deg]

D_{MP}	% covered	contact length / total length
6.00	37	3.33 / 9.00
7.00	41	4.30 / 10.50
8.00	42	5.04 / 12.00
9.00	48	6.26 / 13.50
10.00	52	7.8 / 15.00

5.4.3. FEA study of Mass and Friction Factor

Mass Sensitivity Analysis

A mass sensitivity analysis has been developed to analyse how the maximum Mises Stress is affected from the increase of mass on the flanges. The dimension employed in the considered simulations have been summarised in Table 5-8. The mass has been applied by modifying the tower length, and the increase has been calculated as percentage increase of mass starting from the mass calculated for 15 [m], details have been reported in Table 5-9.

The results have been analysed by taking into consideration the maximum stress value and the stress distribution on the Monopile and the Transition Piece flange. In Figure 5-24, the values of maximum vonMises stress detected on the MP- and TP-flange have been plotted. As expected, the stress value on both flanges increases at the increase of the Mass. The stress value appears to exhibit a linear increase up to reach a value close to the Yield Stress of the material, where it starts to follow a more horizontal trend. These results follow the path described by the increase of stress caused by the mass increase, described in Figure 5-8, following a linear increase.

Table 5-8 Resume of main values used for Mass Sensitivity Analysis

Dimension	
D_{MP}	6 [m]
α/β	1.05/1.00 [deg]
X	1.5

Table 5-9 Mass variation in function of TP tower heigh

Height [m]	Mass [Tons]	Percentage increase
15	232	+0%
29	350	+50%
42	462	+100%
56	580	+150%
70	696	+200%
83.5	812	+250%
112	1044	+350%
152	1392	+500%
289	2552	+1000%

The Stress distribution corresponding to the applied mass have been plotted in Figure 5-25. As it is possible to observe, the stress value increases up to reach the elastic-plastic region, where it starts to propagate along the flange at the increase of the mass, meanwhile with the increase of applied Mass an increase of contact area corresponds accordingly. In Figure 5-26the graphical results from the Final Element Analysis have been reported for the 230 [Tons] and 2550 [Tons] cases. In these results the blue section represents the region where the stress is lower and there is no contact, while the red regions represent where the stress is higher and there is plasticity. The colours from green to orange represent the gradual increase of the stress with the profile already presented in Figure 5-25.
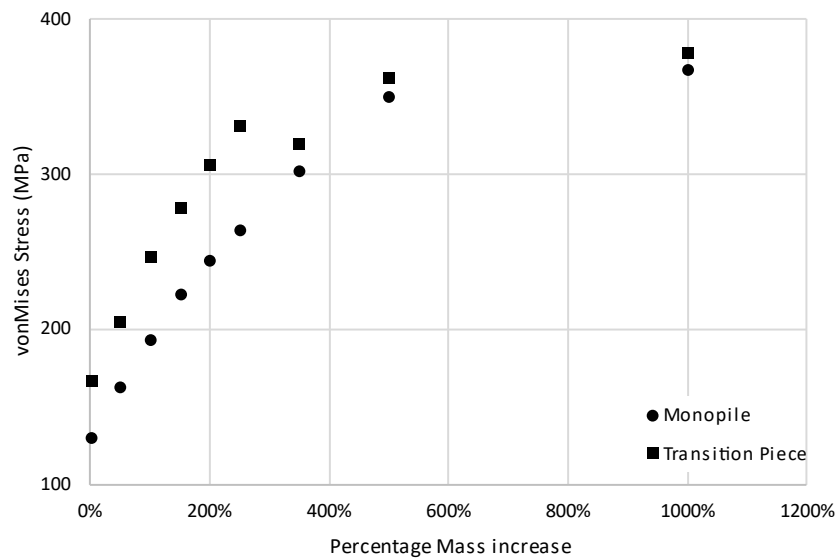
Figure 5-24 Mass sensitivity results: Maximum Mises Stress

(a)   (b)
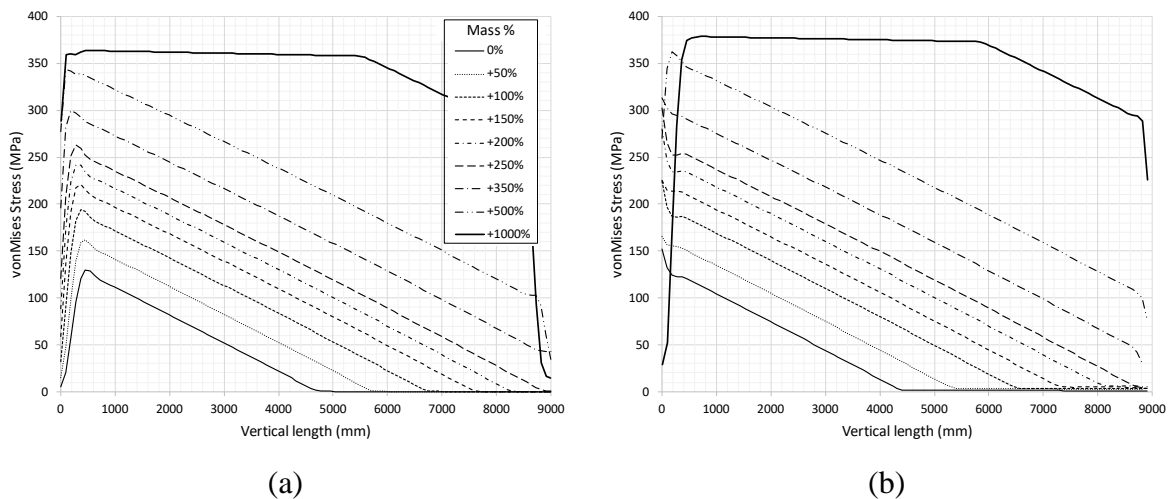
Figure 5-25: Mass sensitivity results: Stress distribution along flange for Monopile (a) and Transition piece (b)

133
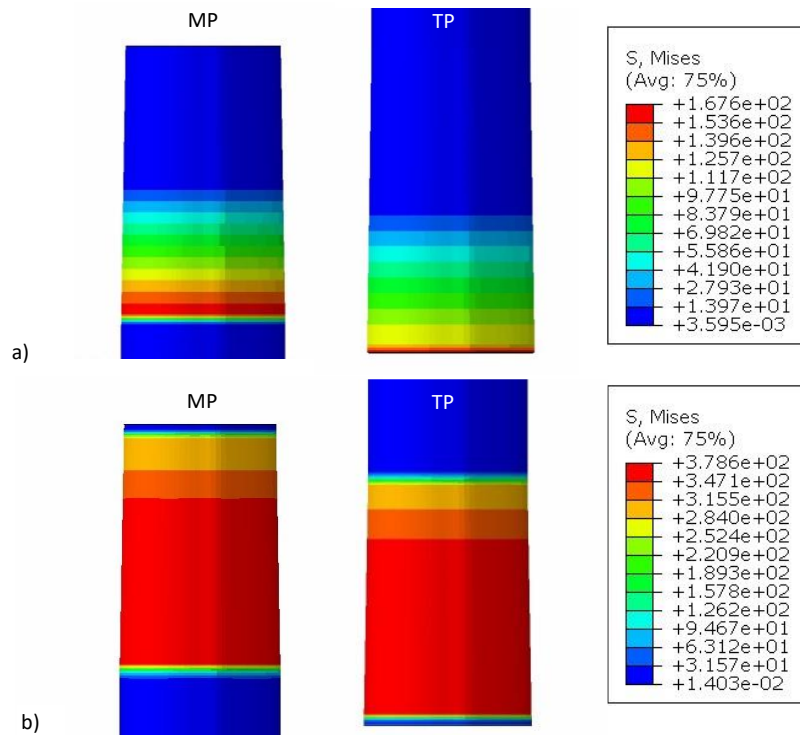
Figure 5-26: Results on MP and TP flanges for a) 230 [Tons] and b) 2550 [Tons]

Stress Variation in Function of Friction Coefficient

A friction coefficient analysis has been developed using as friction factors the values presented in literature for slip contact between coated steel surfaces (0.14-0.42) and rusted steel contact (0.57-0.75) [99]. These simulations have been developed to see how the stress distribution changes in function of the surface conditions. To compare the results with the previous simulations the model SJ-105-alfa-D6 has been used. The maximum stress and Stress distribution along the axial direction have been plotted in Figure 5-27 and Figure 5-28.

As illustrated in Figure 5-27, the maximum stress has been plotted. As illustrated, it is possible to see that an increase of dynamic coefficient of friction a decrease of stress is registered. Comparing the results for 0.03 with the others, it is possible to register a drop of maximum stress around 48 up to 72% for the coated-coated steel interaction and up to 75-82% for the rusted interaction. Similar results have been discussed Figure 5-8, where in accordance with Equation 5-23, at the increase of friction coefficient a decrease of stress is expected.
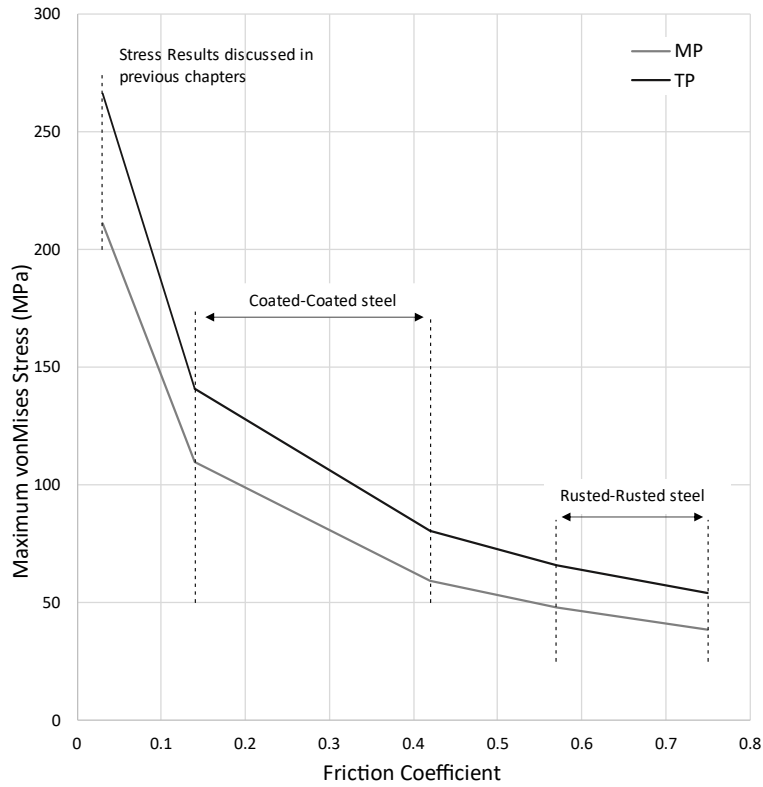
Figure 5-27 Maximum Mises Stress variation in function of friction coefficient for a 6 [m] Mono-Pile diameter, α=1.05 [deg], β=1.00 [deg], X=1.5

Subsequently, the stress distribution along the flange for the different friction factors have been plotted in Figure 5-28, dividing the results for monopile (a) and Transition-Piece (b) flanges. The results have been plotted showing on vertical axis the Mises Stress and on horizontal axis the flange length starting from the bottom of both surfaces. Similar results of those reported in Figure 5-27 can be taken. The increase of friction factor gives as result a drop of the maximum stress, but simultaneously at a reduction of the contact area.

(a)   (b)
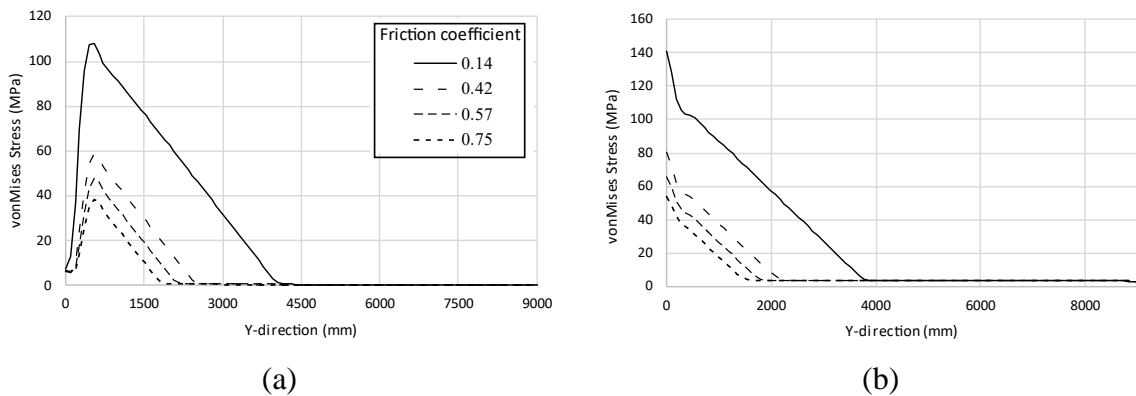
Figure 5-28: Mises stress distribution along flanges for different friction coefficient along the axial direction (Y-direction) for Monopile(a) and Transition Piece contact surfaces (b)

5.5. Further FEA Analyses

In this section more advanced simulations have been developed to fit more realistic cases. In the first sub-section, the study of stress distribution and maximum stress in function of the presence of a manufacturing imperfection and, in the second, a study on the connection have been developed and discussed under bending effect.

5.5.1. Stress Variation in Case of Manufacturing Error

Two models have been developed to simulate the presence of shape deformation. The first case has been designed with one defection, while the second with two identical on diametrical opposite locations, as shown in Figure 5-29. These bunch of simulations has two main goals:

- To study the stress distribution changing compared to the perfect conical shape.
- To verify whether premature structural failure occurs in the case of non-uniform load distribution.

(a)   (b)
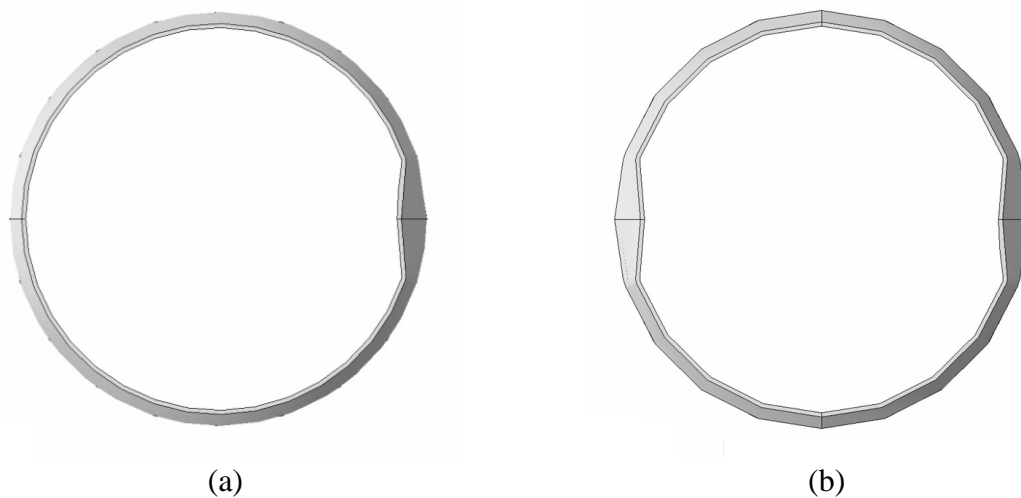
Figure 5-29 Shape deformation top view for a) single and b) double conical defection

To develop the simulations, the same model used for the SJ-105-alfa-D6 has been chosen. The main dimensions have been reported in Table 5-10. A friction coefficient of 0.3 was used to consider a real case design. The results have been reported in Figure 5-30, where the results of the two simulations with the single and double imperfection have been compared with a simulation without any imperfection.

Table 5-10 Main MP-TP dimension used for single and double manufacturing error simulation

Dimension	Value
α	1.05 [deg]
β	1.00 [deg]
X	1.5
D_{MP}	6 [m]
Mass on TP	500 [Tons]
Thickness t	60 [mm]

Figure 5-30 represents the stress distribution along two sections (above and below) and the Slip Joint connection, for three cases: without imperfection, single and double imperfection. The graphs illustrate the Axial (S22) and Mises Stress along the circumference comparing them with their distribution. As observed from the simulation without imperfections, the distribution should remain constant, with the axial stress consistently in compression and the Mises Stress with positive value.

Imperfections are present as single imperfections at 0° (or 360°), and as double imperfections localized at 0° (or 360°) and at 180°. As it is possible to see at these locations the stress distribution presents big variations compared to the simulation without imperfections and a similarity of distribution can be found where the stress around the imperfection has a "three peaks" distribution, covering the same angular space around 90°. In conclusion, this study highlights that variations in the conical section can deeply affect the stress distribution of the connection, creating regions of high stress.
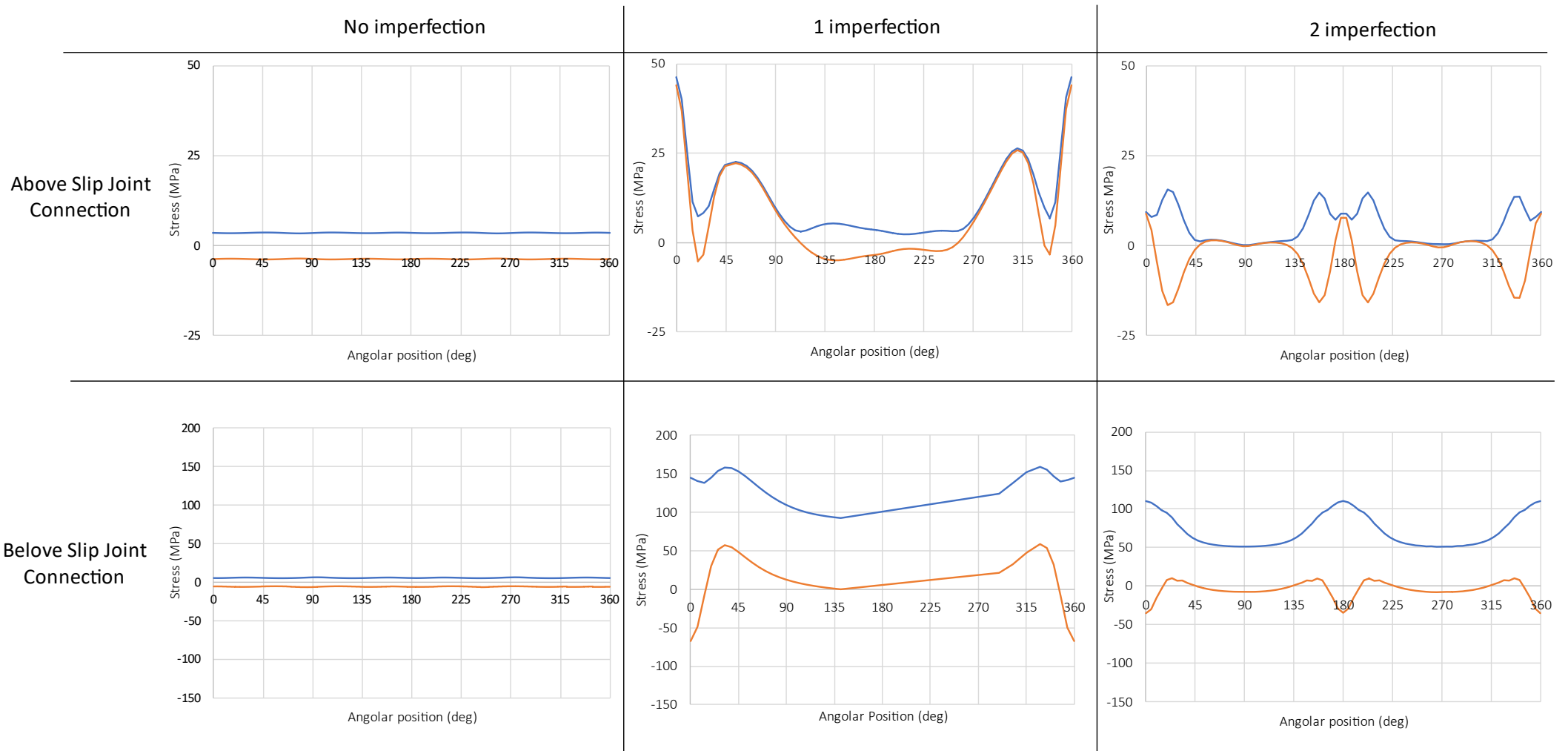
Figure 5-30: Stress distribution scheme for tower without, with one and two imperfections in function of the angular position, divided for above or belove the Slip Joint connection, results plotted as vonMises stress (blue line) and axial stress (orange line)

5.5.2. Distribution Under Bending Load

In this section a case with horizontal load, which simulates the drag effect of the wind on the blades, has been developed. As case study, the SJ-x15-overlap-D6 has been considered with a friction coefficient of 0.3 (average value for the coated-coated surfaces). The simulation has been divided in two main steps: a first step where force applied is coming from the gravity and a second one where the horizontal load is applied, the results will be compared to a second simulation where a simple tower has been tested under same conditions.

To compare the stress distribution along a tower with slip joint connection and one without slip joint connection, it is necessary to apply some geometrical considerations about the diameters used. For the SJ-x15-overlap-D6 the two external diameters are 6 and 5.8[m] for MP and TP, for this reason the average of the two diameters (5.90[m]) has been considered for the tower without connection part. For the different sectional area has been decided that the pressure load from wind presented in Chapter 2 will not be considered.

FEA analysis has been developed into two main simulation steps, as represented in Figure 5-31:

- Step 1: in this step, similarly to previous bunch of simulations, gravity has been applied.,
- Step 2: the wind load is applied slowly for the first time-step from 0 up to the maximum amplitude, from the beginning of the second time-step the load is maintained at its maximum up to the end of the simulation.
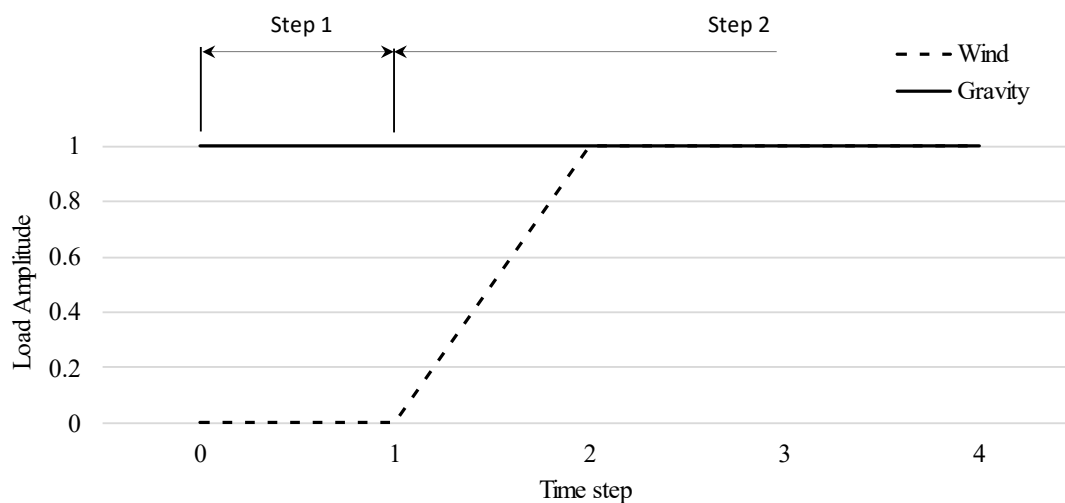
Figure 5-31: FEA time step used to simulate gravity and wind force

The results have been reported comparing how the stress changes around the circumference for the two sections: at 9[m] and 20[m] from the ground. Accordingly, it will be possible to study how the presence of Slip Joint connection can affect the stress distribution along the tower. In Figure 5-33, the stress distribution along the circumference have been plotted for the two sections as Mises Stress and as Stress in axial direction results, indicating on x-axis the angular position as illustrated in Figure 5-32. Meanwhile in Figure 5-34, the stress distribution for a simple tower has been plotted under the same considerations used for the SJ-connection simulation.
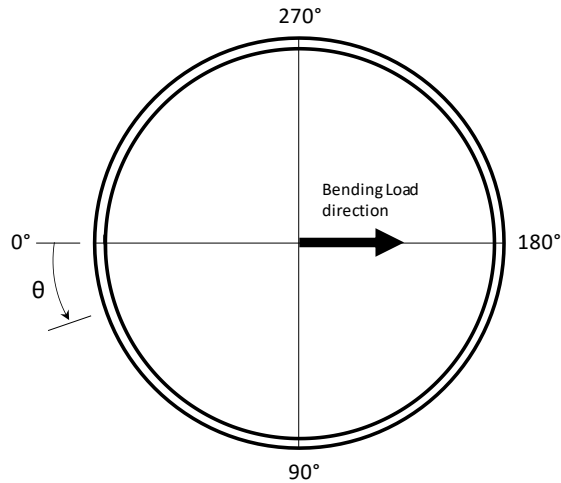
Figure 5-32: Angular position definition for bending test results

Considering Figure 5-33, it is possible to observe the stress distribution along the circumference at 9 and 20 [m] is similar. However, it is possible to detect some differences in terms of stress magnitude. The increase of magnitude between the upper section and the bottom one can be attributed to the increase of load coming from the increase of mass. It is possible to see an increase in terms of propagation for the maximum peak area, at 20 [m] the coverage of the maximum stress from peak to peak is around 75 [deg], while for the lower section the circumferential angle between the peaks is around 115 [deg].

(a)   (b)
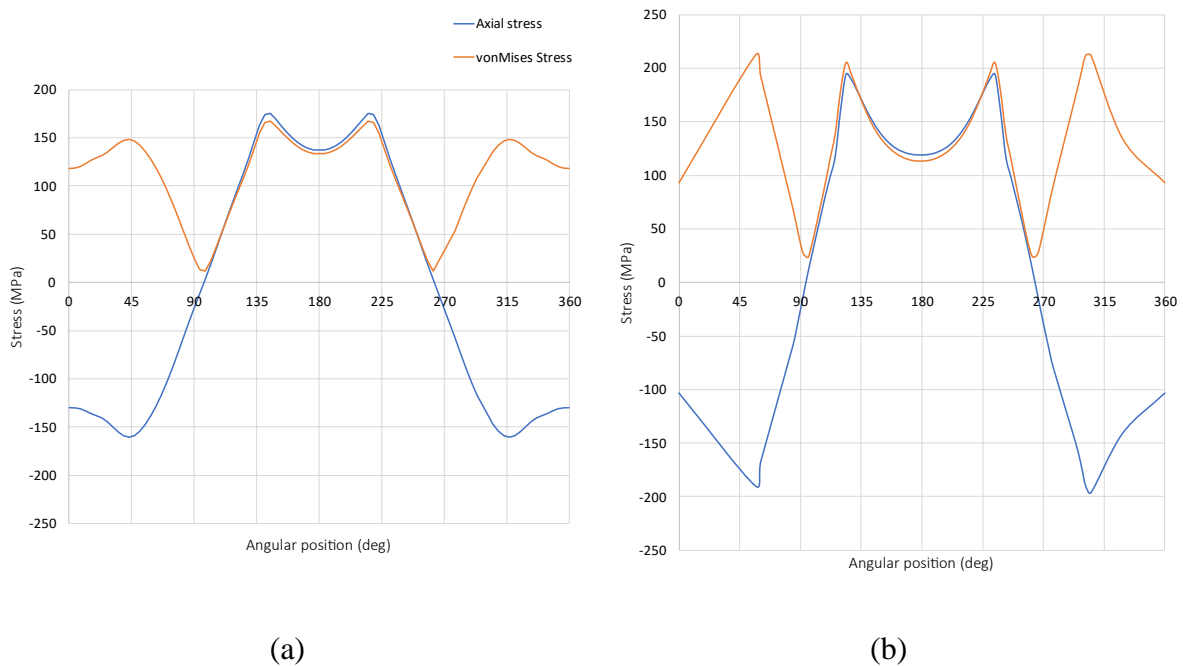
Figure 5-33: Stress distribution along the circumference for SJ-connection at 20 [m] (a) and 9[m] (b) from the ground level

The results discussed for Figure 5-33 and the results obtained from the simulation developed for the tower under bending action (Figure 5-34) are compared with each other. Analysing the results for the 20 [m] section, it is possible to see that the distribution has some differences: where for the SJ-connection results, a double peak is located, only a main maximum stress has

140

been found. Considering the section at 9 [m] from the ground level, a similar distribution can be seen for both simulations, giving two peaks as maximum stress. This comparison indicates how the Slip-Joint can cause some local stress increment in case of high bending load. To understand if this could pose a structural problem, a study along the flanges has been developed and discussed above.

(a)   (b)
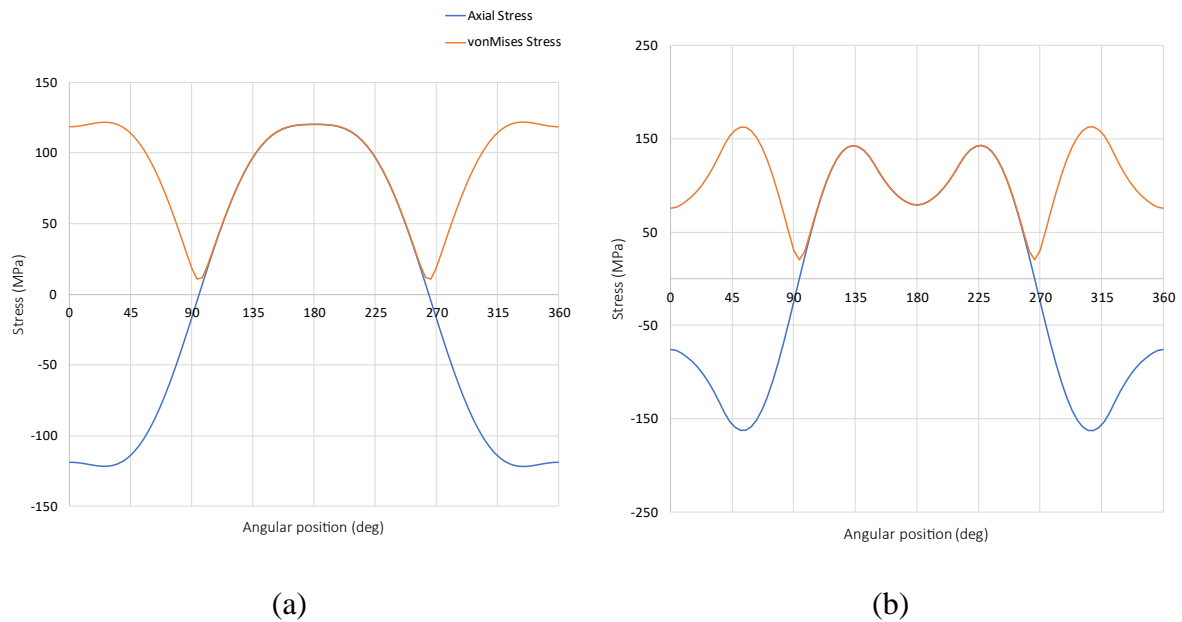
Figure 5-34: Stress distribution along the circumference for general tower at 20 [m] (a) and 9[m] (b) from the ground level

In Figure 5-35 the stress distribution along the MP-flange has been plotted. The results presented are for the two coordinates that can be considered critical: at 0 [deg] (A-A) and at 180 [deg] (B-B). These coordinates have been taken into consideration for the bending nature, where along the A-A should be located the higher tension and along B-B the higher circumferential compression. As expected, the stress distribution follows two opposite trends, at the bottom section, the stress is higher for B-B, where the bending moment is directed, while A-A has a higher load at the upper section. Comparing the two distributions, two secondary results can be evaluated. Firstly, it is possible to see that a small component of stress coming from the gravity is still present, it is visible from a small pick at the lower section for each stress distribution. Secondly, all stresses are higher than 0 [MPa], this can be translated into a continue contact between the surfaces, avoiding any dislocation of the structure.

141
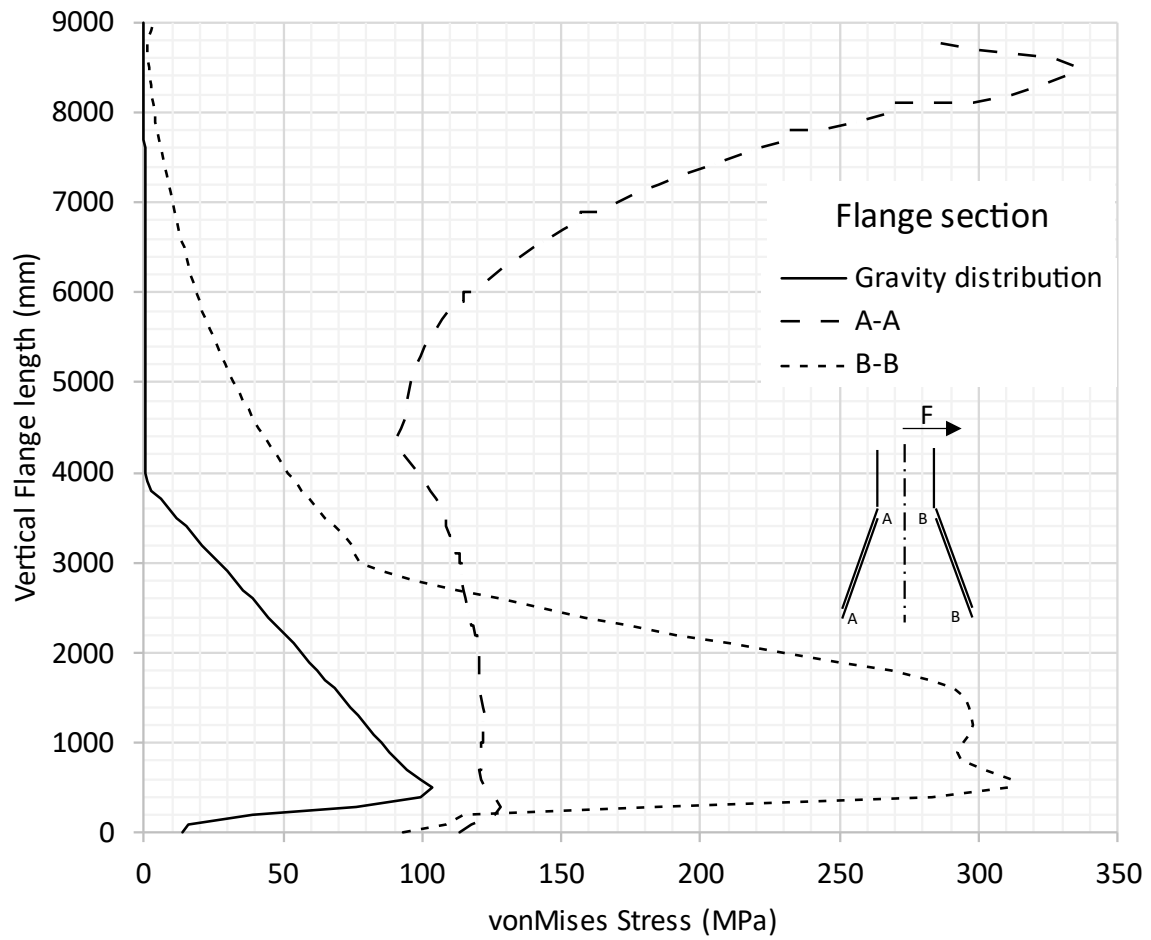
Figure 5-35: Stress distribution along SJ-connection MP flange under bending in comparison with distribution by gravity

5.6. Summary

As this chapter presented, in accordance with results coming from FEA analysis, the results can be divided in two categories: the study of impacts of the different geometry factors and on the maximum magnitude and the distribution of stress along the connection flanges. Additionally, a study has been conducted to analyse imperfections on the flanges and the bending load can affect the structure.

Results from the FEA study of stress variation in function of geometrical and component propriety (Section 5.4.2 and 0) highlighted the following results:

- The variation of the Monopile diameter (D_{MP}) does not affect the maximum stress and stress distribution for the Slip Joint Connection,
- The *X* component for the length of the flange does not affect the maximum stress, however small variation in terms of stress distribution can be detected,
- Even a small variation between the MP- and TP-flange slope (α/β) can heavily affect the maximum stress and the stress distribution along the flanges.
- A mass increase affects the maximum stress and the distribution along the flange; however, the study shows how at the increase of mass a stress plateau is reached.
- The friction coefficient between the contact surfaces has a high impact in terms of stress distribution and magnitude of maximum stress. An inverse relationship is observed, highlighting how, at the increase of friction coefficient, a reduction of stress is detected.

Results from the second part of FEA study (Section 5.5) highlighted the following points:

- The presence of an imperfection increases the stress along the imperfection edges.
- Under bending load, the stress distribution is in function of the section considered, however any loss of contact has been detected, indicating a good resistance under this load.

In conclusion, the MP-TP connection design presented in this chapter has proven to be a valid and promising solution for the threaded connection.

Chapter 6 Discussion, Conclusions and Future work

6.1. Overall Discussion

The main MP-TP technology which is currently used in Offshore Wind turbines (i.e. threaded connection) and the two most promising competitors (C1 connection and Slip Joint connection) have been presented and discussed in this thesis. Threaded connection technology found its application at the beginning of 2010s, when the previous technology (grouted connection) presented different structural issues. It comprises two L-flanges that are securely connected by a threaded fastener. The current State-of-the-Art for the MP-TP connection technology requires threaded connection with M72 bolt. However, meet the growing energy demand, the overall dimension of the structures of wind turbines need to increase. For this reason, to accomplish the structural increase strength requirement, technology can either opt to increase the number of bolts around the circumference or to enlarge the bolt size. However, both results present challenges. For this reason, different layout has been designed to replace the threaded connection. C1 Connection is the first possible competitor to the bolted connection, the technology layout has been designed by C1 Connection in the Netherlands. The technology is based on a special fastener that, by using wedge slopes, applies a high vertical load with minimal horizontal load. The technology moves from the L-flange design to a series of elongated holes that will be accommodated around the circumference of the geometry allowing the positioning of the fastener. Another possible substitute is the Slip Joint connection developed by Van Oord in the Netherlands. This technology is based on a "two cup" design, where a conical flange is welded to the upper part of the Monopile and another to the lower of the transition piece. The connection works through the contact and friction forces between the flanges comes from the load variation from the operational wind turbine and the structural weight itself.

The aim of this thesis was to provide a better view on the State-of-the-Art technology and the two most promising technology for the MP-TP connection. This was achieved by evaluating the Pros and Cons of each technology through   literature review, using of FEA modelling and through large-scale test.

In 0, this thesis delineates the State-of-Art for the MP-TP connection. The exposition involves a deep examination, comparing the S-N curves derived from three principal standards (BS, Eurocode3, and DNVGL) with the empirical data extracted from the literature review and a series of fatigue test run on M72 bolts. Additionally, a mean stress correction methodology, with the Goodman approach, is introduced. The results of fatigue curves bring to light appreciable inaccuracies, particularly in the context of diverse bolt sizes (M36, M46, M64, and M72) and different heat treatment procedures. Consequently, an important consideration emerges about the re-evaluation of specific parameters in the construction of fatigue curves, including thickness correction, intercept value, and curve slope. However, the predictions appear to be much more accurate when all the data-cloud from literature review is considered without accounting for size and treatment conditions. Additionally, a Mean Stress correction approach, to predict the lifespan under fatigue of a preloaded bolt, has been proposed. This concept has been utilised in this thesis on seven samples tested to fatigue with two different

preloads, demonstrating its potential utility. All these results on threaded connection provide valuable insights for the design of this connection technology.

The results available in presented literature, when combined with the test results presented for the M72 bolts, constitute a statistically significant population to analyse the S-N curves. However, it is essential to note that the dataset made of the seven data points of the fatigue test may not be suitable for the mean stress correction approach. As illustrated in Section 3.8, the composition of the two groups, comprising 5 and 2 samples respectively, limits the scope to predicting statistical analyses only. Consequently, this analysis focuses solely on the approach itself rather than on the specific results due to the limited sample size.

In Chapter 4, this thesis presented the first competitor of the future of MP-TP connection. As is well-known, the presence of imperfections in a wall, such as holes, can be a cause of failure in the structure due to increased stress at localized spots. However, in literature different analytical equations have been presented to be able to calculate the SCF along the edges of single hole or for series of holes. As presented, the stress concentration along the edge is affected by the hole shape and the distance between them. This understanding was supported by the FEA simulations that helped to settle a preliminary knowledge of the technology. From this, it has been possible to design a real case scenario, designing a section of the connection, simulating the interaction between the Monopile flange, the "fork" Transition piece flange and the fastener with the application of different loading-step. Through the FEA simulation, it has been subsequently possible to develop and produce a large-scale sample to study the fatigue life experienced by the sample and to see any possible malfunction of the technology. Results showed a longer fatigue life compared to what is expected according to standards. However, only one fatigue test was conducted, making it impossible to perform a statistical analysis to effectively compare the results presented with the S-N curves from codes.

Chapter 5 introduces the final contender in the advancement of MP-TP connection technology, recognized for its straightforward design among the three technologies: the Slip-Joint connection by Van Oord. Despite the apparent simplicity of the Slip-joint's "two cups" concept, in-depth analytical and Finite Element Analysis (FEA) have revealed that the design process demands a deeper examination and optimization of geometric parameters and surface friction. The main studied parameter through FEA modelling have been length of flange in proportion with the monopile diameter, the diameter itself, the flanges-slope (α/β) of the MP and TP and the friction coefficient between them, showing that only the last two parameters have a substantial impact in the maximum stress magnitude and the stress distribution along flanges. The geometrical aspect study has been implemented with an advanced study of stress distribution where the flanges are not perfectly conical as well as a final simulation has tested the connection technology under bending stress from the wind action on the tower. Results showed the necessity of an extensive design process and the need to find a manufacturer capable of working within specific tolerances. The results presented offer only a partial glimpse into the simulations required for a comprehensive understanding of the technology. No studies in the long-term time domain have been conducted, and the influence of the initial velocity of the Transition Piece on the Monopile has not been considered.

Conducting a final comparison between the technologies involves comparing different factors that are not directly connected to the design process presented, important though in the post-design process. These factors encompass macro-groups such as costs, production management

145

and existing literature. Apersonal opinion-based comparison has been conducted. For the Cost category the following voices have been considered:

- Material cost: this prospective takes into account the raw volume of materials utilised to create the entire connection, considering fasteners and flanges. It also includes the material that need to be removed by eventual manufacturing processes.
- Manufacturing cost: this voice takes in consideration the process essential for the technology, starting from the rolling of the flanges to the eventual manufacture of holes and the required precision for the correct work of the connection.
- Assembly cost: in this category has been considered all the process that provides the installation of a single tower, starting from the moment the vessel departs the harbour until its return, plus the costs coming from the technician to install and secure the fasteners.
- Maintenance cost: this prospective takes into account all the expenses necessary to ensure the proper function of the connection technology.

Meanwhile, management consideration pertains to the supply chain, and addresses the main question of *"how many companies can produce the connection technology?"*. On the other hand, for the literature, the extent of fundamental research is considered, defined as how many papers and research are available for analysis.

Starting with the Cost category, when considering Material Cost, it becomes obvious that the three technologies have distinct requirements in terms of material volume. Both Threaded connection and C1 Wedge connection design necessitate a comparable amount of material for creating the two flanges that will be welded to the Monopile and Transition Piece, in detail for the second design the material is required only for the two flanges that create the "fork" on the Transition Piece. Meanwhile, the Slip Joint connection demands a significantly higher amount of material to manufacture the two flanges, that create the "cup -assemble", compared to the other technologies. In contrast with the prior observation, the Manufacturing cost for the threaded connection and the C1 Wedge connection may be higher when compared with the Slip-Joint that would require, excluded the rolling process, only the application of a corrosion-resistant covering layer. Comparing a possible manufacture cost between the first two technologies could be necessary a much higher accuracy for the creation of the C1 Connection design. This precision is imperative to ensure the requisite hole shape and an acceptable alignment between the holes.

In terms of Assembly cost, as known, threaded connection has the need to utilise machinery able to apply very high loads, meanwhile as illustrated in Chapter 4 the load required by the C1 Wedge technology is much lower, thus reducing the cost and time for the assembly phase. Considering the assembly of the Slip-joint technology few cases have been presented in literature, however all of them shows a much faster installation compared with other technologies reducing the costs for a lot. Similar considerations can be taken in terms of Maintenance cost, for the technologies where fasteners are required, the proper functionality of them is imperative, requiring an increase of the cost. However, considering the much lower load magnitude applied on the fasteners of the C1 wedge technology the costs can be considered lower than the threaded connection one. Slip Join Technology, on the other hand, should not require high maintenance cost, however these costs could increase in the case where

the connection is under the sea level, in that case it could become more difficult to reach the maintenance location and eventually find a solution to possible failure spots.

Threaded connection currently boasts the most expensive supply chain compared to the new technologies, thanks to the straightforward flange design and the presence of qualified companies in the production of M72 bolts. However, with the size increase of the structures, the supply chain may potentially shrink due to the challenges of redesigning production for larger bolt sizes. For the two upcoming competitors, the supply chain management could face difficulties in terms of local manufacturing. For the C1 wedge connection, the production and manufacturing of the flanges require high-precision machinery, while for the Slip Joint connection the problem lies in finding companies that can produce large flanges with accurate slopes.

When comparing the amount of research that is possible to find, threaded connection has the highest volume, considering all studies developed in the Oil&Gas industry and Wind Energy combined. Meanwhile, in literature, the C1 Connection presented different papers: the technology was studied and tested under different conditions. Due to the simplicity of Slip-Joint design, fewer papers have been published or are accessible.

The considerations have been classified on a scale from 1 to 5 and have been presented in Table 6-1, a value of 1 indicates the best-case scenario, while a value of 5 the worst-case scenario. The cost categories have been weighted in accordance with a possible impact on technology choice, considering a 10% for the material, 50% for manufacturing cost, 15% for assembling cost and a 25% for the maintenance. Similarly, the general cost result, the supply chain risk, and the need of extra research has been weighted giving a higher impact for the Costs (65%), followed by a supply chain risk of 25% and a 10% for the research.

Table 6-1 Comparison between Bolted, C1 Wedge and Slip-Joint connection

	Bolted connection	C1 wedge connection	Slip Joint connection	Weight	Total weight
Material cost	2	3	3	0.1	
Manufacturing cost	3	3	2	0.5	
Assembly cost	4	3	2	0.15	1.0
Maintenance cost	5	2	2	0.25	
Weighted cost	**3.55**	**2.65**	**2.10**	**0.65**	
Supply chain risk	**2**	**3**	**3**	**0.25**	1.0
Need of Extra Fundamental research	**1**	**3**	**4**	**0.1**	
Overall weight	**2.91**	**2.77**	**2.52**		

6.2. Conclusions

The growing demand for energy from renewable sources has led to the expansion in the size of blades used in offshore wind systems. This growth prompted engineers and designers to investigate the connection between the Monopile (MP) and the Transition Piece (TP) to assess whether the current threaded connection technology remains state-of-the-art or if alternative technologies could be viable replacements. In this thesis, various aspects of threaded technology have been examined, alongside the exploration of two emerging connection technologies, to determine their suitability for the evolving needs of the renewable energy sector: the C1 Wedge Connection from C1 Connection and the Slip-Joint from Van Oord.

Over the past decade, threaded connections have become widely prevalent in the offshore wind industry, largely due to their established use in the Oil&Gas industry, particularly for the Monopile-Transition Piece (MP-TP) connection. With the raising demand for higher load capacities in these strictures, it became imperative to assess how this technology can effectively address such challenges. Two primary solutions have emerged: increasing the size of bolts or incorporating additional bolts around the circumference. Both options entail advantages and drawbacks, primarily linked to heightened assembly and maintenance costs.

Both solutions need to refer to the designing S-N curves, which typically rely on samples of 25 or 30 [mm] diameter, subsequently adjusted through mathematical corrections. This thesis collected data from literature and, through statistical analysis, presented the statistical fatigue curve based on the collected data. Subsequently, the results have been compared with three of the main S-N curves presented in the European (*Eurocode3 EN 1993-1-9*), the British (*BS 7608-2014*) and the DNV (*DNVGL-RP-C203*) codes. Results of fatigue test on four different bolt sizes (M36, M48, M64 and M72) present in literature, taking into consideration the different post-process treatments, have been studied and compared with the respective curves. The study revealed significant disparities between the prescribed codes and the actual outcomes, particularly concerning the slope of the curve (m), the intercept ($Log\ \bar{a}$), and the standard deviation (*SD*). However, it was observed that results curves looked to fit with more accuracy the standard curves only if the heat treatment distinction is not considered and if all the fatigue results are considered together without differentiation between heat treatment or diameter size.

Comprehending the fatigue-induced stress on a single bolt is crucial for determining the optimal preload for fastener setting and predicting the bolt's fatigue life efficiently. Therefore, this thesis introduces a proposed procedure. By using the applied load range and mean load applied to the bolt, it becomes possible to calculate the load range experienced by the bolt. Subsequently, the Goodman method is applied to estimate the fatigue life of the bolts. Initial results indicate a potential correlation between actual fatigue data and the predicted outcomes, demonstrating the feasibility of the suggested approach.

In this thesis, the C1 Connection has been introduced as a significant technology with the potential to be a viable alternative to the threaded connections. The research of this technology has been divided into two crucial aspects: first, the examination and study of the design aspects including fastener and hole geometry; and second, the comprehensive understanding of large-scale behaviour achieved through Finite Element Analysis (FEA) modelling and fatigue tests on a real sample.

For the nature of the C1 connection design, the initial part of the research seeks to investigate the impact that a series of holes around the tower circumference can have on its integrity and aims to devise strategies for minimizing any adverse effects. Through analytical studies and supported by FEA models, it has been demonstrated that two key parameters significantly influence the magnitude and location of the SCF along the hole edge: the ratio between the distance between the holes and the diameter of the hole (l/D) and the shape of the hole. These findings converged to form a clear understanding of layout design, leading to the development of a double-radius hole geometry aimed at reducing the SCF. Simultaneously, the study of the fastener involved the use of a Free Body Diagram, focusing on the different loads and their correlation with the wedge slopes. This analysis resulted in the identification of two defining factors for fastener efficiency: the Load Factor (LF) and the Displacement Factor (DF). Both factors are direct functions of the wedge slopes α and β, exhibiting opposite behaviours. A correlation between the Load efficiency and the friction coefficient between the fastener surfaces has been detected, showing an increase of efficiency at the decrease of the friction between surfaces. Therefore, precise design becomes imperative to optimize the performance of the fastener.

The second phase of the C1 wedge connection study involves designing a full-scale sample based on the knowledge gained in the initial part of the study and utilizing FEA models for development. The FEA analysis enables the identification of critical stress locations and magnitudes, revealing values below the material's yield stress. This suggests that fatigue fracture is the primary failure mechanism. Following this, the sample undergoes fatigue testing, and the results are compared to predictions from standard curves. As a result, attention turns towards producing a full-scale sample for tension-tension fatigue testing. The test concludes with a run-out, and the results are compared with the DNVGL-RP-C203 class B1 curve, revealing a significant deviation from the predicted value. Subsequently, a Dye Penetrant Inspection (DPI) is conducted, and no cracks are detected in the sample.

The second technology presented in this thesis as possible contender for threaded technology for MP-TP connection is the Slip Joint by Van Oord. The technology is based on the simple design of a *"two cup"* interaction, yet the intricacy of its design demands careful attention. In this thesis the technology study has been divided into two main parts. Firstly, a geometrical study has been conducted to identify the primary factors on which the technology relies. Secondly, a series of FEA models were developed to analyse the interaction between the parameters and how this affects the stress magnitude and distribution of stress along the MP- and TP-flanges.

Geometrical analysis studied the correlation between 7 different variables: 4 diameters from the conic shapes, the two slope angles of the cones and the length of the flange. The study showed as all the calculation can be reduced to the variation of only four of them: the flanges slopes (α and β), the Monopile diameter (D_{MP}) and a multiplier factor (X) to calculate the flange length.

The interaction among these parameters has been thoroughly examined through FEA simulations, primarily by comparing results based on maximum stress and stress distribution. The analysis revealed a substantial impact on stress in relation to variations in α and β. A higher difference between these parameters corresponds to elevated stress levels, concentrated in smaller regions. Additionally, two parameters indirectly linked to the structure's geometry have

been considered in simulations: the mass of the Transition Piece and the friction between the surfaces. In the case of the mass parameter, an overall increase in stress has been highlighted though it did not lead to a failure point. On the other hand, where the previous simulations initially neglecting friction between flange surfaces, the study on the friction demonstrated that increasing the coefficient results in a decrease of maximum stress and a more smaller stress distribution along the flanges.

Having comprehended the impact of various geometrical variables and component interactions on stress, the simulation of the individual slip joint considered two distinct operating conditions: the presence of manufacturing imperfections in the flange and the examination of bending loads under high wind conditions. In the first simulation, a high stress concentration region near the imperfection edges has been identified. However, further research is required to fully understand the mechanics behind these results. In the second simulation, under high bending loads, the connection demonstrated a tendency to redistribute stress along the flanges. Importantly, the stress levels did not reach the failure stress value, and the contact area increased, facilitating improved contact between the surfaces.

Overall, the thesis aimed to underscore the similarity and drawbacks between the threaded connection and the two new technologies. As presented, both the C1 Wedge connection and Slip-Joint connection have demonstrated viable alternatives to the current state-of-the-art technology. However, as presented in Table 6-1, when comparing the three technologies in terms of cost, supply chain risk, and the need for additional research, the outcomes vary depending on two cost sub-categories (manufacturing and maintenance). The relative weight of these two parameters can significantly influence the results, either decreasing or increasing the gaps for the decision of which technology could be the most suitable in the future.

6.3. Future Work

As illustrated in 0, the entire analytical and FEA study on the Threaded Connection has been settled around the study of the bolt and nut interaction, without taking into consideration the flange and its interaction. To implement this interaction, it is necessary to develop and run new FEA analysis to verify how stress and SCF change compared to the simulations presented in this thesis. These new simulations should incorporate variations in the environment around the fasteners, such as the preload loosening of adjacent fasteners and the application of different lubrification layers. These simulations are crucial for the optimisation of the Mean Stress correction method, giving a more accurate SCF value for the reduction factor for the Goodman corrected value.

As mentioned in this thesis, the current dataset is insufficient to conduct a comprehensive statistical analysis, particularly when compared to established S-N curves in standards. Consequently, it is necessary to implement the dataset by increasing the number of fatigue test results. The initial focus involves the increase of population for the M72 bolts data with results obtained under dry environmental conditions. However, future testing needs to achieve results beyond this by incorporating environmental factors. Specifically in offshore environment, it is crucial to investigate the impact of corrosion and explore potential coating effects on fasteners. This comprehensive approach aims to increase the dataset and facilitate a more thorough analysis, contributing valuable insights to the comparison and the eventual correction of standard S-N curves.

A significant core for this project was allocated to the investigation of possible new MP-TP connection technologies as future main one. As outlined in Chapter 4, the investigation of the C1 Wedge Connection technology design has been discussed, sustained by the presentation of results from a single large-scale fatigue test. However, it is imperative to note that this result lacks statistical significance. Consequently, additional fatigue tests are essential. The primary objectives of these forthcoming tests are to establish a robust statistical analysis in a dry environment. Following this, a subsequent phase of the study will involve testing under diverse environmental conditions, with a specific emphasis on assessing the structure's performance in wet conditions. Additionally, considerations will be given to potential coating approaches, mirroring practices observed in offshore structures. Based on the insights gained from the large-scale fatigue tests and supported by Finite Element Analysis (FEA) simulations, there is an opportunity to develop a further design for fasteners and structure. This design aims to optimize the Load Factor (LF) and Displacement Factor (DF) (presented in Section 4.6), along with enhancing the stress distribution across the flanges.

Chapter 5 illustrated an FEA modelling of the Slip Joint connection, showing the stress distribution along the flanges in accordance with different parameters, however the study of these parameters can be improved through the develop of analysis with other parameter variation such as wall thickness and friction conditions. Other studies need to be focusing on the study of the structure behaviour presented in Section 5.5, focusing on different manufacturing layout and different bending loads.

Section 6.1 provides a comparison table that illustrates a weighted analysis of costs in different phases of the MP-TP connection life. However, this analysis is based on individual perspectives, necessitating a more comprehensive examination to define more accurate cost estimations.

The threaded connection represents a well-established technology in the offshore environment, with maintenance being a primary concern. To verify whether C1 Wedge connection and Slip-Joint connection exhibit low maintenance requirements, a comprehensive full-scale maintenance study is imperative. This research is designed to validate the maintenance benefits and, if applicable, uncover any potential drawbacks associated with the technology.

References

[1]   UNFCCC, 'The Paris Agreement', 2018.

[2]   'Wind energy'. Accessed: Feb. 20, 2024. [Online]. Available: https://www.irena.org/Energy-Transition/Technology/Wind-energy

[3]   'Guide to Offshore Wind Foundations: Challenges and opportunities in designing and developing offshore wind foundations both now and in the future Guide to Offshore Wind Foundations', 2021.

[4]   M. D. Esteban, J. J. Diez, J. S. López, and V. Negro, 'Why offshore wind energy?', *Renew Energy*, vol. 36, no. 2, pp. 444–450, Feb. 2011.

[5]   J. Wu, Z. X. Wang, and G. Q. Wang, 'The key technologies and development of offshore wind farm in China', *Renewable and Sustainable Energy Reviews*, vol. 34, pp. 453–462, Jun. 2014.

[6]   X. Wu *et al.*, 'Foundations of offshore wind turbines: A review', *Renewable and Sustainable Energy Reviews*, vol. 104, pp. 379–393, Apr. 2019.

[7]   'Offshore wind turbines foundation types - Wind farm BoP'. Accessed: Feb. 15, 2024. [Online]. Available: https://www.windfarmbop.com/offshore-wind-turbines-foundation-types/

[8]   M. Aleem, S. Bhattacharya, S. Biswal, and G. Prakhya, 'Gravity-based foundation for offshore wind turbines', *Wind Energy Engineering: A Handbook for Onshore and Offshore Wind Turbines*, pp. 383–396, Jan. 2023.

[9]   M. D. Esteban, B. Couñago, J. S. López-Gutiérrez, V. Negro, and F. Vellisco, 'Gravity based support structures for offshore wind turbine generators: Review of the installation process', *Ocean Engineering*, vol. 110, pp. 281–291, Dec. 2015.

[10]   'Interactive data & maps | WindEurope'. Accessed: Feb. 15, 2024. [Online]. Available: https://windeurope.org/intelligence-platform/interactive-data-and-maps/

[11]   R. J. S. Whitehouse, J. M. Harris, J. Sutherland, and J. Rees, 'The nature of scour development and scour protection at offshore windfarm foundations', *Mar Pollut Bull*, vol. 62, no. 1, pp. 73–88, Jan. 2011.

[12]   J. van der Tempel, M. Zaaijer, and H. Subroto, 'The effects of Scour on the design of Offshore Wind Turbines', 2004.

[13]   'Fécamp Gravity-Based Foundations Rise, Saipem 7000 to Handle Them | Offshore Wind'. Accessed: Feb. 15, 2024. [Online]. Available: https://www.offshorewind.biz/2022/02/14/fecamp-gravity-based-foundations-rise-saipem-7000-to-handle-them/

[14]   'The Port of Virginia welcomes first shipment of monopiles for offshore wind project | AJOT.COM'. Accessed: Feb. 15, 2024. [Online]. Available: https://www.ajot.com/news/virginia-welcome-first-shipment-of-monopiles-for-offshore-wind-project

[15] 'Tripod (foundation) - Wikipedia'. Accessed: Feb. 15, 2024. [Online]. Available: https://en.wikipedia.org/wiki/Tripod_%28foundation%29

[16] S. Aghasibayli and P. F. Brennan, 'Corrosion Damage Effects on the Structural Integrity Assessment of Offshore Structures', 2019.

[17] A. Mehmanparast, S. Lotfian, and S. P. Vipin, 'A Review of Challenges and Opportunities Associated with Bolted Flange Connections in the Offshore Wind Industry', *Metals (Basel)*, vol. 10, no. 6, p. 732, Jun. 2020.

[18] I. Lotsberg, A. Serednicki, H. Bertnes, and A. Lervik, 'Design of grouted connections for monopile offshore structures', *Stahlbau*, vol. 81, no. 9, pp. 695–704, Sep. 2012.

[19] R. Redondo and A. Mehmanparast, 'Numerical Analysis of Stress Distribution in Offshore Wind Turbine M72 Bolted Connections', *Metals (Basel)*, vol. 10, no. 5, p. 689, May 2020.

[20] P. Schaumann and M. Seidel, 'Fatigue loads of bolted ring flange connections in wind energy converters', Stahlbau.

[21] D.I.R. Eichstädt, 'Experimental and Analytical Fatigue Assessment of High-Strength Bolts for Wind Turbine Structures', 2018.

[22] 'C1 Connections | C1 Wedge Connection Working Principle'. Accessed: Feb. 19, 2024. [Online]. Available: https://c1connections.com/technology/working-principle/

[23] M. Segeren, 'Vibration-induced settlement of a slip-joint connection for offshore wind turbines', Delft University of Technology, 2018.

[24] J. D. Holmes, *Wind Loading of Structures*. CRC Press, 2018.

[25] S. Rehman and N. M. Al-Abbadi, 'Wind shear coefficients and their effect on energy production', *Energy Convers Manag*, vol. 46, no. 15–16, pp. 2578–2591, Jan. 2005.

[26] O. A. Jaramillo and M. A. Borja, 'Wind speed analysis in La Ventosa, Mexico: a bimodal probability distribution case', *Renew Energy*, vol. 29, no. 10, pp. 1613–1630, Aug. 2004.

[27] R. N. Farrugia, 'The wind shear exponent in a Mediterranean island climate', *Renew Energy*, vol. 28, no. 4, pp. 647–653, Apr. 2003.

[28] R. Xi, X. Du, P. Wang, C. Xu, E. Zhai, and S. Wang, 'Dynamic analysis of 10 MW monopile supported offshore wind turbine based on fully coupled model', *Ocean Engineering*, vol. 234, p. 109346, Aug. 2021.

[29] A. A. Shittu, A. Mehmanparast, L. Wang, K. Salonitis, and A. Kolios, 'Comparative study of structural reliability assessment methods for offshore wind turbine jacket support structures', *Applied Sciences (Switzerland)*, vol. 10, no. 3, Feb. 2020.

[30] Bickford John H, *An introduction to the design and behavior of bolted joints*. Taylor & Francis, 1995.

[31] 'Bolt (fastener) - Wikipedia'. Accessed: Jan. 25, 2024. [Online]. Available: https://en.m.wikipedia.org/wiki/Bolt_(fastener)

[32] Z. Tafheem, 'Investigation on bolt tension of flanged pipe joint subjected to bending', 2012.

[33] B. Eccles, 'Fatigue failure of bolts', 2004.

[34] S. Lochan, A. Mehmanparast, and J. Wintle, 'A review of fatigue performance of bolted connections in offshore wind turbines', *Procedia Structural Integrity*, vol. 17, pp. 276–283, Jan. 2019.

[35] R. S. Charlton, 'Threaded Fasteners Part 1: Failure Modes and Design Criteria of Connections', *NACE CORROSION*, pp. 1–11, 2011.

[36] P. Schaumann and R. Eichstädt, 'Ermüdung sehr großer HV-Schraubengarnituren (in German)', *Stahlbau*, vol. 85, no. 9, pp. 604–611, Sep. 2016.

[37] N. G. Pai and D. P. Hess, 'EXPERIMENTAL STUDY OF LOOSENING OF THREADED FASTENERS DUE TO DYNAMIC SHEAR LOADS', *J Sound Vib*, vol. 253, no. 3, pp. 585–602, Jun. 2002.

[38] T. Yokoyama, M. Olsson, S. Izumi, and S. Sakai, 'Investigation into the self-loosening behavior of bolted joint subjected to rotational loading', *Eng Fail Anal*, vol. 23, pp. 35–43, Jul. 2012.

[39] G. Dinger and C. Friedrich, 'Avoiding self-loosening failure of bolted joints with numerical assessment of local contact state', *Eng Fail Anal*, vol. 18, no. 8, pp. 2188–2200, Dec. 2011.

[40] H. Gong and J. Liu, 'Some factors affecting the loosening failure of bolted joints under vibration using finite element analysis', *Proc Inst Mech Eng C J Mech Eng Sci*, vol. 232, no. 21, pp. 3942–3953, Nov. 2018.

[41] J. Liu, H. Ouyang, Z. Feng, Z. Cai, X. Liu, and M. Zhu, 'Study on self-loosening of bolted joints excited by dynamic axial load', *Tribol Int*, vol. 115, pp. 432–451, Nov. 2017.

[42] M. Zhang, Y. Jiang, and C. H. Lee, 'Finite Element Modeling of Self-Loosening of Bolted Joints', *Journal of Mechanical Design*, vol. 129, no. 2, pp. 218–226, Feb. 2007.

[43] Y. Jiang, M. Zhang, and C. H. Lee, 'A Study of Early Stage Self-Loosening of Bolted Joints', *Journal of Mechanical Design*, vol. 125, no. 3, pp. 518–526, Sep. 2003.

[44] J. T. Stephen, M. B. Marshall, and R. Lewis, 'Relaxation of contact pressure and self-loosening in dynamic bolted joints', in *Proceedings of the Institution of Mechanical Engineers, Part C: Journal of Mechanical Engineering Science*, SAGE Publications Ltd, Sep. 2017, pp. 3462–3475.

[45] M. Marshall, R. Lewis, T. Howard, and H. Brunskill, 'Ultrasonic measurement of self-loosening in bolted joints', *Proc Inst Mech Eng C J Mech Eng Sci*, vol. 226, no. 7, pp. 1869–1884, Dec. 2011.

[46] R. I. Zadoks and X. Yu, 'AN INVESTIGATION OF THE SELF-LOOSENING BEHAVIOR OF BOLTS UNDER TRANSVERSE VIBRATION', *J Sound Vib*, vol. 208, no. 2, pp. 189–209, Nov. 1997.

[47] J. Braithwaite, I. G. Goenaga, B. Tafazzolimoghaddam, and A. Mehmanparast, 'Sensitivity analysis of friction and creep deformation effects on preload relaxation in offshore wind turbine bolted connections', *Applied Ocean Research*, vol. 101, Aug. 2020.

[48] J. Braithwaite and A. Mehmanparast, 'Analysis of Tightening Sequence Effects on Preload Behaviour of Offshore Wind Turbine M72 Bolted Connections', *Energies (Basel)*, vol. 12, no. 23, p. 4406, Nov. 2019.

[49] M. D'Antimo, M. Latour, G. F. Cavallaro, J. P. Jaspart, S. Ramhormozian, and J. F. Demonceau, 'Short- and long- term loss of preloading in slotted bolted connections', *J Constr Steel Res*, vol. 167, p. 105956, Apr. 2020.

[50] M. Li, L. Yao, S. Zhang, D. Wang, Z. He, and G. Sun, 'Study on bolt head corrosion influence on the clamping force loss of high strength bolt', *Eng Fail Anal*, vol. 129, Nov. 2021.

[51] C. Johnston and M. Doré, 'Comparison of the Fatigue Performance of Galvanised M72 Bolts With Design Standard Recommendations', *Proceedings of the International Conference on Offshore Mechanics and Arctic Engineering - OMAE*, vol. 3, pp. OMA2121-62758, Oct. 2021.

[52] D. G. Sopwith and M. I. E. Mech, 'The Distribution of Load in Screw Threads', *Proceedings of the Institution of Mechanical Engineers*, vol. 159, no. 1, pp. 373–383, Jun. 1948.

[53] B. Kenny and E. A. Patterson, 'Load and stress distribution in screw threads', *Exp Mech*, vol. 25, no. 3, pp. 208–213, Sep. 1985.

[54] J. Goodier, 'The distribution of load on the threads of screws', 1940.

[55] A. Yamamoto, 'The theory and computation of threads connection', *Youkendo*, pp. 39–54, 1980.

[56] X. Zheng and W. Xia, 'Numerical simulation of blind hole bolt connection with 3-D finite element approach', *Second International Conference on Information and Computing Science*, vol. 4, pp. 164–169, 2009.

[57] S. Lu, D. Hua, Y. Li, F. Cui, P. L.-M. P. in, and undefined 2019, 'Stiffness calculation model of thread connection considering friction factors', *Math Probl Eng*, 2019.

[58] 'BS ISO 68-2:2023 : ISO General purpose screw threads. Basic and design profiles. Inch screw threads'.

[59] L. Martinaglia, 'Schraubenverbindungen-Stand der Technik', *Schweizerische Bauzeitung*, vol. 119, pp. 107–112; 122–126, 1942.

[60] J. J. Chen and Y. S. Shih, 'A study of the helical effect on the thread connection by three dimensional finite element analysis', *Nuclear Engineering and Design*, vol. 191, no. 2, pp. 109–116, Jul. 1999.

[61] D. Zhang, G. Wang, F. Huang, and K. Zhang, 'Load-transferring mechanism and calculation theory along engaged threads of high-strength bolts under axial tension', *J Constr Steel Res*, vol. 172, p. 106153, Sep. 2020.

[62] P. Schaumann, R. Eichstädt, M. Oechsner, and F. Simonsen, 'Ermüdungsfestigkeit feuerverzinkter HV-Schrauben in Ringflanschverbindungen von Windenergieanlagen', *Stahlbau*, vol. 84, no. 12, pp. 1010–1015, Dec. 2015.

[63] D. Ungermann, D. Rademacher, M. Oechsner, F. Simonsen, S. Friedrich, and P. Lebelt, 'Feuerverzinken im Brückenbau', *Stahlbau*, vol. 84, no. 1, pp. 2–9, Jan. 2015.

[64] F. Mang, S. Herion, O. Fleischer, and E. Koch, 'Untersuchung von Zug-Druck-Kalottenlagern im Großversuch', *Stahlbau*, vol. 72, no. 1, pp. 43–49, Jan. 2003.

[65] P. Schaumann, F. M.-P. of the International, and undefined 2009, 'Fatigue resistance of high strength bolts with large diameters', *stahlbau.uni-hannover.deP Schaumann, F MartenProceedings of the International Symposium for Steel, 2009•stahlbau.uni-hannover.de*.

[66] J. Unglaub, M. Reininghaus, and K. Thiele, 'Zur Ermüdungsfestigkeit von feuerverzinkten Zugstäben mit Endgewinden', *Stahlbau*, vol. 84, no. 8, pp. 584–588, Aug. 2015.

[67] J. Luis González-Velázquez, *Fractography and Failure Analysis*. Springer, 2018.

[68] ASM Handbook Commitee, 'Fractography', 1987.

[69] C. Johnston, 'EFFECT OF LOW PRETENSION ON THE FATIGUE PERFORMANCE OF LARGE BOLTS', in *Proceedings of the International Conference on Offshore Mechanics and Arctic Engineering - OMAE*, 2022-78556.

[70] A. Mehmanparast, J. Taylor, F. Brennan, and I. Tavares, 'Experimental investigation of mechanical and fracture properties of offshore wind monopile weldments: SLIC interlaboratory test results', *Fatigue Fract Eng Mater Struct*, vol. 41, no. 12, pp. 2485–2501, Dec. 2018.

[71] A. Mehmanparast, F. Brennan, and I. Tavares, 'Fatigue crack growth rates for offshore wind monopile weldments in air and seawater: SLIC inter-laboratory test results', *Mater Des*, vol. 114, pp. 494–504, Jan. 2017.

[72] J. Braithwaite, I. G. Goenaga, B. Tafazzolimoghaddam, and A. Mehmanparast, 'Sensitivity analysis of friction and creep deformation effects on preload relaxation in offshore wind turbine bolted connections', *Applied Ocean Research*, vol. 101, p. 102225, Aug. 2020.

[73] 'Wind energy in Europe: 2021 Statistics and the outlook for 2022-2026', *Wind EUROPE*, 2022.

[74] K. E. Y. Creusen, G. Misios, J. S. Winkes, and M. Veljkovic, 'Introducing the C1 Wedge Connection', *Steel Construction*, vol. 15, no. 1, pp. 13–25, Feb. 2022.

[75] Walter D. Pilkey and Deborah F. Pilkey, *Peterson's Stress Concentration Factor*. John Wiley & Sons, Ltd, 2009.

[76] W. D. Pilkey, D. F. Pilkey, and Z. Bi, *Peterson's Stress Concentration Factors, Fourth Edition*. wiley, 2020.

[77] W. xun Fan and J. guo Wu, 'Stress concentration of a laminate weakened by multiple holes', *Compos Struct*, vol. 10, no. 4, pp. 303–319, Jan. 1988.

[78] A. Santos, 'Determination of stress concentration factors on flat plates of structural steel', *J Phys Conf Ser*, vol. 466, no. 1, 2013.

[79] U. C. Jindal, 'Reduction of stress concentration around a hole in a uniaxially loaded plate', *J Strain Anal Eng Des*, vol. 18, no. 2, pp. 135–141, 1983.

[80] K. L. Johnson, *Contact Mechanics*. Cambridge University Press, 1985.

[81] Y. Li, R. Huang, S. Zhao, and J. Wang, 'Contact pressure analysis of pin-loaded lug with clearance', *Advances in Mechanical Engineering*, vol. 14, no. 6, Jun. 2022.

[82] K. E. Y. Creusen, G. Misios, J. S. Winkes, and M. Veljkovic, 'Introducing the C1 Wedge Connection', *Steel Construction*, vol. 15, no. 1, pp. 13–25, Feb. 2022.

[83] H. Ryan, A. Annoni, J. Winkes, and A. Mehmanparast, 'Optimising design parameters for offshore wind MP-TP wedge connection technology using analytical techniques', *Ocean Engineering*, vol. 268, p. 113562, Jan. 2023.

[84] H. Ryan, A. Annoni, J. Winkes, and A. Mehmanparast, 'Optimising design parameters for offshore wind MP-TP wedge connection technology using analytical techniques', *Ocean Engineering*, vol. 268, p. 113562, Jan. 2023.

[85] L. Cheng, F. Yang, J. S. Winkes, and M. Veljkovic, 'The C1 wedge connection in towers for wind turbine structures, tensile behaviour of a segment test', *Eng Struct*, vol. 282, p. 115799, May 2023.

[86] J. Hannah and M. Jeans. Hillier, 'Applied mechanics', p. 449, 1971, Accessed: May 21, 2024.

[87] B. Hull and V. John, 'Liquid Penetrant Inspection', *Non-Destructive Testing*, pp. 7–17, 1988.

[88] M. L. A. Segeren, E. M. Lourens, A. Tsouvalas, and T. J. J. Van Der Zee, 'Investigation of a slip joint connection between the monopile and the tower of an offshore wind turbine', *IET Renewable Power Generation*, vol. 8, no. 4, pp. 422–432, May 2014.

[89] J. van der Tempel and B. lutje Schipholt, 'The Slip-Joint Connection - DOWEC', 2003.

[90] S. Suur and F. Hengeveld, 'Borssele V slip joint connection: design, certification and installation of the world's first full-size submerged slip joint', *Steel Construction*, vol. 15, no. 3, pp. 152–159, Aug. 2022.

[91] 'Van Oord shares its knowledge of innovative Slip Joint connection | Van Oord'. Accessed: Nov. 24, 2023. [Online]. Available: https://www.vanoord.com/en/updates/van-oord-shares-its-knowledge-innovative-slip-joint-connection/

[92] 'Sif Group | The Skybox Lite'. Accessed: Nov. 29, 2023. [Online]. Available: https://sif-group.com/en/news/the-skybox-lite/

[93] 'New design streamlines offshore wind farm installation'. Accessed: Dec. 04, 2023. [Online]. Available: https://www.cowi.com/solutions/energy/new-design-streamlines-offshore-wind-farm-installation

[94] 'Offshore structure comprising a coated slip joint and method for forming the same', Apr. 19, 2018

[95] S. Thakor, 'Numerical validation of experimental modal analysis of a Slip-joint connection in offshore wind turbine'. 2019.

[96] A. Cabboi, T. Kamphuis, E. van Veldhuizen, M. Segeren, and H. Hendrikse, 'Vibration-assisted decommissioning of a slip joint: Application to an offshore wind turbine', *Marine Structures*, vol. 76, p. 102931, Mar. 2021.

[97] A. Cabboi, M. Segeren, H. Hendrikse, and A. Metrikine, 'Vibration-assisted installation and decommissioning of a slip-joint', *Eng Struct*, vol. 209, p. 109949, Apr. 2020.

[98] Michal Botló, J. Brodniansky, and M. Magura, 'SLIP-JOINT CONNECTION OF CONICAL TOWER SEGMENTS – EXPERIMENTAL AND NUMERICAL ANALYSIS', *Sofia: Surveying Geology & Mining Ecology Management (SGEM)*, 2017.

[99] R.J.M Pijpers and H.M. Slot, 'Friction coefficients for steel to steel contact surfaces in air and seawater', *J Phys Conf Ser*, vol. 1669, no. 1, Jan. 2020.

[100] H. C. Ho, T. Y. Xiao, C. Chen, and K. F. Chung, 'Determination of true stress strain characteristics of structural steels using Instantaneous Area Method', *J Phys Conf Ser*, vol. 1777, Feb. 2021.

APPENDIX A

In this appendix, the fractography results developed on the seven M72 samples, as presented in Section 3.7.2 have been outlined with the most peculiar regions highlighted.
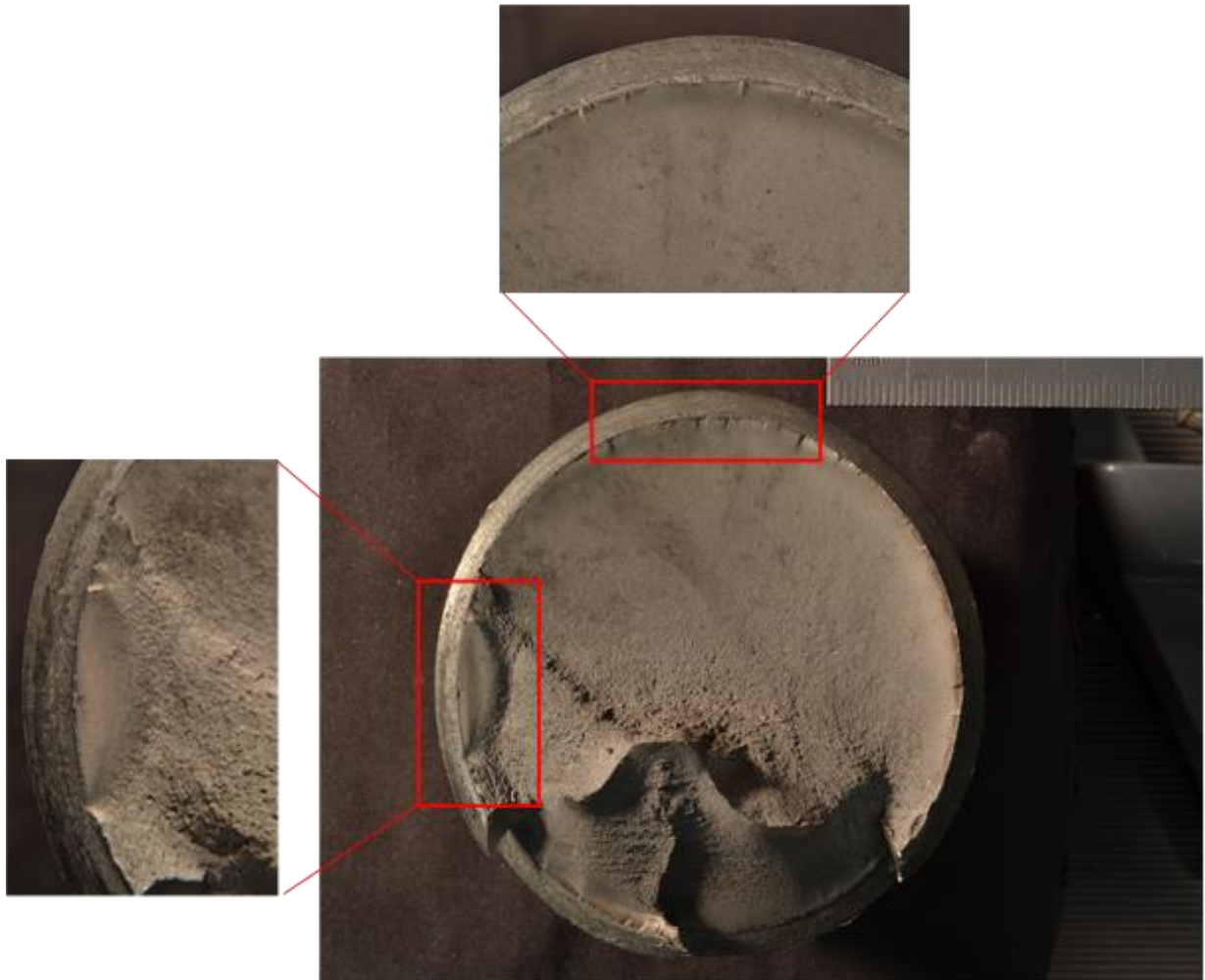

Figure A- 1: Fractography result on M01 sample

Figure A- 2: Fractography result on M02 sample

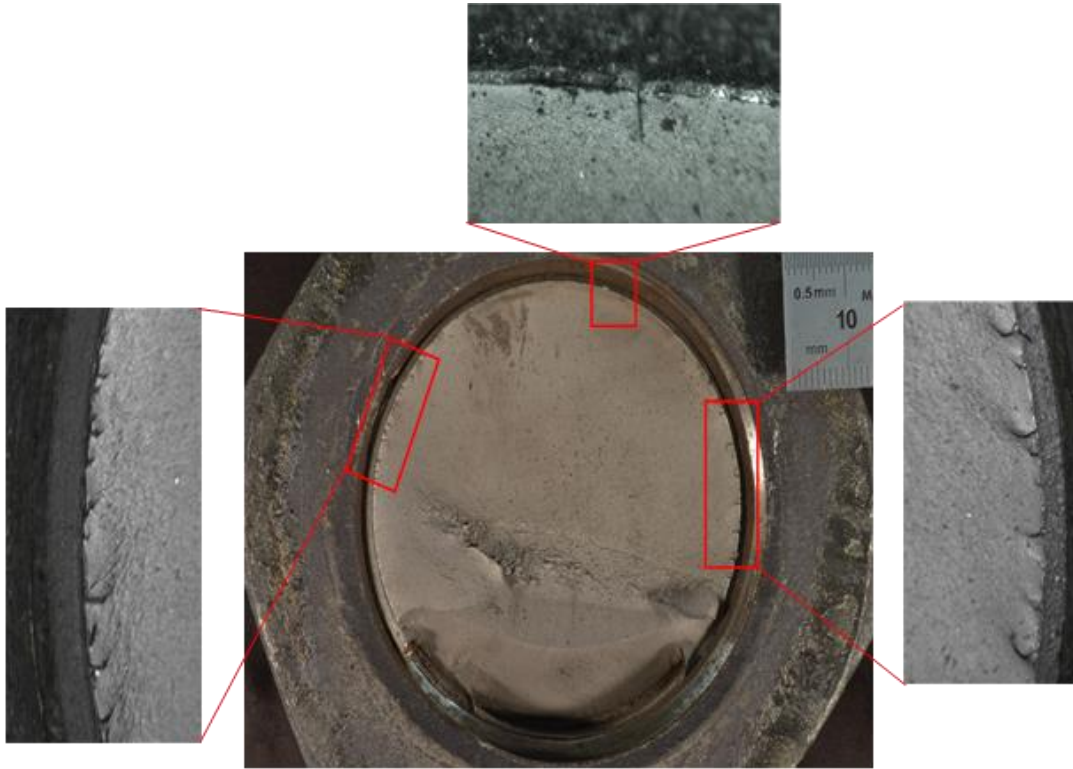Figure A- 3: Fractography result on M03 sample

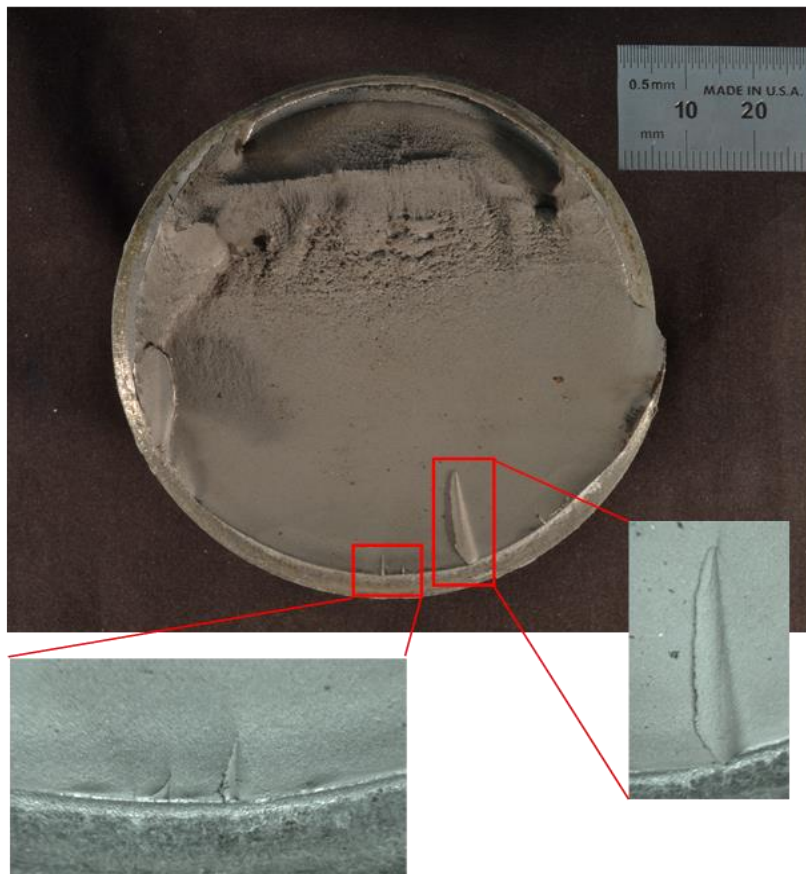Figure A- 4: Fractography result on M04 sample
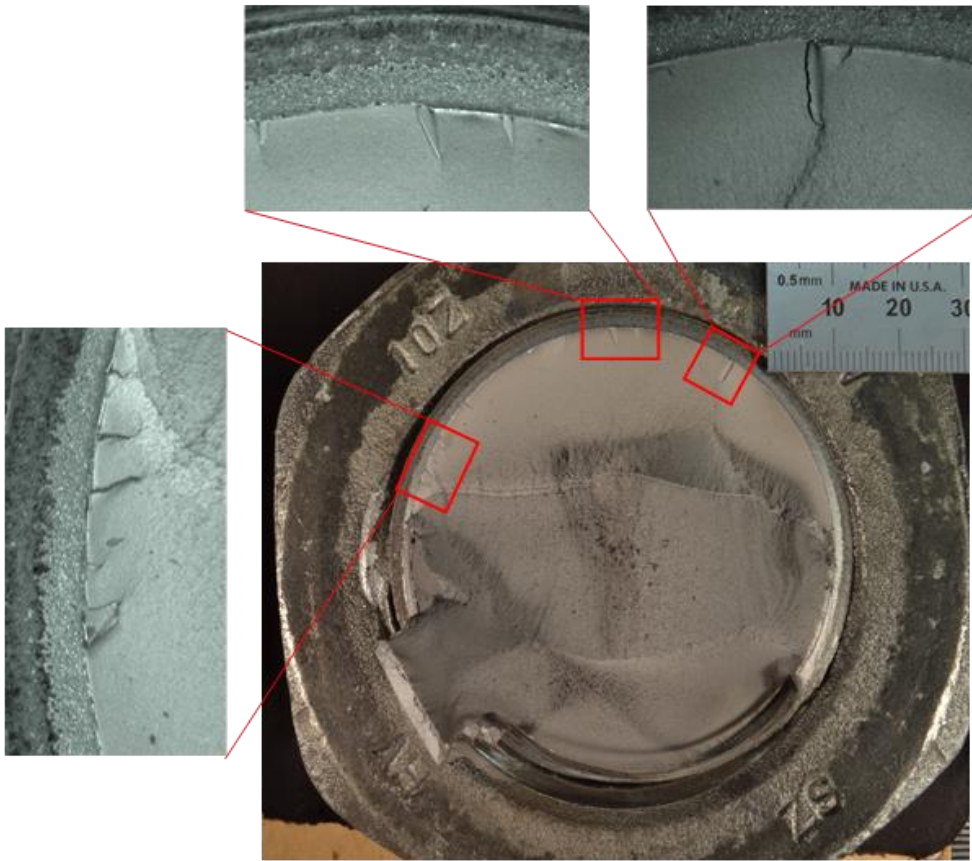

Figure A- 5: Fractography result on M05 sample

Figure A- 6: Fractography result on M06 sample

Figure A- 7: Fractography result on M07 sample